



The  
University  
Of  
Sheffield.

virtual  vehicle

The University of Sheffield  
PhD Mechanical Engineering

-

**Modelling of rolling contact fatigue  
for rail materials being subject to  
severe plastic deformation**

Author: Markus Januschewsky  
Academic Supervisor: Roger Lewis  
Academic Co-Supervisor: Christophe Pinna  
Department: Department of Mechanical Engineering  
Date of submission: 30<sup>th</sup> June 2023  
Date of revision: 19<sup>th</sup> December 2023




Federal Ministry  
Republic of Austria  
Climate Action, Environment,  
Energy, Mobility,  
Innovation and Technology

Federal Ministry  
Republic of Austria  
Labour and Economy



Das Land  
Steiermark  
Wirtschaft, Tourismus,  
Wissenschaft und Forschung



Modelling of rolling contact fatigue for rail materials being subject to severe plastic deformation © 2023 by Markus Januschewsky is licensed under Attribution-NonCommercial-NoDerivatives 4.0 International 

## **ABSTRACT OF THESIS**

Modern railway systems are a beneficial way of transport. However, the operation requires maintenance to compensate for rail degradations. Key issues of degradation regard severe plastic deformation and rolling contact fatigue, which lead to the formation of cracks. A better understanding contributes to improve maintenance and operations. Numerical simulations offer ways to predict these degradations.

State of the art for the simulation of solid mechanics is the Finite Element Method. An inherent limitation, though, is the basic assumption that the material is a continuum. Discontinuities like cracks violate this assumption. Thus, alternatives like Discrete Element Method models and Peridynamics were developed recently. These methods describe the material by a modular assembly of elements. This arrangement allows for a better modelling of discontinuities. Though, modelling of rolling contacts is a case where compressive loads dominate. This fact challenges discrete modelling approaches due to the common assumption that the failure of an element implies its removal. Another challenge models of this type face regards the validation of rolling contact fatigue.

The aim of this work was to develop a discrete element model, which is optimised for the rolling contact application. For this reason, it was called the "Discrete Element Rolling Contact" model. Based on a linear-elastic model, a fatigue capability was introduced. This capability was transferred to the set-up of the rolling contact, which highlighted the first limitation stated above. In order to address this issue, a solution was developed and validated to calibrate the model to crack closure.

Experimental results indicate that the fatigue crack growth behaviour of rails is governed by the severe plastic deformation the materials are subject to. For this reason, data of undeformed and deformed materials was parameterised and validated. A method to interpolate materials of varying degrees of deformation was introduced. Further, a method to transfer the material parameters to other materials of similar strength was developed. The result was a material library which is available for the model.

In order to transfer the fatigue parameters to the rolling contact condition, a set-up to model the behaviour of highly shear deformed material was introduced. In this way, a drawback of the adopted fatigue law was highlighted, which emphasised the requirement to weight the influence of compressive strains. Finally, a procedure for the validation of the rolling contact model was proposed.

In this work, a novel rolling contact fatigue model and a procedure for validation are presented, that consider the anisotropy of severe plastic deformation. With regard to the validation of discrete rolling contact models, the proposed procedure delivers a contribution that addresses key aspects that are not matured yet. These aspects, however, are critical for the development of dependable discrete models to predict rolling contact fatigue.



## ABBREVIATIONS

CMOD	Crack mouth opening displacement
COD	Crack opening displacement
CZM	Cohesive zone model
DEM	Discrete element method
DERC	Discrete element rolling contact model
FCG	Fatigue crack growth
FEM	Finite element method
HPT	High-pressure-torsion
LEFM	Linear elastic fracture mechanics
MBDS	Multi body dynamic simulations
MT	Middle crack tension
PD	Peridynamic
PICC	Plasticity induced crack closure
PE	Pro-eutectoid
RCF	Rolling contact fatigue
SEM	Scanning electron microscope
SPD	Severe plastic deformation
TD	Twin-disc
XFEM	Extended finite element method

## NOMENCLATURE

$A_2$	Fatigue parameter (-)
$\hat{A}_2$	Fatigue parameter for grid scaling (-)
$a$	Semi-contact length (m)
$a_{cr}$	Crack length (mm)
$a_n$	Half notch length (mm)
$B_{exp}$	Specimen thickness (mm)
$C$	Paris proportionality constant (-)
$c$	Elasticity parameter (N/m)
$COD$	Crack opening displacement (m)
$c_{init}, c_{final}$	Elasticity parameter before/after optimisation (N/m)
$c_{rem}$	Remaining elasticity parameter in case of failure (N/m)
$c_{corr}$	Volume correction factor (N/m)
$c_x$	Axial creep (-)
$d_{cr}$	Crack depth (m)
$e_{\sigma VM_n}$	Error of equivalent stress per sampling point "n" (%)
$E$	Young's modulus (Pa)
$E^*$	Combined modulus (Pa)
$f_{edge_i}$	Edge factor of element "i" (-)
$f_i$	Discrete line force (N/m)
$f_{poly}$	Factor for polynomial curve fitting of bond law (-)
$f_{\epsilon VM}$	Interpolation factor (-)
$\vec{F}_{corr_1}$	Correction force vector applied to node "1" (N/m)
$\vec{F}_{el_k_0}$	Element force "k" for state "0" (N/m)

$\vec{F}_{ext\_i\_0}$	External force attached to node "i" for state "0" (N/m)
$\vec{F}_{node\_m\_0}$	Resulting force attached to a node "i" for state "0" (N/m)
$\vec{F}_{react\_l\_0}$	Reaction force attached to node "l" for state "0" (N/m)
$F$	Applied force (N)
$F_{el}$	Normalised element force (-)
$F_{corr}$	Correction force applied to node "1" (N/m)
$F_{final}$	Maximum element force of polynomial fitting (N/m)
$F_{poly}$	Element force of polynomial fitting (N/m)
$F_{el\_max}$	Maximum of element forces (N/m)
$F_{max}$	Maximum load (N)
$F_{min}$	Minimum load (N)
$H_{exp}$	Height of specimen (m)
$H$	Hardness (HV)
$H_{num}$	Height of numerical model (m)
$h_{avg}$	Average height of a module (m)
$h_n$	Notch height (mm)
$h_0$	Height of a DEM module for state "0" (m)
$K_I$	Stress-intensity factor, Mode I (MPa m <sup>1/2</sup> )
$K_{IC}$	Critical stress intensity factor (MPa m <sup>1/2</sup> )
$K_{max}$	Maximum stress-intensity factor (MPa m <sup>1/2</sup> )
$K_{min}$	Minimum stress-intensity factor (MPa m <sup>1/2</sup> )
$K_{op}$	Opening stress-intensity factor (MPa m <sup>1/2</sup> )
$l_{avg}$	Average length of a module (m)
$l_{diag}$	Diagonal length (m)

$l_{init}$	Initial crack length of reference (m)
$l_0$	Length of a DEM module for state "0" (m)
$l_1$	Length of a DEM module for state "1" (m)
$m$	Paris exponent (-)
$m_2$	Fatigue parameter exponent (-)
$n_{adj}$	Number of adjacent, related nodes (-)
$n_{cc\_fail}$	Number of completed cycles where failure occurred (-)
$n_{cc\_i}$	Number of completed cycles, state "i" (-)
$n_{nodes}$	Number of nodes per grid (-)
$n_{poly}$	Exponent for polynomial curve fitting of bond law (-)
$n_{VM\_sample}$	Number of sampling points for parameterisation (-)
$N$	Number of load cycles of a fatigue test (-)
$N_{rot}$	Rotating speed (rpm)
$P$	Load per unit length (N/m)
$P_{max}$	Maximum load (N)
$P_{min}$	Minimum load (N)
$P_{open}$	Crack opening load (N)
$p(x)$	Normal pressure distribution along x-axis (Pa)
$p_0$	Maximum normal contact pressure (Pa)
$P_{i\_0}$	Line force normal to surface, applied to node "i" for state "0" (N/m)
$q(x)$	Tangential pressure distribution along x-axis (Pa)
$R$	Stress ratio (-)
$R_{eq}$	Equivalent stress ratio (-)

$R_{eq}$	Equivalent radius (m)
$R_1, R_2$	Radius of cylinders "1" or "2" (m)
$SVM$	Normalised Von Mises stress (-)
$\vec{u}_i$	Unit vector of element "i"
$u_{i_x}$	Unit vector component of element "i" in x-direction (-)
$V_i$	Module surface at state "i", plane strain assumption (m <sup>2</sup> )
$W_{exp}$	Specimen width (m)
$W_{num}$	Model width (m)
$w$	Contact width (m)
$\vec{x}_{i_0}$	Position vector of node "i" at state "0" (m)
$\alpha$	Plastic angular shear strain (deg)
$\alpha_a$	Crack length to width ratio (-)
$\alpha_{el_j.z}$	Angle of element "j" with respect to x-axis around z (rad)
$\beta$	Surface lowering of RCF model (mm)
$\Delta K$	Stress intensity range (Pa m <sup>1/2</sup> )
$\Delta K_{th\_eff}$	Effective stress intensity factor range threshold (MPa m <sup>1/2</sup> )
$\Delta K_{th}$	Long-crack stress intensity factor range threshold (MPa m <sup>1/2</sup> )
$\Delta n_{cc\_fail}$	Number of cycles to next element failure (-)
$\Delta n_{cc\_k\_fail}$	Number of cycles to failure for element "k" (-)
$\Delta P$	Force range (N)
$t_{proc}$	Processing time (s)
$\Delta V$	Volume ratio between two states (-)
$\Delta x$	Grid discretisation in x (m)

$\Delta x_{ref}, \Delta y_{ref}$	Elastic displacement of analytical solution (m)
$\Delta x_{res}, \Delta y_{res}$	Residual of numerical and analytical displacement (-)
$\Delta x_{num}, \Delta y_{num}$	Elastic displacement of numerical solution (m)
$\Delta \varepsilon$	Cyclic bond strain per element (-)
$\Delta \varepsilon_{avg}$	Average cyclic bond strain around crack tip (-)
$\Delta \varepsilon_{\infty}$	Numerical fatigue limit (-)
$\overline{\Delta \xi}_{k_01}$	Displacement vector (m), for element "k", between states "0" and "1"
$\varepsilon_{k_1}$	Strain of element "k" for state "1" (-)
$\varepsilon_{off}$	Offset strain in case of failure (-)
$\varepsilon_{final}$	Minimum strain of polynomial fitting interval (-)
$\varepsilon_{xx}, \varepsilon_{yy}$	Strains in x and y direction (-)
$\varepsilon_{VM}$	Von Mises strain (-)
$\varepsilon^+$	Maximum tensile strain per load cycle (-)
$\varepsilon^-$	Maximum compressive strain per load cycle (-)
$\varepsilon_{crit}$	Critical strain (-)
$\varepsilon_{trans}$	Transition strain (-)
$\delta_i$	Horizon associated to a node "i" (-)
$\gamma_{xy}$	Engineering shear strain (-)
$\vec{\xi}_{k_0}$	Element vector "k" for state "0" (m)
$\zeta$	Fatigue crack growth phase per element (-)
$\lambda$	Remaining life per element (-)
$\lambda_{k_{fail}}$	Remaining life per element "k" for failed state (-)
$\lambda_{k_i}$	Remaining life per element "k" for state "i" (-)

$\mu$	Coefficient of friction (-)
$\nu$	Poisson ratio of material (-)
$\theta_m$	Strain angle of DEM module (rad)
$\bar{\theta}$	Mean strain angle of DEM module (rad)
$\rho$	Angle of volume correction force (deg)
$\Sigma Resid_{el}$	Residual of elastic deformation (-)
$\Sigma Resid_{force}$	Sum of residuals of force vectors (N/m)
$\Sigma Resid_{svm}$	Sum of residuals of stress vectors (Pa)
$\sigma$	Applied stress (Pa)
$\sigma_{max}$	Maximum stress (Pa)
$\sigma_{min}$	Minimum stress (Pa)
$\sigma_{ij}^I$	Single-mode stress, Mode I, in direction ij (Pa)
$\sigma_{VM}$	Von Mises stress (Pa)
$\vec{\sigma}_{VM\_Ref}$	Vector of Von Mises stresses of reference (Pa)
$\sigma_{VM\_Ref\_max}$	Maximum Von Mises stresses of reference (Pa)
$\sigma_{VM\_Ref\_n}$	Von Mises stresses of reference per point "n" (Pa)
$\vec{\sigma}_{VM\_Sim}$	Vector of Von Mises stresses of simulation (Pa)
$\sigma_{VM\_Sim\_n}$	Von Mises stresses of simulation per point "n" (Pa)
$\sigma_{xx}$	Normal stress in x-direction (Pa), likewise $\sigma_{yy}$ and $\sigma_{zz}$
$\sigma_{yx}$	Shear stress within y-plane, directing towards x-direction (Pa), likewise $\sigma_{xy}$ , $\sigma_{zy}$
$\sigma_y$	Yield stress (Pa)
$T_\sigma$	Stress tensor (Pa)

# TABLE OF CONTENTS

Abstract of thesis .....	iii
Abbreviations.....	v
Nomenclature.....	vi
Table of Contents .....	xii
Acknowledgements .....	xv
1 Introduction .....	1
2 State of the art.....	3
2.1 Rails and wheels in service .....	3
2.1.1 Severe plastic deformation (SPD) and strain-hardening....	4
2.1.2 Rolling contact fatigue (RCF).....	9
2.1.3 Fatigue crack growth (FCG).....	10
2.1.4 Anisotropy of FCG .....	14
2.1.5 Multiple FCG.....	15
2.1.6 Crack closure.....	17
2.1.7 External influences and lubricants .....	20
2.1.8 Interaction of fatigue and wear.....	21
2.2 Modelling of crack initiation and growth.....	23
2.2.1 Finite element method (FEM) .....	24
2.2.2 Discrete element methods (DEM).....	25
2.2.3 Peridynamics .....	26
2.2.4 Review: Bond law set-up in the literature.....	28
2.2.5 Brick model .....	31
2.2.6 Wedge model.....	31
3 Objective .....	33
3.1 Research gap.....	33
3.2 Modelling objective.....	35
4 Rolling contact model.....	37
4.1 Model type selection.....	39
4.2 Basic model assembly.....	42
4.3 Grid pre-processing.....	44
4.4 Visualisation .....	44
4.5 Basic equations .....	46
4.6 Numerical process.....	48
4.7 Basic boundary conditions .....	50
4.8 Load modelling .....	51



4.9	Post-processing of stresses .....	54
4.10	Discretisation of rolling contact.....	61
4.11	Lateral periodic boundary condition.....	61
4.12	Elastic parameterisation .....	63
4.13	Verification of rolling contact simulation .....	66
5	Fatigue Model .....	70
5.1	Modelling of RCF.....	70
5.1.1	Fatigue model.....	71
5.1.2	Initial fatigue capability.....	74
5.1.3	FCG activation.....	78
5.1.4	Load cycle management.....	80
5.1.5	Advanced test of fatigue capability: Mode I.....	82
5.1.6	Improved elastic parameterisation .....	85
5.1.7	Initial rolling contact fatigue simulation .....	88
5.1.8	Crack closure modelling .....	92
5.1.9	Equivalent stress ratio .....	104
5.2	Assessment of orthotropic fatigue crack growth .....	107
5.2.1	Study of periodic boundary condition .....	108
5.2.2	Study of initial crack definition.....	110
5.2.3	Study of grid discretisation.....	112
5.2.4	Study of coefficient of traction.....	114
5.2.5	Study of FCG activation.....	116
5.2.6	Study of grid orientation.....	122
6	Parameterisation of fatigue crack growth .....	127
6.1	Initial FCG parameterisation.....	127
6.2	Near-threshold modelling .....	135
6.3	Scaling of FCG parameters.....	139
6.4	FCG parameters for RCF simulation .....	143
6.5	Interpolation as a function of shear deformation .....	148
6.6	FCG parameters of similar materials.....	152
7	Modelling of severe plastic deformation .....	156
7.1	Explicit modelling of SPD .....	156
7.1.1	Shear deformation of a truss-like grid .....	157
7.1.2	Volume correction.....	159
7.1.3	Limitation of explicit SPD modelling.....	163
7.2	Implicit modelling of SPD .....	164
8	Modelling RCF as a function of SPD .....	169

8.1	Validation case .....	169
8.2	Layer-based concept.....	174
8.2.1	Test set-up for highly-deformed material .....	175
8.2.2	Test set-up for lowly-deformed material.....	179
8.2.3	Review: Modelling of compressive strain weight.....	181
8.2.4	Parameter study of compressive strain weight .....	182
8.2.5	Summary and conclusion.....	184
8.3	Assessment of the DERC model.....	187
9	Outlook.....	192
10	Conclusion .....	194
	References.....	195

## **ACKNOWLEDGEMENTS**

This dissertation has received funding from the Shift2Rail Joint Undertaking (JU) under grant agreement No 101012456. The JU receives support from the European Union's Horizon 2020 research and innovation programme and the Shift2Rail JU members other than the Union. In Austria, the dissertation was also funded by the program "Mobilität der Zukunft" of the Austrian Federal Ministry for Climate Action (BMK) as well as by the Province Styria (Land Steiermark) and the Styrian Business Promotion Agency (SFG).

The dissertation was written at Virtual Vehicle Research GmbH in Graz and partially funded within the COMET K2 Competence Centers for Excellent Technologies from the Austrian Federal Ministry for Climate Action (BMK), the Austrian Federal Ministry for Labour and Economy (BMAW), the Province of Styria (Dept. 12) and the Styrian Business Promotion Agency (SFG). The Austrian Research Promotion Agency (FFG) was authorised for the programme management.

I thank my supervisors Roger Lewis from The University of Sheffield for the excellent supervision and for encouraging me during the journey of my PhD. Furthermore, I thank Christophe Pinna for the co-supervision.

I thank my colleagues Gerald Trummer and Klaus Six from Virtual Vehicle Research GmbH for their contribution and the discussions that paved the way to this work. I thank my colleagues Josef Fuchs, Alexander Meierhofer, Gabor Müller, Dietmar Hartwich, Hamed Davoodi Jooneghani and Rijad Kovacevic for their assistance. Further, I thank Stephan Scheriau and voestalpine Rail Technology GmbH for the support of this work.

Finally, I thank my wife Melissa for her encouragement, patience, and her invaluable support.

Markus Januschewsky

# 1 INTRODUCTION

Modern railway systems offer many advantages for the transport of passengers and freight, especially when considering socio-economic-, environmental- and safety issues (1). Being a technical system, service has an impact, leading to a degradation of wheels and rails. This impact is manifest in rolling contact fatigue (RCF). Besides single RCF cracks, also patterns of multiple fatigue cracks emerge. As a result, maintenance actions are required that affect operating costs and operations. The goal of research is to provide reliable methods of prediction to support maintenance.

This requires a better understanding of the reasons for the development of RCF. A major contribution is that due to the high contact forces in the wheel-rail interface, materials are subject to severe plastic deformation (SPD). This effect leads to an anisotropy of fatigue crack growth (FCG), that governs other degradation forms like RCF and wear. Further, crack face interaction like crack closure plays a role in RCF that must be considered.

The question is how to develop an RCF model that considers these aspects. The desired RCF model must be capable of capturing the FCG anisotropy of SPD, of dealing with multiple cracks and contact cycles and of considering crack closure effects. The development of such a prediction model is the objective of this work.

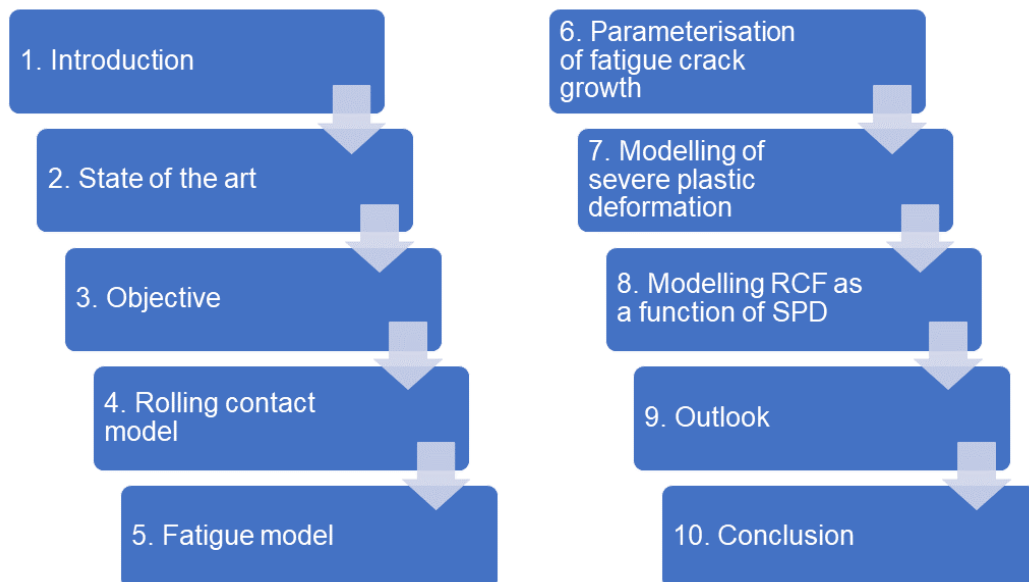


Figure 1 – Overview on the procedure of model development.

In order to deal with multiple cracks, modelling approaches like Discrete Element Method models or Peridynamics are suited. However, modelling of a compressive load regime, SPD, and the anisotropy of FCG impose special challenges. These challenges were dealt with by following the procedure displayed in Figure 1.

The state of the art regarding degradations resulting from railway operations and regarding modelling techniques was assessed (see chapter 2). The research gap and modelling objectives were discussed (see chapter 3). A linear-elastic rolling contact model was set up, including a post-processing of stresses (see chapter 4). A fatigue model was implemented to the rolling contact model, and a constitutive element set-up was introduced and validated (see chapter 5).

The fatigue model was parameterised by experimental FCG data to capture the anisotropy imposed by SPD (see chapter 6). The effect of SPD was modelled in an implicit way for a test case (see chapter 7). An RCF validation case was defined, the limitations of the anisotropic FCG modelling were elaborated and the overall model development was assessed (see chapter 8). Finally, an outlook was provided (see chapter 9) and a conclusion was made (see chapter 10).

## 2 STATE OF THE ART

The aim of this chapter is to provide an overview of the degradation phenomena that rails face due to service (see section 2.1). Based on that overview, different modelling approaches are assessed to capture these phenomena (see section 2.2).

### 2.1 Rails and wheels in service

The preferred material for rails and wheels in Europe is pearlitic steel with a carbon content of 0.5 to 0.8% (1). The main mechanical properties are tensile strength, ductility, resilience, toughness, and hardness, which are discussed by Callister and Rethwisch (2). The two latter properties are significant regarding the resistance to fatigue cracking (toughness) and wear (hardness).

Loads introduced by train services are induced by cyclic rolling and sliding, resulting in multi-dimensional shear- and compression forces which are applied to the contact patch. The patch position(s) vary and are between the rail and wheel tread, flange, or field sides. Within the material, stresses and strains are evoked. Factors defining the contact loads are the type of operation, equipment used, contact geometry, creep, and ambient conditions, representing a complex condition. This is highlighted by the compilation of Lewis and Olofsson (1).

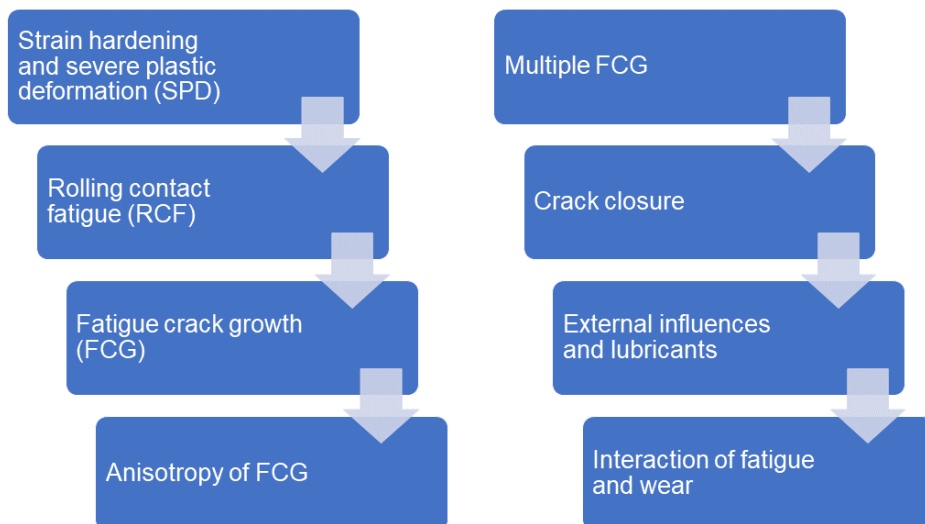


Figure 2 – Overview on the degradation phenomena discussed in section 2.1.

In this section, the impact of service conditions is considered, and the tribological system between wheels and rail is examined (see Figure 2). In section 2.1.1, the phenomena of plastic deformation, SPD and strain-hardening are discussed, which contribute to RCF (see section 2.1.2), which is a form of fatigue crack growth (FCG, see section 2.1.3). Due to the occurrence of SPD, rail- and wheel materials are subject to an anisotropy of FCG (see section 2.1.4). Phenomena with more than one single crack are discussed (see section 2.1.5). The aspect of crack closure is added (see section 2.1.6). External influences and lubricants are discussed (see section 2.1.7). Finally, wear and the interaction between wear and RCF is introduced (see section 2.1.8).

### **2.1.1 Severe plastic deformation (SPD) and strain-hardening**

The high loads at and below the contact surfaces to several millimetres depth lead to elastic-, plastic deformation and ratcheting, resulting in a severely plastically deformed layer (3). This deformation is closely associated with strain-hardening. The material response is displayed in principle in the load-deformation diagram below (see Figure 3).

- If the load is below the elastic limit being defined by yield strength, then only elastic deformation occurs. For cyclic conditions, high-cycle fatigue failure is possible.
- If the load is higher than that, plastic deformation and strain-hardening arise. However, for loads being below the elastic shakedown limit and after an initial plastic strain, the material response is purely elastic again.
- For loads higher than that and lower than the plastic shakedown limit, there can be a cumulative plastic deformation (open / closed loop). Low-cycle fatigue is feasible.
- For loads above the plastic shakedown limit (ratcheting threshold), directional plastic deformation (anisotropic response) accumulates constantly, resulting in ratcheting.

Usually SPD is not final, but a precondition for the damage forms of rolling contact fatigue (see section 2.1.2) and wear (1).

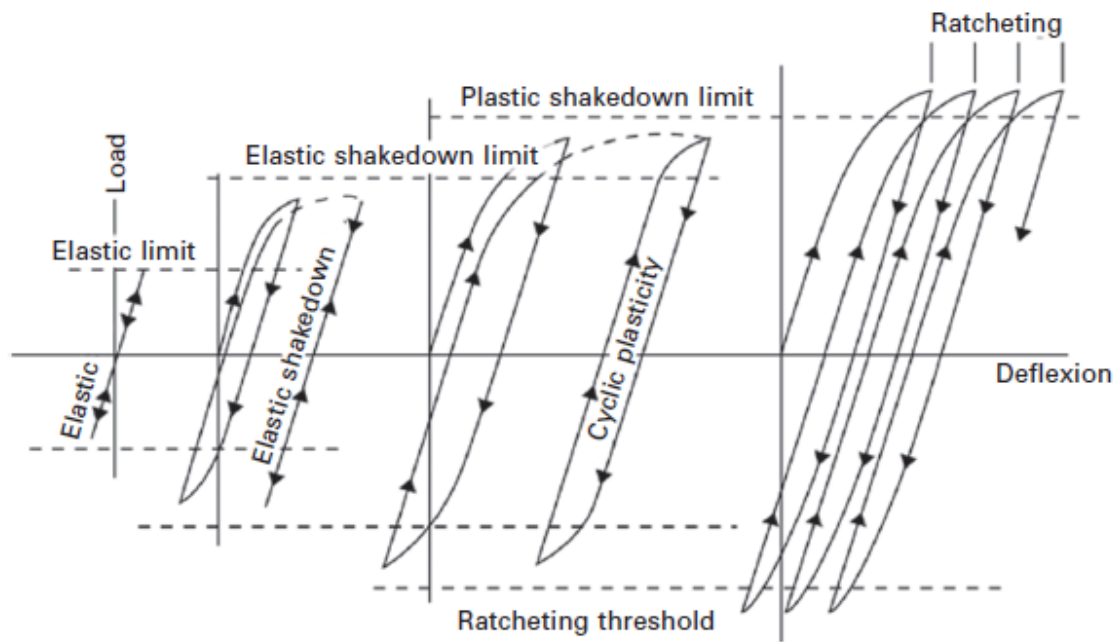


**Figure 3 - Load-deformation diagrams, representing regimes leading to severe plastic deformation of a ductile material, modified from (3).**

In pearlitic steels subject to SPD, the high shear and compression forces result in shear strains of up to 1000 % (3). This has a profound impact on the microstructure. For rails, this concerns thin layers of material close to the surface (“up to 3 mm in depth” (4)) of the rail head and gauge corner and respectively the wheel’s counter parts. That material looks and behaves significantly differently than the original one.

The impact of SPD on the microstructure of pearlitic steels can be evaluated in different ways. One way is to examine worn rail steel specimens (see Figure 4). The result of SPD on pearlitic microstructures is that substructures like pro-eutectoid (PE) ferrite grains and pearlitic nodules are significantly bent, elongated and aligned to the shear layers (3) (see Figure 4). With continuing service, the material is subject to fragmentation and compaction, giving rise to crack initiation and growth. Preferred sites therefore are the weakest and most highly strained parts, which is the PE ferrite phase (see Figure 4).



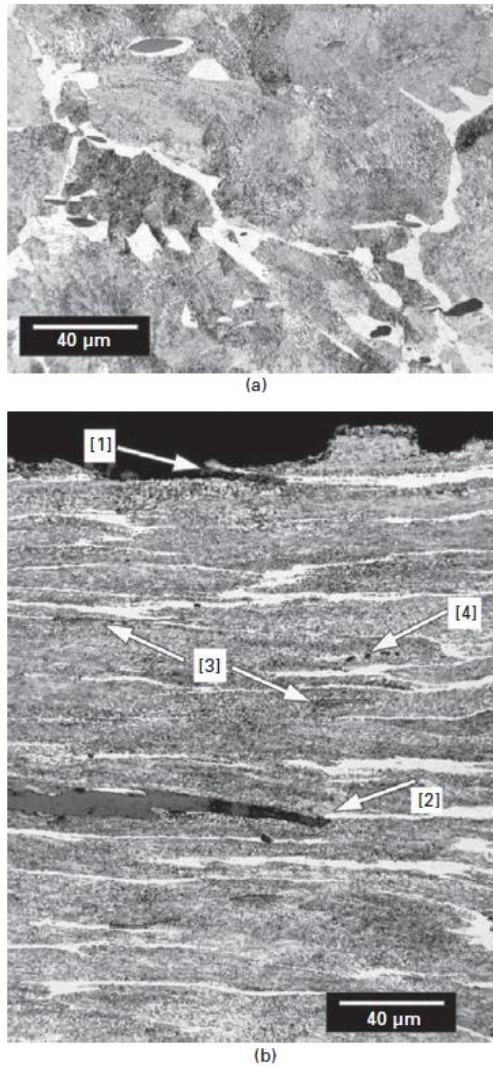


**Figure 4 - Micrographs of undeformed (a) and severely deformed (b) rail grade R220 from the field, modified from (3). The white phases represent pro-eutectoid ferrite being preferred sites of crack initiation [1] and [2], the grey phases formations of pearlite. Ductile- [3] and brittle inclusions [4] are marked.**

The examination of worn rails from service is challenging due to operational requirements, costs, and the variety of influences the rails are subject to. An alternative to examine the impact of SPD is to perform laboratory tests. Two methods of choice for reproducing similar conditions are high-pressure-torsion (HPT) and twin-disc (TD) tests.

In HPT, a material disc is subject to a high pressure before a torsion torque is applied to severely shear-deform the specimen. In this way, SPD microstructures can be processed, which leads to an increase of hardness. The advantages of

HPT are that the deformation history is known and that the SPD layer is thicker than for rails, which facilitates specific material tests (5).

In TD testing, two counter-rotating discs are used to reproduce a defined rolling contact condition. It offers the advantage of scalability, which makes testing more economical and convenient. A TD result is illustrated in Figure 5, where the aligned morphology resulting from the high shear strains as well as related crack initiation sites are displayed (3). There is evidence that cracks do not only preferably initiate, but also propagate and branch along highly strained PE ferrite phases (see Figure 5).

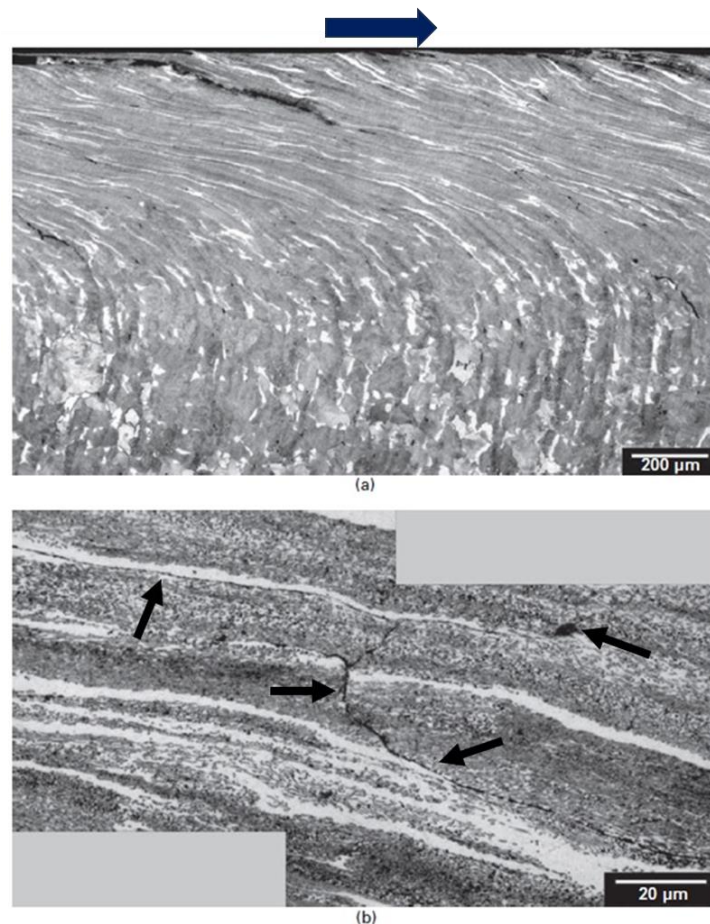


**Figure 5 - Micrographs of a severely deformed rail steel (R220) from twin disc testing with a creepage of -1%, adapted from (3). The rolling direction is marked by a blue arrow. The white phases represent pro-eutectoid ferrite, the greys formations of pearlite. An inclusion (right) and a branching crack (middle) are marked by black arrows.**

Strain- respectively work hardening is mutually related to the process of plastic deformation and corresponds to the strains associated to SPD (see Figure 5). It is

governed by the contact conditions in the wheel-rail interface and the material strength. As soon as the elastic limit of the material is exceeded (see Figure 3), the material below the contact responds with hardening (3).

By examining rail specimens from service, the differences in surface hardness show an increase between 30-70% (1,4). Garnham and Davis highlighted this effect for the rail grades BS11 and R260 (see Figure 6). The measurements suggest the hardening to affect depths up to 5 mm. The figure displays the impact of the contact condition, which is reflected by the different hardening curves for the gauge side and corner. It is interesting that the zones above the gauge corner, which exhibit the highest degree of hardening, are most susceptible to RCF cracks (6).

This suggests a correlation of strain-hardening and the RCF behaviour (see section 2.1.2). Further, Leitner et al. (5) highlight a correlation between hardness and FCG rates (see section 2.1.3) of similar rail materials. This fact reflects an anisotropy of FCG (see section 2.1.4).

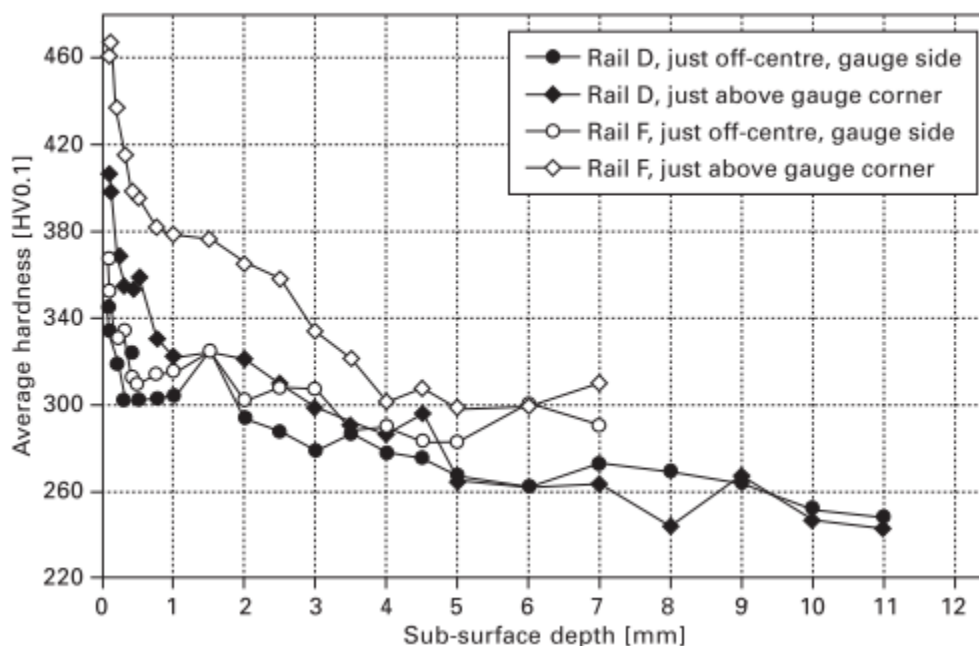


Figure 6 – Hardness profiles of rails from service, adapted from (6). Material “D” refers to rail grade BS11, material “F” to R260. The measurements were performed at different zones of the rails.

### 2.1.2 Rolling contact fatigue (RCF)

Fatigue is the degradation of material's inherent properties due to dynamic, cyclic loads. This leads to the initiation and propagation of cracks. As a result, failure can occur at loads lower than the maximum tensile- or yield stress. Fatigue is potentially catastrophic as fracture emerges without warning. Therefore, inspections aiming for the detection of cracks are required for maintaining safe railway operation.

In the wheel-rail contact, cyclic rolling and sliding loads lead to SPD (see section 2.1.1) on and below the rolling contact surface. This leads to a degradation of mechanical properties, represented by micro-crack initiation and propagation. This phenomenon is called rolling contact fatigue. A micrograph of a rail steel specimen subject to TD testing illustrates effects of RCF (see Figure 5 a).

The cracks can be classified for wheels and rails according to their origin, either as surface- (e.g. head checks for rails) or subsurface cracks (7). The former ones are more frequent, less severe and tend at first to grow at a shallow angle relative to the surface (see Figure 7, case A). These cracks may be subject to delamination and wear (see section 2.1.8). In the next stage, they might grow into the depth (see Figure 7, case B). There is evidence that the mode of crack propagation (wear or RCF) is governed by the degree of plastic deformation (8). Subsurface cracks tend to deviate into the bulk material, either into the hub of wheels or the head and web of rails, with potentially catastrophic results (see Figure 7, case C). Subsurface cracks may interact with surface cracks (see Figure 7, case D) (7).

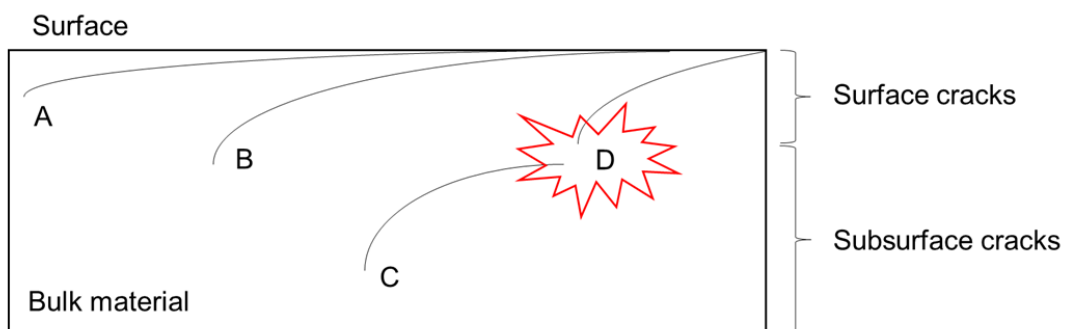


**Figure 7 – Crack modes: Surface cracks that tend to develop into a wear flake (A) or an RCF crack (B), subsurface crack with a tendency to grow into the bulk material (C), interaction between surface- and subsurface cracks (D).**

On rails, RCF takes place frequently in curved tracks at the gauge side. However, it is difficult to predict RCF accurately as the phenomenon is complex. Factors governing RCF are the triaxial stresses and strains, SPD, and the interaction with wear. Further crack face friction, anisotropy and varying environmental conditions are notable as well as.

Regarding the literature available on RCF, Lewis et al. (1), as well as Sadeghi et al. (9) give a comprehensive insight into RCF. With the scope of modelling and prediction, RCF crack initiation and the corresponding role of SPD are considered in several publications (8,10,11). The role of microstructure is considered in (11,12).

### **2.1.3 Fatigue crack growth (FCG)**

Cracks are not necessarily hazardous. Every engineering material contains a degree of cracking at micro- or nano scale from the beginning on. What makes cracks hazardous is their size and the way they grow during extended periods of service. This phenomenon is called fatigue crack growth, which is part of RCF (see section 2.1.2).

In the attempt to understand fatigue, it is paramount to describe the characteristic of the load. That can be of three types, including opening (Mode I), shearing (Mode II) and tearing (Mode III), which are defined by capital letters in this work. Unfortunately, reality is often more complex, and therefore a combination of modes might have to be considered.

In order to explain cyclic damage mechanisms, the research area of fracture mechanics emerged in the 1950's (13). It represents a top-down approach, working on macroscale. They do not cover physics and microstructure appropriately, which in fact have a significant impact. Usually, empirical adjustments are applied to address that shortcoming. An alternative to fracture mechanics are dislocation- or atomistic mechanics, working on micro- and nano scale. Those theories are more precise, but the suitability for engineering is limited.

When investigating FCG in a ductile polycrystalline material like steel, the development of cracks can be classified according to Chowdhury and Sehitoglu in two stages (13): In Stage I, there is a strong dependency on microstructure. The initiation of cracks can be explained on crystallographic level, by the means of dislocation movements on slip systems, which in the case of wheels and rails is often a result of SPD. The initiated crack covers only a few material grains and is still very small. For standard set-ups of FCG experiments, a Stage I crack length is

assumed to be below 500  $\mu\text{m}$  and is not detectable by common methods of non-destructive testing (13). In Stage II, FCG is proposed to be “microstructure independent”. There, the propagating crack already covers a multitude of grains and becomes relevant for most engineering applications. This is where the theory of linear elastic fracture mechanics (LEFM) takes charge.

However, the impact of microstructure dependency becomes more complex when it comes to materials being subject to SPD, which is addressed by Leitner (14). For pearlitic steels, SPD results in a refinement of the grain microstructure. Though, the degree of grain refinement does not necessarily determine the resistance to FCG. According to the findings of Leitner, the resistance depends primarily on the FCG orientation (14), which is modelled in chapter 6. In the case of SPD, a transition between Stages I and II cannot be defined or approximated by a specific crack length.

The theory of LEFM is based on several assumptions. The first one regards the negligible effect plasticity has on overall FCG behaviour. Hence, the material basically fractures in a linear-elastic way. This assumption is justified for material subject to SPD by the fact that the plastic region around the crack tip is small compared to the crack geometry. Furthermore, like Fletcher et al. argue (7), the situation is comparable to material that was plastically deformed during processing and cracks elastically during operation.

As a result, FCG depends on factors like stress and crack geometry, but not on plasticity (13). Another assumption states that there is only one single load parameter (constant stress amplitude), which is a contradiction to variable amplitude loads present in most engineering applications. That concept is called similitude. Both assumptions are the justification for applying LEFM to fatigue problems, which is described in Anderson’s work about fracture mechanics (15).

Within the frame of LEFM, there are different approaches to model FCG (e.g. energy criterion, stress intensity). In the 1950’s Irwin and Williams developed concepts to describe the stress and strain at a crack tip by one single parameter, which led to the introduction of a stress-intensity factor,  $K_I$  (15).

$$K_I = \sigma\sqrt{\pi a_{cr}}$$

**Equation 1**

The subscript of  $K$  refers to the type of load (Mode I-III, see above),  $\sigma$  to the applied stress and  $a_{cr}$  to the crack length of a CT specimen (16). With it, the entire stress distribution at a crack tip for plane stress or plane strain conditions around a linear-elastic element can be calculated, hence normal and shear stresses.

$K_I$  to  $K_{III}$  can be calculated analytically for simple problems (closed-form solution) like specimen according to ASTM standard E647 (16). Therefore, the applied load, specimen geometry and crack length must be known (14). For complex conditions,  $K_I$  to  $K_{III}$  can be estimated by experimental- or numerical analysis (15). Further, an equivalent stress intensity factor may be derived to describe the stress field around a crack for a mixed mode loading condition. Fletcher et al. provide a methodical overview on that topic regarding RCF applications (7). In case of a mixed-mode condition, every stress term ( $\sigma_{ij}$ ) can be composed of the sum of the single-mode stresses ( $\sigma_{ij}^I, \sigma_{ij}^II, \sigma_{ij}^III$ ).

The cyclic constant amplitude load itself can be described by a ratio of minimum- and a maximum stress called R-ratio (15), stress ratio (14) or load ratio (13),  $R$ . The minimum- and maximum stresses ( $\sigma_{min}, \sigma_{max}$ ) can also be described by stress intensity factors ( $K_{min}, K_{max}$ ). By dividing  $K_{min}$  by  $K_{max}$ ,  $R$  can be defined.

$$R = \frac{F_{min}}{F_{max}} = \frac{\sigma_{min}}{\sigma_{max}} = \frac{K_{min}}{K_{max}}$$

**Equation 2**

An equivalent parameter to define cyclic loads is the stress intensity factor range,  $\Delta K$ , which, like  $R$ , represents the driving force for the crack propagation in FCG Stage II (15).  $R$  and  $\Delta K$  are dependent on each other. If one of them is chosen, the other parameter is determined.

$$\Delta K = K_{max} - K_{min}$$

**Equation 3**

Based on that, the fatigue crack advance,  $da$ , per load cycle,  $dN$ , can be defined by:

$$\frac{da}{dN} = f(\Delta K, R)$$

**Equation 4**

Based on that relationship, the standard equation for calculating the FCG rate in dependence of the stress intensity range was formulated by Paris et al. ("Paris-Erdogan equation"). In that empirical equation,  $C$  is the Paris proportionality constant and  $m$  the Paris exponent. Both coefficients are material properties that characterise the behaviour of damage tolerance. They are obtained experimentally for a specific stress ratio,  $R$ .

$$\frac{da}{dN} = C * \Delta K^m$$

Equation 5

Based on that fundamental equation and on the assumption of similitude, the FCG behaviour depends only on the material coefficients ( $C$ ,  $m$ ) and the applied load. With it, the FCG rate can be determined. One consideration regards the load at which Stage I micro-cracks start propagating. Therefore, a threshold stress intensity factor range  $\Delta K_{th}$  was defined. Below that range, crack propagation is negligible (15).

Another consideration concerns fracture, i.e. Stage III. For a Mode I crack, that occurs when the stress intensity factor,  $K_I$ , matches a critical stress intensity factor  $K_{Ic}$  ( $K_I = K_{Ic}$ ), which is also a measure for the material resistance, comparable to the fracture toughness.  $K_{Ic}$  is assumed to be a size-independent material property (15). This concept applies to cracks of Modes II and III equivalently.

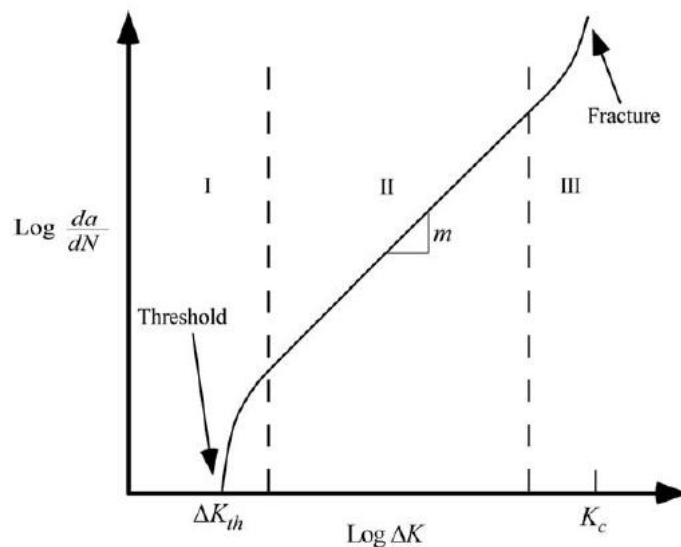


Figure 8 - Typical fatigue crack growth diagram for a steel material, modified from (15). Stage I refers to near-threshold, Stage II to the Paris regime, Stage III to fracture.

FCG can be summarised in a double-logarithmic diagram (see Figure 8). There, crack growth is dependent on the stress intensity factor range, hence the applied cyclic loads. The diagram is composed of three stages. Stage I is referred to as near-threshold, Stage II to Paris regime where the basic equation is valid. There,



coefficient  $m$  represents the slope of the logarithmic diagram. Stage III refers to fracture.

In order to summarise, LEFM is state of the art when it comes to modelling FCG in pearlitic steels. However, its capability is limited when it comes to the integration of microstructural phenomena. In such a case, LEFM must be extended by what Chowdhury calls geometrical- or plasticity-based (crack plasticity) models (13).

In the available literature, the evolution of FCG in pearlitic steels with respect to microstructure was evaluated in several publications. A review on fracture mechanisms of rails and wheels in general is given by Zerbst et al. in (17).

#### 2.1.4 Anisotropy of FCG

Rail service has a fundamental impact on rail and wheel microstructure, changing the almost isotropic original material into an anisotropic one. This concerns thin layers being close to the running surfaces of rails and wheels. The bent, aligned and fragmented microstructure (see Figure 4 and Figure 5) represents a different material compared to the original one. Fatigue cracks seem to run preferably along predefined paths being parallel to the main shear direction, which represents an anisotropy of FCG.

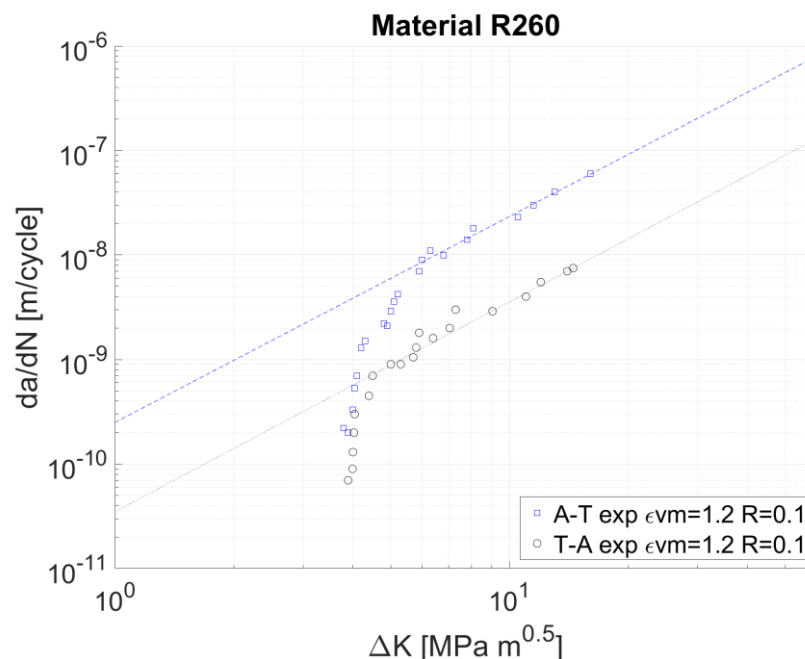


**Figure 9 – FCG behaviour of two different orientations of deformed rail steel R260. The FCG orientation A-T approximates the main shear direction, whereas T-A refers to a**

direction perpendicular to that, modified from (14). The degree of deformation,  $\varepsilon_{VM}$ , and the applied stress ratio,  $R$ , are defined in the legend.

Leitner presented evidence for that phenomenon by processing SPD specimens of materials R260 and R350HT (14). For these steels, he selected HPT processing. Based on that, he performed FCG tests for different orientations with respect to the main shear direction, analysing anisotropic FCG as well as fracture surfaces. According to his findings, there are significant deviations in the material's resistance to FCG (14). The orientation parallel to the main shear direction (A-T) exhibited FCG rates eight times higher than those perpendicular to that direction (T-A), which is displayed in Figure 9. For a description of the procedure, an explanation of the FCG orientations A-T and T-A, and the results, the reader is referred to (14) and to section 6.1.

Leitner et al. concluded that the observed FCG anisotropy is notably related to SPD microstructure, whereas triaxial loading conditions are not a determining factor (5). Another finding was that cracks propagating into directions less prone to FCG (i.e. a direction with a higher FCG resistance) tend to deviate to a direction parallel to the main shear orientation (i.e. a direction of lower FCG resistance).

A similar analysis of anisotropic FCG was performed by Toribio et al., however by applying a different processing technique to achieve a form of SPD (18). They compared the FCG behaviour of two pearlitic steels of the same chemical composition: A hot-rolled one representing an isotropic pearlitic microstructure, and a cold-drawn one with an anisotropic microstructure. The latter exhibited an improved FCG resistance, which was attributed to a change in crack paths due to local micro-deflections. As a result, this led to an increase in fracture surface. Those effects lead to a modification of FCG Paris curves. The work confirmed a correlation between SPD microstructure and the anisotropy of FCG.

### **2.1.5 Multiple FCG**

It is common that wheels and rails in service degrade not only at one specific position, but at various locations, which manifests itself in the form of multiple fracture zones. A major consideration is the spatial distribution of fracture zones to each other. Examples of closely spaced defect zones on rail surfaces are head checks or in some cases squats.

Head checks are surface cracks that initiate on the gauge corners of rail (see Figure 10 left). They may propagate along the surface and spall or grow into the

bulk material (see Figure 7). Head checks in close proximity to each other tend to interact and form more complex crack patterns (7). Squats are characterised by a darkened rail surface and an enlarged running band (see Figure 10 right). They are caused by a horizontal crack that leads to a lateral flow of the material. Also squats may interact with other cracks in close proximity and form damage patterns (7).

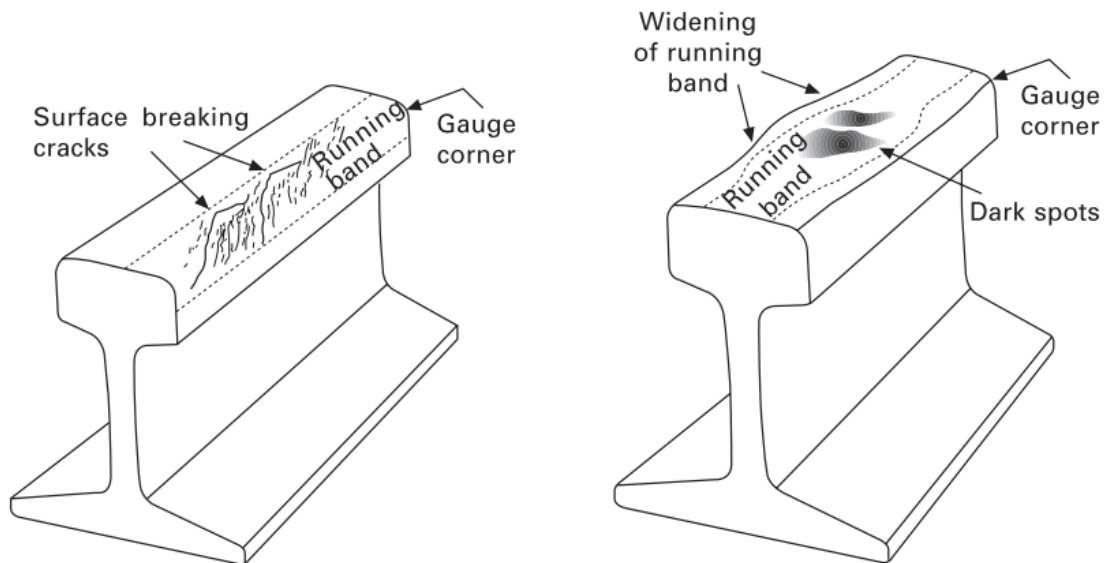


**Figure 10 – Rail damage forms that represent multiple crack patterns: Head checks on the gauge corner (left) and squats on the running band of a rail (right), modified from (7).**

Besides closely located defect zones, there are remotely located defect zones, where cracks initiate and propagate independently from each other. At a certain stage, however, also these cracks may interact.

The result of crack interactions are complex fatigue crack patterns, displaying a branching or merging (coalescence) behaviour (see Figure 5, below). Those phenomena may have catastrophic effects when the crack grows into the depth (see Figure 7, cases C-D) or may lead to a spalling on the surface. Thus, it is of high relevance to understand the interaction between cracks, particularly how cracks affect each other.

For a simplified arrangement of two cracks subject to a Mode I condition, Anderson explained the interaction with respect to their relative position. Cracks positioned in the same plane (coplanar cracks) tend to increase the stress intensity factor,  $K_I$ , of a crack, whereas parallel cracks tend to shield each other,

effectively decreasing stress concentrations at crack tips, at least for Mode I (15). Hence, parallel cracks tend to be less hazardous than coplanar ones. For an RCF set-up, however, the interaction of cracks is more complex as the geometry, arrangement, loading and number of interacting cracks (see Figure 10) differs from the theoretical set-up and must be considered.

Another important consideration refers to the crack growth mechanism. There may be more than one mechanism active for a specific load case. In that case, a competition between different mechanisms is possible, where the knowledge of mechanism hierarchy is necessary (7).

Thus, there is no general explanation for the crack interaction behaviour subject to a cyclic rolling contact. This stresses the requirement for more research to obtain a better understanding of the matter.

#### **2.1.6 Crack closure**

Crack closure is an FCG related phenomenon, emerging under dynamic loads at pre-cracked components. Due to the interaction between two opposite crack faces, a component exhibits a reduced displacement behaviour for certain load conditions. In fact, that crack face interaction retards the opening and closure of the crack. This behaviour is called crack closure (15). The phenomenon was studied primarily for tensile loads, which is addressed and assumed in the first part of this section. In the second part, the effect under compressive loads is reviewed.

Crack closure itself can be explained by different mechanisms working inside a crack and impeding the crack to open. Suresh and Ritchie (19) proposed five distinctive mechanisms: Plasticity-, roughness-, oxide- and transformation induced crack closure, as well as that induced by viscous fluid. Further, they provided a major contribution for modelling crack closure induced by fracture surface roughness (19).

Related to roughness-, corrosion- and viscous fluid induced crack closure, there is another phenomenon called wedging, which means that the crack cannot close completely due to a blocking wedge. Hence, wedging evokes an offset in the crack opening displacement (COD), which is synonym to the term crack mouth opening displacement (CMOD). From now onwards, the term COD is used. Wedging implies a residual stress. In brief, crack closure mechanisms have different implications on crack geometry, opening behaviour and stress intensity. This has an impact on load carrying capacity and the FCG behaviour (15).

FCG starts when the stress intensity factor range around the crack tip,  $\Delta K$ , rises above the threshold stress intensity range,  $\Delta K_{th}$  (see Figure 8). However, it is not clear whether crack closure affects that threshold or not. A prominent concept of explanation is the closure model, which assumes that crack closure has a major effect on the threshold (15).

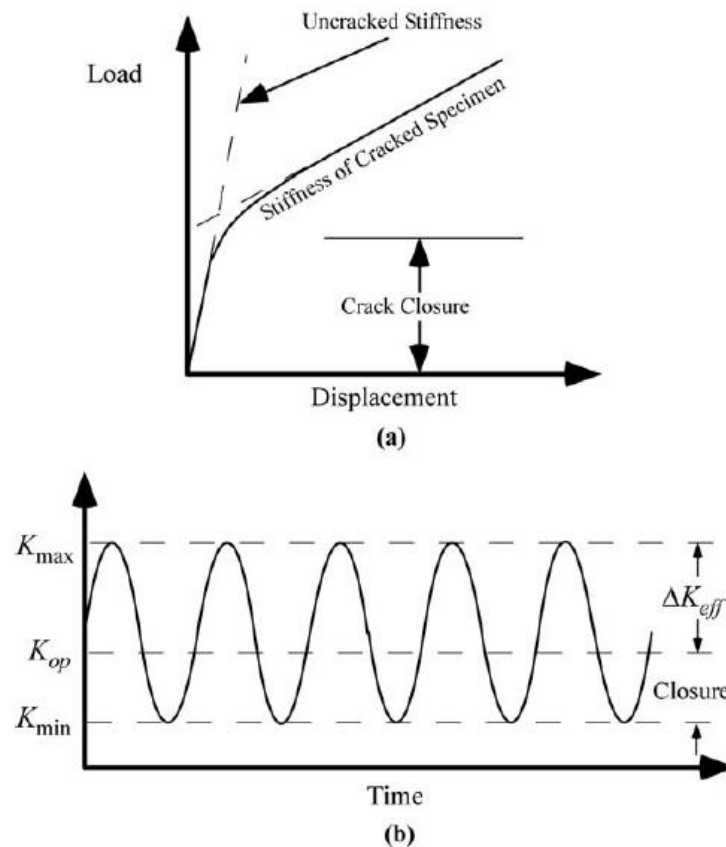


**Figure 11 - Principle of crack closure under a tensile loading: Due to a crack, the stiffness of a material is decreased (a). This effect is reduced by crack closure leading to a diminished, effective stress intensity range (b) of  $\Delta K_{th\_eff}$ , modified from (15).**

According to the closure model, crack closure can be implemented into FCG models by employing stress intensity factors and ranges. When considering a cyclic load between  $K_{max}$  and  $K_{min}$ , the effective crack opening takes place at a stress intensity factor  $K_{op} > K_{min}$  (see Figure 11 b). In this case, the crack tip is not subject to the original stress intensity range  $\Delta K$  anymore, but to a reduced  $\Delta K$ , i.e.  $\Delta K_{th\_eff}$  (see Figure 11 b). Consequently, Elber suggested a modified Paris-Erdogan equation, taking that adjustment into account (15).

$$\Delta K_{eff} = K_{max} - K_{op}$$

Equation 6

Assuming a constant maximum load,  $K_{max}$ , the closure model suggests that crack closure works the best in shielding a crack for low  $R$  ratios, i.e. for a minimisation of the minimum stress intensity factor,  $K_{min}$  (see Figure 11, below). An increase of the latter, i.e. an increase of  $R$ , decreases the shielding effect. This is valid until  $K_{min}$  equals the opening stress intensity factor,  $K_{min} = K_{op}$ . If  $K_{min}$  exceeds the opening value,  $K_{min} > K_{op}$ , the crack closure effect vanishes (see Figure 11 b).

An alternative to the crack closure model is the Two-Criterion model, which assumes crack closure to have a minor impact on the threshold,  $\Delta K_{th}$ . In this work, however, the assumption of the crack closure model is adopted with regard to (15).

The effect of crack closure is displayed in a more practical way in a load-displacement diagram (see Figure 11 a). There, the reduced component stiffness due to cracking is illustrated. The effect of crack closure is highlighted, which tends to shield the damaged material and reduces the FCG rate (15). This description of the macro-mechanical behaviour refers to a tensile load range.

For modelling a compressive range, which is predominant in railway applications, crack closure under compression is addressed in the next step. A review of the available literature regarding the mechanical response of a cracked material loaded in compression led to the finding that crack closure plays a major role, which is highlighted by the studies of Fleck et al. (20), Hermann (21) and Kasaba et al. (22). These studies agree about the fact that plastic deformation and a resulting residual stress field in tension around the crack tip are prerequisites for FCG under compressive loading. For cyclic hardening materials like steel, Silva suggested plasticity induced crack closure (PICC) to be the dominant mechanism (23).

The crack opening is described by a crack opening load,  $P_{open}$ , for which the crack is considered to be fully open, i.e. no wedging of the crack faces. However, the experimental derivation of  $P_{open}$  is challenging (24). A major fact about the opening load was highlighted by Silva (23) and Romeiro et al. (25). For a structural steel, they showed that  $P_{open}$  depends on the stress ratio  $R$ , and that  $P_{open}$  is positive for  $R > 0$  and negative for  $R < 0$ . This suggested that in the case of RCF, where compressive loads prevail, opening loads are negative.

The effect of crack closure is investigated by measurements that assess the COD behaviour (15). The result of Kasaba et al. (22) for a crack closure measurement

under a compressive load is displayed in Figure 12. Due to plasticity effects, the experimental load-COD curves vary, which makes it challenging to define states where cracks are fully open or closed. Thus, the behaviour was approximated by a linearisation, whereby an effective opening load was derived (see Figure 12).

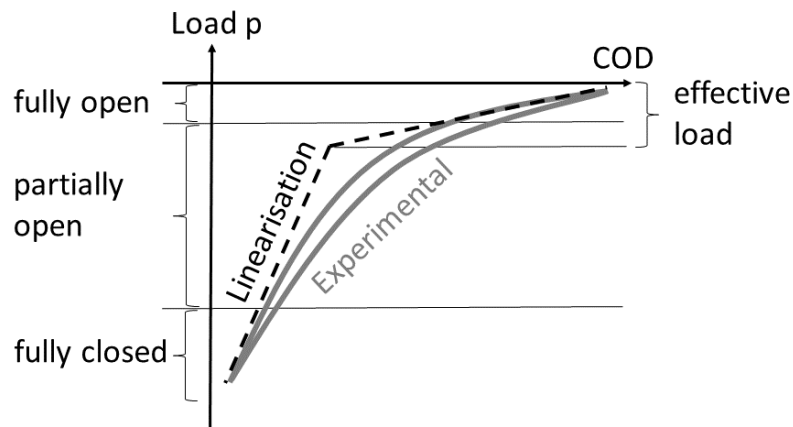


**Figure 12 - Load-COD curves of FCG tests (12): The experimental results are illustrated in grey, the simplification in dashed black, modified from (26).**

In this section, the phenomenon of crack closure was assessed, which has a major effect on FCG. With regard to RCF applications, crack closure under compressive loads (i.e.  $R < 0$ ) must be considered. For that case, experimental results suggest opening loads to be negative.

### 2.1.7 External influences and lubricants

External influences including environmental conditions and lubricants have a huge influence on the degradation and wear of rails and wheels in service.

Environmental conditions like temperature, humidity, contaminations (rain, ice, snow, organic deposits) likewise may have an ambivalent impact when acting as lubricants or promoting crack initiation, growth, or wear. Fluid pressurisation may occur as a result of fluid penetration, which may contribute to crack growth. Air and oxygen have an impact on the FCG threshold, whereas moisture may modify the interaction between displacing crack faces (7).

Lubricants such as oil and grease are applied to reduce friction and wear, hence delaying the initiation of surface cracks. However, they may also promote the growth of existing cracks by lubricant pressurisation. Further they affect shakedown limits and RCF (7). As a result, the role of lubricants towards

degradation is ambivalent. Another matter of importance are friction modifiers, whose task is to modify the friction within the wheel-rail contact in a desired way. For these, there can be various influences on degradation as well (7).

In summary, the impact of external influences and lubricants is controversial, as all contributors and phenomena (RCF, wear, oxidation) are mutually linked to each other, resulting in a complex interaction (7). For reasons of simplicity, the effects of external influences and lubricants were not considered for the modelling.

### **2.1.8 Interaction of fatigue and wear**

"Wear is the loss or displacement of material from a contacting surface" (7). In the case of a railway, this refers to rolling and sliding in the contact patch, affecting the wheel's tread and flange and the rail's head and gauge. The result is the displacement and/or removal of material at the contact surfaces. For rails, this implies a degradation of profile and a widening of rail gauge. For wheels, wear implies the degradation and reduction of profile or an out-of-roundness. The main parameters determining wear are contact pressure, sliding velocity and creep, friction coefficient and contact area (7).

Wear in a rolling and sliding contact has many reasons. Those can be described by different wear mechanisms. Basically, those mechanisms are closely related to SPD and RCF as well. Wear and fatigue often correlate to each other in different ways and the interaction is complex. Basically, service induced SPD leads to ratcheting and RCF, degrading the material's mechanical properties. This supports the effectiveness of wear mechanisms and promotes the wear rate, hence reducing component's lifetime (7).

Fatigue is also detrimental by itself because cracks grow and compromise component integrity. In order to reduce that risk, grinding - the intentional removal of surface layers of the material - is a reasonable solution. As a result, the effect of grinding is comparable to wear, which can be beneficial to impede FCG when truncating small cracks (see Figure 13a). The cracks cannot propagate anymore or at least crack growth rate is reduced (1,27). A summary of that behaviour is displayed in Figure 13.

In order to prevent wear, improving the hardness of a component is desired. However, a hard material is also more brittle and prone to FCG. As a conclusion, hardness and wear life must be optimised against toughness respectively ductility and fatigue life.



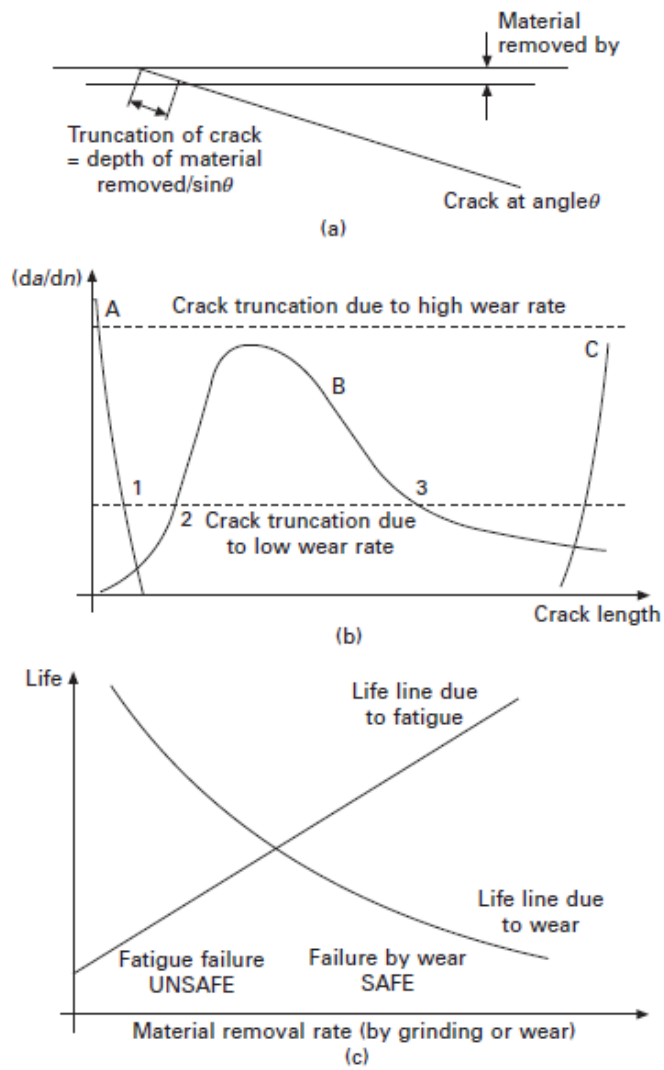


Figure 13 - Interaction of wear and fatigue: Truncation of cracks by surface material removal (a). Crack growth mechanisms and impact on crack length with respect to wear rate (b). Lifetime of material as a function of material removal rate (c), modified from (7).

## 2.2 Modelling of crack initiation and growth

In section 2.1, the degradation of wheels and rails during service was summarised. Based on that knowledge, wheel- and rail degradation with respect to crack growth and wear can be modelled numerically. The aim is to enhance the understanding of different degradation mechanisms and to predict the degradation in service as a function of specific input parameters.

For modelling solid mechanics, a standard engineering approach is the design of a macroscale model, covering the macroscopic behaviour of a material. The basic principle of that approach is to simulate the physics being above microscopic level (e.g. dislocation mechanisms) by a set of simplifications in form of constitutive rules and effective properties, thereby drastically reducing degrees of freedom (28). A drawback, however, is that the macroscale model is less accurate.

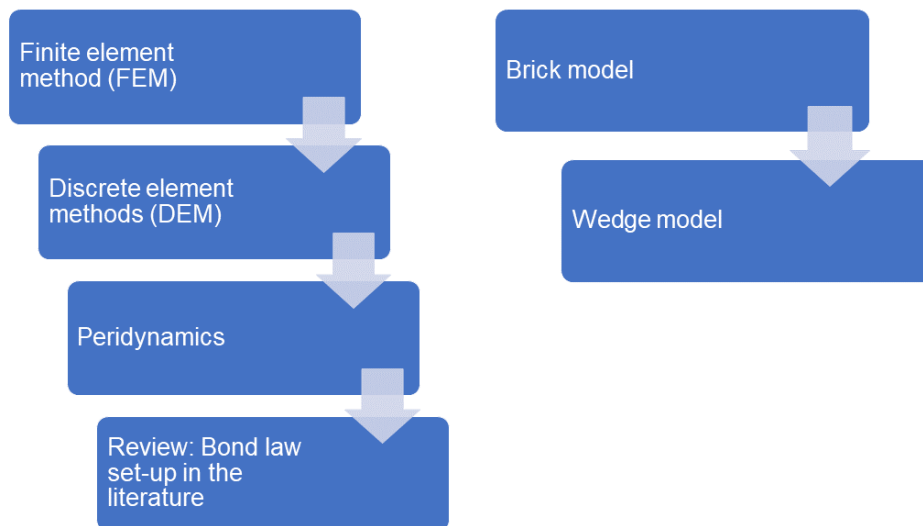


Figure 14 - Overview on the numerical modelling approaches discussed in section 2.2.

An overview on macroscale modelling approaches applicable to RCF modelling is given here (see Figure 14). The state-of-the-art for the numerical simulation of solid mechanics is the finite element method (FEM), which is discussed in section 2.2.1. Alternatives with an emphasis on fracture and fatigue are discrete element method (DEM) and peridynamic (PD) models, which are introduced in sections 2.2.2 and 2.2.3. Both models have a constitutive relationship (bond law), which is discussed in section 2.2.4. Modelling approaches with a focus on RCF initiation- and wear are discussed in sections 2.2.5 - 2.2.6.

### 2.2.1 Finite element method (FEM)

State of the art in engineering for numerically simulating solid mechanics behaviour is FEM. Based on that platform, special solutions are developed for the simulation of SPD and FCG. An extensive review on FEM approaches for modelling SPD is given by Vinogradov and Estrin in (28). A review of different FEM techniques for modelling FCG is given by Rege and Lemu in (29).

A major contribution for modelling FCG in railway applications by means of FEM was provided by Larijani, who modelled high pressure torsion tests of pearlitic steels (30). Based on the assumption of large plastic deformations, she analysed the anisotropy of FCG for rail steels (31).

For modelling SPD with FEM, there are two main approaches (28): The standard one is a pure phenomenological one, the other is microstructure-based phenomenological. This means that the latter includes mechanisms which directly address the physics of microstructure. By using phenomenological models, this can be done indirectly.

The general routine for modelling FCG with FEM is to calculate the stresses and strains for a mesh, determine the stress intensity factors around a crack tip, calculate the direction of crack propagation, and represent the crack advancement. This iteration is repeated for every load cycle. The stop criterion is when the maximum stress intensity factor at a certain point of the mesh equals the critical stress intensity. This is where fatigue fracture occurs (29).

The main limitation of that method is that irregularities and discontinuities like cracks violate the basic assumption of FEM that the mesh is a continuum. This has consequences. One is that crack initiation must be set as a precondition. Hence, it cannot be simulated directly as that would violate the basic assumption of a continuous mesh.

Another limitation concerns fatigue crack advancement (FCG Stage II) which distinguishes between two cases: 1) Under LEFM, the mesh must be updated locally for each step. This renders the procedure complex, requires effort, and reduces efficiency. 2) Under elastic-plastic fracture mechanisms, either node release- or cohesive zone techniques (cohesive zone model, CZM) are applied to facilitate crack advancement within the mesh (29). CZM's are regularly applied to FEM models, e.g. for modelling intergranular FCG (32). A review on the topic of CZM is given by Park in (33).

In order to overcome these limitations and to better deal with discontinuities, the extended FEM (XFEM) was developed in the 1990's (29). Nodes and elements of the mesh are modified in a way that remeshing is obsolete during FCG. However,

accuracy strongly depends on the use of fine meshes which already refers to the main limitation of XFEM: It provides accurate results for simple geometries. For more complex geometries like 3D or for multiple loads (multimode) accuracy decreases. A further refinement of the mesh leads to high computational effort (29).

Due to the shortcomings of FEM especially regarding the modelling of FCG, alternative models are currently being considered for the simulation of the given railway application (see chapter 2.1). Potentially suited alternatives are illustrated in the subsequent chapters.

### **2.2.2 Discrete element methods (DEM)**

A main drawback of FEM is its primary assumption of material as a continuum, which leads to a set of differential equations describing the basic problem. In order to overcome that limitation when dealing with discontinuities, new methods of computational mechanics were developed in the 1960's (34). Among those, the DEM emerged. Generally, DEM is applied to simulate mechanics of granular media. However, when implementing proper contact laws between the discrete elements, it is capable to cope with solid-state material. This makes it attractive for simulating fracture mechanics or material anisotropy (35).

DEM covers a variety of models, consisting of discrete elements that interact with each other, based on the equations of motion (Newton's laws). The mechanical behaviour of the loaded elements is defined by a so-called bond law (see section 2.2.4). It describes how nodes displace against each other. The simplest form is a linear-elastic bond law, describing the force-strain relation in a purely linear way.

For modelling solid-state materials with DEM, there are different approaches. Criteria for classifying DEM models for solid applications are the topological order concerning the structure of element assembly (order or disorder) and the contact law, hence the type of bond between the discrete elements (beam, spring/damper networks). Topological order and contact laws have a fundamental impact on the model behaviour, exhibiting model specific advantages and disadvantages. As a result, topological order and contact laws must be selected carefully.

An overview of DEM modelling solutions regarding FCG is given here: Ordered spring network DEM models were applied by Cheng et al. (36) for composite materials and by Liu et al. for ductile materials like steels (37). Truss-like spring network models for ductile materials were used by Kosteski et al. (34,38) as well as by Zhu and Feng et al. (39,40). Further, Iturrioz et al. introduced lattice

imperfections to the model in order to reduce the model inherent orthotropy and finally for achieving more realistic crack patterns (41).

Disordered models based on a spring/damper network for simulating cemented materials were used by Nguyen et al. (42). For simulating fatigue crack initiation in ductile polycrystalline materials like roller bearing steels, Raje et al. (43) applied structures consisting of Voronoi-type 2D flakes. The contact law is defined by spring networks too. Deviating from that kind of contact law, André et al. (44), Le and Maheo et al. (45,46) introduced disordered cohesive beam models for simulating FCG, predominantly for composite materials.

A few DEM models were applied to model RCF. Raje et al. (43) developed a Voronoi type mesh with normal and tangential spring patterns along the edges to model a polycrystalline microstructure. In order to describe the damage accumulation of each bond, they introduced a damage variable. The variable was multiplied by the spring stiffness', which effectively reduced the bond forces. For parameterisation, the damage variable was correlated to experimental stress-life data (S-N curves). This approach was quite similar to that of Leonard et al. (47).

Plasticity and SPD is another matter of importance when modelling the material behaviour in the wheel-rail contact. When researching the referenced literature on DEM, ductile materials were modelled either by truss-like spring network models or disordered polycrystalline models. However, for the latter, plasticity effects were not considered. For the referenced truss-like DEM models, plasticity effects are partly available (34,39,48), but not to an extent like that for SPD.

Generally, DEM models are well suited for modelling FCG behaviour of ductile materials due to their discrete structure. Fracture within an element assembly can be introduced naturally. This enables those models to reproduce not only single, but also multiple fatigue fractures. Though, implementing the required plasticity for SPD might be a challenge for some of the referenced model types.

### **2.2.3 Peridynamics**

Peridynamics is a continuum mechanics theory that was developed in 2000 by Silling for dynamic fracture problems. Like solid mechanic DEM models (see section 2.2.2), Peridynamics can model discontinuities naturally, as the basic equations do not rely on spatial derivations. This means that crack formation (FCG Stage I), growth (Stage II) and fracture (Stage III) as well as the interaction between multiple cracks can be modelled simultaneously. An extensive introduction into modelling FCG by the means of Peridynamics is given in (49).

A peridynamic (PD) model basically consists of a discretised grid of nodes. To each node “i”, a spherical horizon,  $\delta_i$ , is applied, which can be set deliberately. All nodes within the horizon are connected by bonds (comparable to discrete elements, see 2.2.2), representing forces (50). Like for DEM, the basic equations of motion (Newton’s laws) apply to each bond. This model design is called bond-based Peridynamics. By modifying the bonds, damage like fatigue cracking or an anisotropic behaviour like in a composite material can be modelled.

According to Silling, bond-based Peridynamics exhibit at least three model inherent limitations (51): the assumption that a pair of particles depends only on one potential between them is often oversimplified, leading to a fixed Poisson’s ratio of  $\nu=0.25$ ; further, the definition of pairwise forces does not correlate with the established concept of a stress tensor; and finally, plasticity cannot be modelled appropriately as the resulting volumetric strain violates the concept of incompressibility (see section 7.1). In order to overcome that basic limitation of bond-based models, a state-based peridynamic formulation was developed by Silling et al. (51), which, however, is more complex.

In order to model fatigue, Oterkus et al. were the first to introduce a fatigue law to a PD model (52). As damage criterion, they defined a critical bond stretch per bond, which degraded as a function of the accumulated load cycles. Silling and Askari proposed a fatigue law that was derived in close relation to the LEFM theory (49), which was adopted to several applications (53–55). It captured not only FCG (Stage II), but also crack initiation and failure (Stages I and III). The driving force for fatigue is a cyclic bond strain, which reduces a damage parameter called “remaining life”. Due to the correlation to LEFM theory, a direct adoption of experimental parameters is feasible.

PD models are capable of modelling different kinds of material anisotropy (56). These include the anisotropy of elastic properties (50,57,58), damage response (55) or a combination of both (59,60). In this way, specific properties, and damage mechanisms of anisotropic materials like composites or polycrystalline ceramics can be modelled. An overview on experiments for the validation of PD models covering different materials is given by Diehl et al. (61).

The modelling of rolling contact and RCF by PD models is a recent development, which was initiated by Ghaffari (62) and Freimanis and Kaewunruen before 2019 (53). Later developments were proposed by Ma et al. (54,63) and Wang et al. (64,65). These RCF models have two basic assumptions in common. First, failed bonds are assumed to have no load carrying capability. This issue is evaluated in detail in section 2.2.4. Second, the RCF models are based on the fatigue model proposed by Silling and Askari (49), which effectively set a standard for fatigue

simulation with Peridynamics. The fatigue model assumes compressive bond strains to contribute in the same way to fatigue like tensile strains (this issue is assessed as part of the validation, see section 8.2.3).

In summary, PD models are well suited for modelling all stages of multiple FCG as well as different kinds of anisotropic material behaviour, which makes them a promising approach to deal with RCF. Though, when it comes to RCF, basic assumptions must be reviewed carefully. When it comes to plasticity, potential limitations must be considered. As the constitutive relationship of PD and DEM models in case of failure is paramount for the RCF application, it is reviewed in detail in section 2.2.4.

#### 2.2.4 Review: Bond law set-up in the literature

DEM and PD models (see sections 2.2.2 and 2.2.3) represent similar modelling approaches that describe the behaviour of a continuum by an assembly of discrete elements respectively bonds. The constitutive relationship between element strain,  $\varepsilon$ , and element force,  $f$ , is called bond law (see Figure 15). It is differentiated for healthy and failed elements. Regarding healthy elements, a linear-elastic relation was assumed in this work (see Figure 15). By the application of more advanced bond law set-ups (bilinear, tri-linear), elastoplastic behaviour can be modelled (34).

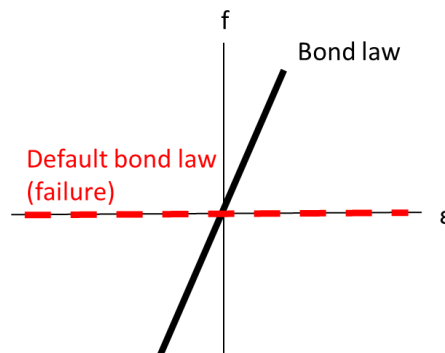


**Figure 15 - Linear-elastic bond law for healthy- (black) and failed elements (red). The latter features a removed compressive stiffness for failed elements.**

Regarding the case of an element (bond) failure, the basic assumption prevails that failure implies the removal of the load carrying capability of an element (34,49) (see Figure 15), which was called default bond law in this work.

However, with regard to RCF modelling, where compressive loads prevail, this basic assumption is expected to lead to significant shortcomings. For a surface crack loaded by a rolling contact, a lowering of the surface and a potential interpenetration of the crack faces (53) are expected. This is a result of the applied set-up, as the default bond law makes a grid with a crack loaded in compression too soft

Thus, the state-of-the-art in the literature regarding DEM- and peridynamic models applied for rolling contact simulations is reviewed in this section. The focus is laid on the bond law in case of failure and on the question of whether there are approaches of bond law modifications to address the mentioned issues.

Freimanis and Kaewunruen were one of the first to apply a PD model to simulate a rolling contact problem (53). They selected a state-based PD model, employed the fatigue model of Silling and Askari (49) and the default set-up for the bond law in case of failure (see Figure 15). In their results, they highlighted the effect of what they called "matter-interpenetration" problem, i.e. nodes that are insufficiently attached due to associated multiple element failure. As a result, the nodes displaced in a rather undefined way within the grid. In order to address the problem in the future, they suggested the use of "contact models", as proposed by Silling, Askari and Littlewood (50,66). However, this nomenclature does not refer to rolling contact problems, as the approach addresses primarily impact- and fragmentation problems, where fragmented particles impact each other.

By "contact model", Silling and Askari referred to a method where fragmented nodes, which are in the vicinity to other nodes, are subject to "short-range repulsive forces" (50), i.e. "spring-like repulsive forces are applied between nodes that are in close proximity to one another" (66). These forces are independent of the reference configuration (i.e. the initial grid), and they serve to avoid non-physical contact (50). The method is based on the default bond law, which implies a complete removal of a failed element.

In this model, however, failed elements are retained as this reflects the basic character of a cracked steel loaded in compression, where material inside a crack does not vanish. Further, additionally introducing a "contact model" in a solid material makes the model more complicated than required. Thus, "contact models" were not deemed to be an appropriate solution to the given problem.

Ghaffari et al. (62,67) acknowledged the requirement to retain broken bonds instead of removing them. They indicated a modification of the bond law for failed elements in a way that the elastic modulus (i.e. the elasticity parameter) is "decreased to a very small number" (62). Unfortunately, they did not specify the modification or discuss the matter in more detail.



Ma et al. employed a PD model to simulate crack initiation and growth at rail heads (54,63). They applied the default set-up as well, i.e. they completely removed broken elements. For modelling the full-scale wheel-rail contact, they highlighted the importance of selecting a fine grid discretisation, "no coarser than 0.1 x 0.1 mm" (54). Finally, they did not report on the adverse effects due to failed elements, like mentioned above. The grid refinement may be a possibility to circumnavigate these issues under certain conditions like small crack lengths. Although, it does not resolve the basic problem that a failed element under compression cannot be removed completely.

Wang et al. (64,65) highlight another aspect of failure modelling in PD models, i.e. that damage can be described not only by elements that fail due to exhaustion of their remaining life, but also by a cluster of elements with an advanced state of damage before failure. In such a case, many elements have a significant reduction of their remaining lives, but still exhibit full load sustainment. Also in this case, the adverse effects are circumnavigated, if there remains a sufficient number of not-failed elements in the grid.

A review besides the scope of rolling contact modelling reveals that approaches exist in the literature where a bond law modification was performed. Gok et al. applied a bilinear failure model (i.e. a bond law for failure) to model crack softening of composite materials (68). This, however, refers to the tension regime only. An alternative approach is to modify the bond law for healthy elements in a way that the load carrying capability reduces with an increase of damage, which was done, for example, by Kostas et al. (34). Finally, though, a considerable number of elements fail, which again results in the issues mentioned above.

What are the implications of these findings? First, regarding the modelling of RCF, the problem of the default bond law in case of failure, which produces unattached nodes, is acknowledged partially. Therefore, "contact models" are suggested to tackle the issue. This approach, however, was considered to be inconsistent with the RCF problem. Second, there are ways to postpone the effect of the problem, i.e. a grid refinement or focussing on the damage evolution rather than on element failure. Thus, this does not solve the issue. Third, a reasonable option, which indeed agrees with physics, is to stiffen failed elements that are loaded in compression. Although, the question is how.

This highlights the importance of the matter to find a novel approach (research gap) to adjust the bond law in case of failure under compression. Without modification, these shortcomings are inherent to solid-state DEM- and PD models that are applied for rolling contact simulations.

### **2.2.5 Brick model**

In the early 2000's Franklin, Kapoor et al. developed the numerical brick model with the objective of predicting RCF initiation and wear as a result of SPD and ratcheting during operations. The phenomenological 2D model consists of brick wall elements which are subject to progressive ductility exhaustion. That was implemented by having different horizontal layers of elements, absorbing, and accumulating certain degrees of shear stress. Work hardening and the resulting anisotropic behaviour were considered. When ductility is exhausted in an element, it fails. According to the support of adjacent elements, the failed material behaves either as microcrack (in case of support) or as wear debris (in case of no support) and detaches (69).

Further they introduced a variation of material, considered surface roughness and creep in order to evaluate the impact on wear rate (10). Then they advanced by applying a 3D contact stress distribution and implementing microstructural features, distinguishing between pearlite and PE ferrite in a simple hexagonal microstructure. With it, the influence of microstructure and particularly of PE ferrite content on wear and RCF reflecting a material inhomogeneity was evaluated (12,27).

The brick model provides a simple, but effective, tool to simulate multiple load cycles. It covers the major influence SPD has on RCF and wear behaviour, and it considers the microstructural composition focussing on PE ferrite content. However, due to its phenomenological character, an extension to model effects like FCG at Stage II and III or the interaction of cracks is restricted. In order to address this issue, a physical model type like FEM (see section 2.2.1), DEM (see section 2.2.2) or Peridynamics (see section 2.2.3) is required.

### **2.2.6 Wedge model**

With the same objective as Franklin and Kapoor's brick model (see section 2.2.5), Trummer developed a novel RCF model to predict crack initiation and wear at the surface of rails (8,70), which was referred to as the wedge model (8). Based on the high plastic shear deformation that occurs in the surface area, it describes the interaction of wear and crack initiation.

Two models were developed and integrated: a model to estimate plastic shear deformation on the surface, and a model to predict crack initiation based on the SPD microstructure of the material (70).

The shear deformation model was parametrised with respect to TD tests that were performed using the SUROS machine at The University of Sheffield. The generated discs were examined with a focus on hardness and shear deformation. In order to integrate the average shear deformation, a novel method (70) was developed by Trummer. The crack initiation model considers the state of shear deformation, the linear-elastic contact stresses, and the creep condition as an input. With it, preferred FCG directions are defined. The model was parametrised by means of data from a full-scale test rig. A validation was performed using a test case with reference to an underground crossing section.

By coupling the wedge model to model body dynamic simulations (MBDS), the overall vehicle dynamics can be associated to the local RCF development (70), which closes the gap between operations, maintenance and vehicle design on the one hand and RCF damage on the other hand. A limitation is that fatigue crack growth is not captured by the model.

### 3 OBJECTIVE

The state of the art was summarised in chapter 2. In section 3.1, existing research gaps of RCF modelling are identified. In section 3.2, the objective of the thesis is discussed, a specific research gap is defined, and a modelling objective specified.

#### 3.1 Research gap

In order to identify research gaps, an evaluation of the existing modelling concepts regarding wheel- and rail degradation (see section 2.2) was performed by the means of an evaluation matrix (see Table 1). On the abscissa, relevant aspects to be considered for modelling, i.e. criteria, were stated.

- Plasticity: Modelling of elastoplastic material behaviour
- SPD: Modelling of SPD (see section 2.1.1)
- Strain-hardening: Modelling of strain-hardening (see section 2.1.1)
- RCF: Modelling of RCF (see section 2.1.2)
- FCG I-III: Modelling of FCG Stages I-III (see section 2.1.3)
- Anisotropy: Modelling of fatigue- (see section 2.1.4) and elastic anisotropies
- Multiple FCG: Modelling of multiple FCG phenomena (see section 2.1.5)
- Crack closure: Modelling of crack closure effects (see section 2.1.6)
- Wear: Modelling of wear (see section 2.1.8)
- Geometrical dimension: Modelling dimension, i.e. 2D or 3D

On the ordinate, different modelling approaches and referenced publications are added (see Table 1, left column). A match of a criterion was marked by “x”. With regard to the frame of thesis, the criteria “wear” and “modelling dimension” were considered to be secondary but were added for information.

<b>Model types</b>	<b>Brick &amp; Wedge</b>	(12)	2008	x	x	x	x		x			x	
		(27)	2007	x	x	x	x		x			x	
		(10)	2003	x	x		x		x			x	
		(8)	2016	x	x	x	x		x			x	
		(70)	2016	x	x	x	x		x			x	
	<b>Peridynamic state based</b>	(71)	2023				x				x		
		(54)	2022				x			x			
		(72)	2016	x		x							
		(73)	2019	x		x							
		(53)	2018				x	x		x			
		(74)	2009	x		x				x			x
		(58)	2018	x						x			x
	<b>Peridynamic bond based</b>	(52)	2010	x									
		(57)	2017					x	x	x			x
		(65)	2022				x	x	x	x			
		(64)	2022	x			x	x		x		x	
		(62)	2016				x	x		x	x		x
		(63)	2020				x			x			
		(75)	2019					x					x
		(59)	2014					x	x	x			
		(60)	2016					x	x	x			x
		(49)	2014					x		x			x
	<b>DEM solid-state</b>	(47)	2013				x	x	x	x		x	
		(44)	2012						x	x			
		(43)	2009				x	x	x	x	x		
		(42)	2017	x		x		x		x	x		
		(40)	2019	x		x							x
		(34)	2011	x						x			x
		(36)	2009	x		x				x			
		(35)	2013	x		x				x			
	<b>FEM</b>	(76)	2013	x		x				x			
		(31)	2014		x		x			x			
		(30)	2015	x	x	x	x			x			x
(32)		2018	x		x	x			x	x			
(33)		2011	x		x				x		x	x	
	<b>Ref</b>	<b>Year</b>	<b>Plas ticity</b>	<b>SPD</b>	<b>Strain hard</b>	<b>RCF</b>	<b>FCG I-III</b>	<b>Aniso</b>	<b>Multi FCG</b>	<b>Crack clos</b>	<b>Wear</b>	<b>3D geom</b>	
	<b>Publication</b>		<b>Modelling criteria</b>										

**Table 1 – Evaluation matrix of modelling approaches (see left column) with regard to modelling criteria (see bottom row).**

The brick model (see section 2.2.5) and the wedge model (see section 2.2.6) were developed to describe RCF initiation and wear as a function of SPD and strain-hardening (see Table 1). However, these models are based on a phenomenological approach which limits an extension to model FCG (Stages II-III) and multiple cracks. This is highlighted by the blank columns of these criteria.

Table 1 displays the broad modelling spectrum that is covered by PD models. This stresses their main purpose to model all kinds of fracture and fatigue phenomena. Regarding the modelling of plasticity and strain-hardening, state-based PD models

were applied. Bond-based models were selected to model FCG crack initiation and propagation as well as material anisotropies regarding damage and elasticity. The similarity between PD models and solid-state DEM models is emphasised, as most capabilities except for plasticity and hardening overlap (see Table 1). SPD was neither modelled by PD or DEM models.

Regarding plasticity modelling, FEM models are the model of choice. However, the selection of Table 1 discloses that crack initiation and propagation (FCG Stage I-II) is not modelled comprehensively, as FEM requires the set-up of an initial crack. Further, the fact that predominantly single cracks rather than patterns of multiple cracks are modelled is highlighted. With regard to RCF, this makes alternatives to FEM desirable.

Disregarding brick and wedge model and some pioneering work in the field of FEM, plastic deformation and SPD are hardly considered by RCF models. This represents one research gap. A gap addressed recently is the application of RCF models to model all stages of FCG, i.e. from crack initiation to fracture. Material anisotropies of the elastic and fatigue behaviour are adopted to some degree by RCF models. Crack closure is considered in a marginal way.

In summary, there is no modelling approach that captures all specified criteria. With respect to modelling approaches and selected criteria, several research gaps were identified. Thus, the research gap to be addressed by this work is specified in the next section in order to define a modelling objective (see section 3.2).

### **3.2 Modelling objective**

In section 3.1, several research gaps were identified with regard to RCF modelling. With respect to available modelling approaches (see section 2.2), these gaps were illustrated (see Table 1) and discussed. In this section, the goal of this thesis, i.e. the research gap to be tackled, is discussed. In this way, a modelling objective was defined. In the next chapter, a modelling approach is selected (see section 4.1) to minimise the specified research gap.

The goal of this work was to develop an RCF model (see section 2.1.2) with a focus on FCG Stage II (see section 2.1.3), that considers the material anisotropy implied by SPD (see section 2.1.1). This is reflected by the title of the work. The model was desired to be of macroscale character, which required a contact stress field as an input. Due to the macroscale set-up, an explicit modelling of microstructure was not intended. However, in order to capture the impact of SPD (see section 2.1.4), the associated anisotropy of FCG (see Figure 9) had to be considered. With regard to the study of surface cracks (see Figure 10), the

modelling and interaction of multiple cracks (see section 2.1.5) was required. Further, experimental results of FCG under compressive loads (see Figure 12) suggested to consider crack closure effects (see section 2.1.6) for RCF modelling.

A look on the introduced evaluation matrix (see Table 1) revealed that there is no model available that captures all these criteria. In this way, a unique research gap was identified to serve as modelling objective, which is displayed in Table 2.

Modelling objective		x		x	x	x	x	x		
	Plasticity	SPD	Strain hard	RCF	FCG I-III	Aniso	Multi FCG	Crack clos	Wear	3D geom
	Modelling criteria									

**Table 2 – Modelling objective to be addressed by this work. The table represents a supplement to Table 1.**

Due to the complexity of rolling contact modelling, several aspects were disregarded within the frame of the thesis. With respect to Table 2, this regards the plastification process including strain-hardening that leads to a state of SPD (see section 2.1.1), the interaction of wear and RCF (see section 2.1.8) and 3D modelling to resolve geometry issues. Furthermore, aspects related to the environment like temperature, fluid interaction, third body layer, lubrication (see section 2.1.7) and corrosion were neglected. Dynamic processes were omitted, as the degradation was assumed to be quasi-static. Thermo-mechanical processes like phase transformations of the material were neglected. The influence of the microstructure was not considered explicitly, but implicitly.

All these aspects are relevant to understand the multiple degradation phenomena rails and wheels are subject to. However, simplifications are a precondition for each modelling approach. Thus, these aspects were defined to be non-objectives of the modelling.

In summary, a unique research gap was defined in this section. With it, a modelling objective for an advanced RCF model was specified (see Table 2). For clarification, non-objectives were discussed. In order to address the modelling objective, a rolling contact model was set up in chapter 4 and a modelling type was selected in section 4.1.

## 4 ROLLING CONTACT MODEL

Based on a specified research gap, the modelling objective was defined in section 3.2. The discussion of the modelling objective was based primarily on the key issue of fatigue and RCF modelling. A precondition for RCF modelling, though, is a rolling contact model, which was assumed tacitly.

With regard to the modelling objective (see Table 2), a model is developed in this chapter which represents a rolling contact in service or under laboratory conditions (see section 2.1). The contact is characterised by an applied load and the resulting stress or strain field in the rail. Assumptions are introduced and discussed, and a development methodology is presented. In chapter 5, fatigue is introduced.

Contact mechanics provide the theoretical framework to describe a rolling contact. Based on the modelling objective (see Table 2), the problem was simplified to the 2D domain. The following basic assumptions were made with respect to Johnson (77). The contact body was assumed to be semi-infinite, bounded by a plane surface. A state of plain strain was assumed. Line loads,  $p(x)$  and  $q(x)$ , were applied in normal- and tangential directions over a narrow strip (see Figure 16).

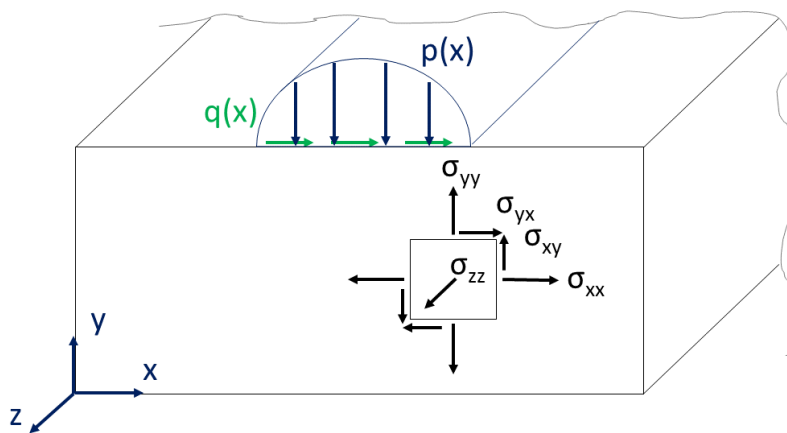


**Figure 16 – Semi-infinite body with applied normal- and tangential line loads as well as with stress tensor.**

Deviating from Johnson's approach, the coordinate system was rotated around the  $x$ -axis by 90 degrees to have the reference point within the bulk material. As a state of plane strain was assumed, this required that the components the model was designed to describe were relatively thick ( $z$ -axis) compared to the width of the loaded region. This is the case for a rail head (not gauge) and a wheel tread (not flange), which specified the model's applicability. A further consequence of



the plane strain assumption was that the model deforms within the xy-plane only. All strain components in z are zero. This, however, evoked a normal stress in z-direction,  $\sigma_{zz}$ . In this way, the stress tensor was assembled (see Figure 16).

The normal component of the running load,  $p(x)$  (see Figure 16), was modelled with respect to the Hertz theory, which is a standard approach in contact mechanics. With respect to Johnson's summary (77), the following assumptions were applied to the contact: The contacting bodies were considered to be elastic half-spaces, both cylindrical and subject to small strains only. Plastic deformation was disregarded. The surfaces were regarded as being continuous, non-conforming and frictionless. Deviating from the Hertz theory, but in agreement with a common assumption in contact modelling, a tangential component,  $q(x)$ , was introduced (see Figure 16). Full sliding and a semi-elliptic stress distribution were assumed. These are the basic assumptions of the rolling contact model.

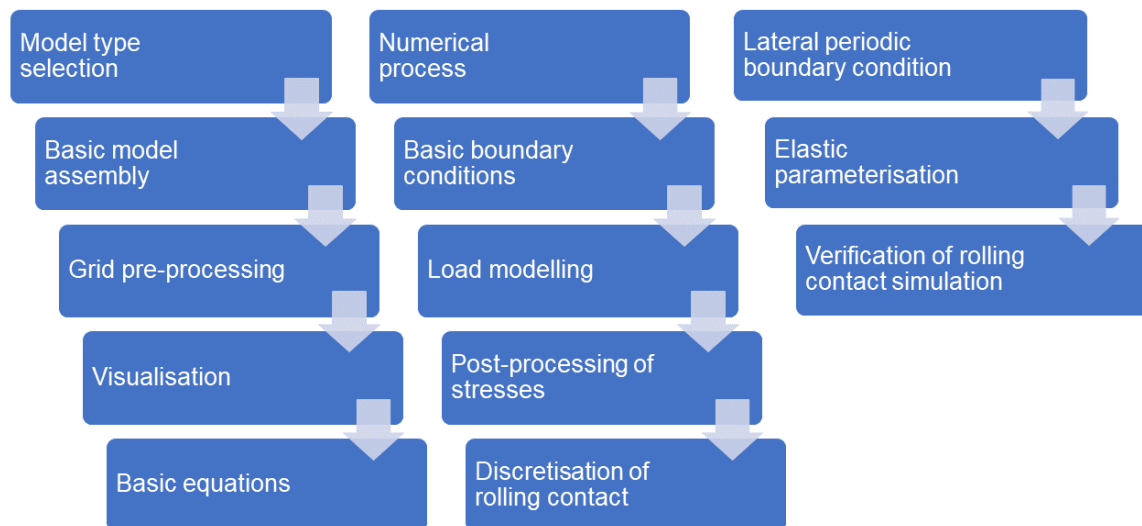


**Figure 17 – Overview on the procedure to set up the linear-elastic rolling contact model.**

In the next step, the procedure of the contact model development is discussed. The first step was to select a model type to discretise a solid continuum (see section 4.1) by assembling basic units (see section 4.2) to a grid (see section 4.3) that was visualised (see section 4.4). The governing equations were set-up (see section 4.5) and integrated to a numerical process (see sections 4.6). In order to facilitate simulations, boundary conditions had to be defined (see section 4.7) and a load was applied (see section 4.8).

A post-processing was required to transform the results into solid mechanic terms (see section 4.9). A general issue was to facilitate the simulation of a series of simulations (see section 4.10). Therefore, a lateral periodic boundary condition (see section 4.11) was applied. Finally, a parameterisation regarding the stress field below a Hertzian contact was performed to derive the elasticity parameter (see section 4.12). The method was verified in section 4.13. Basically, this sequence reflects the evolution of the model. Though, the actual development was complex and required sometimes more than one iteration.

In summary, the basic assumptions of the rolling contact model were introduced. The model assumes a linear-elastic semi-infinite body which is subject to a Hertzian and a tangential load. A procedure for the model development was presented, which starts with the selection of a model type (see section 4.1).

## **4.1 Model type selection**

Based on a literature review (see section 2.2), available modelling approaches were discussed with regard to modelling criteria (see section 3.1), which is summarised in Table 1. In the next step, a modelling objective was specified which focussed on the development of an advanced RCF model (see section 3.2, Table 2). In order to address the modelling objective, a contact model was required as a basis for the RCF model. The basic assumptions of the contact model were discussed in the section above (see chapter 4).

The aim of this section is to select a model type for the development of the contact and RCF model. Therefore, the evaluation matrix of Table 1 served as a point of reference as it negotiates available modelling approaches with required modelling criteria. Besides the matrix, the criterion to easily implement experimental data for the parameterisation of the model was considered.

For modelling solid mechanics, FEM (see section 2.2.1) is state of the art as it offers multi-domain modelling and maturity. However, due to its basic assumption of being a continuum, the modelling of multiple cracks (see Figure 10) and of capturing the whole spectrum of FCG (Stage I-III) is challenging (see Table 1). As these criteria are key criteria to fulfil the modelling objective (see Table 2), a FEM based approach was disregarded for the selection.

A key requirement regards the modelling of fatigue crack propagation (see Table 2), i.e. FCG Stage II. This aspect is not covered by the brick- (see section 2.2.5) or the wedge model (see section 2.2.6) as these models represent phenomenological approaches (see Table 1). Due to this fact, an extension to model FCG at Stage II

is not supported. As a result, these approaches were not considered for the model type selection.

PD and DEM models match a broad spectrum of modelling aspects (see Table 1). However, there is no model that captures all criteria, which highlights the complex nature of rolling contact modelling. A comparison of PD models to solid-state DEM models revealed a similarity of these approaches (see Table 1). This fact suggested the possibility of a hybrid approach, i.e. to selectively integrate specific aspects of PD and DEM approaches to a novel RCF model.

As a result, DEM and PD models were assessed with respect to a hybrid modelling approach. In the first step, a focus was laid on models that capture the RCF criterion (see Table 1). The DEM models of Raje et al. (43) and Leonard et al. (47) were designed by means of Voronoi tessellation in order to model microstructure. As this grid structure contradicted the objective to draft a macroscale model and to omit explicit modelling of microstructure (see section 3.2), these approaches were not pursued.

The first approaches to model RCF by PD modelling were performed by Ghaffari et al. (62,67) and Freimanis and Kaewunruen (53), who demonstrated the applicability. The models suggested to be a potential starting point and highlighted requirements for further improvement. The latter regarded the insufficiency of the bond law in case of failure (see section 2.2.4) and the absence of a stress representation. The PD RCF models of Ma et al. (54,63) and Wang et al. (64,65,71) represented recent developments that were not available at the time of type selection.

Kosteski et al. introduced a post-processing routine to model a stress tensor, which was implemented to the 3D truss-like DEM model (34). This feature was considered important for the contact model. Regarding FCG modelling, Silling and Askari (49) developed a fatigue law applicable to PD and solid-state DEM models. This damage law emerged to be the standard approach adopted by later modelling works, which potentially offered synergies. Further, it facilitated a straight-forward implementation of experimental FCG data (see Figure 9), which was deemed to be important.

Based on this discussion, the development of a hybrid model derived from truss-like DEM and PD models was selected (see Table 3). The intention was to integrate specific features from each approach. In the first step, a 2D contact model was derived from the truss-like DEM model (see chapter 4, section 4.2). A post-processing routine to describe the stress field was adopted for verification reasons. In the second step, the PD fatigue model was integrated and modified to deal with the rolling contact regime (see chapter 5, section 5.1.1).

		<b>Modelling approaches</b>	<b>Challenges</b>
<b>DERC model</b>	<b>Fatigue model</b>	PD fatigue law <ul style="list-style-type: none"> <li>• Cyclic degradation of elements (bonds)</li> <li>• Parameterisation to experimental FCG data</li> </ul>	<ul style="list-style-type: none"> <li>• RCF modelling: Bond law in case of failure</li> <li>• Crack closure modelling</li> <li>• FCG anisotropy of deformed materials</li> <li>• Plasticity, SPD, hardening</li> </ul>
	<b>Rolling contact model</b>	Truss-like DEM model (Kosteski et al. (34)) <ul style="list-style-type: none"> <li>• Scaling from 3D to 2D</li> <li>• Linear-elastic model</li> <li>• Post-processing of stress tensor</li> </ul>	

**Table 3 – Hybrid approach for the development of the DERC model. The model is based on a rolling contact model, which is complemented by a fatigue model. The modelling approaches and challenges are summarised.**

Challenges of the approach were considered to regard the bond law in case of failure (see section 2.2.4), the modelling of crack closure (see section 2.1.6) and the implementation of FCG anisotropy (see section 2.1.4) in relation to SPD (see section 2.1.1). As the hybrid model was developed around the idea of “discrete elements” that serve to model RCF, it was called Discrete Element Rolling Contact (DERC) model. An overview on the concept is displayed in Table 3.

In this section, different model types were assessed to develop a combined rolling contact and fatigue model. Based on the assessment of an evaluation matrix (see Table 1), a hybrid approach (see Table 3) was selected to address the modelling objective (see Table 2), which was implemented in a sequential way. In the next step, the rolling contact model is set up (see section 4.2).

## 4.2 Basic model assembly

In this section, a basic assembly of the rolling contact model (i.e. basis of the DERC model, see Table 3) is performed, which was derived from the truss-like DEM. Therefore, the original model is explained, applied simplifications are discussed and the basic entity of the novel model is described.

The first approach to develop a discrete model of a continuum can be traced back to Hrennikoff in the 1940's. Though, the first truss lattice models to deal with solid materials were not developed before the early 2000's (34). In a reverse approach, the truss-like DEM introduced by Kostaski et al., which was selected to be the reference for the rolling contact model (see section 4.1), was derived from an actual mechanical assembly of interconnected bars. The goal was to model damage and fracture of ductile solid materials. A representation of the stress tensor and of stress intensity factors was implemented (34).

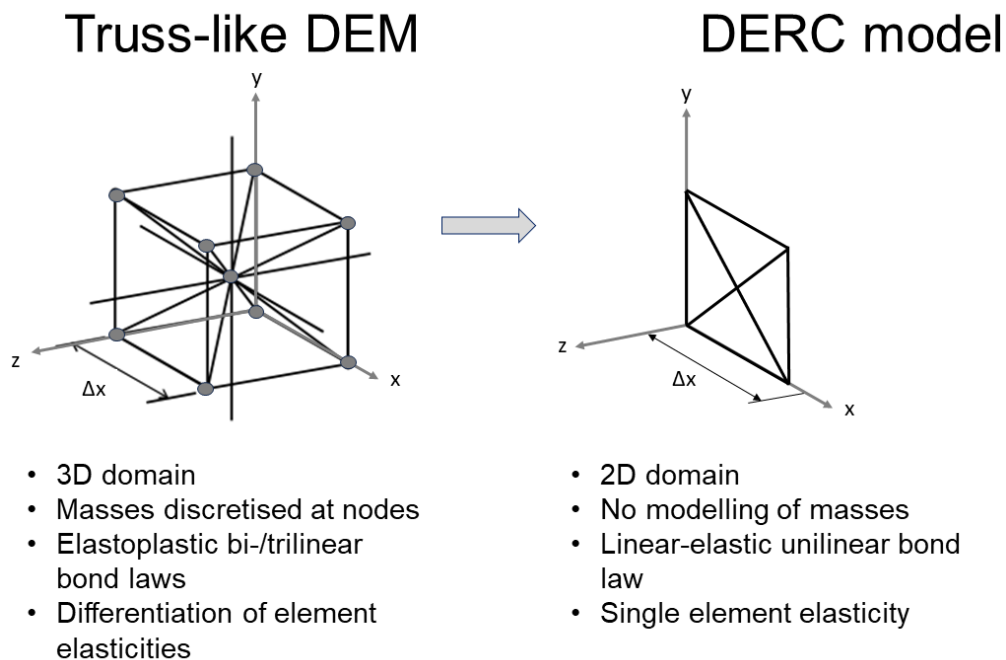


**Figure 18 – Comparison of truss-like DEM (left, modified from (34)) and derived DERC model (right). The applied simplifications are summarised below.**

The truss-like DEM consists of 20 bars connected at 9 nodes that represent masses (see Figure 18, left). Each node has three translational degrees of freedom. The bars represent longitudinal and diagonal elements that have a specific length and axial elasticity. The elasticities depend on Young's modulus,  $E$ , and Poisson's ratio,  $\nu$ , which is fixed for  $\nu = 0.25$ . The element's constitutive

relation (see section 2.2.4) was defined by bi- and tri-linear bond laws to address elastoplastic deformation. By application of Newton's laws, the equations of motion were set up (34).

In order to derive a contact model from the truss-like DEM, following simplifications were applied to the DERC model (see Figure 18, right). The domain was reduced from 3D to 2D, the point masses were omitted, and the bond law was simplified to be linear-elastic (see Figure 15). For reasons of simplicity and compliance to the fatigue model (see section 5.1.1), only one elasticity was applied to longitudinal and diagonal elements. The basic entity of the derived model is illustrated in Figure 19 and was called DEM module. By connecting multiple DEM modules, a grid was assembled (see chapter 4.3).

The DEM module consists of four nodes, four longitudinal- and two diagonal elements. All nodes and elements were assumed to be without mass, as effects due to gravity and inertia were disregarded. Generally, each node can displace in x- and y-direction, representing two degrees of freedom. The constitutive element of the model and of each module are the discrete elements (bonds) that connect two nodes of the grid in a truss-like arrangement (see Figure 19). The 1D elements carry load in tension and compression only, but no transverse forces or torque. Buckling of the elements is disregarded. External forces can be applied in x- and y- direction to the nodes. Torque cannot be applied to the nodes.

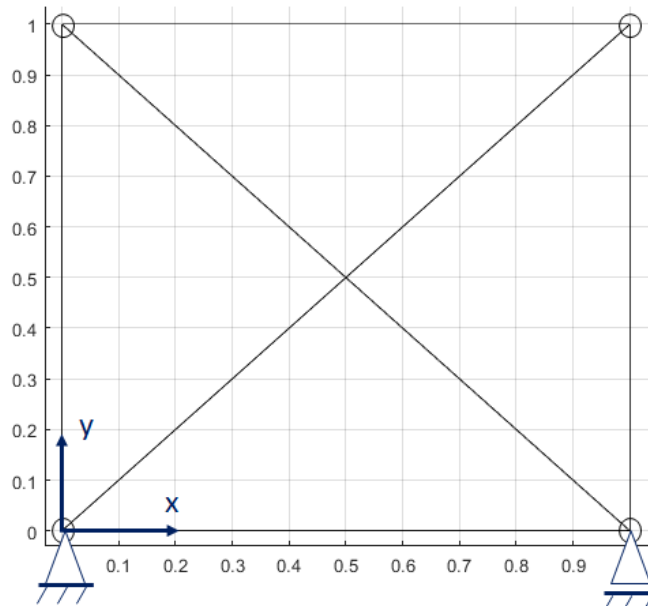


**Figure 19 – Basic 2D DEM module consisting of four nodes (corners), four longitudinal- and two diagonal elements. The module is supported by a fixed- and a floating bearing.**

The characteristic of a DEM module is that external forces are distributed to the elements (element forces) and to the bottom nodes, which were fixed by boundary conditions (see chapters 4.7, 4.11). The bottom nodes were modelled to bear forces like a bearing. Thus, they give rise to reaction forces.

In order to describe the system of connected nodes, the basic equations based on Newton's laws were formulated for every node (see chapter 4.5), taking external forces and boundary conditions into account.

### **4.3 Grid pre-processing**

A basic DEM module (see chapter 4.2) is the simplest form of a DEM grid (1 x 1 grid). The objective for simulating fatigue was to scale up the module to form larger grids. Therefore, a pre-processing routine was designed. Based on data derived from the user input, the method was intended to define equidistant nodes that interact with each other by means of elements.

As a result, large grids were assembled. Specific characteristics were assigned to the elements. The linear-elastic behaviour of all elements was defined by an elasticity parameter,  $c$ , which defined the bond law (see section 4.5).

In summary, the method loaded the user specified data regarding grid dimension, discretisation, and element properties. With it, nodes and elements were defined by vectors and visualised (see section 4.4). The pre-processing and all other simulation files were implemented in MatLab®.

### **4.4 Visualisation**

An important issue when working with a numerical model is the user interface. Thus, a visualisation for the grid (see chapter 4.3) was developed, which is explained in this section. The visualisation was designed to provide the following functions:

A visualisation of the grid in the initial and final states, of the quality and quantity of the element strains, and of the applied external loads as vectors. Only the elements were illustrated. The nodes were omitted, as this would not offer any additional benefit for the user.

An objective of the model was to simulate a continuous component like a rail or a wheel. Hence, the lateral edges were designed to be interconnected to each other

(see chapter 4.11). This was visualised by adding the specific elements on both edges.

A key feature to be displayed regarded the quality (tension or compression) and quantity of element strains. To support an effortless way of perception, a variation of line widths related to the quantity was applied, as well as a colour code which reflects the quality of load or deformation. Thus, bold element lines were selected to represent highly strained elements, thinner lines for lower charged elements. Elements loaded in tension were coloured in red, those loaded in compression in blue (see Figure 20).

External forces were illustrated by means of vectors. They indicate the direction of the forces assigned to the surface nodes. The shaft length is also an indication of the force size, which eases the display of force distributions like a discretised Hertz contact (see Figure 20).

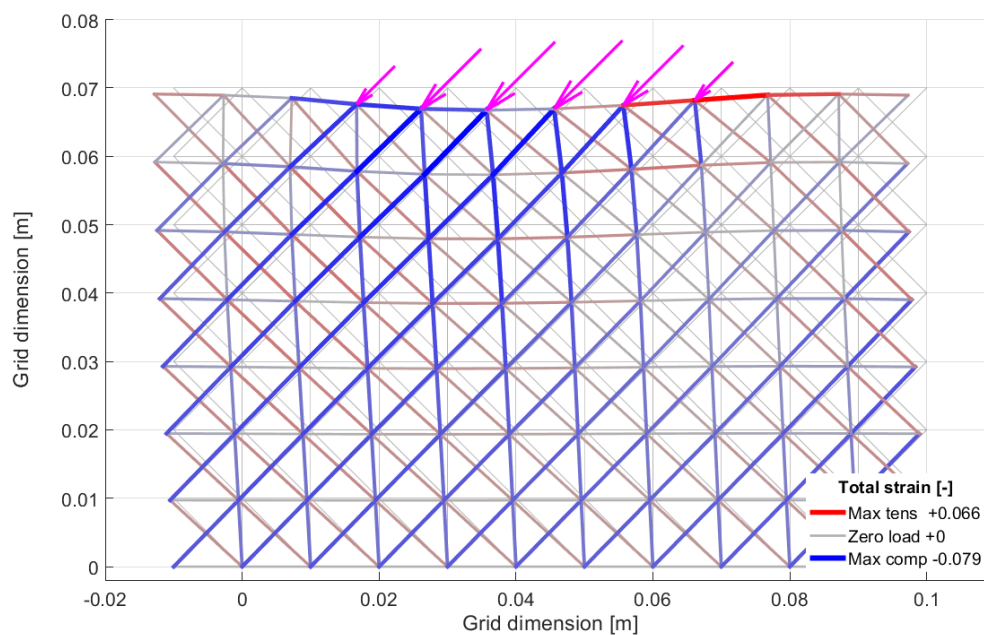


**Figure 20 – Visualisation of a deformed grid: The relative values of the external forces are illustrated as vectors on the surface. A colour coding highlights the quality of element strains (tension red, compression blue). A line width coding displays the strain quantity (high strains in bold lines). In the background, the initial grid is illustrated.**



## 4.5 Basic equations

In this section, the procedure to set-up the equations that govern grid deformation (see Figure 20) as a result of a rolling contact are described.

Based on the assumptions discussed in the beginning of chapter 4, the effect of an applied load was simulated. The grid was designed to consist of displaceable nodes (see Figure 21) where forces act. The position of a node “i” for state “0” was defined by a vector  $\vec{x}_i$ :

$$\vec{x}_{i_0} = \begin{pmatrix} x_{i_0} \\ y_{i_0} \end{pmatrix}$$

Equation 7

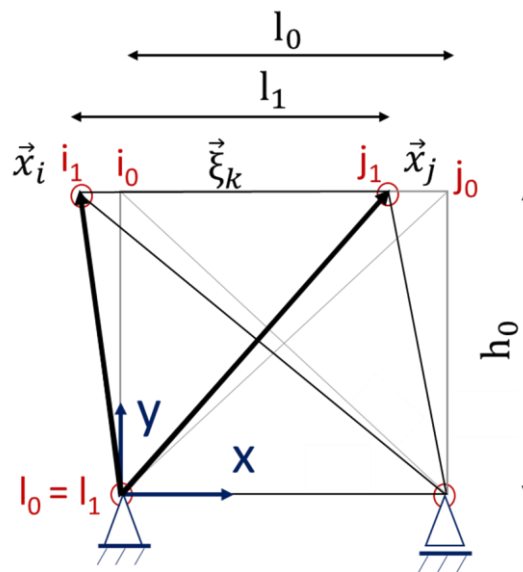


Figure 21 – Principle of node displacement from state “0” to state “1”.

Then, an element “k” was defined for state “0” between the two adjacent nodes “i” and “j” by a Euclidean vector  $\vec{\xi}_{k_0}$  that stretches from node “i” to node “j”:

$$\vec{\xi}_{k_0} = \vec{x}_{j_0} - \vec{x}_{i_0}$$

Equation 8

A displacement between state “0” and “1” was described by the displacement vector  $\overline{\Delta \vec{\xi}_{k_01}}$ :

$$\overline{\Delta \vec{\xi}_{k_01}} = \vec{\xi}_{k_1} - \vec{\xi}_{k_0}$$

Equation 9

The element strain was described as a scalar  $\varepsilon_{k_1}$ . An elongation by tension loading ( $\varepsilon_{k_1} > 0$ ) results in a positive strain, a compression loading ( $\varepsilon_{k_1} < 0$ ) in a negative one.

$$\varepsilon_{k_1} = \frac{|\vec{\xi}_{k_1}| - |\vec{\xi}_{k_0}|}{|\vec{\xi}_{k_0}|} = \frac{l_1 - l_0}{l_0}$$

**Equation 10**

Thereby, the element lengths  $l_0$  and  $l_1$  represent the vector amounts of  $\vec{\xi}_k$ .

$$l_0 = |\vec{\xi}_{k_0}|$$

**Equation 11**

The unity vector,  $u_k$ , was set up for each element.

$$\vec{u}_k = \begin{pmatrix} u_x \\ u_y \end{pmatrix}$$

**Equation 12**

The constitutive relation that defines the mechanical behaviour of an element was defined by a bond law (see Figure 15). A linear-elastic behaviour of the elements was assumed. An elasticity parameter,  $c$ , was assigned to each element. The parameter was determined as part of the parameterisation (see section 4.12). Element force vectors,  $\vec{F}_{el_{k_1}}$ , for state “1” were formulated as a function of the strain, the elasticity parameter, and the unit vector,  $\vec{u}_k$ .

$$\vec{F}_{el_{k_1}} = c * \varepsilon_{k_1} * \vec{u}_k =$$

**Equation 13**

As a result of the semi-infinite assumption, the element force and all other force types were line forces with the unit of force per metre. Each element force acts on both nodes it was assigned to, however in opposite directions.

Besides the element forces, nodes were also designed to be subject to external- and reaction forces. External forces ( $\vec{F}_{ext}$ ) were applied to surface nodes only (see Figure 20) to simulate contact stresses, which is described in section 4.8.

Reaction forces ( $\vec{F}_{react}$ ) were applied to nodes to resist the element forces. Hence, they represent mechanical bearings. In this model, the reaction forces were applied to bottom nodes only and not to the lateral edges due to the periodic boundary conditions that are predominantly used (see section 4.11). As static equilibrium was assumed, the reaction force assigned to a node “i” for state “0”

(see Figure 21) was defined as being opposite to the sum of all adjacent,  $n_{adj}$ , element forces. Generally, this sum comprised the forces of eight elements.

$$\vec{F}_{react\_l\_0} = - \sum_{j=1}^{n\_adj} \vec{F}_{el\_j\_0}$$

**Equation 14**

In the final step, the element-, external- and reaction forces were summed for each node “m” at state “0” to a resulting vector force  $\vec{F}_{node\_m\_0}$ . The equation was derived from Newton’s 2<sup>nd</sup> law, which was simplified by the assumptions of omitting mass effects and by having a static equilibrium (no dynamic analysis, see section 3.2) and is illustrated below (Equation 15). Due to static equilibrium, the sum is zero:

$$\vec{F}_{node\_m\_0} = \sum_{j=1}^{n\_adj} \vec{F}_{el\_j\_0} + \vec{F}_{ext\_m\_0} + \vec{F}_{react\_m\_0} = 0$$

**Equation 16**

By applying Equation 16 to all nodes of the grid, the system of equations for the model was assembled. At this stage, where the model does not consider damage, the linear system of equations resembles that of a hyperstatic truss-like beam structure. A difference, though, is that truss-like beam structures are assumed to be rigid (78), whereas the model allows for a linear-elastic deformation of the elements (see Figure 20). In chapter 5, damage will be introduced to model RCF, whereby a non-linearity is introduced. This makes solving the system of equations more challenging, wherefore a solver was required (see section 4.6).

The model was designed to be governed by applied external forces resulting in a grid deformation. This approach was selected according to the conditions in service, where wheel-rail contact stresses imply a material deformation.

In the next step, the system of equations is processed (see section 4.6).

## 4.6 Numerical process

The objective of this section is to highlight the numerical process which solves the simulation problem (see section 4.5) by means of a solver function (solver).

The numerical process consists of a preprocessing-, a simulation- and a post-processing section (see Figure 22). In the preprocessing, the initial grid is defined

once. Then, the simulation uses this data as well as the data from the user input (material, load, boundary conditions, simulations control) to perform the simulation. Finally, the post-processing routine is run to visualise and export the results.

In order to complete one simulation cycle (simulation increment), each of the three sections must be run at least once. However, the simulation- and the post-processing sections can be run multiple times (see Figure 22) to simulate cyclic loads leading to RCF.

The prerequisites used for the numerical process were a discretised model (for preprocessing, see section 4.3), the basic equations (see section 4.5), an applied load (see sections 4.8) and the boundary conditions (see sections 4.7, 4.11).

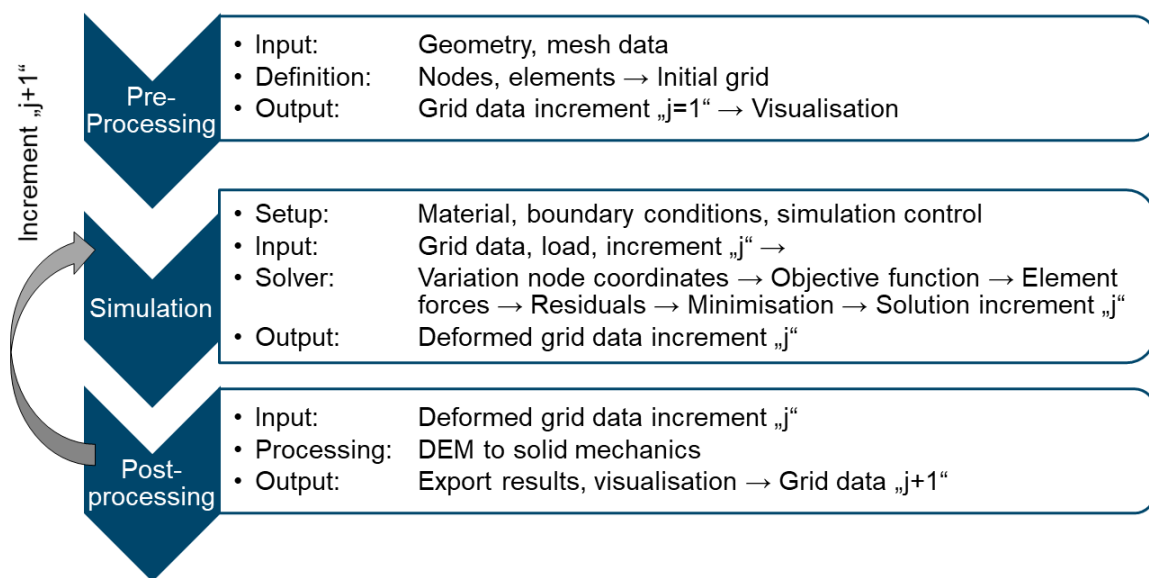


**Figure 22 – The numerical process consists of the sequential routines preprocessing, simulation and post-processing. The simulation can be run for multiple (j) increments.**

In agreement with the selected procedure (see section 4.5), the simulation starts with an initial set of node coordinates. Those are used by the solver as an input for the objective function. This function calculates a set of target variables (residuals) as a function of the input variables, here the node coordinates. The scope of the solver is to minimise those residuals by using a specific input which is a standard method for numerical processing. In order to run the process, an appropriate solver was required.

The solver function "fsolve" of MatLab® was adopted. Reasons therefore were that the solver is based on a proven algorithm and due to the availability of a detailed

documentation. The solver applied the Levenberg-Marquardt algorithm. A detailed documentation is provided by MatLab® (79).

The objective function uses the node coordinates for the processing of vectors that describe the DEM element's relative positions, lengths, axial strains, and forces as well as the reaction forces by utilising the equations from section 4.5. By adding the element- and reaction forces, the force sums in x- and y-directions (see Equation 16) can be calculated for each node "i". As static equilibrium was assumed, the sums for each node ( $F_{node\_i\_x}$ ,  $F_{node\_i\_y}$ ) must approximate zero.

By compiling all force sums per node, the residual of the force vector ( $\sum_{Resid\_force}$ ) can be assembled (see Equation 17). This vector is the minimisation target of the solver.

$$\sum_{Resid\_force} = \sum \begin{pmatrix} F_{node\_1\_x} \\ F_{node\_1\_y} \\ \vdots \\ F_{node\_i\_x} \\ F_{node\_i\_y} \end{pmatrix}$$

**Equation 17**

Hence, the solution of the simulation is a set of node coordinates for which the residual vector  $\sum_{Resid\_force}$  is minimal, this means below a predefined function tolerance. In the next step, the basic boundary conditions were defined (see section 4.7).

## 4.7 Basic boundary conditions

In order to run the basic DEM simulation, boundary conditions must be set, the process for which is detailed in this section. As the objective of the model is to simulate mechanical processes, only mechanical boundary conditions are discussed. Those constraints are part of the simulation set-up, which is highlighted in Figure 22 that displays the numerical process. Further, the boundary conditions are essential for the calculation of the grid's reaction forces (see section 4.5, Equation 14).

Two basic types of boundary conditions were initially defined to fix the bottom nodes of a grid. One type comprised fixed nodes only, the other type included one fixed node in the origin and multiple floating nodes positioned along the x axis. Both types are illustrated in Figure 23. The floating boundary condition was applied as was the simplest one, which for example is required to carry out tension

tests. The fixed boundary condition was selected with respect to high shear loads, where no lateral displacement of the bottom nodes was permitted.

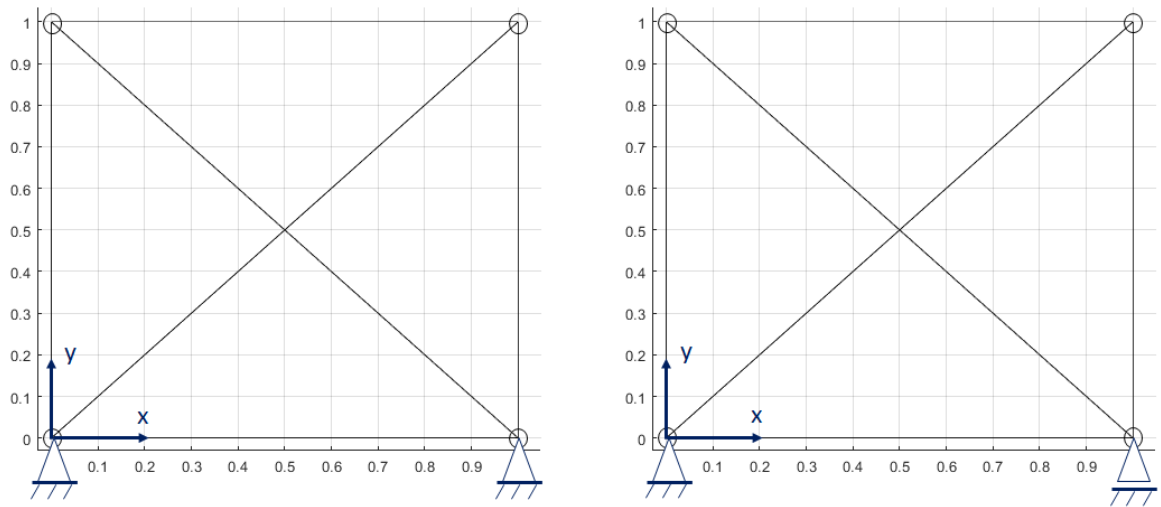


**Figure 23 – Arrangement of basic boundary conditions for bottom nodes: Fixed nodes (left) and fixed/ floating nodes (right).**

In this section, boundary condition constraints were applied to the bottom nodes. In the next section, external loads are applied to the top nodes.

## 4.8 Load modelling

The aim of this section was to model a contact patch (rolling or sliding) in a simplified way. The patch was modelled to consist of a normal and tangential load component, i.e.  $p(x)$  and  $q(x)$  (see Figure 16).

Based on the defined assumptions (see introduction of chapter 4), the normal load,  $p(x)$ , was modelled as a Hertzian contact of two contacting cylinders (see Figure 24 left), which is described by a patch length,  $2a$ . With respect to Johnson (77), half of the contact patch length,  $a$ , (semi-contact length) was derived (see Figure 24):

$$a = \sqrt{\frac{4PR_{eq}}{\pi E^*}}$$

**Equation 18**

Equation 18 consists of the load per unit length  $P$  and an equivalent radius  $R_{eq}$  that incorporates the radii  $R_1$  and  $R_2$  of both contacting bodies:

$$R_{eq} = \left( \frac{1}{R_1} + \frac{1}{R_2} \right)^{-1}$$

Equation 19

Furthermore, a combined modulus  $E^*$  was used to capture different materials of the contacting bodies, which however simplified for the given case that both bodies are made of steel:

$$E^* = \frac{E}{2(1 - \nu^2)}$$

Equation 20

The load per unit length  $P$  refers to an applied force  $F$ , a contact width  $w$  (see Figure 24) and was derived with respect to the maximum normal contact pressure  $p_0$ :

$$F = P w$$

Equation 21

$$P = \frac{p_0 \pi a}{2}$$

Equation 22

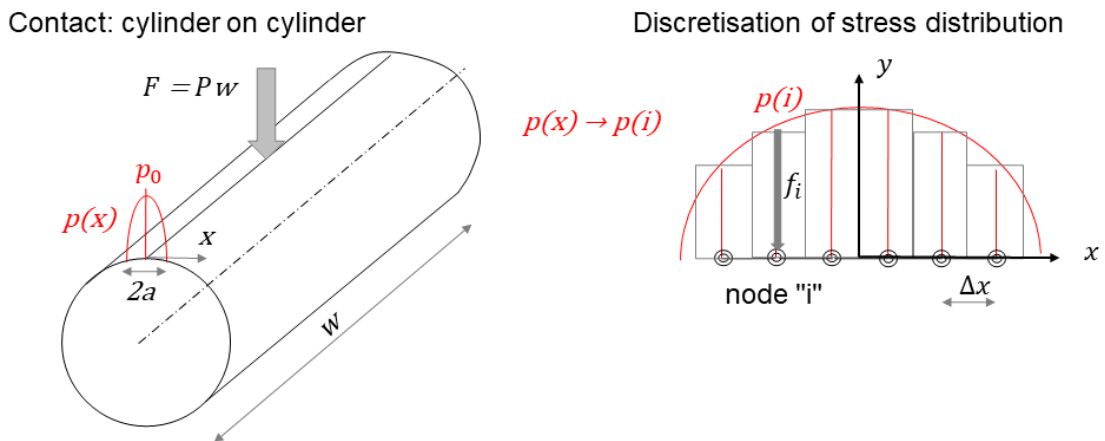


Figure 24 - Line contact with pressure distribution  $p(x)$  on the left and the associated discretisation  $p(i)$  on the right.

Further, a normal pressure distribution  $p(x)$  was defined for the length of the contact  $x$  (see Figure 24, left), which is given by  $-a \leq x \leq a$ :

$$p(x) = \frac{2 P}{\pi a^2} \sqrt{(a^2 - x^2)}$$

**Equation 23**

Equation 22 was integrated in Equation 23 to derive the stress distribution  $p(x)$  as a function of the maximum contact pressure  $p_0$  and the semi-contact length  $a$ :

$$p(x) = p_0 \sqrt{\left(1 - \frac{x^2}{a^2}\right)}$$

**Equation 24**

The pressure distribution of the patch,  $p(x)$ , was discretised with respect to the grid's discretisation,  $\Delta x$  (see Figure 24). It was applied to the top nodes of the grid, i.e. the model's surface (see Figure 20, Figure 24). The centre of the contact patch was positioned between two nodes (see Figure 24, right). The discretised pressure distribution  $p(i)$  per node "i" was calculated with Equation 24, and a discrete line force  $f_i$  was derived with respect to the applied grid discretisation  $\Delta x$ :

$$f_i = p(i) \Delta x$$

**Equation 25**

The discrete line force  $f_i$  was transformed in a vector to describe the external force  $\vec{F}_{ext\_i\_0}$  at state "0", that could be applied to a grid node "i".

$$\vec{F}_{ext\_i\_0} = \begin{pmatrix} 0 \\ f_i \end{pmatrix}$$

**Equation 26**

In this way, a Hertzian contact was modelled by an external force vector,  $\vec{F}_{ext}$ . The input is an applied maximum pressure  $p_0$  which was transformed to an assembly of vectors  $\vec{F}_{ext\_i\_0}$  that were applied to surface nodes (see Figure 24). The nodes were selected with respect to the contact position of an increment "j" and the semi-contact length  $a$ .

In order to model not only pure rolling, but also traction or breaking, a tangential load component introducing sliding was required. Full sliding and a semi-elliptic stress distribution were assumed, whereas a coefficient of friction of  $\mu$  was applied. With it, Equation 26 was expanded to integrate the tangential load component in x-direction. The result is a combined load:

$$\vec{F}_{ext\_i\_0} = \begin{pmatrix} f_i \mu \\ f_i \end{pmatrix}$$



The employment of a tangential load superposed to the normal Hertzian load is a contradiction to the Hertz assumption. This, however, was accepted as it is a standard approach in contact mechanics.

Due to the applied discretisation method for modelling the normal and tangential stresses, i.e. the finite number of nodes the load attaches, there is a discretisation error per contact patch. This error can be minimised by decreasing the grid discretisation  $\Delta x$ . In this way, loads in a wheel-rail contact were approximated and discretised.

## 4.9 Post-processing of stresses

At this point, the simulation was capable of processing element strains and forces that describe the reaction of the grid to an applied load. In the next step, a post-processing routine was designed to transform element forces into stresses. Besides stresses, strains were also an issue, and in particular shear strains as the goal was to simulate rolling contacts. Thus, the focus was a post-processing of shear strains, whereas normal strains were neglected.

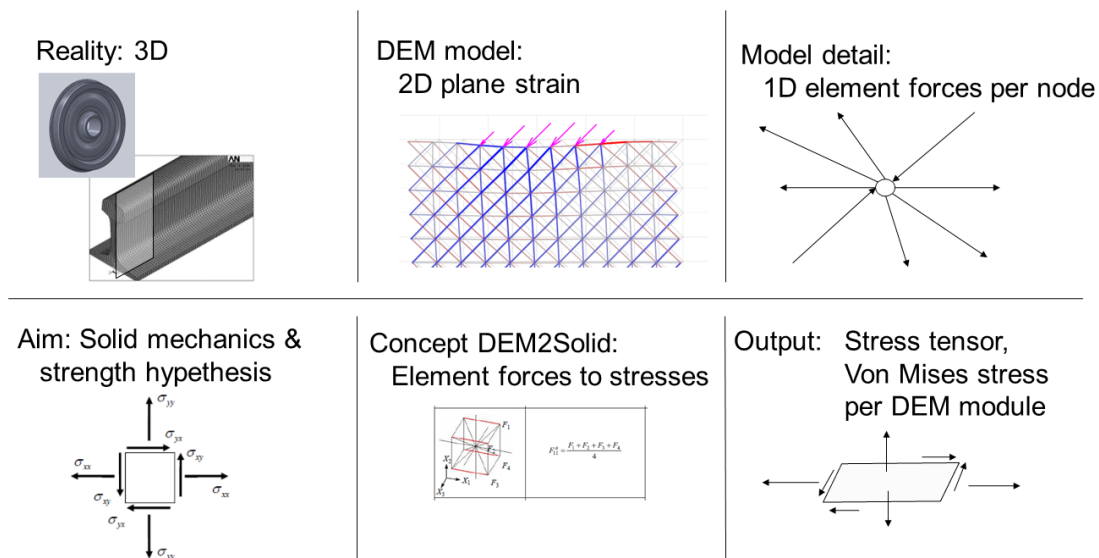


Figure 25 – Overview of the modelling (top) and principle of the concept (bottom).

The main idea of the post-processing is displayed in Figure 25, which gives an overview of the model discretisation and highlights the demand to transform results from the DEM domain to solid mechanics. The objective was to determine

the stress tensor, an equivalent stress, and the shear strain for each module of the grid. It was important to consider that all the element forces mentioned are line forces and have the unit force per length.

Under the plain strain assumption (see introduction of chapter 4, Figure 16), the stress tensor  $T_\sigma$  contains stresses that are zero by definition (80). These are  $\sigma_{xz}$ ,  $\sigma_{zx}$ ,  $\sigma_{yz}$  and  $\sigma_{zy}$ .

$$T_\sigma = \begin{pmatrix} \sigma_{xx} & \sigma_{yx} & \sigma_{zx} \\ \sigma_{xy} & \sigma_{yy} & \sigma_{zy} \\ \sigma_{xz} & \sigma_{yz} & \sigma_{zz} \end{pmatrix}$$

Equation 28

With respect to the semi-infinite body introduced in the introduction of chapter 4 (see Figure 16), the normal stress in the z-direction is not zero either, but a function of the other two normal stresses and the Poisson coefficient  $\nu$ . It was important to note that, in agreement with the plain strain assumption, the processing does not consider element forces in z-direction. As  $\sigma_{zz}$  is dependent of  $\sigma_{xx}$  and  $\sigma_{yy}$ , it can be derived from these stresses (77). Thus, it is not mentioned in the derivation below.

$$\sigma_{zz} = \nu * (\sigma_{xx} + \sigma_{yy})$$

Equation 29

For transforming element forces into stresses, the concept originally applied to the 3D domain by Kostas et al. (34) was tailored to the 2D domain. In agreement with the reference, stresses over a DEM module were assumed to be constant. Element forces were summed up to form an equivalent force, which is divided by the corresponding mean edge surface, resulting in the desired stress. With it, the remaining components of the stress tensor were derived (see Figure 26).

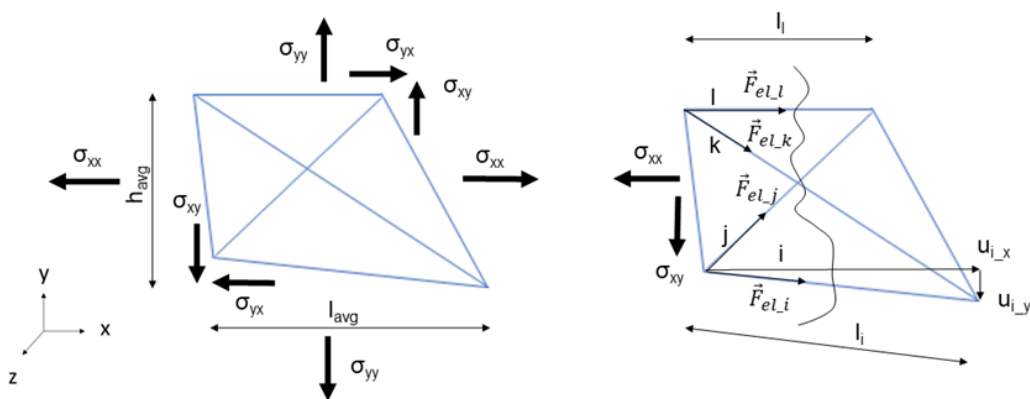


Figure 26 – Concept: Module edges are averaged and projected onto the main directions. Stresses are derived from equivalent forces and the averaged edges.

An important aspect was the fact that edge elements of a module are generally shared by other modules. Therefore, edge factors  $f_{edge}$  were introduced for those elements. They halve the element force in such a case. If the element is part of a free edge (surface, lateral or bottom), the edge factor equals one. For diagonal elements, no edge factor was required.

Another aspect was the projected mean edge length  $l_{avg}$  and height  $h_{avg}$ . These were derived by taking the average of both opposite edges "i" and "l" (see Figure 26) multiplied by the associated unit vector component  $u_x$ , which is displayed for the mean edge length in Equation 30 below. The formula is equivalent for the height.

$$l_{avg} = 0.5 * (l_i * u_{i_x} + l_l * u_{l_x})$$

**Equation 30**

The normal stress in x-direction was then defined:

$$\sigma_{xx} = \frac{(\vec{F}_{el_i} * u_{i_x} * f_{edge_i} + \vec{F}_{el_l} * u_{l_x} * f_{edge_l} + \vec{F}_{el_j} * u_{j_x} + \vec{F}_{el_k} * u_{k_x})}{h_{avg}}$$

**Equation 31**

The normal stress in y-direction was formulated equivalently. In the same way, the shear stresses were derived. Finally, opposing shear stress pairs e.g.  $\sigma_{xy}$  and  $\sigma_{yx}$  were averaged. The shear stress  $\sigma_{xy}$  acting in a plane orthogonal to the x-direction (see Figure 26) was defined by:

$$\sigma_{xy} = \frac{(\vec{F}_{el_i} * u_{i_y} * f_{edge_i} + \vec{F}_{el_l} * u_{l_y} * f_{edge_l} + \vec{F}_{el_j} * u_{j_y} + \vec{F}_{el_k} * u_{k_y})}{h_{avg}}$$

**Equation 32**

Using this approach, the stress tensor for each DEM module was obtained. With respect to the standard approach in the solid mechanics theory, a "module" was assumed to be equivalent to an "element". In contradiction to the derivation in solid mechanics where forces that act on an element are balanced, the module was sliced, and an internal force balance was made. Due to this approach, external- and reaction forces were disregarded.

Another aspect is the differentiation between true- and engineering stresses. True stresses refer to the actual edge length they are associated to, engineering stresses refer to the original length. In this approach, true stresses were processed. For the rolling contact model, only minor deformations were assumed,

as the modelling of plasticity was neglected. Thus, the true stresses were assumed to approximate the engineering stresses.

The scope of modelling rolling contacts and plastic deformation required not only stresses to describe the material state, but also a "failure theory" (80) that explains the transition from elastic- (failure) to elastoplastic behaviour. For ductile materials, the maximum shear stress (Tresca) theory and the von Mises theory provide yield stress limits. As the von Mises theory is more common and usually more accurate (80), it was selected here. Applying it, the elastic limit for each DEM module was described by an equivalent von Mises stress  $\sigma_{VM}$  (see Equation 33).

$$\sigma_{VM} = \sqrt{\sigma_{xx}^2 + \sigma_{yy}^2 + \sigma_{zz}^2 - (\sigma_{xx}\sigma_{yy} + \sigma_{yy}\sigma_{zz} + \sigma_{zz}\sigma_{xx}) + 3(\sigma_{xy}^2 + \sigma_{yz}^2 + \sigma_{xz}^2)}$$

**Equation 33**

It was important to bear in mind that generally the stresses in the normal direction were not principal, so the appropriate definition for the von Mises stress had to be used. Further, the equation was simplified by the fact that, due to the plane strain state, two of the shear stresses equal zero. In this way, the stress tensor as well as the equivalent von Mises stress were defined for each DEM module.

Finally, the engineering shear strain  $\gamma_{xy}$  within the xy-plane (80) was defined in a simplified way to model plastic deformation (see section 7.1). Therefore, the strain angles  $\theta_m$  and  $\theta_n$  of the vertical edges "m" and "n" of the module were averaged, whereas the angles  $\theta_i$  and  $\theta_l$  were neglected as only a minimum variation of these angles was assumed for the rolling contact case (see Figure 27).

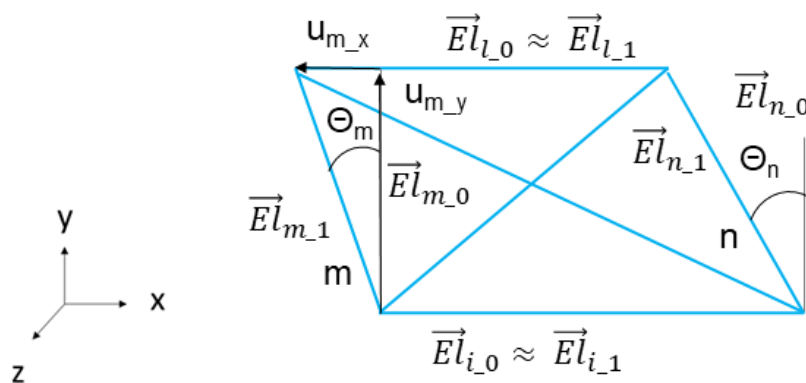


**Figure 27 - Geometry of shear deformation of a DEM module.**

The tangent of each strain angle (here for element "m", for "n" it is equivalent) was defined by the ratio of the unit vector multiplied by the element vector:

$$\tan(\theta_m) = \frac{u_{m,x}}{u_{m,y}}$$

**Equation 34**

With the strain angles  $\theta_m$  and  $\theta_n$ , a mean strain angle was calculated for the module:

$$\bar{\theta} = 0.5(\theta_m + \theta_n)$$

**Equation 35**

In the end,  $\gamma_{xy}$  was determined by inserting  $\bar{\theta}$  into the defining equation of the shear strain (1) which is given by:

$$\gamma_{xy} = \tan(\bar{\theta})$$

**Equation 36**

In this way, the stress tensor, the equivalent von Mises stress and the engineering shear strain were determined. In the next step, the results were visualised so that the stresses could be illustrated. For the visualisation of the stresses, a colour coding was applied by using a colour map supported by MatLab®, and a colour bar was added to the figure which was associated to the stress results. A transparent colour shading was used to retain the existing visualisation of elements (see section 4.4, see Figure 28).

With respect to the goal of the simulation, the von Mises stress was selected to be the stress type to be displayed. The shear strain was not visualised explicitly as it is an implicit result of the deformed grid.

In the end, the procedure was verified. Simple test cases were designed to compare the stress tensor and the equivalent stress to an analytical solution under defined conditions. Single modules were used to simulate the application of a compressive and a shear load (see Figure 28 and Figure 29). For the element elasticity, values derived from the parameterisation were adopted (see section 4.13). Only small deformations were applied to agree with the assumptions of the analytical approach.

In test case 1, a module was loaded in compression with 1.5 GPa by using a floating boundary condition (see Figure 28). The latter was required to avoid the introduction of additional stresses  $\sigma_{xx}$ . The applied load equals the stress in y-direction  $\sigma_{yy}$ . Due to the plain strain condition, a  $\sigma_{zz}$  was introduced as well. In this

case, the stress tensor as well as the equivalent stress agree well with the analytical solution. The result is listed in Table 4.

Test	BC	Analytical [Pa]					Model [Pa]				
		$\sigma_{xx}$	$\sigma_{yy}$	$\sigma_{zz}$	$\sigma_{xy}$	$\sigma_{VM}$	$\sigma_{xx}$	$\sigma_{yy}$	$\sigma_{zz}$	$\sigma_{xy}$	$\sigma_{VM}$
1	FLO	0.00E+00	-1.50E+09	-4.50E+08	0.00E+00	1.33E+09	1.04E+02	-1.50E+09	-4.49E+08	-2.97E+00	1.33E+09
2	FIX	0.00E+00	0.00E+00	0.00E+00	-1.50E+09	2.60E+09	3.78E+07	1.69E-01	1.13E+07	-1.50E+09	2.60E+09

**Table 4 - Comparison of analytical- and simulation results to assess the method.**

In case 2, the same element was loaded in shear only with 1.5 GPa by using a fixed boundary condition (see Figure 29). The latter was required to prevent a lateral flow which might have resulted in a violation of the assumption of small deformations. The simulation results reveal that for  $\sigma_{xx}$  there is a deviation from zero. The reason for this was that, due to the discretisation, the two reaction forces in x were not equally sized, which introduced a stress in the x-direction, resulting in a  $\sigma_{zz}$  not equal to zero. It must be noted that for the analytical solution, continuous forces were assumed. In this case, the impact of this discretisation effect on the von Mises stress was negligible.

One issue regarded the discretisation of reaction- and external forces on the bottom- and top edges of a grid. As described for case 2, a discretisation effect might lead to edge effects where the stresses deviate from a reference solution. This limitation had to be considered as well.

In summary, a post-processing tool was developed that transforms results from the DEM domain into solid mechanics terms. It delivers the stress tensor, the von Mises equivalent stress and the engineering shear strain for each DEM module. In order to verify the results, test cases were simulated and a comparison to analytical results was performed, demonstrating a good agreement. A critical aspect, however, is potential discretisation effects on the edges of a grid.

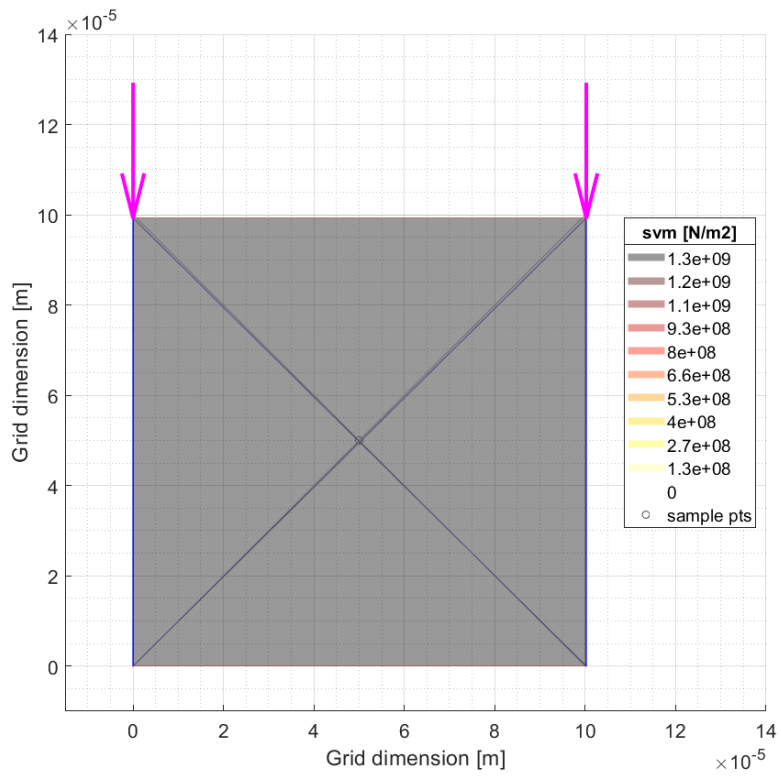


**Figure 28 - Test case 1: Compressive loading of a module under a floating boundary condition.**

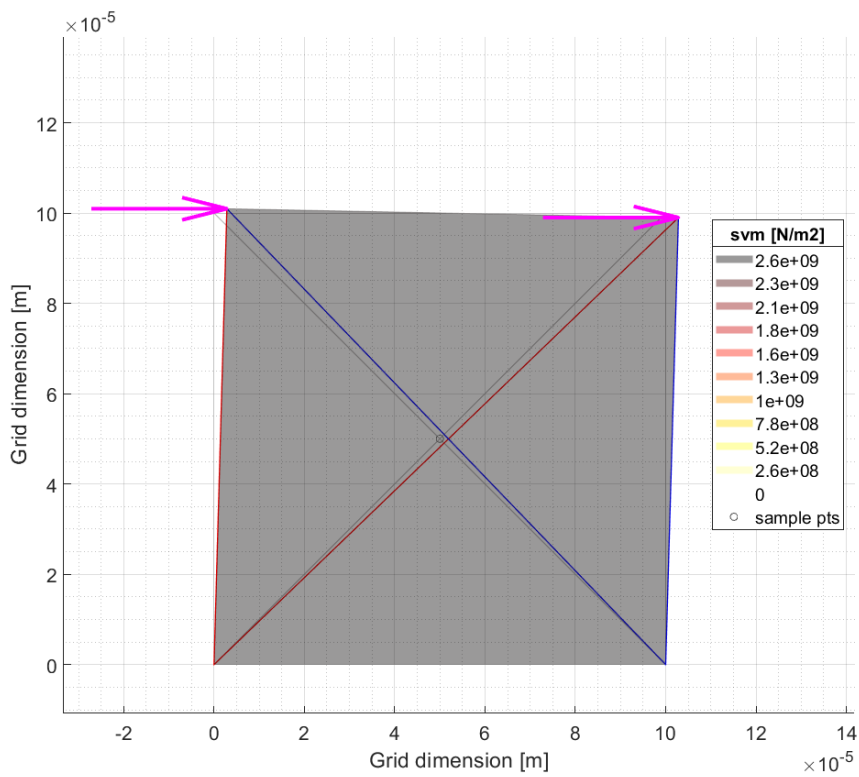


**Figure 29 - Test case 2: Shear loading of a module under a fixed boundary condition.**

## **4.10 Discretisation of rolling contact**

In order to model rolling contact fatigue, multiple contact cycles had to be simulated. Therefore, not only one, but a sequence of simulation increments (see section 4.6) was required to model one or more rolling contact cycles. Such a cycle was defined by the sequence of all simulation increments that describe one complete pass of a running load from a passing wheel.

The first increment "j" of a rolling contact cycle is visualised in Figure 20. For the next increment "j+1", the grid data from the previous state "j" was required as an input. The applied procedure is displayed in Figure 22. The running load had to be shifted to the left or right by one increment. The precondition for this shift, as well as for the modelling of a continuum by means of a discrete grid, was a periodic boundary condition, which is discussed in the next section 4.11.

The result of each succeeding increment "j+1" was the update of the node coordinates, the element strains, the element forces and of the stress per module. The required grid data (input for next simulation increment) consisted of the node coordinates only plus the external load. In this way, a sequence of associated static results was utilised to simulate a rolling contact cycle, where the load passes from the left to the right or vice versa.

## **4.11 Lateral periodic boundary condition**

In this section, the lateral periodic boundary condition is discussed, which was relevant for the modelling of an elastic rolling contact. Basically, a grid had the form of a block with free lateral edges (see Figure 30). The applied running load could not be shifted continuously along the surface but had to be faded in and out. Thus, a solution was required to connect both lateral edges to form a continuum.

This objective was implemented by the application of a lateral periodic boundary condition. First, a grid was pre-processed. Then, the lateral nodes of each edge were selected (see Figure 30, columns #1 and #27) and connected to those of the opposite edge. This was done by the introduction of additional elements that provided the mechanical connection between both edges and resulted in an additional column of elements and modules (see Figure 30, magnification).

However, in order to connect the opposite nodes, a constraint had to be applied to define the additional elements correctly. The x coordinates (horizontal direction) of the opposite nodes had to be manipulated ("mirrored"). By adding (respectively subtracting) "x+1" unit lengths (for a grid with "x" lateral modules) to (respectively from) the actual node coordinates, the new elements were defined correctly (see



example in Figure 30, mirroring of node #16 to #16'). Regarding the y coordinates (vertical direction), no manipulation was required as these were adopted from the opposite nodes. In this way, the lateral edges were connected mechanically via elements (boundary elements) to form a continuum.

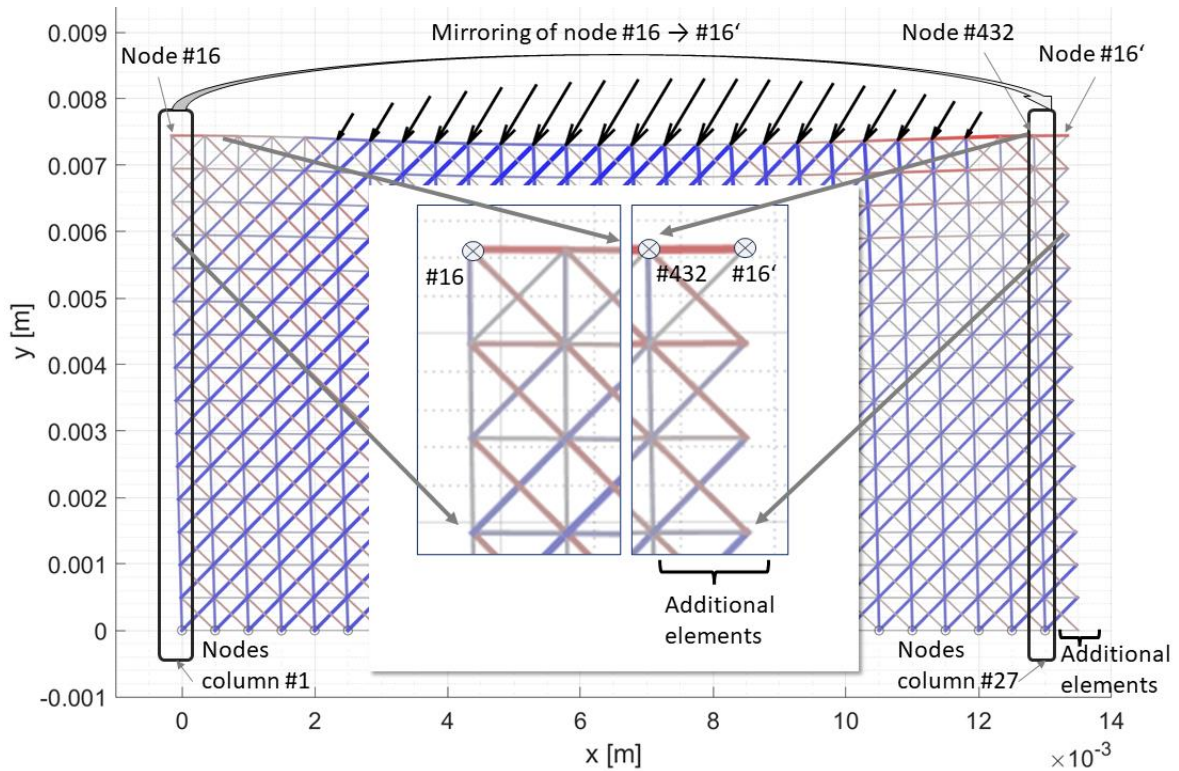


**Figure 30 – Lateral periodic boundary condition:** The left and the right columns of nodes (#1, #27) were connected by the introduction of additional elements on both lateral edges (displayed for the right edge only). For connecting node #432 to #16, this required a mirroring of node #16, resulting in node #16' (see grid top right), and vice-versa (not displayed). The procedure was applied to all nodes of the marked node columns.

A model with the applied lateral boundary condition is displayed in Figure 30. The nodes mirrored from the left edge to the right edge are displayed (see example for node #16 and #16'). The y coordinates of mirrored node pairs agree (see Figure 30, magnification). The additionally introduced lateral elements are displayed for the right edge (see Figure 30). Mind that the procedure is applied to both lateral edges, but for reasons of simplicity it is visualised only for the right edge.

The implication of the lateral periodic boundary condition was that a laterally discrete grid was transformed into a continuous grid. In this way, the model

reproduced a continuum behaviour. Further, the applied external load could be moved laterally without any limitation.

#### 4.12 Elastic parameterisation

In this section, the elasticity parameter,  $c$ , (see section 4.5) was derived (26). The goal was to reproduce an accurate result for the stress field below a rolling contact. The derived parameter represented the core of the applied elastic, strain driven bond law (see Equation 13). In the next section, a verification was performed to demonstrate the agreement of the model with the selected reference (see section 4.13).

The first step was to derive the elasticity parameter. For each grid discretisation,  $\Delta x$ , one parameter,  $c$ , was derived, which was applied to all elements of the grid. At the initial stage of the model development, the application of non-squared modules was considered with regard to the explicit modelling of SPD (see section 7.1). For this set-up, no appropriate method was identified in the literature. Thus, a novel procedure for the derivation of the elasticity parameter was developed. However, after the abandoned attempt to model SPD explicitly (see section 7.1.3), only squared modules were applied, which is assumed in this section.

In the first step, a reference for the stress tensor under Hertz- or combined load was required, whereas the assumptions made in sections 4.5 and 4.8 were considered. In compliance to that, the derivation of Johnson (77) was selected to specify the stress tensor for a given normal contact pressure  $p_0$  and a coefficient of friction  $\mu$ . Therefore, the coordinate system applied in the literature was transformed to match the system applied to the model (see introduction of chapter 4).

In this way, the stresses  $\sigma_{xx}$ ,  $\sigma_{yy}$ ,  $\sigma_{xy}$ , and by Equation 29  $\sigma_{zz}$ , were determined, referring to a specific sampling grid ( $x$  in  $[-2a, +2a]$ ,  $y$  in  $[0, -2a]$ ), which was defined with respect to the semi-contact length  $a$ . With it, the equivalent stress  $\sigma_{VM}$  was processed (see Equation 33). In Figure 31, the equivalent stress distribution as a result of a combined load ( $p_0= 1500$  MPa,  $\mu =0.4$ , contact cylinder-cylinder, both radii 23.5 mm) is interpolated and visualised. Further, the sampling grid is illustrated.

The sampling grid was integrated in the DEM model. Therefore, the sampling grid had to be aligned correctly. The vertical axis of the sampling grid was fixed to the axis of the applied load (see Figure 24). However, the upper edge of the sampling grid (surface, horizontal axis) was not aligned to the top of the DEM grid, but to the

centre of the surface modules in the undeformed state to account for the stress discretisation per module (see section 4.9). This horizontal alignment is visualised by the inner frame in Figure 31 (dash-dotted line).

In this way, the sampling grid was implemented to the DEM model. Then, stresses from the simulation related to the DEM grid were interpolated to match the sampling grid (see Figure 33). The data set of the stress reference (vector  $\vec{\sigma}_{VM\_Ref}$ ) was then made comparable to that of the simulation (vector  $\vec{\sigma}_{VM\_Sim}$ ). Finally, a stress residual  $\Sigma Resid\_svm$  was defined by taking the square root of the sum of the squared residuals of both vectors, and by dividing it by the number of sampling points  $n_{VM\_sample}$  (26).

$$\Sigma Resid\_svm = \frac{\sqrt{\sum (\vec{\sigma}_{VM\_Sim} - \vec{\sigma}_{VM\_Ref})^2}}{n_{VM\_sample}}$$

**Equation 37**

The last step was to set up an optimisation routine. As an input, the elasticity parameter was varied by a solver to minimise the stress residual  $\Sigma Resid\_svm$ . The result was an optimised parameter, which provided an approximation to the reference stress distribution of Figure 31.

The developed method introduced an error due to the horizontal alignment of the sampling grid to the model grid, as the "surface" of the sampling grid was "lowered" by  $\Delta x/2$ . This was reasonable for a sufficiently fine discretisation of the grid ( $\Delta x/2 \ll a$ , criterion A). Moreover, the definition of the residual (Equation 37) was based on the assumption of small deformations ( $\overline{\Delta \xi_{k_01}} \ll \Delta x$ , criterion B). Both criteria must be checked before (criterion A) respectively after (criterion B) the optimisation. Only in that case, the application of the reference  $\vec{\sigma}_{VM\_Ref}$  (criterion A) and the comparison of  $\vec{\sigma}_{VM\_Ref}$  and  $\vec{\sigma}_{VM\_Sim}$  were justified.

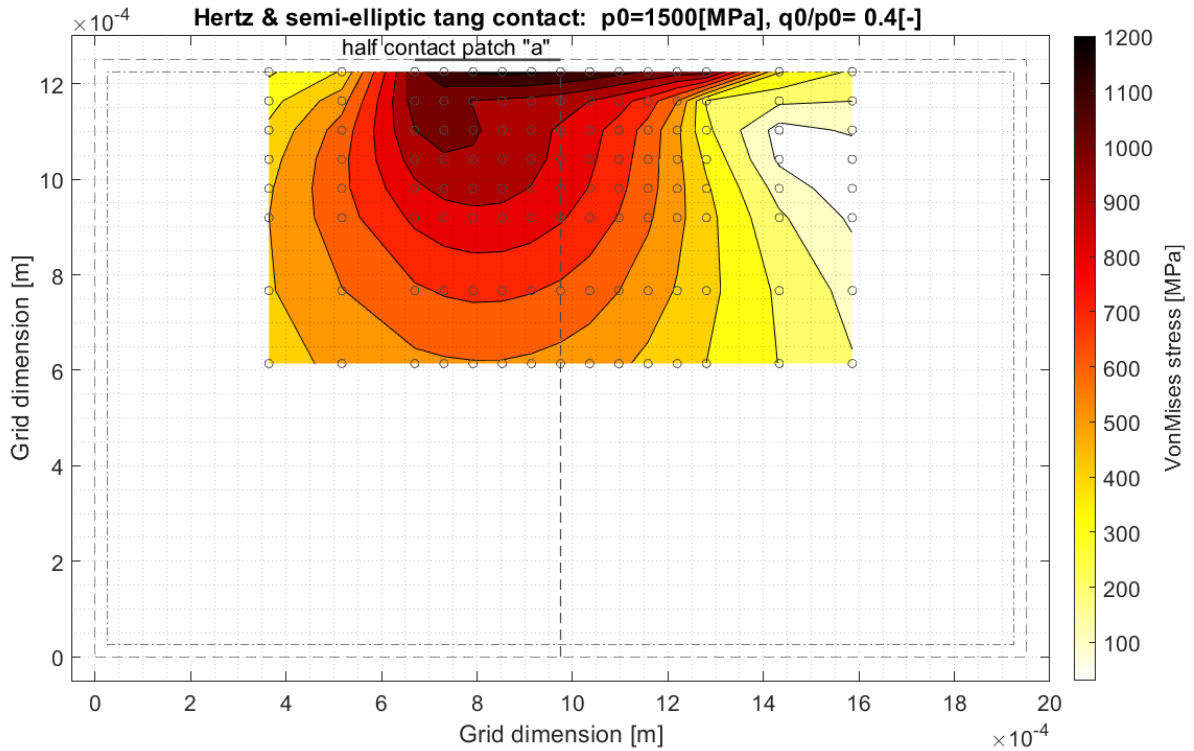


**Figure 31 - Stress reference for a sampling grid that is subject to a combined load (adapted from (77)). The reference is applied to a grid (outer frame, dashed line).**

The definition of the residual  $\sum Resid_{svm}$  by the sum of the squared residuals is a standard approach. The division by  $n_{VM\_sample}$  was adopted to make the residual comparable in case of differently sized of the sampling grids.

One issue was that the method depended on the grid discretisation,  $\Delta x$  (see Figure 18). This meant that each coarsening or refinement of the grid required a specific elasticity parameter,  $c$ , and an update of the optimisation procedure. For a case with Hertzian load of  $p_0 = 1500 \text{ MPa}$ , a convergence study was performed (26). The goal was to assess the impact of the discretisation on the elasticity parameter,  $c$ , and the residual sum,  $\sum Resid_{svm}$ .

Three different discretisations were applied. The results revealed that the elasticity parameter is linearly dependent on the discretisation (see Figure 32). The study proved the residual sum to be convergent with a reduction of the grid discretisation (see Figure 32), which promotes the parameterisation method. The remaining error was attributed to the model's limitation to Poisson's ratios of  $\nu=0.25$  (26), which was described by Silling for similar bond-based peridynamic models (51)

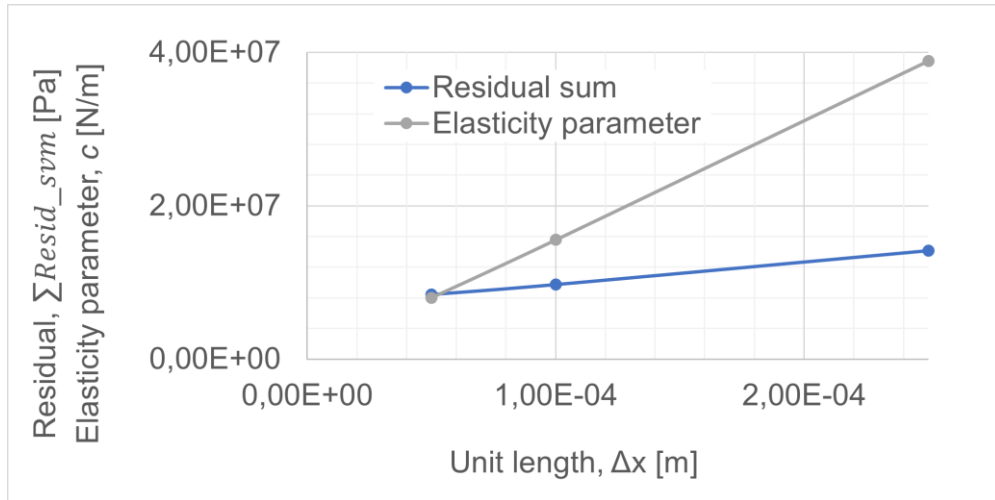


**Figure 32 – Elasticity parameter,  $c$ , and residual sum,  $\Sigma Resid_{svm}$ , as a function of grid discretisation,  $\Delta x$ , modified from (26).**

The conclusion of this section is that a method was developed to derive the elasticity parameter,  $c$ . As a stress field reference, the derivation of Johnson was adopted. A convergence study proved the residual sum of the method to be minimised for a refined grid discretisation. In the next section, this method was verified.

### 4.13 Verification of rolling contact simulation

The method which developed in section 4.12 was verified in this section. For a test case, the agreement of the stress distribution of the DEM model was compared to the reference given in the literature (77).

In order to model the contact, a TD test using the SUROS machine of The University of Sheffield and applied by Trummer (70) was adopted. The contact curvature was neglected. The load as well as the corresponding stress reference are given in section 4.12.

An important issue of the optimisation was the proper set-up of the horizontal- and vertical grid dimensions. In case of a tightly dimensioned grid, edge effects due to the applied boundary conditions may be introduced. In case of an over-dimensioned grid, the optimisation process is inefficient. Hence, the dimensions of  $[-3a, +3a]$  in  $x$  and  $[0, -4a]$  in  $y$  were selected, which provided a good dimension to accommodate the sampling grid within the DEM grid (see Figure 33).

Furthermore, the specification of the boundary conditions was relevant. With regard to the TD rolling contact simulation, a fixed boundary condition was applied

to the bottom nodes, and a periodic boundary condition was applied laterally. The initial value for  $c$  for the specific grid discretisation was derived in an empirical way, which is displayed in Table 5.

Elasticity parameter	$c$ (N/m)
Initial value	1e+8
Optimisation	8e+6

**Table 5 - Initial- and optimised elasticity parameters for a discretisation  $\Delta x = 5e-5$  m.**

Finally, the accuracy of the optimisation per sampling point "n" was evaluated by an error  $e_{\sigma VM_n}$ , which was defined by the difference between the simulation results  $\sigma_{VM\_Sim\_n}$  and the reference stresses  $\sigma_{VM\_Ref\_n}$ , divided by the maximum reference stress  $\sigma_{VM\_Ref\_max}$  and multiplied by 100.

$$e_{\sigma VM_n} = \frac{(\sigma_{VM\_Sim\_n} - \sigma_{VM\_Ref\_n})}{\sigma_{VM\_Ref\_max}} * 100$$

**Equation 38**

The derived elasticity parameter is displayed in Table 5, the result of the simulation based on the parameter is illustrated in Figure 33, and the errors per sampling point  $e_{\sigma VM_n}$  in Table 6.



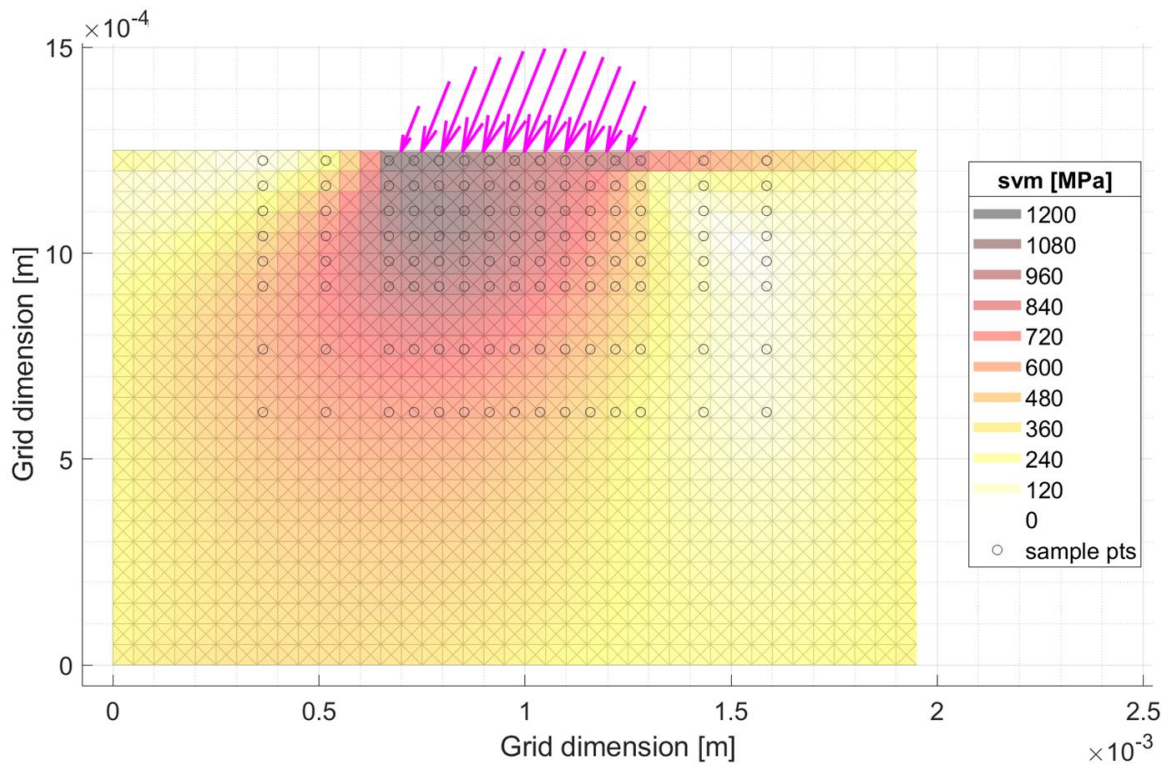


**Figure 33 - Optimised simulation result of a TD test case being subject to a combined load. In the centre, the sampling grid is visualised.**

-18%	-14%	-8%	-12%	-13%	-13%	-13%	-14%	-15%	-16%	-17%	-18%	-30%	5%	6%
-15%	-13%	-2%	8%	8%	6%	4%	2%	0%	-2%	-3%	-1%	8%	-3%	-1%
-11%	-5%	5%	9%	11%	9%	7%	4%	2%	1%	1%	4%	7%	2%	0%
-5%	3%	9%	10%	10%	8%	5%	3%	1%	0%	0%	2%	4%	2%	2%
1%	9%	11%	10%	8%	6%	3%	0%	-2%	-2%	-2%	0%	1%	0%	1%
6%	12%	12%	10%	7%	4%	1%	-2%	-3%	-4%	-3%	-3%	-2%	-2%	-1%
12%	14%	10%	7%	3%	0%	-3%	-5%	-7%	-7%	-8%	-7%	-7%	-7%	-6%
12%	11%	7%	4%	1%	-2%	-4%	-6%	-8%	-9%	-9%	-10%	-10%	-11%	-9%

**Table 6 - Error of equivalent stresses for the TD test case with respect to the stress reference.**

A comparison of the simulation and the reference (see Figure 31, Figure 33) reveals a reasonable agreement of the equivalent stress distribution. The average stresses (simulation 680 MPa, reference 670 MPa) deviate by 2%. The maxima (simulation 1120 MPa, reference 1220 MPa) deviate by less than 10%.

Though, on the surface below the contact, where for  $\mu = 0.4$ , and according to the reference, the maximum occurs, the simulation underestimates the stress by around -15%, which must be considered.

The deviations from the reference stress field were caused by the grid's inherent limitation to Poisson's ratios of  $\nu=0.25$ , which was described by Silling for similarly structured bond-based peridynamic models (51). For a simulated steel material with a ratio of  $\nu=0.29$ , this inevitably led to a decrease in accuracy. In order to assess that hypothesis, the same test result was compared against a stress field reference for  $\nu=0.25$ , which led to a decrease of the residual sum by more than 2%, which promoted the hypothesis.

Edge effects were not identified in the simulation, which is a positive indication for the grid dimensioning.

The criteria highlighted in section 4.12 were scrutinised. Criterion A required  $\Delta x/2 \ll a$ , which was given for the case ( $2.5e-5 \ll 3e-4$ ). However, the discretisation error, which was checked by criterion A, may have contributed to the underestimation of the surface stresses that was described above. A grid refinement would definitely improve this issue, which, however, would cost numerical efficiency. Criterion B required small deformations, which was given, as the lowering of the surface (maximum expected deformation for this case) was negligible. In this case it was clear that there was no interference of the sampling grid's superposition due to the grid deformation.

One remark regards the differentiation of different rail- and wheel materials. As all of these materials have approximately the same Young's modulus,  $E$ , and Poisson's ratio,  $\nu$ , and the stresses  $\sigma_{xx}$ ,  $\sigma_{yy}$  and  $\sigma_{xy}$  (except for  $\sigma_{zz}$ ) are independent of  $\nu$  (77), the stress distribution for will be the same for all these materials. As a result, the elasticity parameter did not provide a means of differentiation.

In brief, the optimisation procedure provides a tool to deliver the elasticity parameter. The resulting accuracy of the simulation was agreeable.



## 5 FATIGUE MODEL

The aim of the work described in this chapter was to introduce a fatigue capability to the rolling contact simulation (see chapter 4, Table 3). Within it, fatigue crack growth (FCG) was modelled as a result of multiple load cycles.

The first step was the introduction of an initial RCF model (see section 5.1). In the next step, the grid's inherent FCG behaviour was assessed (see section 5.2). In chapter 6, the FCG model was parameterised.

As the effect of SPD governs the anisotropic FCG, high shear deformation was modelled in an implicit way (see section 7.2). With it, an "SPD grid" was established. Finally, the developed fatigue- and deformation capabilities (see chapters 5 and 7) were integrated to model anisotropic rolling contact fatigue (see chapter 8).

### 5.1 Modelling of RCF

The scope of this section was to model RCF in an isotropic way, i.e. that FCG has no preference to a specific direction, which was assumed initially. This agrees with the assumption of a standard solid mechanics simulation (i.e. FEM) for a steel. The assumption of isotropic FCG, i.e. the grid's inherent FCG behaviour, is checked in the next step (see section 5.2).

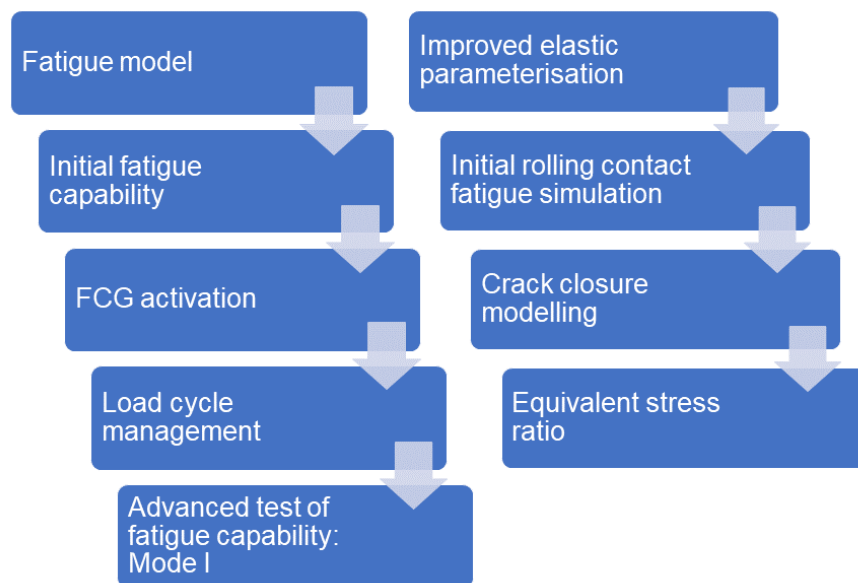


Figure 34 - Overview on the procedure to set up the RCF model.

The RCF modelling procedure is summarised in Figure 34. A fatigue model from the literature was selected (see section 5.1.1) and implemented (see section 5.1.2). The method how to activate elements for FCG was discussed (see section 5.1.3). An optimisation procedure was implemented (see section 5.1.4) and a Mode I test was performed (see section 5.1.5).

The parameterisation of the elasticity parameter was reviewed (see section 5.1.6). Based on that, the initial RCF model was set up and shortcomings of the constitutive relationship, i.e. the bond law, were discussed (see section 5.1.7). In order to address these shortcomings, a novel bond law set-up was developed with respect to crack closure modelling (see section 5.1.8). Finally, the applied assumption regarding the stress ratio was checked (see section 5.1.9).

### **5.1.1 Fatigue model**

The aim of this section was to select and adopt an applicable model for fatigue crack initiation and growth. By "applicable" it is meant that the method shall be compatible with the developed rolling contact model (see chapter 4).

Based on the review in section 2.2 and of the evaluation matrix (see Table 1), fatigue models applied to DEM (see section 2.2.2) and PD models (see section 2.2.3) were examined. The approaches based on FEM/XFEM (see section 2.2.1) and brick and wedge models (see sections 2.2.5 and 2.2.6) were neglected as the model structure did not fit to the rolling contact model.

The DEM fatigue models of Raje et al (43) and Leonard et al. (47) applied Voronoi type meshes instead of a trussed one, which impeded a direct adoption to the rolling contact model. A better compatibility was given by bond-based PD models. These were applied to RCF applications (see section 2.2.3), whereas the fatigue model from Silling and Askari (49) emerged to be the standard approach. The model is based on a derivation referring to the LEFM theory and covers all three stages of FCG (near-threshold, crack growth and fracture). For these reasons, the fatigue model of Silling and Askari was selected.

Another contributing factor was the availability of parameters, at least for the crack growth Stage II. As the fatigue law (see Equation 39) correlated to the Paris law of LEFM (see section 2.1.3), the exponential parameter for the crack growth Stage II can be adopted directly from experimental results. This was of particular importance for the modelling of different FCG rates (see chapter 6).

For PD models, "pairwise bond force densities" are defined (equivalent to "element forces") by a constitutive law (bond law, see section 2.2.4), which resembles the adopted bond law (see Equation 13). In Peridynamics, the interaction of adjacent bonds (i.e. the number of adjacent nodes and bonds to be included) can be varied by modulation of a radius,  $\delta$ , around each node, which is called the horizon. For the DERC model, this horizon is a constant, thereby defining that each node is linked to eight adjacent nodes. The horizon,  $\delta$ , is detailed in section 5.1.2 (see Figure 37).

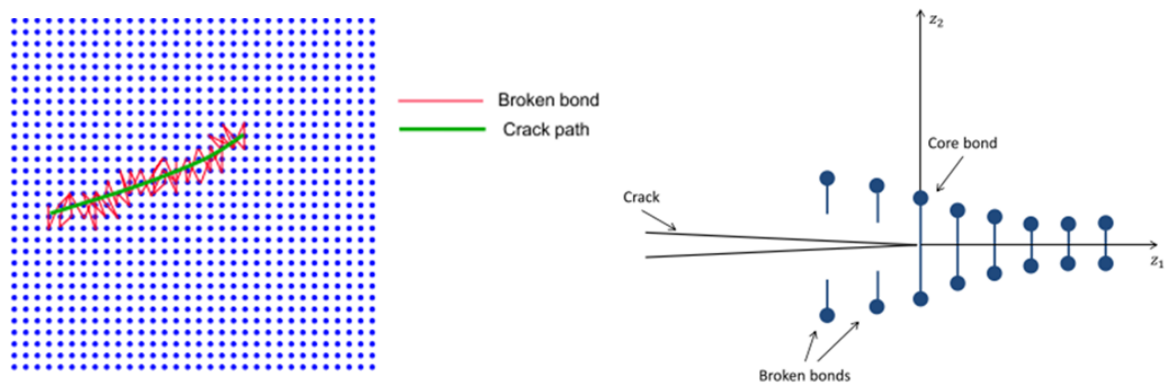


**Figure 35 - Principle of crack growth in a peridynamic solid (left), and detail of a crack tip (right), modified from (49).**

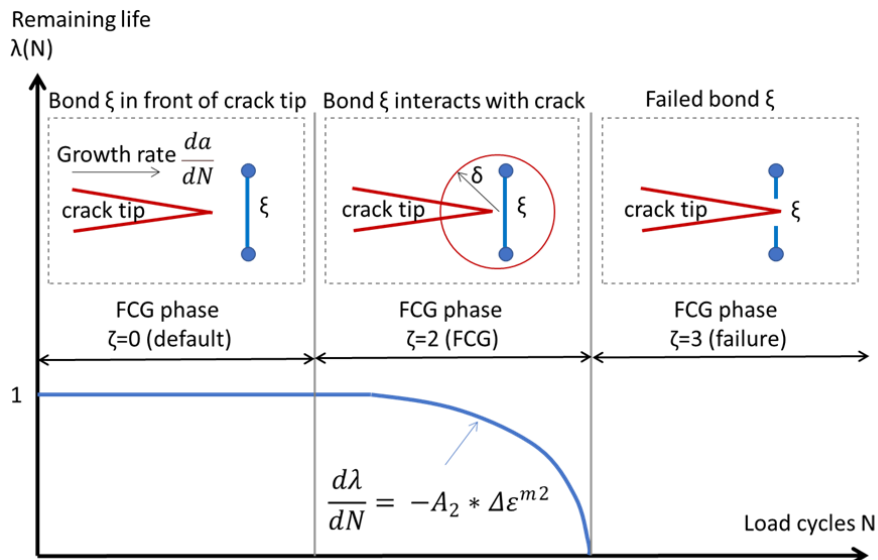


**Figure 36 - Fatigue law: In the case that a bond  $\xi$  is within the horizon  $\delta$ , the fatigue law is activated (phase  $\zeta$ ), which reduces the remaining life  $\lambda$  until failure, modified from (49).**

Due to the applied fatigue law, the progressive failure of bonds results in a pattern of broken bonds, which resembles a crack path (see Figure 35, left). A crack tip is represented by broken bonds in front of a highly strained "core bond", which is illustrated on the right of Figure 35. The principle of the fatigue law is illustrated for a single element in Figure 36. In this figure, the key parameters of FCG phase and remaining life are described.

Each element has an "FCG phase"  $\zeta$ , which describes the state of the fatigue process and determines the mechanical characteristic. The phases basically refer to the LEFM theory of regions I to III (see section 2.1.3):

- Phase  $\zeta=0$  represents a default state, where the fatigue law is inactive. This has no impact on the element's mechanical behaviour.
- Phase  $\zeta=1$  represents the near-threshold Stage I, which was neglected at this initial stage, but modelled in section 6.2.
- Phase  $\zeta=2$  describes the degradation due to fatigue. This is where the fatigue law is active. For this phase, the full mechanical capability is still available.
- Phase  $\zeta=3$  refers to the failure of an element. This implies the loss of the mechanical capability, respectively a reduced capability (see section 5.1.2).

In order to activate the fatigue law, elements must be within the horizon  $\delta$  of a crack tip (see Figure 36). With respect to the DEM model, this means that a failed element ( $\zeta=3$ ) sets all adjacent elements to a phase of  $\zeta=2$ . This is detailed in section 5.1.2.

The second key property is the parameter "remaining life",  $\lambda$ . Initially, it is set to "1" for each element. Then, during phase  $\zeta=2$ , it is decreased gradually per load cycle  $N$ , which is specified by the fatigue law (see Equation 39). For the case of  $\lambda \leq 0$ , failure occurs and the FCG phase is set to  $\zeta=3$ , which by definition is irreversible.

$$\frac{d\lambda}{dN} = -A_2 * \Delta\varepsilon^{m_2}$$

**Equation 39**

The fatigue parameters  $A_2$  and  $m_2$  are discussed in section 6.1. The crack driving parameter is the cyclic bond strain,  $\Delta\varepsilon$ , which resembles the difference between the maximum strains  $\varepsilon^+$  and the minimum strains  $\varepsilon^-$  per load cycle.

$$\Delta\varepsilon = |\varepsilon^+ - \varepsilon^-|$$

The utilisation of the cyclic bond strain instead of the stress intensity factor as the crack driving force is a deviation from the LEFM. This, however, facilitated a direct fatigue processing, as the element strain,  $\varepsilon$ , is the primary result of the peridynamic and DEM processing.

In this section, the basics of the fatigue model proposed by Silling and Askari were introduced. The core of the model is the fatigue law, which reduces the remaining life  $\lambda$  per element. In the next section, the integration of a fatigue capability to the existing DEM model, based on the fatigue model described in this section, as well as deviations from the original approach, are detailed.

### 5.1.2 Initial fatigue capability

In this section, the introduction of an initial fatigue capability, which is based on the approach described in section 5.1.1, is discussed. By the term "initial fatigue capability", it was meant that exclusively fatigue crack growth (Stage II) is modelled, and that isotropic FCG was assumed. The underlying assumptions are summarised. The principle of FCG activation is captured. The deviations from the original fatigue model are discussed. Finally, a Mode I simulation was performed to assess the initial fatigue capability.

The first assumption regarded the formation of long cracks (FCG Stage I). As this region was omitted at this stage, initial cracks were introduced by setting elements selectively to a failed state ( $\zeta=3$ ). The modelling of Stage I is discussed in section 6.2. Moreover, the FCG behaviour was assumed to be isotropic. Finally, element failure was defined to be irreversible if the remaining life reached a value of  $\lambda \leq 0$ . These are the applied assumptions.

The fatigue model of Silling and Askari was applied to simulate Mode I tests, which have one maximum- and one minimum load. Thus, one load cycle consists of two simulation increments. In this way, the cyclic bond strain  $\Delta\varepsilon$  can be derived easily for each element (see Equation 40).

However, in order to simulate a rolling contact, there are multiple increments that must be analysed to determine a minimum- and maximum strain per element. Thus, a load cycle for the rolling contact case comprises all increments that are part of a complete pass of the wheel. A result of this fact is that the fatigue capability cannot update the fatigue state instantaneously, but it must be post-processed after one complete pass of the contact (rolling contact cycle). The impact of an instant failure within one contact cycle was neglected. This, however,

was not considered to be a drawback as the simulation targets the simulation of the impact of thousands of rolling contact cycles. Hence, an instant fatigue update was not required.

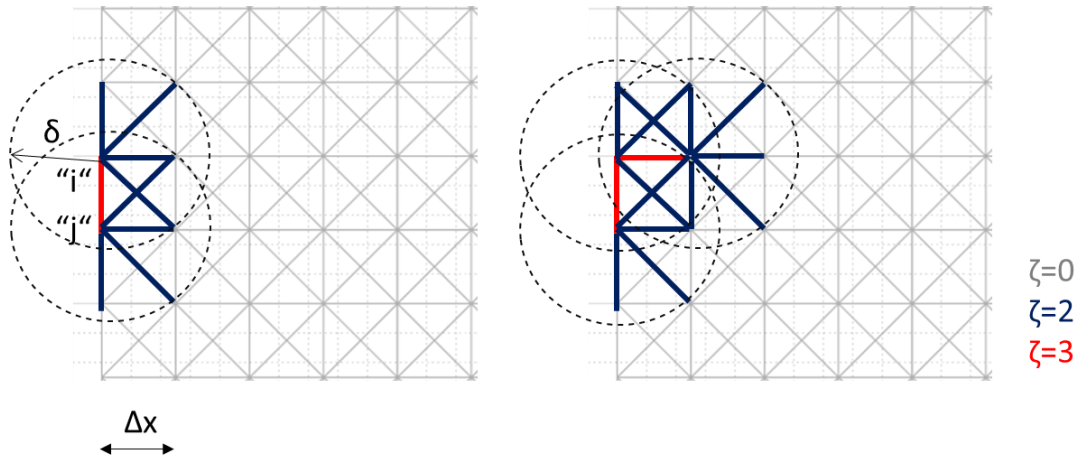


**Figure 37 - Simplified FCG activation around nodes "i" and "j" for a grid discretisation,  $\Delta x$ : Initial crack (left) and proceeding crack (right). Elements in the default phase are marked grey, in the FCG phase blue, in the failed phase red.**

During the fatigue update, the remaining life  $\lambda$  was updated for each element. With it, the state of FCG phase  $\zeta$  was updated. According to Silling and Askari (49), the fatigue law (see Equation 39) is applied to all "bonds within the horizon of material points on a pre-existing crack tip." Therefore, an horizon  $\delta_i$  was introduced with respect to the grid discretisation,  $\Delta x$  (see Figure 18, Figure 24), which referred to a node "i", and captured all elements that originate from that node (see Figure 37).

$$\delta = \sqrt{2\Delta x^2}$$

**Equation 41**

By the introduction of a horizon,  $\delta$ , the DERC model resembled a special case of a bond-based peridynamic model. The key difference is that for peridynamic models, the horizon can be adjusted, whereas for the DERC model it is fixed to the grid discretisation,  $\Delta x$ . Basically, an increase of the horizon facilitates a better resolution of the model as more elements are captured. This, however, comes at the cost of a higher processing effort.

However, for the commissioning of the model, this method called "FCG activation" was simplified in a way that only bonds attached to a failed element were FCG activated (from  $\zeta = 0$  to  $\zeta = 2$ , see Figure 37) to facilitate easy traceability. In this

way, an initial FCG activation was implemented, which is reviewed in section 5.1.3.

If the failure criterion  $\lambda \leq 0$  applied to an element, its FCG phase was set from  $\zeta=2$  to  $\zeta=3$ . This in turn triggered an update of the FCG activation. In this way, a crack tip (i.e. one or multiple failed elements) could potentially proceed in all remaining directions. An illustration of this behaviour is given in Figure 37.

With respect to the original model of Silling and Askari, the following modification was performed. It concerned the mechanical behaviour of failed elements (failure law). Failed elements were assumed to still bear compressive loads for the rolling contact simulation. Thus, for phase  $\zeta=3$ , the mechanical capability was reduced only partially (see Figure 38). This meant that failed elements could bear compressive forces, but no tensile forces. A closer examination of the bond law was performed in the later sections of this chapter.

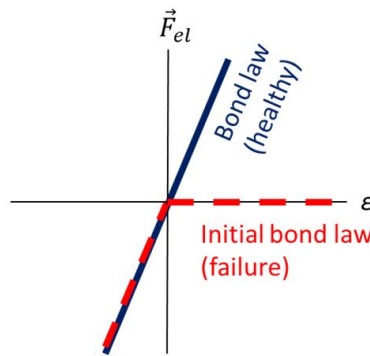


**Figure 38 – Linear-elastic bond law for healthy- (blue) and failed elements (red). The latter features a full compressive stiffness for failed elements.**

In this way, the initial fatigue model, which was derived from the literature, was integrated to the rolling contact simulation. In the next step, the initial fatigue capability was assessed. By "initial" it is meant that a progressive failure of elements due to a cyclic loading was evaluated. A focus was laid on the qualitative behaviour. At this stage, the quantitative behaviour was neglected, as the required parameterisation had not been performed yet (see chapter 6).

The standard approach was a Mode I test. In order to ease the traceability, a small  $5 \times 5$  grid with a discretisation length of  $l_0 = 50 \mu m$  was selected. The fatigue parameters ( $A_2 = 1800$ ,  $m_2 = 3.0$ ) were adopted from Silling and Askari (49) as a default set-up. A repeated load of  $\sigma_{max} = 1500 MPa$  and a stress ratio of  $R = 0$  were applied. The elasticity was adopted from Table 5.

The result of the initial test is displayed in Figure 39. The result demonstrated that the crack propagated, starting from the initially failed element. The tendency of the crack to grow into the centre of the grid agreed with the basic behaviour of experimental specimens. As a result of the lost load carrying capability of the failed elements, the stress field at the crack mouth was reduced to zero. This confirmed that the initial capability worked as expected.

The simulation worked stably for the applied load cycles. However, the processing was inefficient, as for most of the cycles, no change of the fatigue state (phases  $\zeta$ ) occurred. Thus, an improvement was adopted to boost the numerical efficiency (see section 5.1.4).

In brief, an initial FCG capability was introduced to the DERC model. The applied assumptions and simplifications were discussed. An initial bond law was applied. A Mode I test was performed, which demonstrated the capability of progressive element failure as a function of the adopted fatigue law. In the next section, the principle of FCG activation is discussed.

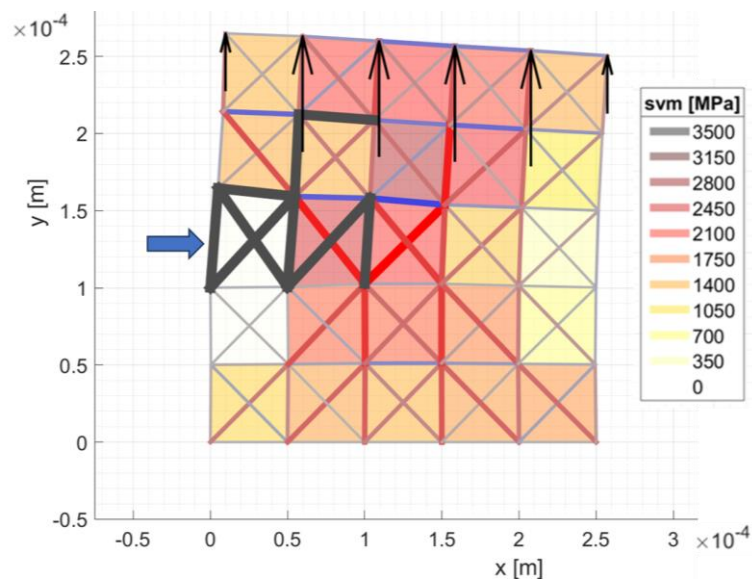


**Figure 39 - Initial fatigue test: The grid is cyclically loaded in tension. The initially failed element is marked by the arrow. The progressively failed elements are marked in black. Elements strained in tension are coloured red and those in compression in blue.**



### 5.1.3 FCG activation

An initial FCG capability was introduced in section 5.1.2. A key issue regarded what method to use to activate elements from FCG phase  $\zeta=0$  to  $\zeta=2$ , for which the fatigue law (see Equation 39) was applied. Initially, a simplified FCG activation (see Figure 40, left) was employed, that deviated from the original fatigue model (49).

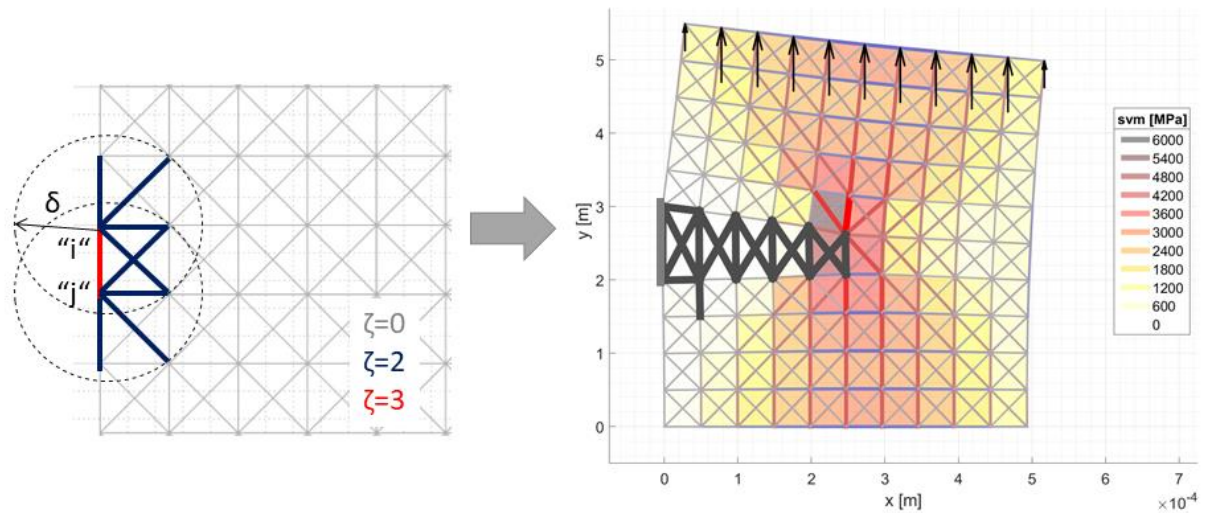


Figure 40 - Simplified FCG activation (left): Failed elements are coloured in red, FCG activated elements in blue. Result of the Mode I test (right): Initially failed elements are marked in grey, successively failed elements in black, elements strained in tension in red, elements strained in compression in blue.

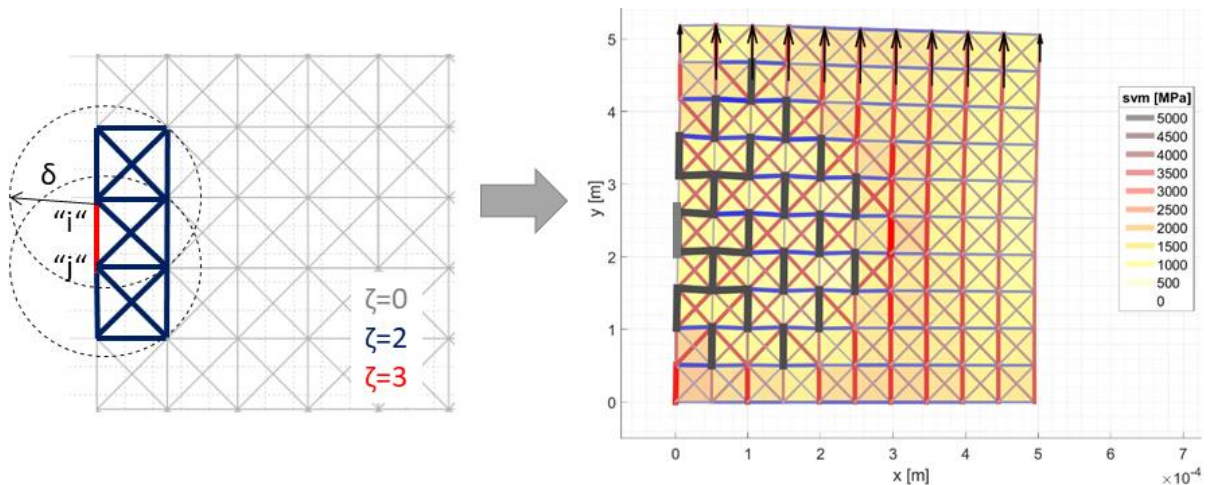


Figure 41 - Original FCG activation (left): Failed elements are coloured in red, FCG activated elements in blue. Result of the Mode I test (right): Initially failed elements are marked in grey, successively failed elements in black, elements strained in tension in red, elements strained in compression in blue.

The model was tested under Mode I condition (see section 5.1.2) which led to a reasonable failure pattern (see Figure 39) as the crack basically proceeded perpendicular to the load axis, which is in agreement to experimental observations (see Figure 44). The aim of this section is to assess the impact of the two FCG activation methods on the FCG behaviour.

In order to assess the impact of the two methods, the grid was increased to 10 x 10 to reduce grid effects. A single element was initially set to failed state, and the model was run for the simplified FCG activation. It can be seen that the crack proceeded in a linear way along the axis perpendicular to the applied load (see Figure 40, right). This is in agreement with similar experimental results for isotropic FCG (5). The result suggests that the simplified FCG activation works for the relatively small grid and the applied load.

The same case was simulated for the case of the original FCG activation proposed by Silling and Askari, which is detailed in Figure 41. A single failed element activates all elements that are encompassed by the horizons  $\delta$  of the nodes attached to the failed element (see Figure 41, left). For the illustrated case, this increased the number of FCG activated elements by nearly 50%, compared to the case of the simplified method (see Figure 40, left).

The FCG pattern resulting from the original FCG activation consisted exclusively of vertical and horizontal elements (see Figure 41, right), not of diagonals. This was in contrast to the basic consideration, i.e. that the initially failed element leads to an increased strain of the two diagonals to the right of it, which as a consequence are expected to fail successively. Actually, the failure pattern proceeded along the horizontal- and diagonal elements. With respect to the initial results (see Figure 39), this result suggested to be a step back.

A potential reason for the abnormal FCG pattern was suspected to be the definition of the initial crack (single element). An alternative explanation was considered to be the applied boundary condition (floating) in combination with a continuously applied load. Based on the results, the simplified FCG activation was adopted at this stage for the further development. A review of the FCG activation was performed at a later stage (see section 5.2.5). In the next step, the efficiency was optimised (see section 5.1.4).

### 5.1.4 Load cycle management

The initial test in section 5.1.2 revealed an inefficient numerical process, as there were thousands of cycles processed, whereas the fatigue state of the grid changed only a dozen times. Thus, it was required to simulate exclusively the "effective cycles", i.e. the cycles where the fatigue phase  $\zeta$  of at least one element changed.

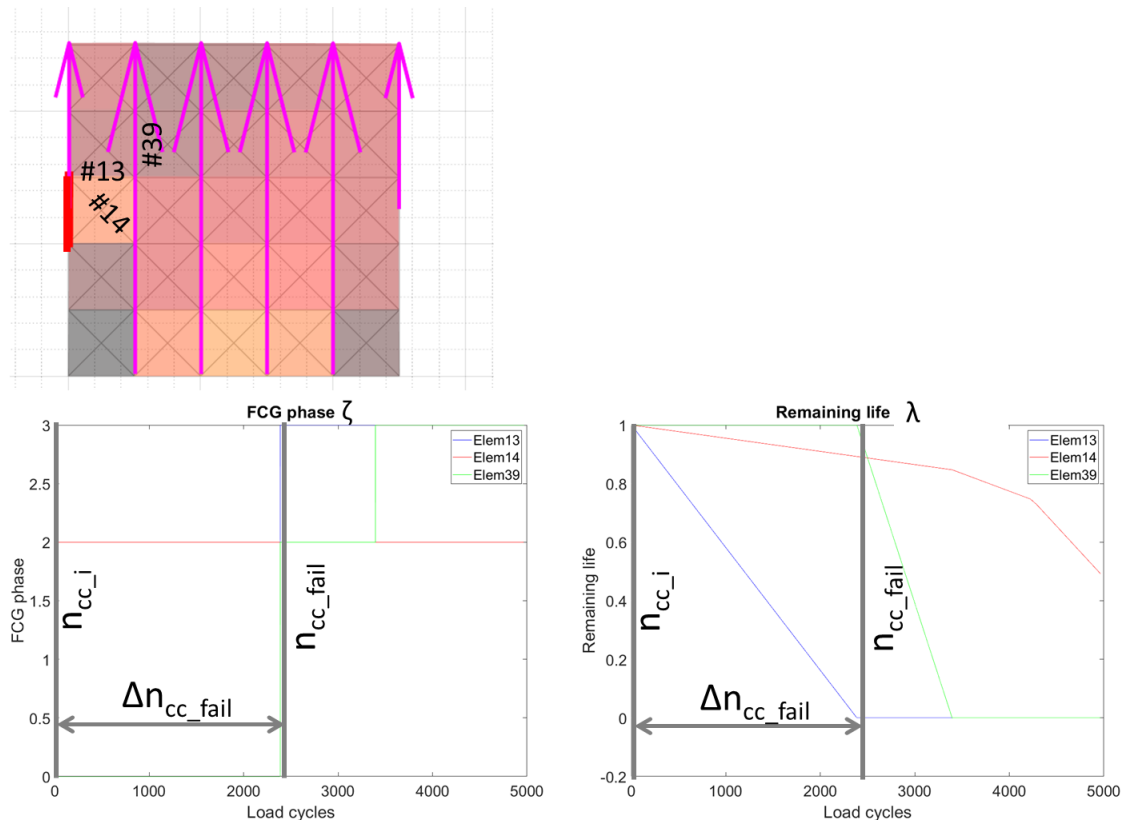


**Figure 42 - Principle of load cycle management: Grid with selected elements for the state  $n_{cc_i}$  (above, initial crack in red), evolution of the FCG phase  $\zeta$  (below left) and for the remaining life  $\lambda$  (below right).**

Starting from a given cycle  $n_{cc_i}$ , the first step was to determine the number of cycles  $\Delta n_{cc\_fail}$  to the next failure of an element. Within that period no change of  $\zeta$  had to occur for any element, but the remaining life  $\lambda$  reduced constantly in a linear way. In this way, the degradation was analysed for a cycle  $n_{cc_i} = 1$  (see Figure 42). For the sake of simplicity, only three elements of the grid are illustrated. In the actual analysis, however, all healthy elements (FCG phase  $\zeta < 3$ ) were assessed.

For the cycle  $n_{cc,i} = 1$  (see Figure 42, all parts), the pre-crack represented the only failed element at that stage. In the next step, a prediction of the remaining life  $\lambda$  (see Figure 42, below right) was performed for all healthy elements, whereas no change of phase  $\zeta$  was assumed (see Figure 42, below left). With respect to the fatigue model (see section 5.1.1), this meant that the cyclic bond strains  $\Delta\varepsilon$  for all elements remained constant within the period  $\Delta n_{cc,fail}$ . As a result, the degradation of  $\lambda$  per element (see Equation 39) was predicted by the following derivation.

For any state  $n_{cc,i}$ , the remaining life per element "k" was described by the property  $\lambda_{k,i}$ . Based on the fatigue law (see Equation 39), the reduction of remaining life  $\frac{d\lambda_k}{dN}$  for each element "k" per cycle  $N$  was calculated. As mentioned, (see Figure 42, below), failure for each element "k" occurred under the subsequent condition.

$$\lambda_{k,fail} \leq 0$$

**Equation 42**

The remaining life  $\lambda_{k,fail}$  at a failed state was processed by addition of the remaining life  $\lambda_{k,i}$  for state  $n_{cc,i}$  (for  $n_{cc,i} = 1$ ,  $\lambda_{k,1} = 1$ ), and the gradient  $\frac{d\lambda_k}{dN}$  which was defined by Equation 39, multiplied by the number of load cycles to failure  $\Delta n_{cc,k,fail}$  per element "k".

$$\lambda_{k,fail} = \lambda_{k,i} + \frac{d\lambda_k}{dN} * \Delta n_{cc,k,fail}$$

**Equation 43**

By a rearrangement of Equation 43, the number of cycles to failure was processed for an element "k".

$$\Delta n_{cc,k,fail} \leq -\frac{\lambda_{k,i}}{\frac{d\lambda_k}{dN}}$$

**Equation 44**

Finally, the required number of cycles  $\Delta n_{cc,fail}$  was determined by selecting the minimum of all  $\Delta n_{cc,k,fail}$ , as the weakest element defined the next cycle of failure.

In Figure 42 (below right), it can be seen that for the period  $\Delta n_{cc,fail}$ , all remaining lives developed in a purely linear way (which was also the case for all not illustrated elements), which justified the prediction of Equation 44. In this way, the whole simulation process was "discretised" in "effective cycles".

Regarding the practical implementation, the load cycle management was designed to jump from  $(n_{cc_i})$  to  $(n_{cc_i} + \Delta n_{cc_{fail}})$ . The fatigue update was performed after each cycle as part of the post-processing.

With respect to the initial test example (see Figure 39), the number of processed cycles was reduced from 5000 to less than 10, which facilitated a reduction of the processing time by -99%. That represented a significant gain in efficiency.

### **5.1.5 Advanced test of fatigue capability: Mode I**

The initial test of the fatigue capability was performed by a Mode I test applied to a small 5 x 5 grid (see Figure 39). The applied 5 x 5 grid was well suited for identifying potential errors of the fatigue simulation capability. A disadvantage, however, was that edge effects induced e.g. by boundary conditions impeded a detailed analysis of the FCG progress. Moreover, the small grid size made it difficult to distinguish between the FCG Stage II and the fracture Stage III.

Thus, the goal for the advanced testing under FCG Mode I was to assess the general FCG behaviour and to differentiate between regions II and III by the introduction of an up-scaled grid size (30 x 30). Furthermore, an examination of the equivalent stress field around the crack tip was performed.

The test was performed for a stress of 300 MPa and a load ratio  $R = 0.1$ , which represented a purely tensile load. A fixed boundary condition was applied to the bottom nodes. The fatigue- and elasticity parameters were adopted from the test in section 5.1.2 (unparametrised). A first crack was introduced to the left edge by three failed elements.

With respect to the initial test, the visualisation of elements was adjusted for better comprehensibility. Failed elements were marked black, elements being subject to compressive strain were marked blue, and elements under tensile strain red.

The simulation result is illustrated in Figure 43 (81). The test revealed that the simulation worked for multiple load cycles. The crack progressed from the initially failed elements on the left edge to the centre in a steady, linear way, which agrees with experimental results for Mode I tests (see Figure 44 from (5)). The crack pattern in Figure 43 exhibited exclusively vertical and diagonal elements, which is reasonable for the loading case.

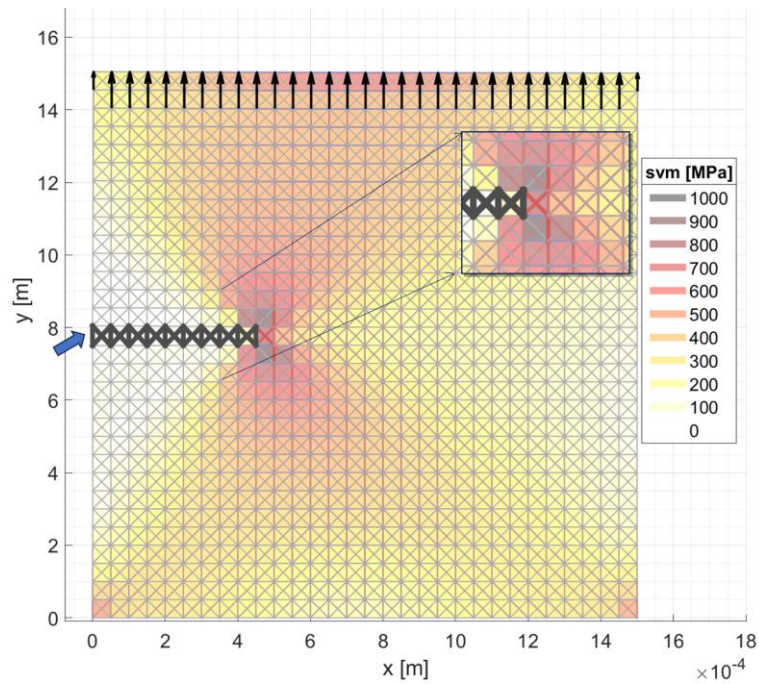


Figure 43 - Mode I FCG test: The initially failed element is marked by the arrow, propagating failed elements are marked in black, elements under compressive strain in blue and under tensile strain in red.

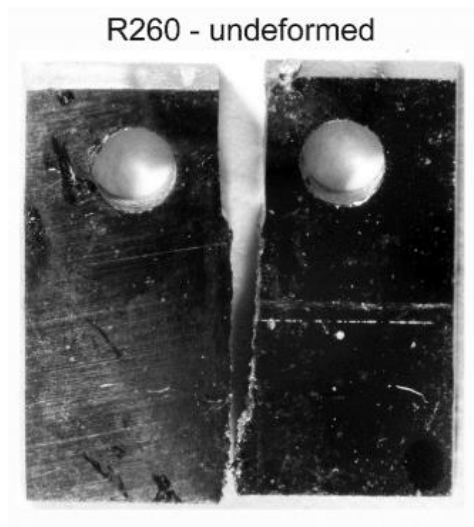
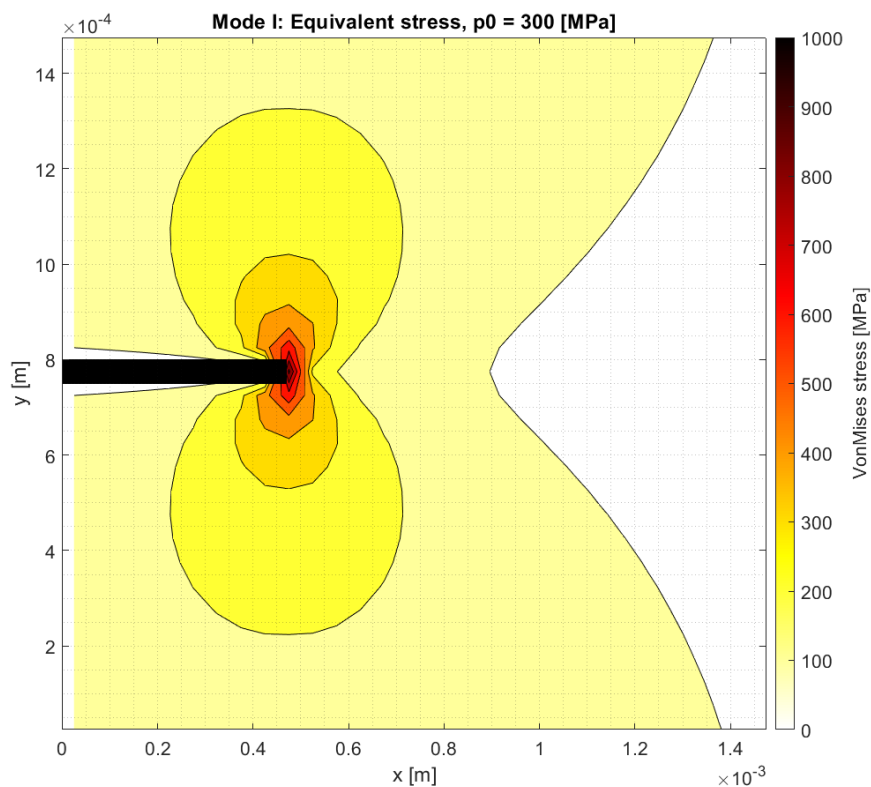


Figure 44 - Fatigue crack path of an R260 specimen after a Mode I test, modified from (5).

The crack advance in Figure 43 can be described by the failure of DEM modules (see section 4.2), progressing from the left edge to the right. The first module failed after approximately 108.000 cycles (108 k cycles), the next ones after 588,

800, 915, 984, 1027, 1055, 1073 and 1084 k cycles. The moderate crack propagation rate as a result of the applied fatigue parameters ( $A_2, m_2$ ) indicated that the FCG process takes place exclusively in FCG Stage II. There is still a margin to the transition to fracture Stage III, which is not analysed in this section.

Besides the FCG pattern, the distribution of the stress field around the crack tip was examined with respect to an analytical solution (15). Anderson assumed an isotropic, linear-elastic material behaviour, a semi-infinite plate, and a closed form of the crack to derive the stress tensor. Under these assumptions, the stress intensity factor  $K_I$  for Mode I was derived. With it, the stress tensor and the equivalent von Mises stress field ahead of the crack tip were calculated. Finally, the stress field was distributed to a grid which is congruent to the nodes of the DEM model, but not congruent to the stress visualisation (see section 4.9). This, however, improves the resolution of the reference figure.



**Figure 45 - Reference stress field for a Mode I crack of closed form. The crack is illustrated by the black bar.**

The result is displayed in Figure 45. Compared to the simulation result of Figure 43, it can be seen that the simulation captures the hour-glass shape of the stress



field around the crack tip well. This proves that the model is capable of reproducing the quality of the stress field around a crack. Regarding the quantity, a comparison is difficult as the stress field around the crack tip is sensitive to the distance between a sampling point and the tip, where the stress maximum grows to infinity (15). This does not permit a comparison of the stress maxima.

In the vicinity of the tip (radius of  $1e-4$  m), the stress level of the reference is about 500 - 800 MPa, which agreed with the simulation. In the extended vicinity (radius of  $4e-4$  m), the simulation displays stresses that are about twice as high as those of the reference. This was attributed to the grid deformation at this stage of the crack propagation, which did not fully agree with the closed-form assumption of the reference anymore. Generally, however, the stress field of the DEM model agrees with the analytical reference in a satisfactory way, as the scope of the model is not a stress representation, but the simulation of crack propagation.

In brief, the FCG capability works well for an intermediate sized grid under Mode I and pure tensile load ( $R > 0$ ). In the next step, the fatigue capability is introduced to a rolling contact simulation (sections 5.1.6 and 5.1.7).

#### **5.1.6 Improved elastic parameterisation**

In order to introduce the fatigue capability to the rolling contact simulation, a grid of a discretisation of  $\Delta x = 2.5e-5$  m was selected, and the elastic parameterisation (see section 4.12) was performed. This revealed a shortcoming of the parameterisation method, as no singular elasticity parameter (micro modulus function in peridynamic terms) could be derived. Initial values of  $c = 5e6$  (N/m) to  $c = 1e11$  (N/m) delivered stress residuals,  $\sum Resid_{svm}$ , that differed only insignificantly ( $< 1/1000$ ). Thus, the current method of elastic parameterisation was not sufficient to identify a singular elasticity parameter, and a second, complementary method was required. This improvement is described in this section.

The standard approach to set-up the elastic behaviour of a solid is to incorporate the two material parameters, Young's modulus  $E$  and Poisson's ratio  $\nu$  for steel ( $E = 210$  GPa,  $\nu = 0.3$ ). With it, the elastic deformation ( $\Delta x_{ref}, \Delta y_{ref}$ ) under compression was analysed, whereas plane strain was assumed (see Figure 46).



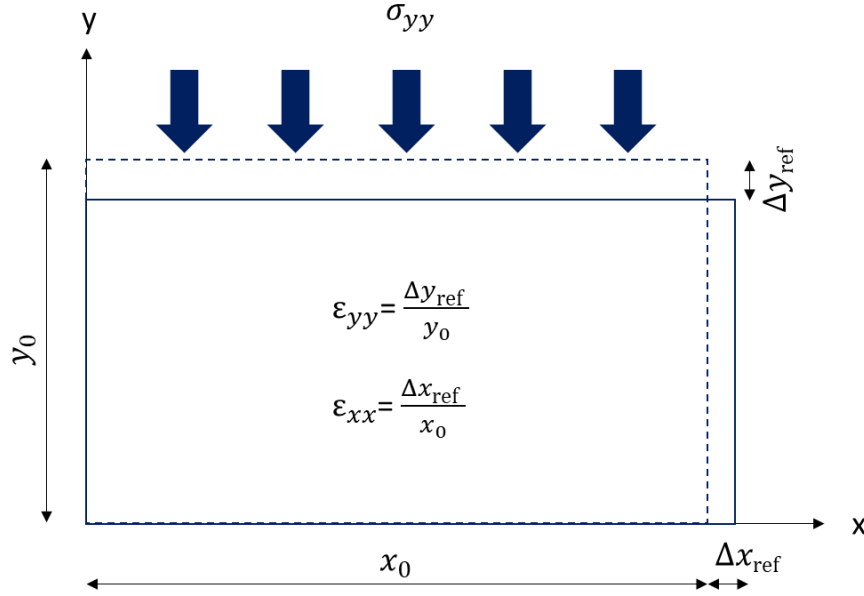


**Figure 46 - Elastic deformation of a block under compression by the stress  $\sigma_{yy}$ .**

The analytic solution for the strains ( $\epsilon_{xx}$ ,  $\epsilon_{yy}$ ) in the x and y directions under plane strain are described by the following formulae (80). Under plane strain, the strain in the z direction is  $\epsilon_{zz} = 0$ .

$$\epsilon_{xx} = \frac{1 + \nu}{E} [(1 - \nu)\sigma_{xx} - \nu\sigma_{yy}]$$

**Equation 45**

$$\epsilon_{yy} = \frac{1 + \nu}{E} [-\nu\sigma_{xx} + (1 - \nu)\sigma_{yy}]$$

**Equation 46**

The Poisson's ratio  $\nu$  is defined by the negative ratio between the lateral strain  $\epsilon_{xx}$  and the vertical strain  $\epsilon_{yy}$ .

$$\nu = -\frac{\epsilon_{xx}}{\epsilon_{yy}}$$

**Equation 47**

In this way the strains  $\epsilon_{xx}$  and  $\epsilon_{yy}$  were calculated as a function of the applied stress  $\sigma_{yy}$ . No stress was applied in lateral direction ( $\sigma_{xx} = 0$ ). Then, the

displacements were derived from  $\varepsilon_{xx}$  and  $\varepsilon_{yy}$  by means of Equation 10 (see also Figure 46) for the analytical references  $\Delta x_{ref}$  and  $\Delta y_{ref}$ .

$$\Delta x_{ref} = \varepsilon_{xx} * x_0$$

**Equation 48**

$$\Delta y_{ref} = \varepsilon_{yy} * y_0$$

**Equation 49**

In this way, the analytical reference for the elastic deformation was derived. In the next step, the actual displacements of the model  $\Delta x_{num}$  and  $\Delta y_{num}$  were calculated by averaging the displacements of the edge nodes of the upper- and the right-side edges. A floating boundary condition was used to facilitate a lateral displacement ( $\Delta x_{num} \neq 0$ ). With it, the residuals  $\Delta x_{res}$  and  $\Delta y_{res}$  were defined.

$$\Delta x_{res} = \frac{|\Delta x_{num} - \Delta x_{ref}|}{|\Delta x_{ref}|}$$

**Equation 50**

$$\Delta y_{res} = \frac{|\Delta y_{num} - \Delta y_{ref}|}{|\Delta y_{ref}|}$$

**Equation 51**

Finally, an elastic residual  $\sum Resid_{el}$  was formed by  $\Delta x_{res}$  and  $\Delta y_{res}$  to serve as a target variable for the optimisation.

$$\sum Resid_{el} = \Delta x_{res} + \Delta y_{res}$$

**Equation 52**

The optimisation employed the elasticity parameter  $c_{init}$  as an input, which was varied in order to minimise the residual  $\sum Resid_{el}$ . In this way, the elastic deformation of the grid was optimised to match the analytical behaviour in the best way.

The new method facilitated a decrease in the elastic residual from  $\sum Resid_{el} = 0.45$  for  $c_{init} = 4.58e6$  N/m to  $\sum Resid_{el} = 0.09$  for  $c_{final} = 3.89e6$  N/m. The softening implied that the vertical strain  $\varepsilon_{yy}$  of the deformed grid agreed by 100% with the analytical solution, whereas the lateral strain  $\varepsilon_{xx}$  achieved 91% agreement. This means that the DEM grid expanded 9% less in the lateral direction than it did in the analytical case, which can be attributed to the model's limitation to a Poisson's ratio of  $\nu=0.25$  (see section 4.13). Ultimately, the stress

residual  $\sum Resid\ sv m$  was checked for the derived elasticity  $c_{final}$ , which demonstrated a negligible deviation.

The summary of this section is that a refinement of the discretisation revealed the requirement for an additional parameterisation method to derive a singular elasticity parameter. This method was based on the elastic deformation behaviour of solids under plane strain. A parameterisation optimisation was developed that minimises the difference between the analytical- and the numerical deformation. The impact of the optimised grid on the stress distribution (initial parameterisation) is negligible.

In the next section, the derived elasticity parameter  $c_{final}$  and the developed fatigue capability are applied to the rolling contact.

### 5.1.7 Initial rolling contact fatigue simulation

In this section, the fatigue capability (see section 5.1.2) was applied to the rolling contact simulation (see chapter 4) to simulate RCF. The aim of this initial RCF model was to simulate FCG in a basic way. This means that a crack propagated as a result of multiple rolling contacts, starting from an initial crack. Thus, the goal of the initial RCF model was to simulate a directional FCG behaviour below the surface (81).

Therefore, an isotropic material behaviour was assumed. Further, an initial crack was introduced. Fatigue on the surface layer was neglected (this concerned the first row of the grid's DEM modules), as surface effects represent a special issue for models of a peridynamic character (82). Moreover, the definition of the cyclic bond strain  $\Delta\varepsilon$  (see Equation 40) was modified in order to capture the minimum- and maximum strains of each element during a rolling contact cycle (see section 4.10) in an accumulative way.

In the next step, an experimental reference for the RCF development in an isotropic material was required. Therefore, the results of a full-scale rig test were adopted, which were provided by voestalpine Rail Technology GmbH. The set-up included a driven wheel which was applied to the rail under a normal load of  $F=150\text{ kN}$ , which translated to a pressure of  $p_0=555\text{ MPa}$ . The coefficient of friction was estimated to be  $\mu=0.3$ . Before the test, a vertical initial crack of length  $l_{init} = 2.8\text{ mm}$  was introduced by cutting. Two micrographs after the application of multiple cycles are illustrated in Figure 47.

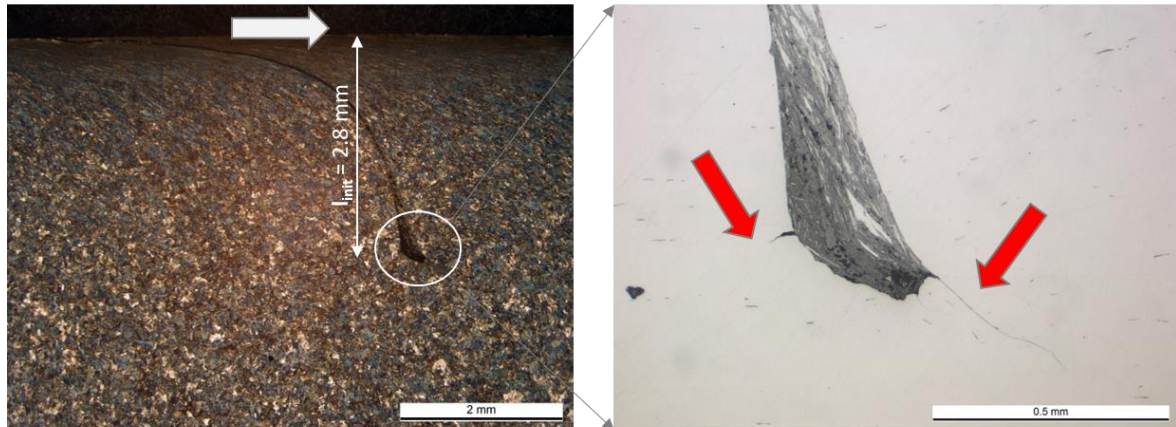


**Figure 47 - Metallographic sections from a full-scale rig test (left) including the indication of the running direction, and magnification of the crack tip (right) [courtesy of voestalpine Rail Technology GmbH] (81).**

The deformed microstructure above the initial crack tip can be seen (see Figure 47, left). The initial crack tip itself, however, is located in a region which was considered to be without plastic deformation, which agreed with the modelling assumption. Thus, an isotropic FCG around the tip was assumed. Further, a magnification around the crack tip is shown (see Figure 47, right), which illustrates the formation of two separate cracks that branch from the initial crack tip. These micrographs were used as a reference for the initial RCF simulations.

In order to capture the length of the initial crack  $l_{init}$ , a 57x25 grid with a discretisation of  $\Delta x = 5e-4 \text{ m}$  was set-up (see Figure 48, Figure 49). Due to the limited numerical performance, a more detailed resolution of the crack tip of the experiment (see Figure 47, right) was not feasible. However, the discretisation was considered to be a minimum to resolve FCG effects resulting from the full-scale rig test. Within the frame of the initial RCF study, this fact was deemed to be acceptable. For future applications, a model optimisation is recommended to refine the resolution.

The initial crack was modelled by a vertical array of 19 initially failed elements (see Figure 48, Figure 49, black elements) (26). This implied that the numerical crack was shorter by approximately -7% with respect to the experimental crack. This error was considered to be acceptable within the frame of the initial RCF simulation. The applied load was set in accordance with the experimental load.

The main consideration regarded the set-up of the bond law in case of failure. As the model was developed for a rolling contact, it was assumed that a failed element was still capable of bearing a full compressive load (see section 5.1.2) in

order to prevent effects like crack face penetration. Thus, the bond law illustrated in Figure 38 was adopted initially ("initial bond law").

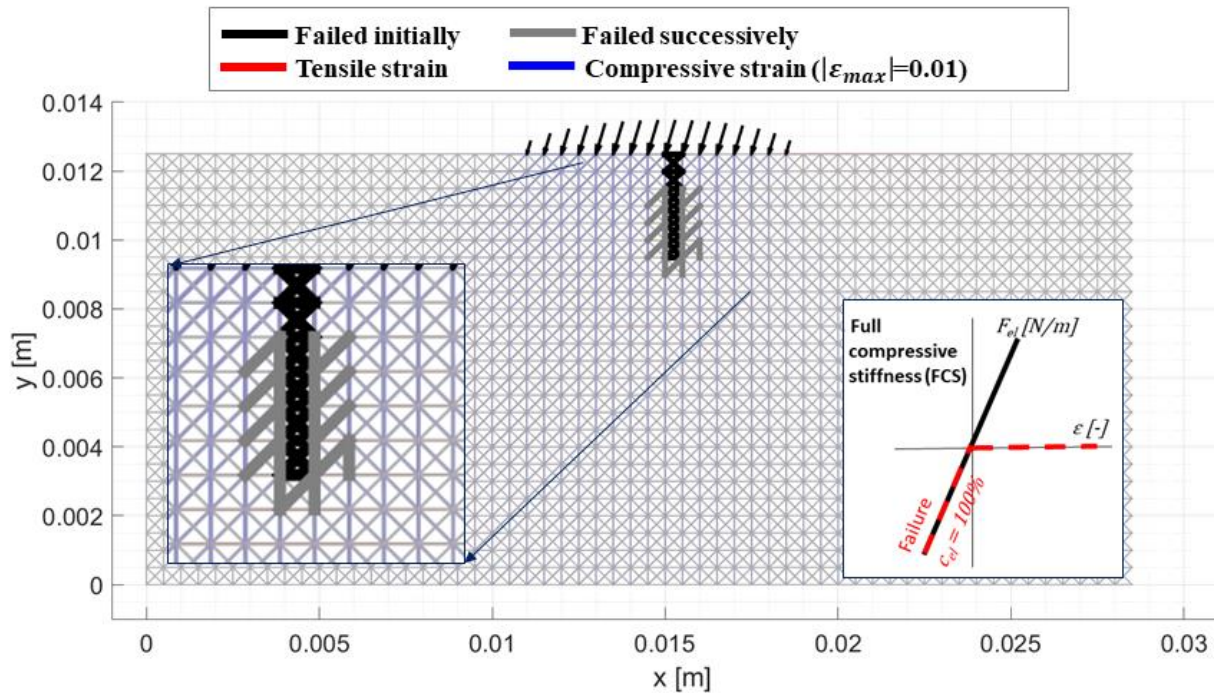


**Figure 48** RCF simulation for the initial bond law (full compressive stiffness, see subfigure right). The strain field is visualised by the line width, normalised to the magnitude of the maximum bond strain (26).

The result for this set-up is displayed in Figure 48. It can be seen that the progressive failure of elements led to a cluster of failed elements around the initial crack, rather than a crack propagation starting from the crack tip (directional FCG) which was the objective. As a result, this initial set-up was deemed to be insufficient for the RCF model.

Thus, the standard set-up of failed elements in solid-state DEM or PD models (34,49,53) was adopted as a default ("default bond law"). A detailed review concerning the state-of-the-art in the literature is given in section 2.2.4. This set-up implies that in the case of failure, the element does not sustain a tension- or a compression force (see Figure 15). A disadvantage of this set-up is that a crack loaded in compression is prone to non-physical effects, i.e. interpenetration of crack faces or excessive deformation of the grid around the crack faces, as the crack is completely soft.

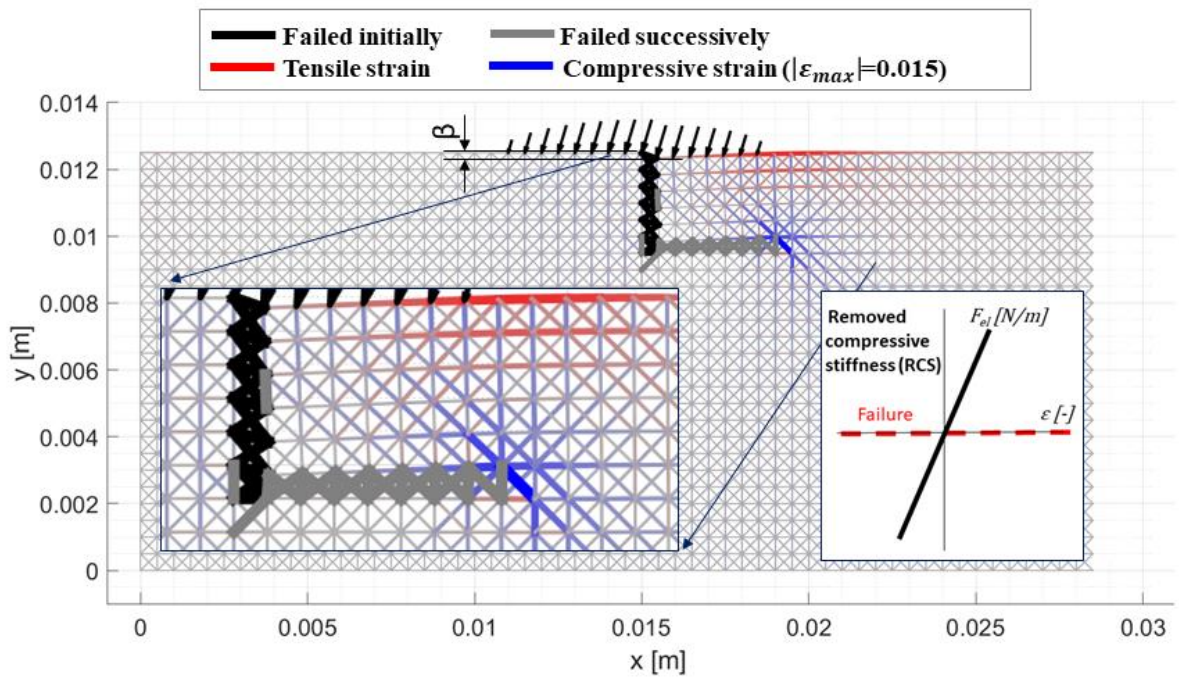


**Figure 49 - RCF simulation for the default bond law (removed compressive stiffness, see subfigure right). The strain field is visualised by the line width, normalised to the magnitude of the maximum bond strain. The lowering of the surface,  $\beta$ , is marked (26).**

The result of the default bond law is displayed in Figure 49. It highlights a directed crack that propagates from the initial crack tip at an angle of  $90^\circ$ , parallel to the moving direction of the contact. This is in general agreement with the main crack of the experimental reference, that branches to the right from the initial crack tip (see Figure 47, right). This demonstrates that the default bond law is capable of facilitating a directional FCG, which was the goal of this section.

The fact that the default bond law delivers directional FCG (see Figure 49), and the initial bond law (see Figure 48) does not, can be explained by the distribution of strains within the strain fields. It is important to mention that the illustration of strain per element in both figures cannot be compared quantitatively, but only qualitatively. The default set-up displays a highly inhomogeneous strain field with strain maxima around the crack tip (see Figure 49). With respect to the fatigue law (see Equation 39 and Equation 40), this is what drives FCG. The initial set-up, though, displays a rather homogeneous strain field (see Figure 49), which resulted in a cluster of failed elements around the initial crack.

The finding is that a directional FCG requires an inhomogeneous strain field around the existing crack. This is provided only by a bond law set-up with a



significant softening under compressive strain or a complete removal of the failed element.

A shortcoming of the default bond law is that it prohibits a transfer of load from the contact on the surface to the grid area below the crack. This is evidenced by the fact that the element strains below the kink of the crack are close to zero (26). As a result, the crack cannot grow into the depth like in the reference (see Figure 47, right) but grows in an "orthogonal way" (forced FCG direction), which is not acceptable. Thus, the bond law for failed elements loaded in compression must be stiffened in order to permit a load transfer and to facilitate omnidirectional FCG. This improvement will be addressed in the next section (see section 5.1.8).

Besides the FCG development, the grid deformation around the crack was an issue. Due to the default bond law, the surface lowering is significant,  $\beta = 0.16 \text{ mm}$  (see Figure 49). For a Hertzian contact without a crack, the analytical solution gives a lowering of  $\beta = 0.065 \text{ mm}$ . This means that the default bond law delivers a lowering that approximates 250% of the analytical solution (26). This effect leads to highly strained elements on the surface due to tensile loading (see Figure 49, bold red lines). These elements, however, do not fail as FCG was disabled for the first row. Although, the lowering evidenced a weak point of the default bond law, as it generated a non-physical effect. Another potential implication of the set-up is that the crack faces may interpenetrate, which is unacceptable as well. Thus, a modification of the bond law set-up was required to stiffen failed elements in compression.

In this section, the fatigue capability was applied to a rolling contact simulation. Two different bond law set-ups were evaluated, whereas the standard set-up from literature was adopted as default. Due to the complete removal of load sustainment for failed elements, it provided for inhomogeneous strain fields that were identified to be a precondition for a directional FCG. In this way, the initial RCF model approximated the experimental reference. Thus, shortcomings regarding the FCG development and the behaviour of a crack under compressive load were discovered, which are addressed in the next section (see section 5.1.8).

### **5.1.8 Crack closure modelling**

With respect to the default bond law (see Figure 15), the initial RCF simulation (see section 5.1.7) raised the question of how failed elements strained in compression can be stiffened. This is required to counter the adverse effects of surface lowering and grid interpenetration, and to facilitate a transfer of element forces across crack faces. A literature review (see section 2.2.4) was performed.

The outcome was that there is no solution applicable to the DERC model and that a novel approach was required.

A review of the available literature regarding the mechanical response of a cracked material loaded in compression (see section 2.1.6) led to the finding that the phenomenon of crack closure plays a major role (22). In this section, the effect of crack closure was modelled in a macroscale way (see Figure 12) in order to calibrate the bond law with respect to experimental results (26). A review of the RCF behaviour for the derived bond law was performed.

With respect to the literature review performed in section 2.1.6, the following assumptions were adopted to the crack closure modelling.

- Plastic deformation and a residual stress field were assumed at the crack tip (20–22), but were not explicitly modelled;
- PICC was assumed to be the dominant mechanism of crack closure (23);
- Plane strain prevails, as the crack tip is located in the bulk material and not on the surface (24); Potential edge effects at the mouth of a surface crack were disregarded;
- The cracks were assumed to be large ( $> 1$  mm). Thus, the opening load was assumed to be independent of the microstructure (83);
- The closure behaviour was assumed to be independent of the crack length, a residual COD was neglected, and the LEFM was assumed to be applicable in order to calculate the COD (83);
- The stress ratio was assumed to be negative, resulting in negative opening loads (23,25);
- Due to the limited availability of experimental data, the closure behaviour of steel DIN Ck45 was adopted to model rail steel;

The aim of the modelling was to capture the macro-mechanical load-displacement behaviour (see Figure 12) for different load points, i.e. the load-COD figure, by an appropriate bond law (26). The bond law set-up was determined in an incremental way (see Figure 50). This included a review of the RCF behaviour and a comparison of the load-COD figure to the reference.



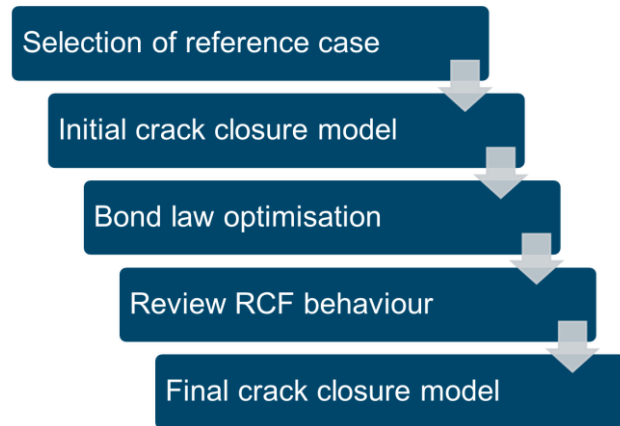


Figure 50 - Procedure for crack closure modelling.

The first step of the modelling (see Figure 50) was the selection of a reference case. From the available data, the work of Romeiro et al. (25) was selected as negative stress ratios up to  $R = -3$  were captured, a standardised specimen geometry was applied and the test procedure was clearly described. The results obtained for the opening loads are displayed in Table 7, the opening loads as a function of the stress ratio  $R$  are displayed in Figure 51.

R [-]	$P_{\max}$ [kN]	S [mm <sup>2</sup> ]	$P_{\text{open}}$ [kN]	$P_{\text{open}} / P_{\max}$
-3	30	43 x 10	-5	-0.17
-2	40	43 x 10	-3	-0.08
-1	80	43 x 10	-8	-0.10
-1	40	43 x 10	0	+0.00
0	30	43 x 10	4	+0.13

Table 7 - Approximated values for the opening loads  $P_{\text{open}}$  as a function of the stress ratio  $R$  and the maximum load  $P_{\max}$ , modified from (25). The selected reference case is marked in red (26).

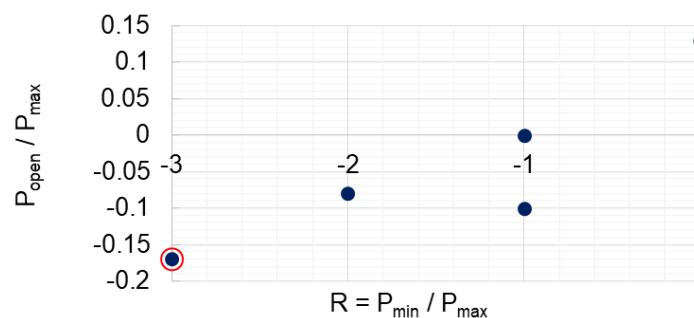
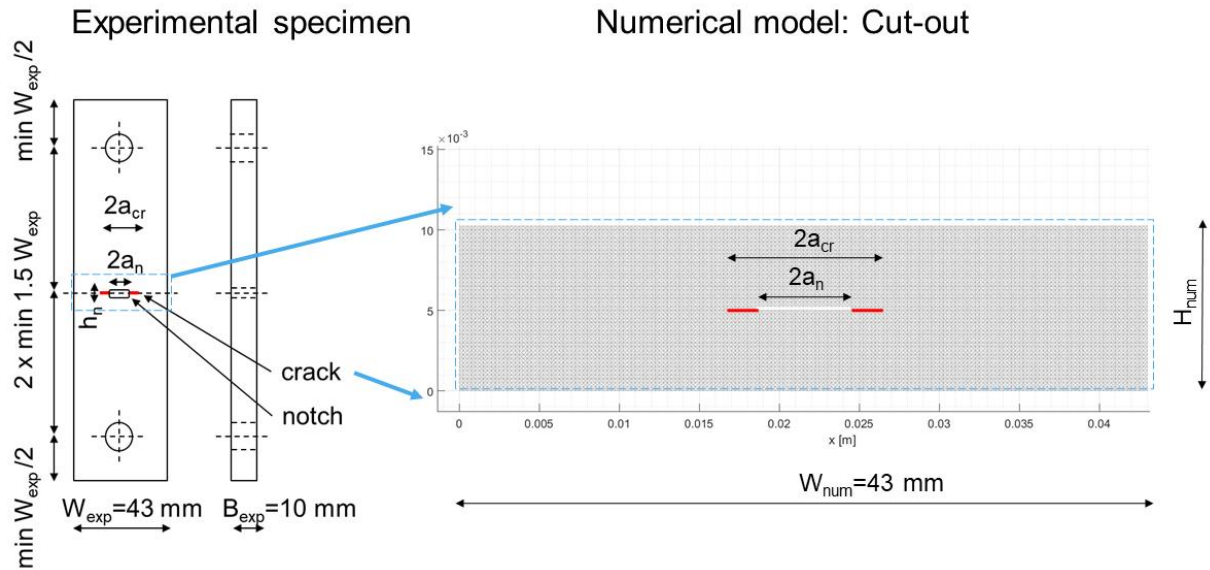


Figure 51 - Opening loads  $P_{\text{open}}$  as a function of the stress ratio  $R$ , referenced to the maximum load  $P_{\max}$ , modified from (25). The reference case is marked in red.

As high compressive stresses were expected for the RCF simulation, a stress ratio of  $R = -3$  was assumed to identify a reference case (see Table 7). A problem, though, was that  $R$  is defined for a Mode I test (see Equation 2), but not for a rolling contact case. Thus, an "equivalent stress ratio" was derived (see section 5.1.9).



**Figure 52 - Middle-crack specimen modified from (16,84) (left) and model cut-out (right). In the centre, the notch and the pre-crack (marked in red) are illustrated (26).**

In the second step (see Figure 50), the middle crack tension (MT) specimen of thickness  $B_{exp} = 10 \text{ mm}$  and width  $W_{exp} = 43 \text{ mm}$ , applied by Romeiro et al. (25), was discretised to get an initial crack closure model. The layout of the specimen was based on the ASTM standard E647-95. The specimen featured a central notch of  $2a_n = 6 \text{ mm}$  length and  $h_n = 0.25 \text{ mm}$  height. A fatigue pre-cracking was applied to both edges of the notch, so that a total crack length of  $2a_{cr} = 10 \text{ mm}$  was introduced to the specimen (see Figure 52, left).

The geometry was discretised in a way that the unit length  $l_0$  was aligned to the notch height  $h_n$ , which resulted in  $l_0 = 0.25 \text{ mm}$ . Initially, the specimen was modelled in its complete size of  $W_{exp} = 43 \text{ mm}$  and  $H_{exp} = 3 * W_{exp} = 129 \text{ mm}$ , resulting in a grid of  $172 \times 516$  modules. From a numerical point of view, this grid size was too large to be processed by the available computer resource. Thus, a cut-out of the grid was made in a way that just the section around the crack was modelled by a  $172 \times 41$  grid (see Figure 52, right). Then, the reduced grid was

checked for potential edge effects on the bottom and top edges, but none were found. A floating boundary condition was applied (see section 4.7). In this way, the initial crack closure model was established.

The crack opening displacement COD was defined by the y-displacement of nodes positioned on the centreline on the top- and bottom of the notch, which agrees with the definition of ASTM standard E647 (16). The displacements were calculated by the differences of y-coordinates  $y_{top}$  and  $y_{bot}$  for the states "0" (no displacement) and "1" (with displacement).

$$COD = (y_{top1} - y_{bot1}) - (y_{top0} - y_{bot0})$$

**Equation 53**

In this way, the grid was set-up, and the COD was defined. The next step concerned the bond law set-up. Potential modifications concerned the case of failure under compressive strains ( $\varepsilon < 0$ ), i.e. the left part of a bond law diagram (see Figure 53).

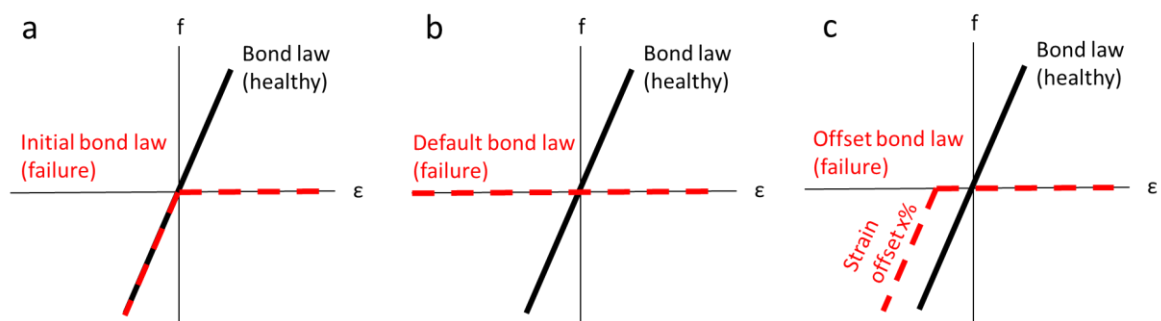


**Figure 53 - Bond law set-ups in case of failure (see red markings): Initial- and default set-ups (a, b), concept with strain offset (c).**

The goal was to model the incremental crack closure behaviour, i.e. the smooth transition from reduced- to full elasticity, illustrated in a load-COD diagram. In order to facilitate this transition, the default bond law (see Figure 53 b) had to be stiffened. The simplest approach therefore was to apply a strain offset to the initial bond law (see Figure 53 c).

With respect to the RCF simulation, however, the number of elements increased, which revealed a weakness of the offset set-up. The unsteadiness of the bond law reduced the convergence behaviour of the numerical process. Thus, the bond law

was optimised by smoothing in order to minimise the unsteadiness (see Figure 54).

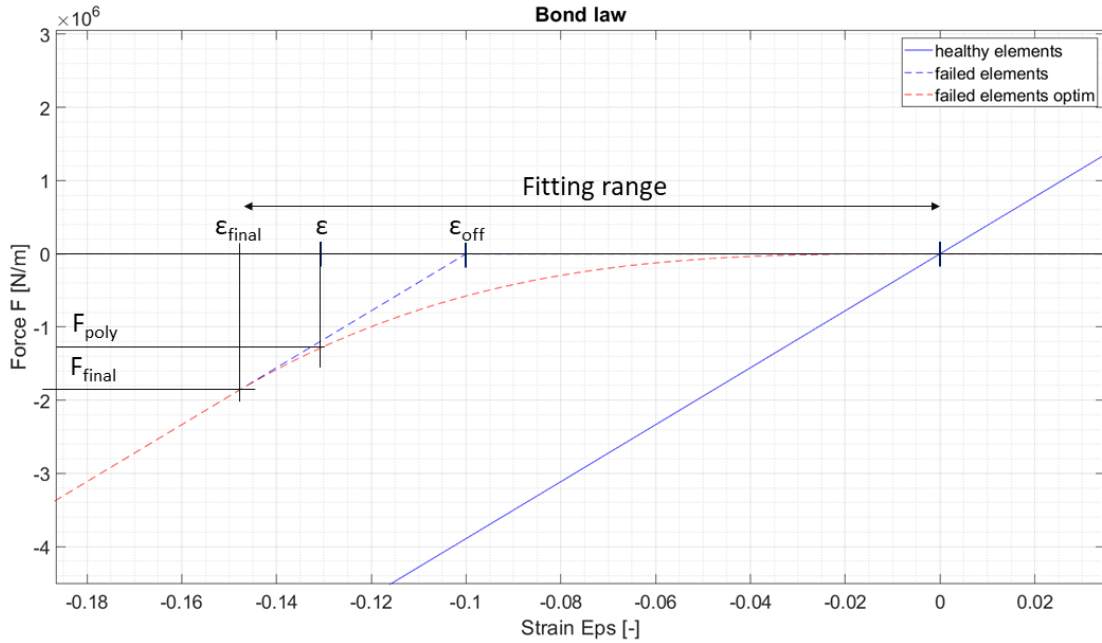


**Figure 54 - Optimisation of the bond law with offset (see blue dashed line) by polynomial curve fitting (see red dashed line).**

Therefore, a strain fitting interval was defined from  $\epsilon = 0$  to  $\epsilon = \epsilon_{final}$ . The maximum element force  $F_{final}$  at the end of the interval was defined by the relationship of the linear-elastic bond law (see Equation 13) and the difference between the strains  $\epsilon_{final}$  and  $\epsilon_{off}$ .

$$F_{final} = c * (\epsilon_{final} - \epsilon_{off})$$

**Equation 54**

With it, the element force  $F_{poly}$  was derived by a polynomial fitting within the interval  $\epsilon = [\epsilon_{final}, 0]$  with the parameter  $n_{poly}$ .

$$F_{poly} = F_{final} * \left( \frac{\epsilon}{\epsilon_{final}} \right)^{n_{poly}}$$

**Equation 55**

The final strain  $\epsilon_{final}$  of the interval was defined by a factor  $f_{poly}$  with respect to the offset strain  $\epsilon_{off}$  (see Figure 54).

$$\varepsilon_{final} = f_{poly} * \varepsilon_{off}$$

Equation 56

In this way, an optimised bond law was defined for the initial crack closure model (see Figure 50). In the next step, the bond law was applied to the initial RCF set-up of section 5.1.7 (see Figure 48, Figure 49). Regarding the bond law set-up, the offset strain was varied. As an offset of  $\varepsilon_{off} = 0\%$  approximated the initial bond law (see Figure 53 a) and the known result (see Figure 48), offsets of  $\varepsilon_{off} = -2\%$ ,  $\varepsilon_{off} = -6\%$  and  $\varepsilon_{off} = -10\%$  were employed. The fitting parameters,  $f_{poly} = 1.5$ , and  $n_{poly} = 3.0$  were derived in an empirical way, as they provided a good tangential fitting of the smoothed curve (see Figure 54), and were kept constant.

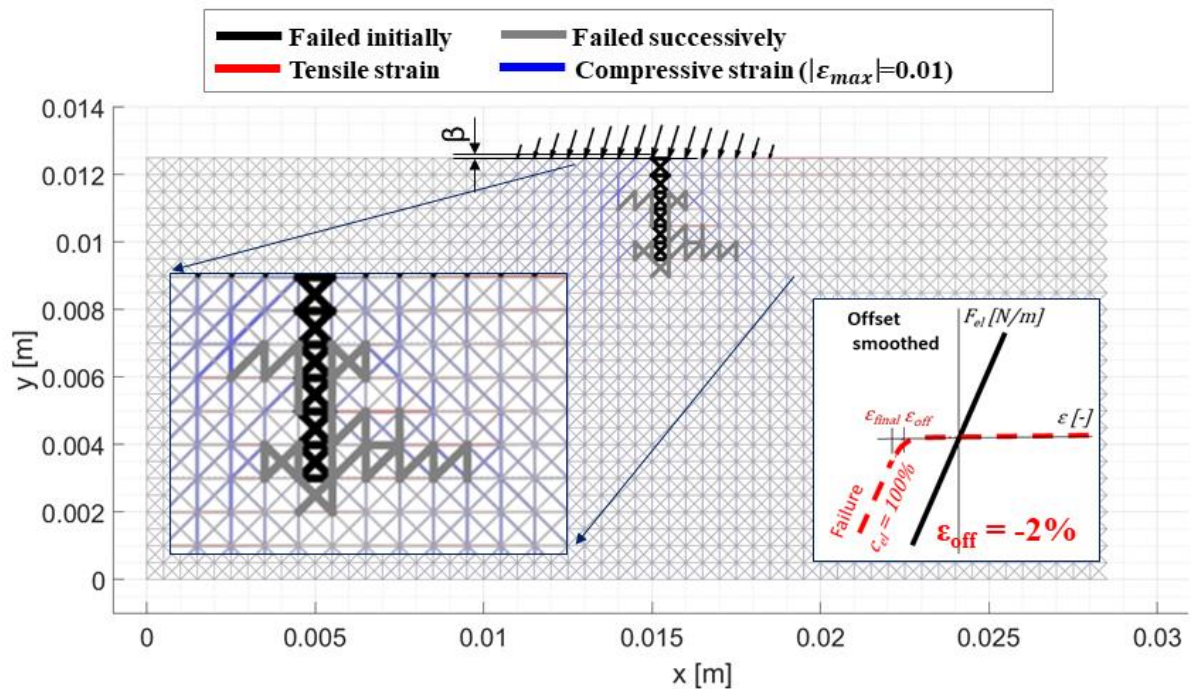


Figure 55 - RCF result for a bond law set-up with an offset strain of  $\varepsilon_{off} = -2\%$  (see subfigure right).



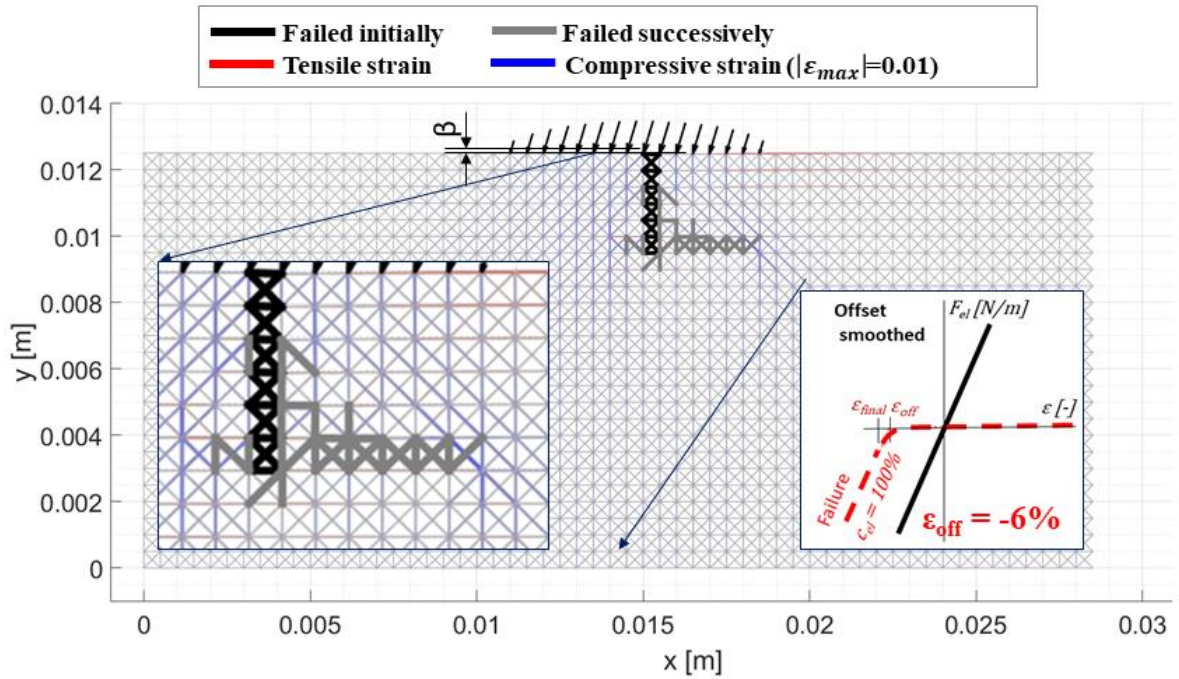


Figure 56 - RCF result for a bond law set-up with an offset strain of  $\epsilon_{off} = -6\%$  (see subfigure right).

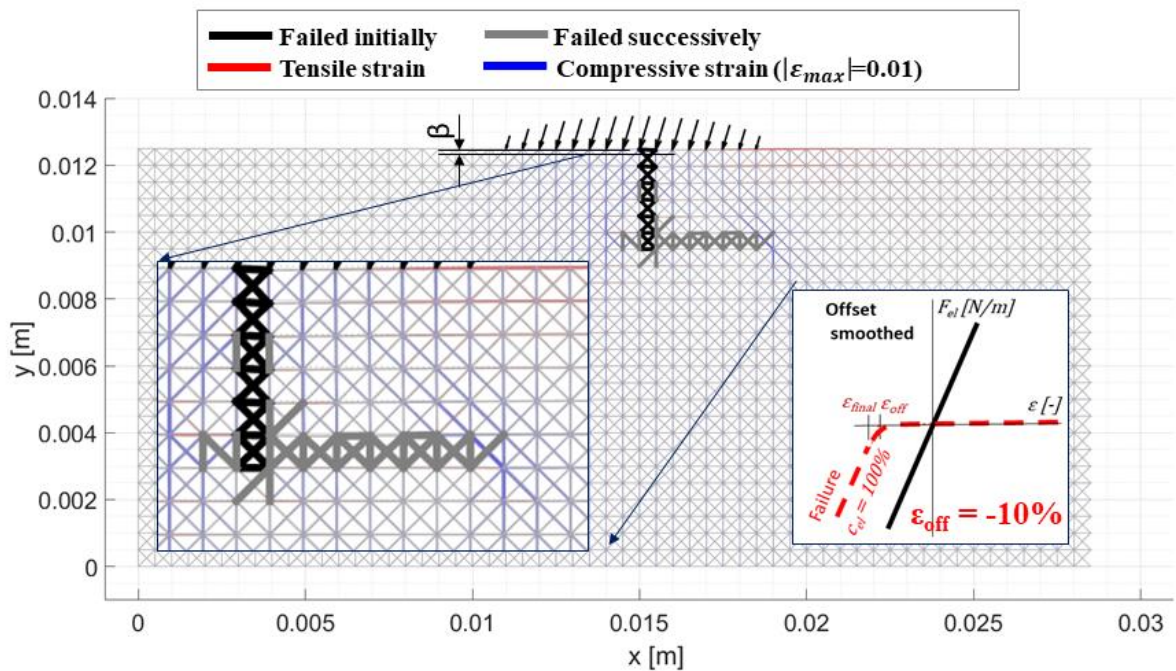


Figure 57 - RCF result for a bond law set-up with an offset strain of  $\epsilon_{off} = -10\%$  (see subfigure right) (70).

The results were compared to the that of the initial- and the default bond laws (see Figure 48, Figure 49). The result of the bond law with an offset  $\epsilon_{off} = -2\%$  (see

Figure 55) suggested to represent a transition state between the cluster of failed elements of the initial bond law (see Figure 48) and the directed FCG of the default bond law (see Figure 49), as multiple directed cracks emerged around the initial crack. With respect to the experimental reference (see Figure 47), this suggested the bond law to be stiffer than required. The convergence behaviour was improved by the smoothing of the bond law.

The increase in offset strain softened the grid around the initial crack, which led to higher element strains. The results for offsets of  $\varepsilon_{off} \leq -6\%$  (see Figure 56 - Figure 57) revealed a directional FCG, resulting in a primary crack that propagated in parallel to the rolling direction. These crack representations were considered to be comparable to the result of the default bond law (see Figure 49). The difference in offset strains for the two cases led to local variations of the strain fields around the initial crack, which is the reason for slightly different FCG patterns. Additionally, both cases indicated a secondary crack tip, which branched from the initial- and primary cracks in the opposite direction of the rolling contact direction. This is in basic agreement with the experimental result from section 5.1.7 (see Figure 47, right). Thus, set-ups of  $\varepsilon_{off} = -6\%$  and  $\varepsilon_{off} = -10\%$  were considered in the further analysis.

Another aspect regarded the capability of the grid to transfer compressive element forces across a crack. The default bond law caused a "mechanical void", which was manifest by the unstrained elements below the crack (see Figure 49, below and left of the crack kink). This has a potential impact on the FCG direction. The bond laws with the offset strains addressed this issue as healthy elements to the left and below of the crack kink were strained more (see Figure 56 - Figure 57) than the reference case of the default bond law (see Figure 49). This aspect is critical to facilitate a crack growth into the depth and to prevent preferred directions of FCG. However, a rather orthogonal FCG pattern was found for the considered cases (see Figure 56 - Figure 57). This topic was analysed in detail in section 5.2.

Besides the FCG behaviour, the surface lowering of the default bond law (see Figure 49),  $\beta = 0.16 \text{ mm}$ , was put under scrutiny. The results of the bond law set-ups with an offset of  $\varepsilon_{off} < 0\%$  (see Figure 55 - Figure 57) indicated that the surface lowering was minimised by the stiffening of the failed elements. The case of the softest bond law,  $\varepsilon_{off} = -10\%$ , delivered a surface lowering of  $\beta = 0.05 \text{ mm}$ . Compared to the analytical solution for a Hertzian contact without a crack,  $\beta = 0.065 \text{ mm}$ , this yielded 76%. The stiffer response of the model was attributed to the model's reduced Poisson's ratio (51). Compared to the lowering of the default bond law, this represented a major improvement (26). Further, a

potential interpenetration of the grid like discussed in the literature (53) was mitigated by the offset. This promoted the application of an offset strain.

Another aspect concerned convergence, i.e. the solver's capability to find a solution. A guideline for simulations is that solvers do not like unsteadiness. In the case of  $\varepsilon_{off} = 0\%$  and without smoothing (Figure 48), the effect of the unsteadiness of the bond law was the highest. Thus, only a few failed elements were processed until the simulation stopped, as the solver did not find a solution. Due to the smoothing and the offset, the effect of the unsteadiness was minimised. This fact was highlighted by the higher number of failed elements that were simulated (see Figure 55 - Figure 57) and the improved numerical efficiency.

In summary, the modified bond law with offset strains of  $\varepsilon_{off} = -6\%$  and  $\varepsilon_{off} = -10\%$  were applied to the RCF model. With it, major drawbacks of the default bond law from the literature (see introduction of this section) were improved.

Finally, the crack closure model was set-up (see Figure 50) with the optimised bond law. In order to model the reference case (see Table 7,  $R = -3$ ), eight load points were simulated. The results for the maximum-, opening- and minimum load are illustrated in Figure 58. The figures for the two bond law set-ups did not show a major difference. Thus, only the result for  $\varepsilon_{off} = -10\%$  was illustrated.

For the maximum load  $P_{max}$  it can be seen that the stress maxima are located exactly at the two crack tips (see Figure 58, subplot above). For the minimum load  $P_{min}$ , however, the grid exhibited a different stress field (see Figure 58, subplot below). Within- and around the cracks there are white stress spots, which indicated that the cracks were not closed completely. This occurred due to the stiffening set-up of the failed elements. At first, the incomplete closure seemed to be a contradiction, as for  $P_{min} \ll P_{open}$ , the crack was assumed to be closed. Though, a crack, which is subject to plastic deformation (PICC), probably does not close completely due to wedging of asperities. In this way, the model result is in general agreement with a physical crack closure.

In order to assess the crack closure behaviour, the load-COD figure is of importance (see Figure 59). The figure includes the minimum- and maximum series of the experimental reference (see also (84)), as well as the simulation results for the two bond law set-ups  $\varepsilon_{off} = -6\%$  and  $\varepsilon_{off} = -10\%$ .



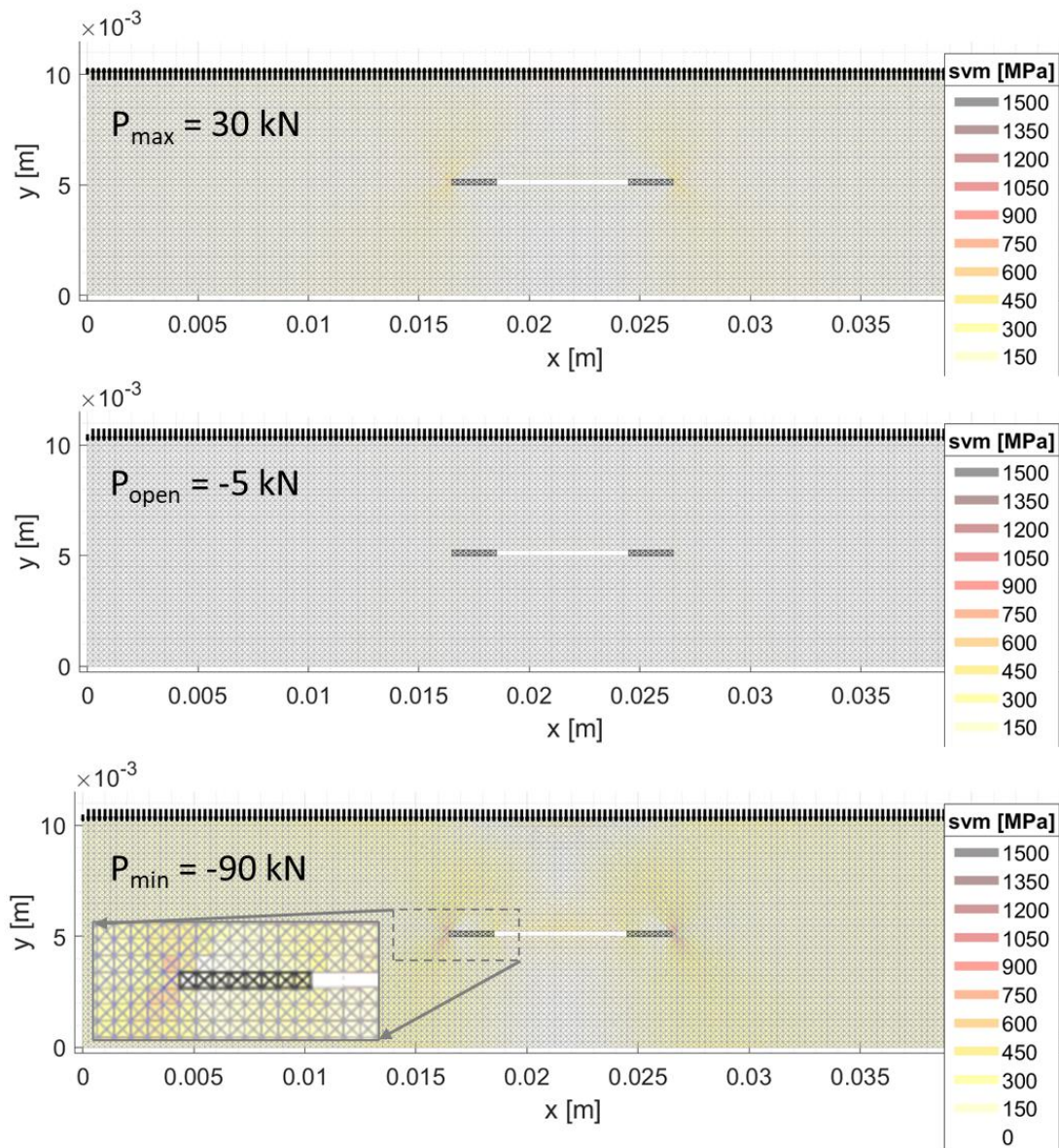


**Figure 58 - Results for the maximum- (top), opening- (centre) and minimum (bottom) loads for the reference case. For the minimum load case, a magnification around the crack (black elements) is displayed. The result refers to the set-up  $\epsilon_{off} = -10\%$  (26).**

Regarding the reference, there is a significant divergence of the curves in the tensile area. In the compressive area, there is a closer fit. Romeiro et al. state that the crack opening process is progressive due to crack tip plasticity (25), which explains the lateral shift of the experimental curves.

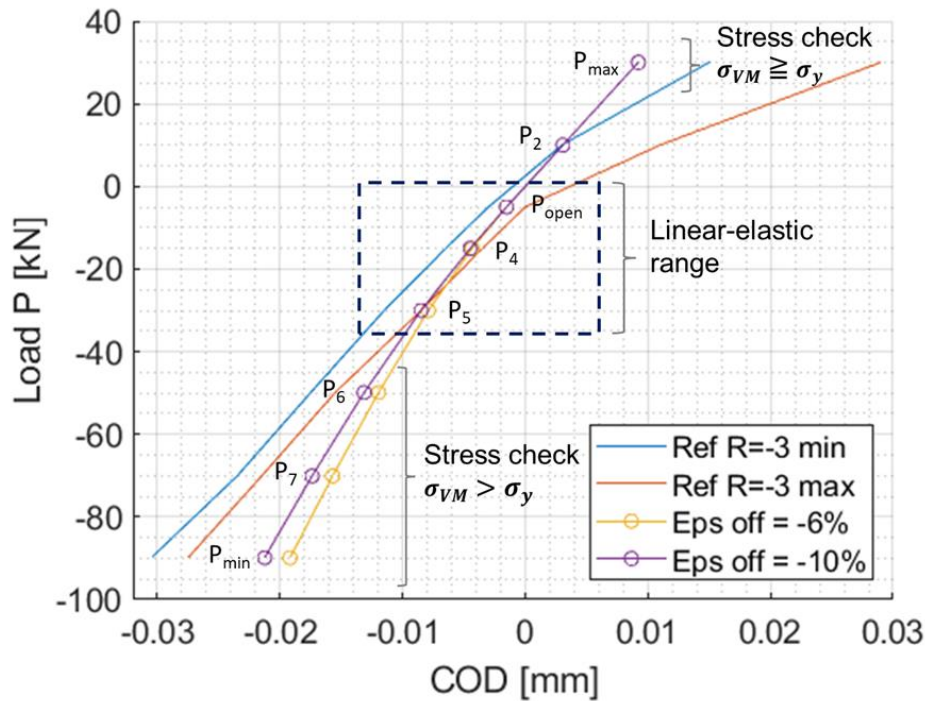


Figure 59 - Load-COD curves for the minimum- and maximum reference cases, modified from (84), and simulation results for the set-ups of  $\epsilon_{off} = -6\%$  and  $\epsilon_{off} = -10\%$ . The range of linear elasticity is marked (26).

	$P_{max}$	$P_2$	$P_{open}$	$P_4$	$P_5$	$P_6$	$P_7$	$P_{min}$
Load P (kN)	30	10	-5	-15	-30	-50	-70	-90
Max $\sigma_{VM}$ (MPa)	327	109	54	158	293	443	572	685

Table 8 - Maximum equivalent Von Mises stresses of the simulation for  $\epsilon_{off} = -10\%$  (26).

The simulation exhibited a good agreement with the reference for lower loads, i.e. the interval between  $P_{open} = -5 \text{ kN}$  and  $P = -30 \text{ kN}$ . This interval represented the linear-elastic range. For higher loads, the model behaved stiffer than the reference. This deviation was attributed to the fact that the model did not account for plasticity, whereas in the experiment, local plastification took place. In order to check this assumption, the maximum equivalent stresses  $\sigma_{VM}$  for the set-up  $\epsilon_{off} = -10\%$  were summarised in Table 8.

The stress maxima were compared against the yield stress of the Ck45 reference, i.e.  $\sigma_y = 350 \text{ MPa}$  (25). The comparison indicated that for  $P_{max}$ , the yield stress  $\sigma_y$

was approached. For loads  $P < P_{max}$ , the spread of the experimental curves indicated that plastification started already at loads below  $P_2$  (see Figure 59). In the compressive range, the maximum stresses for the load points  $P_6$  to  $P_{min}$  clearly exceeded the yield limit (see Table 8). As a result, the range of linear elasticity from  $P_{open}$  to  $P_5$  was marked explicitly in Figure 59. In this range, a comparison between the reference and the model is permissible to calibrate the bond law.

Within the linear-elastic range, the model tended, for both set-ups, to behave slightly stiffer than the reference (see Figure 59). This was assumed to be due to the model's inherent limitation to a Poisson's ratio of  $\nu=0.25$  (see section 4.13). This reduced the lateral movement of the model during tension or compression, which, in turn reduced the COD. The limitation itself could not be removed. However, the resulting adverse effect of stiffening was at least reduced by the set-up  $\varepsilon_{off} = -10\%$ . An alternative offset  $\varepsilon < \varepsilon_{off}$  was not applied, as this would increase the surface lowering under RCF conditions.

In this way, a novel bond law set-up was derived with respect to the crack closure behaviour of an experimental reference. It is important to acknowledge that crack closure is complex, and that several assumptions and simplifications were required. Based on that, the potential for future work is emphasised, i.e. experimental work to determine the crack opening loads for rail steels.

The calibration was performed within the linear-elastic range. Within these limits, the model approximated the reference in a satisfying way. An increase in offset improved the agreement. Thus, the set-up of  $\varepsilon_{off} = -10\%$  was selected to proceed. The set-up was applied to the RCF model, which highlighted that major drawbacks of the initially employed bond laws were addressed.

In the next section, the underlying assumption of a stress ratio of  $R = -3$  is checked (see section 5.1.9).

### 5.1.9 Equivalent stress ratio

In the previous section, crack closure was modelled to calibrate the bond law (see section 5.1.8). The calibration was based on a correlation of experimental data to the bond law set-up. The former was determined with respect to a specific test set-up, which was characterised by a stress ratio  $R$ , that in turn defined the condition of a uniaxial loading (see Equation 2). In a rolling contact condition, though, the stress state is multiaxial, not uniaxial. This raised the question of how the data from the experiments could be associated to the RCF simulation.

The employed method was to use the stress tensor per module (see section 4.9), derive the two principal stresses  $\sigma_1$  and  $\sigma_2$  and calculate an equivalent stress ratio  $R_{eq}$ . A look at Mohr's circle revealed that  $\sigma_1$  characterises the maximum principal stress, which generally represents a tensile stress, and  $\sigma_2 < \sigma_1$  the minimum principal stress which is oriented in orthogonal direction to that of  $\sigma_1$  (80). In this way, an equivalent stress  $R_{eq}$  can be defined, which resembles the stress ratio  $R$ .

$$R_{eq} = \frac{\sigma_2}{\sigma_1}$$

**Equation 57**

The principal stresses  $\sigma_1$  and  $\sigma_2$  were derived from the stresses  $\sigma_{xx}$ ,  $\sigma_{yy}$  and  $\sigma_{xy}$  of the stress tensor with the formulae of stress transformation (80) per DEM module.

$$\sigma_1 = 0.5 * (\sigma_{xx} + \sigma_{yy}) + \sqrt{0.25 * (\sigma_{xx} - \sigma_{yy})^2 + \sigma_{xy}^2}$$

**Equation 58**

$$\sigma_2 = 0.5 * (\sigma_{xx} + \sigma_{yy}) - \sqrt{0.25 * (\sigma_{xx} - \sigma_{yy})^2 + \sigma_{xy}^2}$$

**Equation 59**

This derivation was applied to one cycle of the initial RCF simulation (see section 5.1.7). The bond law derived by the crack closure calibration was applied to the elements of the initial crack (see section 5.1.8). The result for the first five rows of modules located below the surface is illustrated in Table 9. The results of the rows below were omitted, as these tended to negative infinity.

The results of Table 9 show that all values of  $R_{eq}$  are negative. This means that there is no module which is loaded purely in tension ( $\sigma_2 \geq 0$ ), but each module is loaded in compression as well.

The deeper a module is located, the smaller its value of  $R_{eq}$  becomes, which means that  $\sigma_1$  diminishes, and the principal compressive stress  $\sigma_2$  prevails. The dominance of  $\sigma_2$  is also highlighted by the fact that the amount of all equivalent ratios is  $|R_{eq}| > 1$ . The highest values of  $R_{eq}$  are located below the surface. This is where the influence of  $\sigma_1$  is the highest. However, also for the top three rows, the average of  $R_{eq}$  is about -9.

-2.2	-2.4	-2.7	-2.9	-3.2	-3.7	-4.7	-7.3	-14.1	-47.0	-4.3	-2.0	-1.7	-1.6	-1.5	-1.6	-1.7	-1.8	-2.0
-4.6	-5.0	-5.4	-6.0	-6.4	-6.7	-6.4	-5.7	-6.7	-18.2	-15.8	-22.4	-10.9	-7.4	-5.5	-4.7	-4.3	-4.3	-4.5
-7.4	-8.0	-8.6	-9.4	-10.1	-9.9	-9.0	-6.1	-3.0	-15.4	-20.0	-20.5	-28.1	-41.2	-27.4	-12.2	-8.6	-7.6	-7.3
-9.5	-9.5	-10.0	-10.9	-12.4	-15.5	-22.2	-40.5	-5.6	-13.3	-88.0	-44.3	-34.4	-41.2	-62.6	-58.0	-17.5	-12.0	-10.2
-12.7	-12.0	-12.2	-13.8	-16.9	-25.4	-42.0	-19.6	-16.9	-13.7	-96.4	-108.0	-68.3	-66.3	-103.9	-300.7	-131.3	-24.1	-15.3

**Table 9 - Equivalent stress ratios  $R_{eq}$  of the rows 1 to 5, located below the surface of the initial RCF grid (see Figure 48Error! Reference source not found.).**

With respect to the experimental crack closure results (see Table 7, Figure 51), the results of Table 9 suggest that the best correlation to the stress field of the rolling contact is for the case of  $R = -3$ , which was selected as reference for the calibration (see section 5.1.8). Thus, the derivation of equivalent stress ratios  $R_{eq}$  for the RCF grid justified that selection.

## 5.2 Assessment of orthotropic fatigue crack growth

The scope of section 5.1 was to model FCG in an isotropic way, i.e. assuming that FCG has no preference to a specific direction. This objective was achieved partially, as RCF as a result of multiple load cycles was simulated (see sections 5.1.7 and 5.1.8). However, the RCF results indicated a crack that proceeded in a distinctive preferred direction, i.e. along a horizontal path (see Figure 49). The Mode I simulations revealed a similar FCG behaviour (see Figure 43). The results agreed in the way that the crack tips proceeded exclusively in horizontal or vertical direction with respect to the grid's layout. As a result, this behaviour was called orthotropic FCG.

Due the model's layout, a certain degree of inherent FCG orthotropy was expected (34). Though, the extent of the effect encountered in the RCF simulations was surprising. The aim of this section is to better understand the effect of orthotropic FCG, identify contributing factors and find ways to mitigate or even eliminate it. In other words, the influence of the grid on the FCG behaviour of the model is assessed in this section.

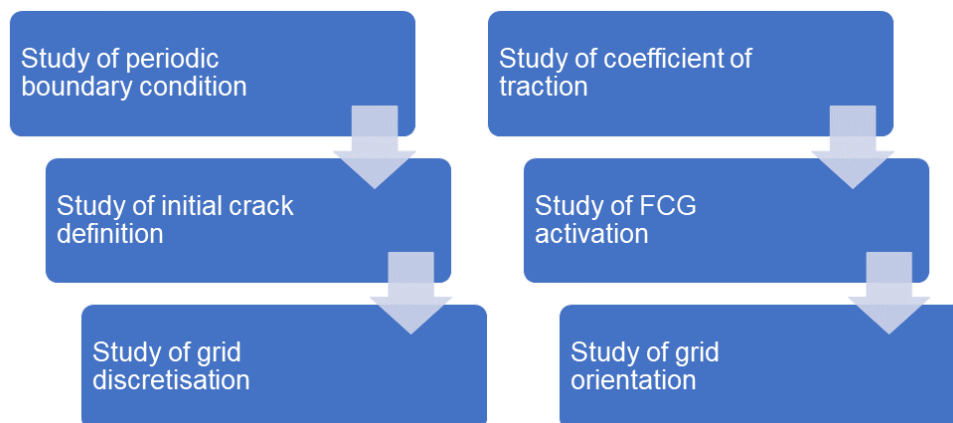


Figure 60 - Overview on the procedure to assess the orthotropic FCG behaviour.

Therefore, several assessments were performed (see Figure 60). The impact of the lateral periodic boundary condition (see section 5.2.1), the layout of the initial crack (see section 5.2.2), the grid discretisation (see section 5.2.3), the applied lateral load (see section 5.2.4) and the FCG activation method (see section 5.2.5) were analysed. The latter section provided the finding that the FCG activation is key to an improved FCG behaviour. The adopted method minimised the effect of orthotropic FCG and finally facilitated an isotropic FCG behaviour. Furthermore,

the influence of the grid orientation on the strain field was investigated (see section 5.2.6).

In section 5.1, the results were compared against an experimental reference (see Figure 47), which required a relatively fine grid. However, the scope of this section was the assessment of the model behaviour, not physics. For this reason, coarser and more efficient grids were applied, which do not facilitate a comparison to the experimental reference.

### 5.2.1 Study of periodic boundary condition

In order to examine the effect of orthotropic FCG (see section 5.2), the influence of the periodic boundary condition (see section 4.11) was assessed in this section. The question was "by how much can the width of the grid be reduced?". On the one hand, a tight grid makes the simulation more efficient, which is desirable. On the other, this set-up introduces edge effects. Thus, the grid was intended to be as tight as possible, but as wide as required to minimise edge effects.

The required grid width was defined with respect to the semi-contact length  $a$  of a Hertzian contact (see Equation 18). The aim of this section is to identify the required width as a function of  $a$  that rules out edge effects, i.e. effects that are introduced artificially by the lateral edges of a narrow grid.

First a literature review was performed in order to find recommendations for an optimum grid width. Though, as there are many factors contributing to the RCF modelling, i.e. discretisation, elastoplastic set-up or applied load, it is difficult to formulate a general guideline. Thus, a parameter study was performed, where the width of the grid was varied. As target variable, the FCG pattern was selected, which directly refers to the investigation of orthotropic FCG. The aim was to identify a multiple of  $a$  for which the lateral boundary condition has no impact on the FCG pattern anymore.

An efficient 19x10 grid, modelling a twin-disc contact with a normal pressure of  $p_0=555 \text{ MPa}$  and a coefficient of friction of  $\mu=0.3$ , as well as the bond law calibrated to crack closure (see section 5.1.8), were adopted. The initial crack was modelled by three vertically arranged DEM modules, including horizontal and diagonal elements (see Figure 61). With respect to the basic dimensions (see Figure 46), this reference grid corresponded to a width of  $x_0 = 4.2 a$ . From this starting point, the grid was extended laterally step by step with respect to the semi-contact length  $a$  to define four different widths (see Table 10).



Grid dimension (-)	Grid width (-)
19 x 10 (reference)	4.2 a
23 x 10	5.1 a
27 x 10	6.0 a
32 x 10	7.1 a

**Table 10 - Set-ups for the parameter study of different grid widths.**

The results of the parameter study are illustrated in Figure 61. It can be seen that the FCG patterns of the widths  $5a$  to  $7a$  are identical. This suggests that there is no influence of the lateral periodic boundary condition anymore. For the width of  $4a$ , however, the secondary crack to the left of the initial crack develops in a different way. This indicates that the width is already too narrow, which has an effect on the FCG pattern. As a result, it was concluded that a minimum grid width of  $5a$  is recommended to avoid edge effects introduced by the periodic boundary condition. This was adopted for the subsequent modelling.

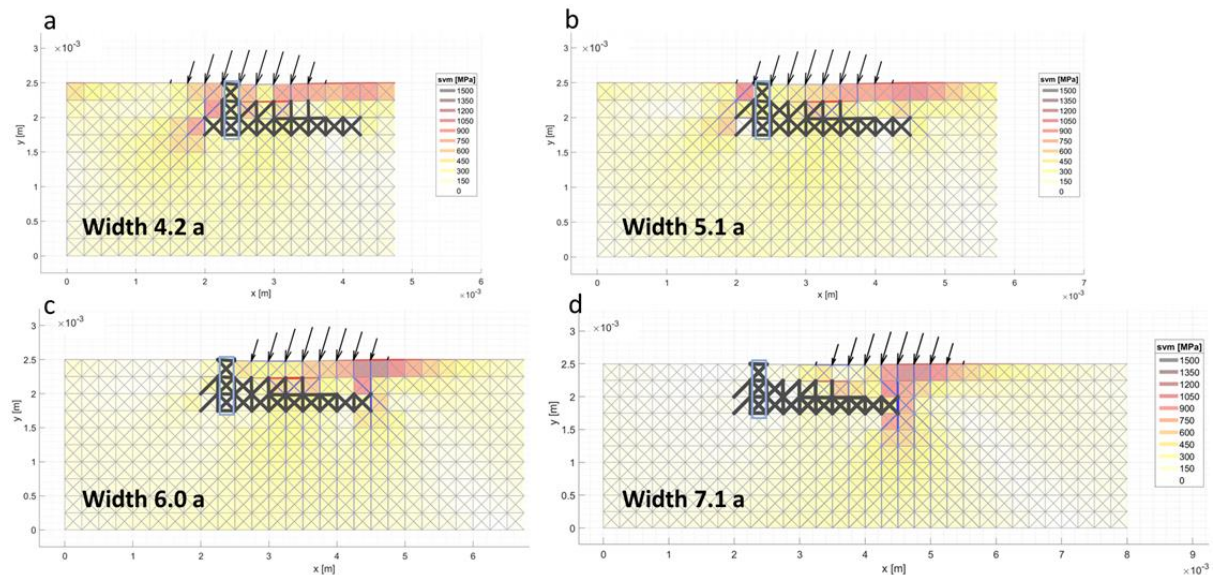


**Figure 61 - Results of the grid width variation with respect to the semi-contact length  $\alpha$ : Failed elements are marked in black. Elements of the initial crack are marked by the blue frame.**



Regarding the initial question, it was concluded that the grid width in association to the periodic boundary condition do not have an impact on the effect of orthotropic FCG. In the next step, the set-up of the initial crack was assessed (see section 5.2.2).

### 5.2.2 Study of initial crack definition

In order to understand the effect of orthogonal FCG (see section 5.2), the influence of the lateral boundary condition was analysed in the first step (see section 5.2.1). In the next step, the impact of the definition of the initial crack was investigated.

The initial crack definition used to this point was a simple vertical crack (see Figure 48, Figure 49). In this section, the initial crack definition was varied as part of a parameter study. The target variable is the FCG pattern. The goal was to find out the impact of the initial crack on the FCG pattern.

Therefore, the model set-up from section 5.2.1 was adopted. A grid width of  $5a$  was selected. In order to compare the new results, the FCG pattern of the original initial crack definition was used as reference (see Figure 61 b).

The assumption applied previously that elements of the module row at the surface were excluded from FCG (see section 5.1.7), might have introduced surface effects to the previous results. In order to minimise this effect for the given discretisation, the initial crack length was elongated by two unit lengths  $l_0$  to extend more into the material depth. In this way, the agreement to the experimental reference (see Figure 47) was violated. This was thought to be not an important concern for this study though.

The initial crack set-up was varied in different ways. First, vertical failed elements were added to the left and right of the reference initial crack (see Figure 62 a) to soften the crack. Second, the crack tip was formulated in a star type pattern (see Figure 62 b) in order to maximise the number of elements that are FCG activated (see Figure 37). Third, a crack of head check type with an angle of 45 degrees to the surface was introduced to substitute for the vertical layout (see Figure 62 c). The RCF simulation was run for these set-ups. The results are displayed in Figure 62.

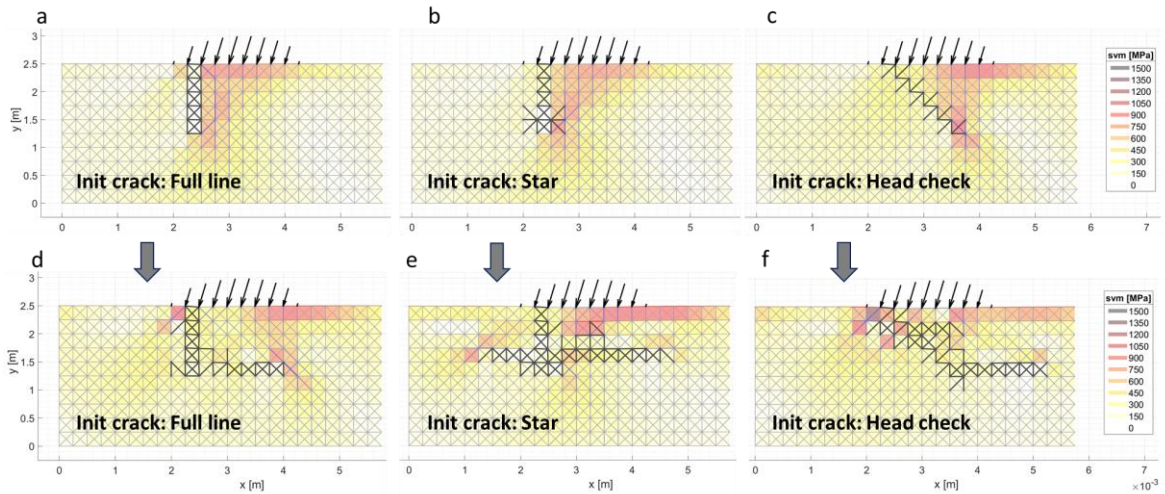


**Figure 62 - Initial set-up (top line) and results (bottom line) of a variation of the initial crack definition: Failed elements are marked in black.**

The set-up with the full line developed in a conventional way (see Figure 62 d). The main crack proceeded from the initial crack tip straight to the right, which agreed with the reference (see Figure 61 b). Obviously, the softening of the initial crack had no impact on the orthogonal FCG. A difference between the result and the reference was that the latter exhibited the tendency for more elements to fail above of the main crack. This effect was associated to the closeness of the surface, which was reduced by the elongation of the initial crack in this study.

The star type pattern resulted in the formation of two straight cracks, a primary one to the right and a secondary one to the left (see Figure 62 e). Both cracks had a linear shape, representing orthogonal FCG. With respect to the reference (see Figure 61 b), this initial crack type promoted the growth of the secondary crack. An interesting aspect is that a crack branched from the primary crack to the surface, which was facilitated by the increased depth of the initial crack. Due to the limited depth of the reference in combination with the surface boundary condition, a cluster of failed elements emerged rather than a single crack (see Figure 61).

The head check type generated two distinct main cracks running in parallel to the surface (see Figure 62 f). Both cracks are comparable to the one of the reference case. Furthermore, a branched crack between the two cracks emerged.

The result of all three cases suggests that preferred FCG directions are an inherent characteristic of the model. This is in contrast to an isotropic FCG behaviour, which was assumed initially (see section 5.1). This characteristic might be reduced by a refinement of the grid (see section 5.2.3).

In summary, the results of Figure 62 evidence that the effect of orthogonal FCG is not caused by the definition of the initial crack. The latter, though, has a major impact on the resulting FCG pattern. In the next step, the influence of the discretisation on orthogonal FCG is assessed (see section 5.2.3).

### 5.2.3 Study of grid discretisation

The results of the RCF simulations revealed a tendency for orthotropic FCG to occur (see section 5.2). In order to better understand this effect, the lateral boundary condition (see section 5.2.1) and the initial crack definition (see section 5.2.2) were analysed. However, neither the lateral boundary condition nor the initial crack definition were identified to be the reason for the orthotropic FCG. The next issue to be analysed regarded the grid discretisation, which is assessed in this section.

Generally, a grid refinement facilitates a better resolution of numerical results. Thus, the expectation was that a refinement of the grid would lead to a reduced degree of orthotropic FCG. In order to scrutinise this hypothesis, a reference solution with a standard grid was required. Therefore, a grid width of  $5a$  was selected (see section 5.2.1), which resulted in a  $23 \times 10$  grid of 230 modules. A unit length of  $l_0 = 2.5e^{-4}m$  and an initial crack depth of  $l_{init} = 7.5e^{-4}m$  were adopted. The initial crack was defined to be of type "full line" (see Figure 62 a).

The refined grid was designed to have the same overall dimensions. For the scaling, a factor 0.4 was applied so that the unit length was reduced to  $l_0 = 1e^{-4}m$ . This resulted in a  $57 \times 25$  grid containing 1425 modules, which corresponded to 620% of the module number of the reference. The initial crack depth was approximated by  $l_{init} = 8e^{-4}m$ .

In this way, the two simulation cases (reference and refined) were set-up. The results are displayed in Figure 63. The scope of the study was the analysis of the FCG patterns, not of the stress fields. As a result, the difference between load positioning with respect to the crack position can be neglected.

The results revealed that the orthotropic FCG prevailed for the reference as well as for the refined grid (see Figure 63). There was no major difference of the FCG patterns. Minor differences occurred on the top of the primary crack, and on the tip of the initial crack where the secondary cracks branched. With respect to this study, though, these differences were neglected. In summary, the results suggested that the discretisation had no impact on the orthotropic FCG behaviour, at least not for the employed level of grid refinement.

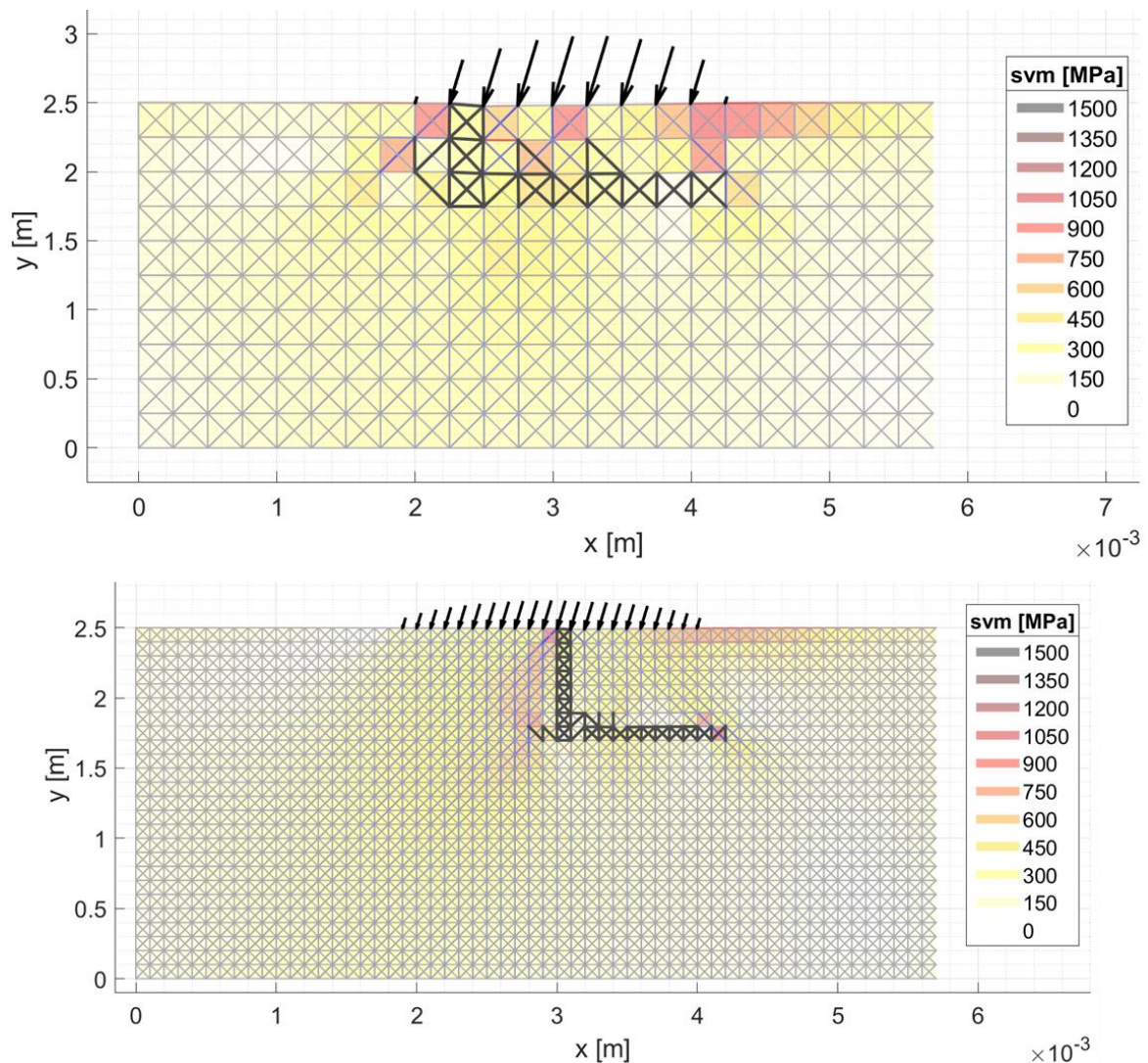


**Figure 63 - Results for different grid discretisations: The reference grid is illustrated above, the refined grid below. Failed elements are marked in black, elements under compression in blue and under tension in red.**

Finally, the numerical performance was assessed. For this purpose, the processing times per rolling contact cycle were compared. The reference grid required about 2 minutes, whereas the refined grid took approximately 2 hours per cycles, which is a difference of factor 60. As a result, another grid refinement was considered carefully. However, the convergence behaviour for the refined grid, which exhibited many more failed elements than the reference, was satisfactory.

The conclusion was that the effect of orthotropic FCG was not caused by the lateral boundary condition, the initial crack definition, or an insufficient grid discretisation. It is possible that an even more advanced grid refinement could



reduce the effect. This, though, could not be evaluated due to the limited numerical performance and the available computing power. In the next step, the influence of the tangential load was assessed (see section 5.2.4).

#### 5.2.4 Study of coefficient of traction

In this section, the impact of the applied tangential load on the effect of orthotropic FCG (see section 5.2) was evaluated. As full sliding was assumed, the coefficient of friction,  $\mu$ , was varied.

The  $23 \times 10$  grid from section 5.2.2 with a unit length of  $l_0 = 2.5e^{-4}m$  was adopted. The initial crack length was set to  $l_{init} = 1e^{-3}m$  to reduce surface effects. An initial crack of standard type was applied (see Figure 64 a).

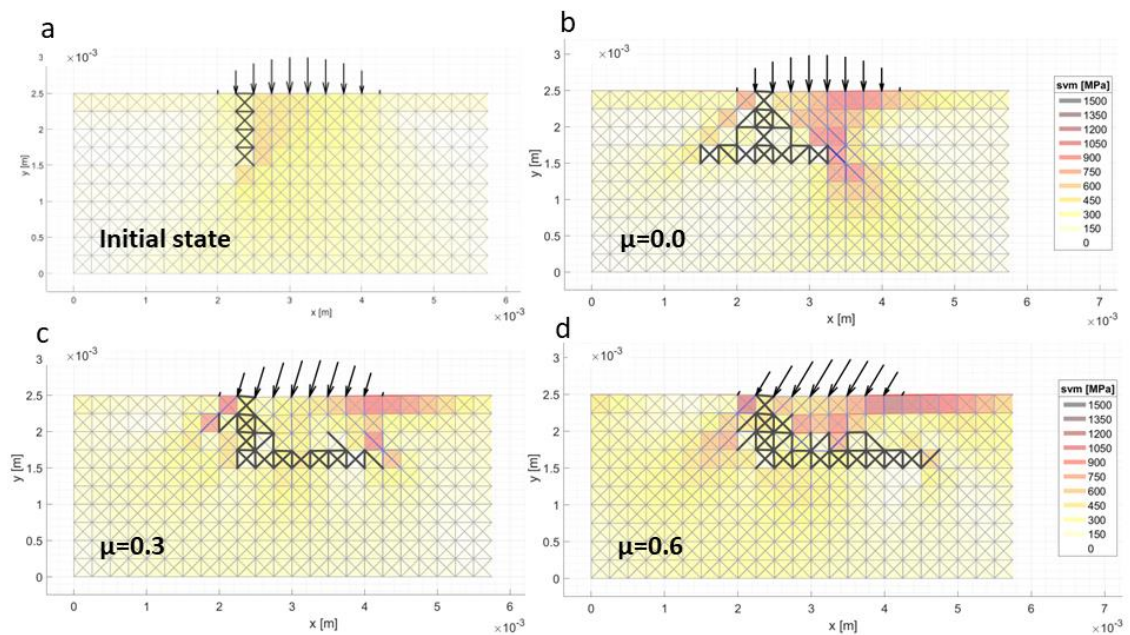


**Figure 64 - Initial set-up (a) and results (b - d) for different coefficients of friction  $\mu$ : Failed elements are marked in black, elements under compression in blue and under tension in red.**

For the applied load, a normal component of  $p_0=555 MPa$  was set as in the previous sections (see sections 5.2.1 - 5.2.3). Regarding the tangential load, full sliding was assumed and a variation of the coefficient of friction,  $\mu$ , was performed. In this way, the cases of pure rolling  $\mu=0$ , moderate traction of  $\mu=0.3$  and highest traction of  $\mu=0.6$  were implemented.

For the case of pure rolling, two primary cracks branched from the initial crack tip and proceed straight to the right and left (see Figure 64 b). This result corresponded to an orthotropic FCG. Additionally, cracks between the initial crack and the primary cracks emerged.

For moderate traction (see Figure 64 c), the primary crack demonstrated basically the same FCG pattern seen in the previous studies (see sections 5.2.1 and 5.2.3). This was also the case for high traction (see Figure 64 d). Though, an interesting aspect of the case of high traction was that also close to the initial crack and above of the primary crack several elements failed. This resulted in an FCG pattern that resembled the primary crack path of the original experimental reference (see Figure 47), where the crack grew with an angle of 30° to 45° degree with respect to the surface.

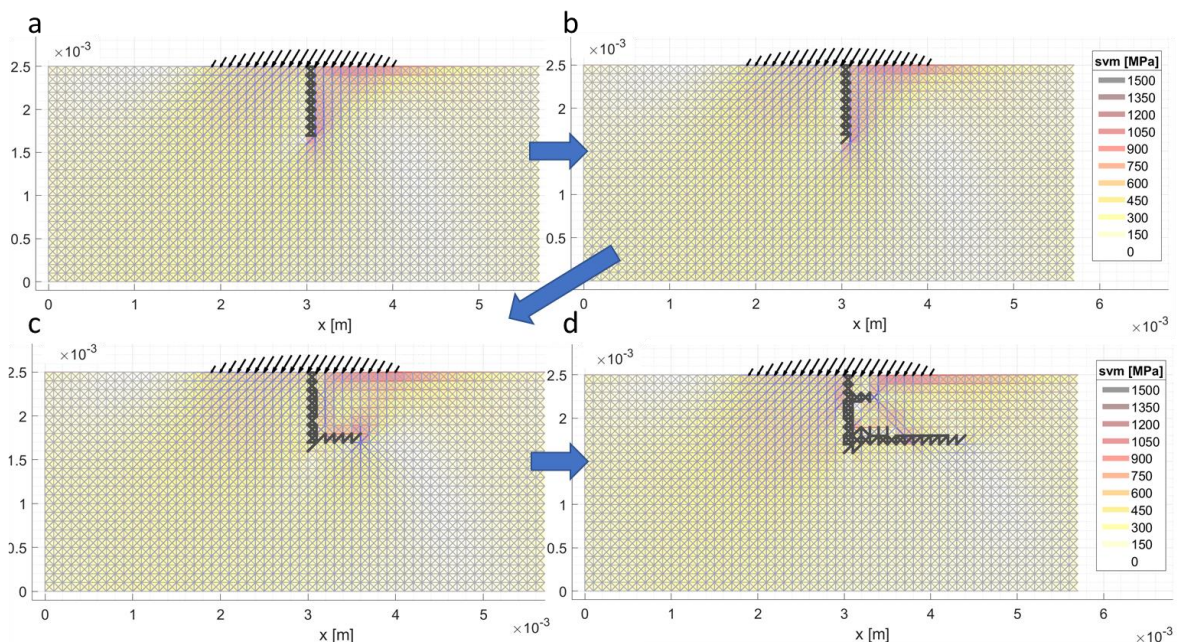


**Figure 65 - Initial set-up (a) and sequence of progress (b - d) for a coefficient of friction  $\mu=0.6$ . Failed elements are marked in black, elements under compression in blue and under tension in red.**

This finding suggested that for the case of high traction, a "less orthotropic" FCG pattern may be possible for a finer grid discretisation. Thus, the refined grid of section 5.2.3 was adopted (see Figure 63 below) and high traction load of  $\mu=0.6$  was applied in order to assess this configuration.

A sequence of results is displayed in Figure 65. The first element to fail was a diagonal below the initial crack (see Figure 65 b), which was a first indication of a non-horizontal FCG path. However, the next elements to fail followed the same pattern of orthotropic FCG (see Figure 65 c - d). This indicated that a crack propagated much faster along a horizontal path than along a vertical or more organic path. In other words, the horizontal FCG overruled potential alternative FCG paths.

Additionally, a second crack branched from the initial crack close to the surface (see Figure 65 d). It propagated in the same orthotropic way as the primary crack.

These results suggested that also the tangential load, in combination with a refined grid, was not the cause for the effect of orthotropic FCG, but that the effect was rather inherent to the model. A major aspect, though, regarded the way the elements were FCG activated as part of the FCG process (see Figure 37). This aspect is evaluated in the next section (see section 5.2.5).

#### **5.2.5 Study of FCG activation**

In the previous sections 5.2.1 to 5.2.4, various factors and their contribution to the model's tendency to orthotropic FCG behaviour, i.e. the fatigue crack growth along the main directions of the DEM grid, were assessed. No factor was identified to have a significant contribution. In the last step, the impact of the FCG activation (see section 5.1.3) on the inherent directional FCG is investigated.

With respect to the previous studies, an analysis was performed initially for an RCF case. Afterwards, a Mode I analysis was added. For the RCF analysis, the test case of section 5.1.7 (full-scale test rig) with a Hertzian load of  $p_0 = 555 \text{ MPa}$  and a coefficient of friction of  $\mu = 0.3$  was adopted. The standard initial crack type (see Figure 48, Figure 49) was set, and the refined grid of section 5.2.3 was applied. This set-up was run for the simplified- (see Figure 40) and the original FCG activation (see Figure 41).

The result for the simplified FCG activation is displayed in Figure 66. It features the familiar FCG pattern where the primary- and secondary cracks propagated on a strictly horizontal path. This is the reference for the comparison.



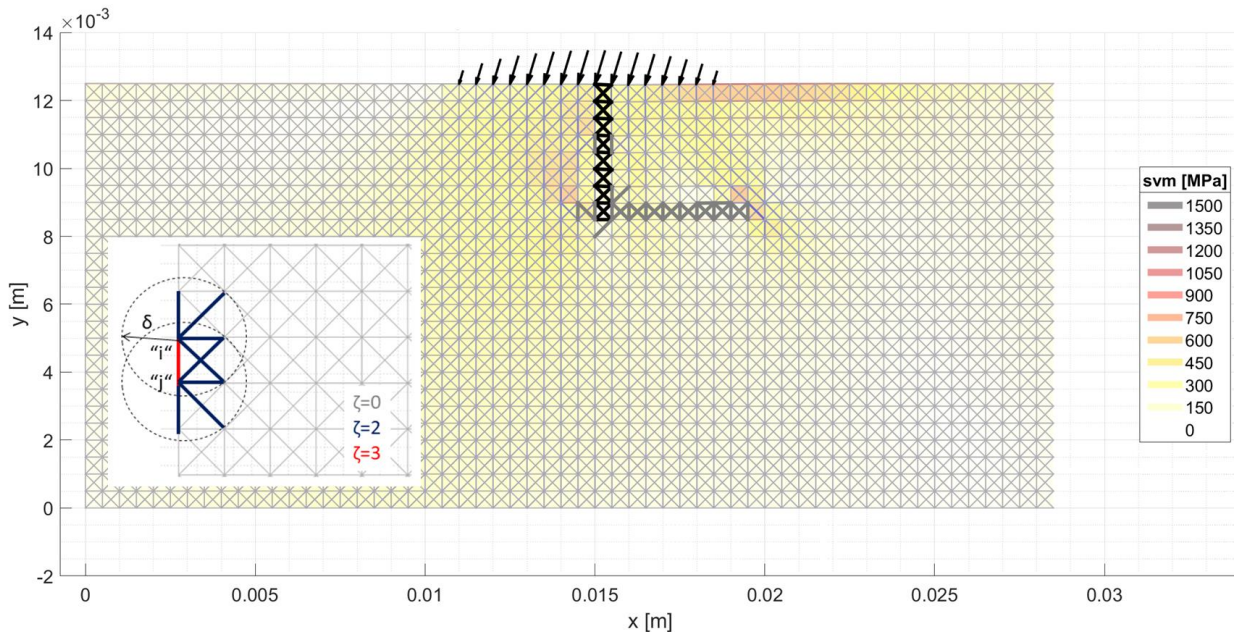


Figure 66 - RCF result for the simplified FCG activation (main figure): Initially failed elements are marked in black, successively failed elements in grey, elements under compression in blue and under tension in red. The principle of FCG activation is displayed in the subfigure.

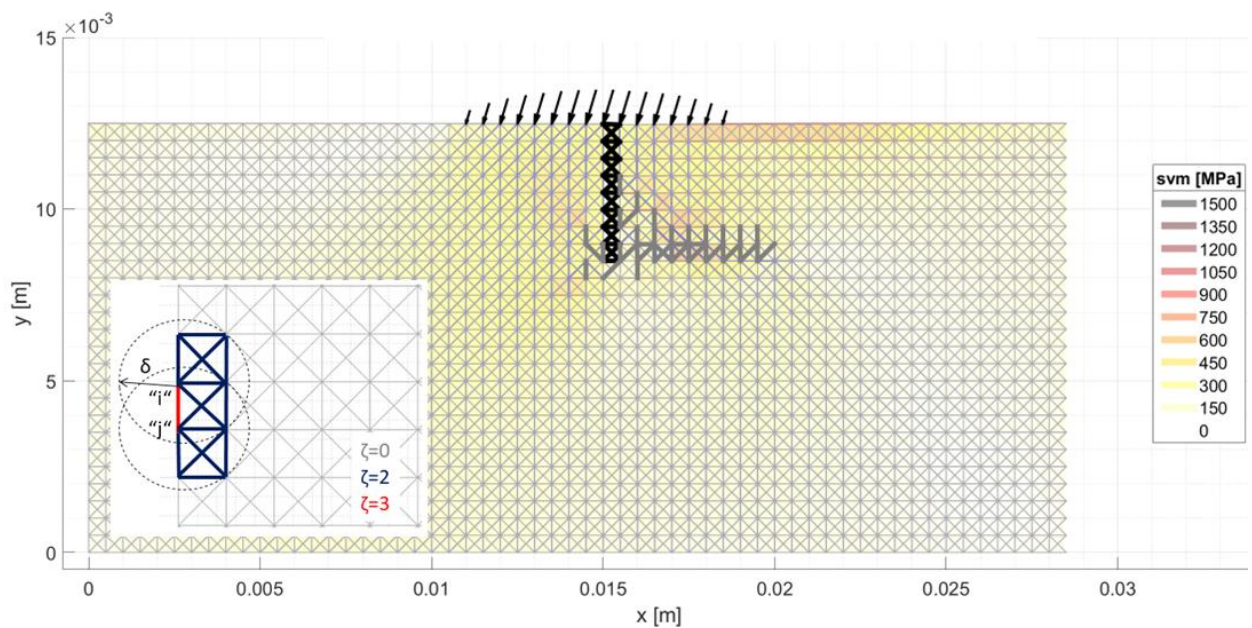


Figure 67 - RCF result for the original FCG activation (main figure): Initially failed elements are marked in black, successively failed elements in grey, elements under compression in blue and under tension in red. The principle of FCG activation is displayed in the subfigure.



The result for the original FCG activation, where all elements within the horizon of a failed element are activated, is displayed in Figure 67. The primary crack basically grows at the same horizontal path as the reference (see Figure 66). However, at the root of the primary crack there is a smoothing that fits to the initial crack. This gives the primary crack a certain deviation from the orthogonal crack pattern, which is seen to be an improvement.

The secondary crack has a less distinctive appearance than that of the reference (see Figure 66), which at this stage of the crack development does not matter. An interesting aspect is that below the initial crack there is a cluster of failed elements. This is at least an indicator that the crack potentially can grow into the depth of the material, which is observed in the experiment, but not in the results of the simplified FCG activation (see Figure 66).

In summary, the pattern of the original activation still tends to orthotropic FCG for the RCF condition, but it is reduced compared to the simplified activation. With respect to the experimental result (see Figure 47) it can be stated that the grid discretisation is still not sufficient to resolve the crack development around the initial crack tip. However, the result of the original FCG activation suggests this method to be more capable of resolving the observed pattern (see Figure 47).

In a second attempt, the FCG activation methods were analysed for a Mode I case. The experimental work of Leitner et al. (5) was adopted as a reference for the specimen layout, with a width of the specimen,  $W_{exp} = 5.4 \text{ mm}$ , and an initial crack length,  $a_{cr} = 1.3 \text{ mm}$ . Further dimensions were derived with respect of the ASTM standard E647 for a specimen of C(T) type (16). With regard to the reference, the grid was reduced laterally to gain an efficient processing (see Figure 68).

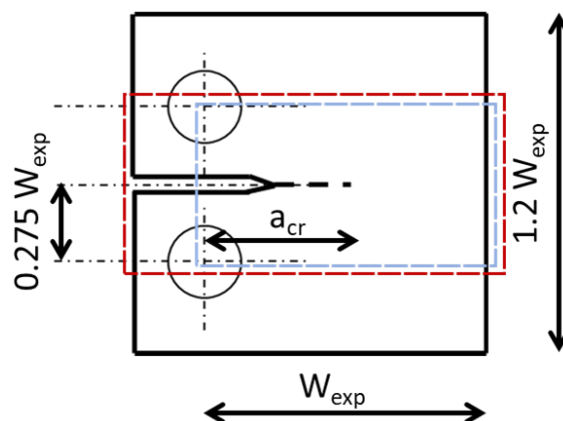


**Figure 68 - C(T) type specimen with dimensions, modified from (16). The reduced grid is illustrated by the dashed blue frame, the extended grid by the red dashed line.**

A floating boundary condition was applied to the bottom nodes. The external load was applied continuously along the surface (see Figure 69). The reference derived by the simplified FCG activation is displayed in Figure 69. The familiar straight horizontal pattern is illustrated. A few outliers of failed elements exist.

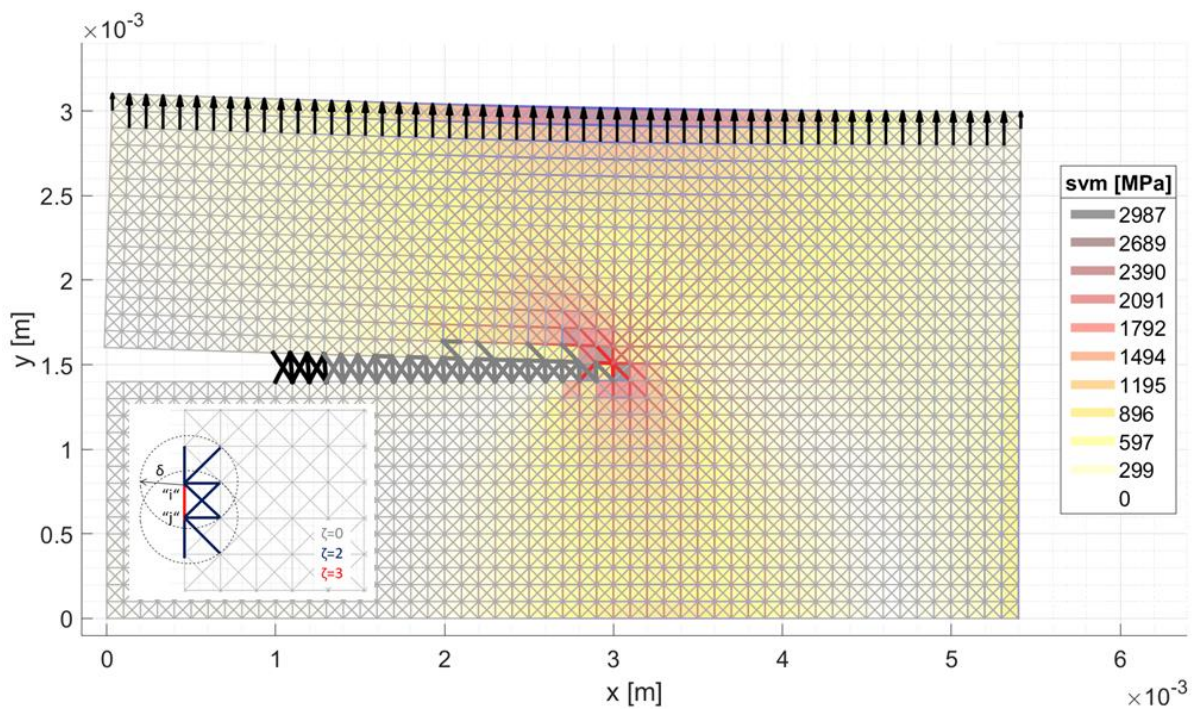


**Figure 69 - Mode I result for the simplified FCG activation (main figure): Initially failed elements are marked in black, successively failed elements in grey, elements under compression in blue and under tension in red. The principle of FCG activation is displayed in the subfigure.**

Regarding the result of the original FCG activation, a similar crack pattern was expected. However, the result demonstrated a remarkable FCG pattern (see Figure 70). The crack propagated in a directed way, i.e. there is a continuous crack and a distinctive crack tip. The sequence of element failures suggested that there was no preferred relative orientation of the elements (diagonals, verticals, horizontals). The crack deviated by approximately 30° from the horizontal axis, which is in contrast to the existing RCF- and Mode I results. It can be seen that the crack followed the gradient of the highest strains. The FCG pattern suggested a basically isotropic FCG pattern, where the crack direction is not governed by the grid, but by the prevalent strain field.

This highlighted that the full-horizon FCG activation (see Figure 70, subplot) has a significant impact on the quality of the FCG behaviour. It made the FCG process more sensitive, as the number of available elements to fail was increased by 50%.

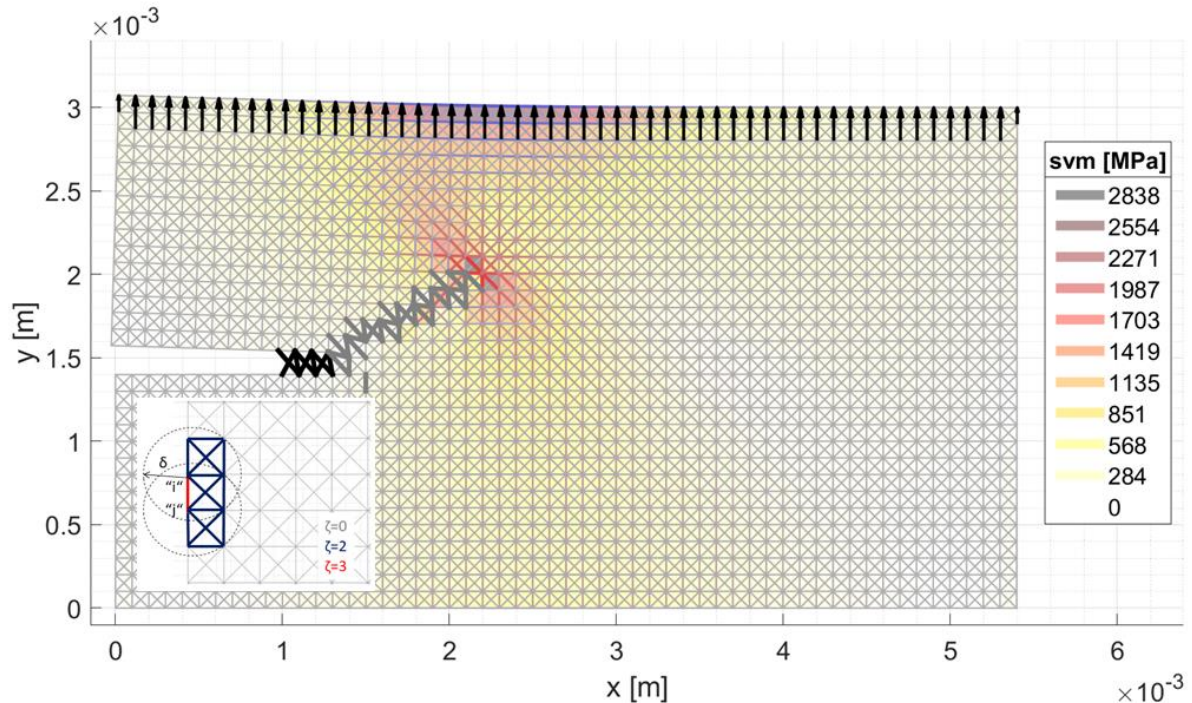


**Figure 70 - Mode I result for the original FCG activation (main figure): Initially failed elements are marked in black, successively failed elements in grey, elements under compression in blue and under tension in red. The principle of FCG activation is displayed in the subfigure.**

This finding, however, gave rise to the question as to why there is a crack deviation of  $30^\circ$ , which is not the case for the experimental result (5) where the crack grew perpendicular to the applied load. The answer was suspected to be the type of boundary condition and the applied load, as the set-up of Figure 69 and Figure 70 disagreed with the arrangement of the experiment (see Figure 68). There, the applied load and the support were transmitted by a 2-hole support.

In the next step, the external load,  $p_0 = 100 \text{ MPa}$  and  $R = 0.5$ , plus a fixed boundary condition were applied to the specific nodes that resembled the 2-hole support of the experimental specimen (see Figure 68). The grid was extended laterally to reduce the effects introduced by the discrete load and support (see Figure 68). The updated result confirmed the assumption that the load and the boundary condition deviated the crack in Figure 70, as the crack grew perfectly



along the horizontal path (see Figure 71), based on the full-horizon activation. It emphasised the improved sensitiveness of the FCG capability, as it better resolved the impact of the mechanical constraints (see Figure 70) than the simplified method (Figure 69). The latter demonstrated the degree of constraint imposed to the FCG behaviour.

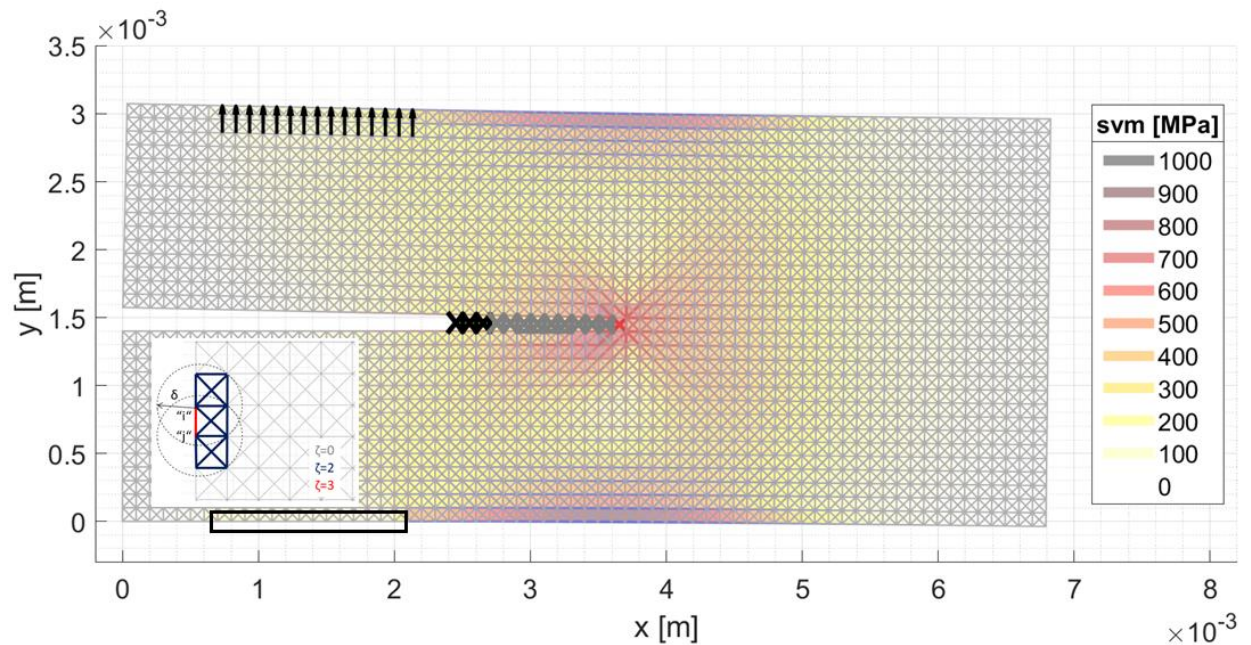


**Figure 71 - Mode I result (main figure) for the original FCG activation with modified load (top) and boundary condition (black frame): Initially failed elements are marked in black, successively failed elements in grey, elements under compression in blue and under tension in red.**

Another aspect of the extended grid (see Figure 71) concerned effects on the top and bottom of the grid, where stress maxima occurred. These were attributed to a lack of "material" above and below of the grid (see Figure 68), which was cut for efficiency reasons. Regarding the basic FCG behaviour, these effects are assumed to be negligible. Though, with regard to a parameterisation, the edge effects must be eliminated.

A retrospective of the study in section 5.1.3 was performed to clarify why the initial results suggested the simplified FCG activation to be preferred. It revealed that a combination of insufficient initial crack definition and high load led the model based on the original activation to fail in an abnormal way (see Figure 41), whereas the restraint of the simplified FCG activation forced the crack to proceed in a more

conventional way (see Figure 40). This led to a misinterpretation at the initial stage (see section 5.1.3). The impact of this fact is discussed in the final assessment of the model (see section 8.3).

In summary, two methods of FCG activation were assessed in order to determine the tendency to orthotropic, non-isotropic FCG behaviour. This was done through RCF- and Mode I case studies. The method with a full-horizon FCG activation, which was proposed in the literature, proved to have a superior resolution of the FCG process.

For the Mode I simulation, this indicated an isotropic FCG pattern. By means of the full-horizon FCG activation, shortcomings of Mode I simulations with respect to the boundary conditions, load application and grid layout were identified and partially rectified. For the RCF simulation, the tendency to orthotropic FCG was reduced. Though, further improvements may be gained by a grid refinement.

This promotes the full-horizon FCG activation to be adopted to the model.

#### **5.2.6 Study of grid orientation**

The overall goal of section 5.2 is to understand the influence of the grid on the FCG behaviour. One consideration regards the question if all element types (horizontal, vertical, diagonal) have the same susceptibility to fatigue, which is a precondition for the assumption of isotropic FCG. This assumption would ease the introduction of anisotropic FCG (see section 8.2).

The aim of this section is to find out if there are preferably strained element types, as strain is the driving force for FCG (see Equation 39, Equation 40), and to discuss the implications for RCF modelling.

The working hypothesis was that the element type, which is aligned to the direction of the applied load, takes the majority of the strain. This implied that there is no preferred element type which tends to take more strains than others. In order to test the hypothesis, a simple test case under uniaxial tension load was applied.

A squared model was defined, which was set up by two differently oriented grids, a reference grid of 0° rotation (standard grid, "ref") and a tilted grid of 45° rotation ("rot"). The reference grid was modelled by a simple 5 x 5 arrangement to ease the strain analysis (see Figure 72 left).

For reasons of simplicity, the rotated grid was cut out of a standard grid (0° rotation) by the removal of elements (see Figure 72 right). Thus, the lateral edges were constituted by diagonal elements, and the "diagonals" of the rotated grid consisted of horizontal and vertical elements. In this way, the same nomenclature

of element types from the reference grid was adopted to the rotated grid. In order to obtain the same edge lengths established by five elements, a reduction of the unit length,  $l_{0\_rot}$ , with respect to the reference length,  $l_{0\_ref}$ , was required, as the edges of the rotated grid were modelled by diagonals. This required a specific diagonal length,  $l_{diag\_rot}$ .

$$l_{diag\_rot} = l_{0\_ref}$$

**Equation 60**

By triangulation with Pythagoras' law and with Equation 60, a relation for the unit length of the rotated grid,  $l_{0\_rot}$ , was derived.

$$l_{0\_rot} = \frac{\sqrt{2}}{2} l_{diag\_rot} = \frac{\sqrt{2}}{2} l_{0\_ref}$$

**Equation 61**

Consequently, a discretisation with a modified unit length,  $l_{0\_rot}$ , required an update of the elastic calibration to derive the elasticity parameter,  $c_{rot}$ , which was performed in accordance with the procedure specified in section 5.1.6. Further, the reduced discretisation implied an increase in the number of elements. A summary of the grid set-up is displayed in Table 11.

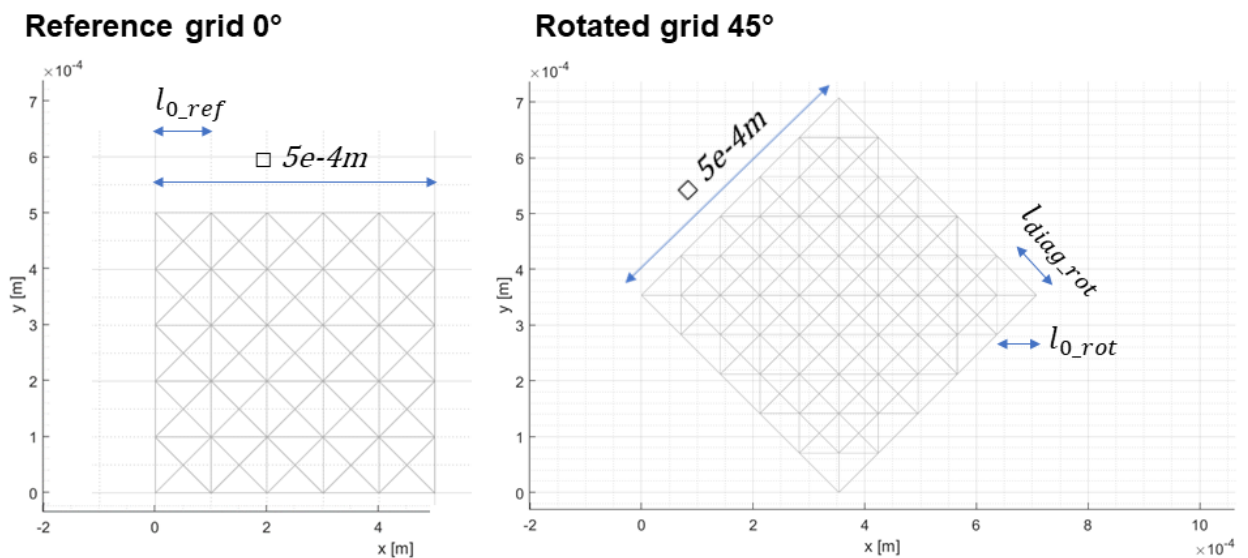


**Figure 72 - Assembly of the reference grid (0° rotation, left) and the rotated grid (45° rotation, right). The unit lengths,  $l_0$ , are marked.**

	Reference grid	Rotated grid
Rotation	0°	45°
Lateral grid width (m)	5e-4	5e-4
Unit length, $l_0$ (m)	1e-4	7.07e-5
Elasticity coefficient $c$ (N/m)	1.55e7	1.07e9
Number of elements (-)	110	200

**Table 11 - Grid set-ups for the reference- and the rotated grid.**

In this way, the two grids were set up. An arbitrary load of 40 MPa was applied to the nodes of one edge. A fixed boundary condition (see section 4.7) was applied to the nodes of the opposite edge. For the strain analysis, a focus area was defined for both grids to assess elements of the central region, but to omit elements of the edges to avoid edge effects. A common reference for the strain- and stress visualisation was adopted. The result for both grids is illustrated in Figure 73.

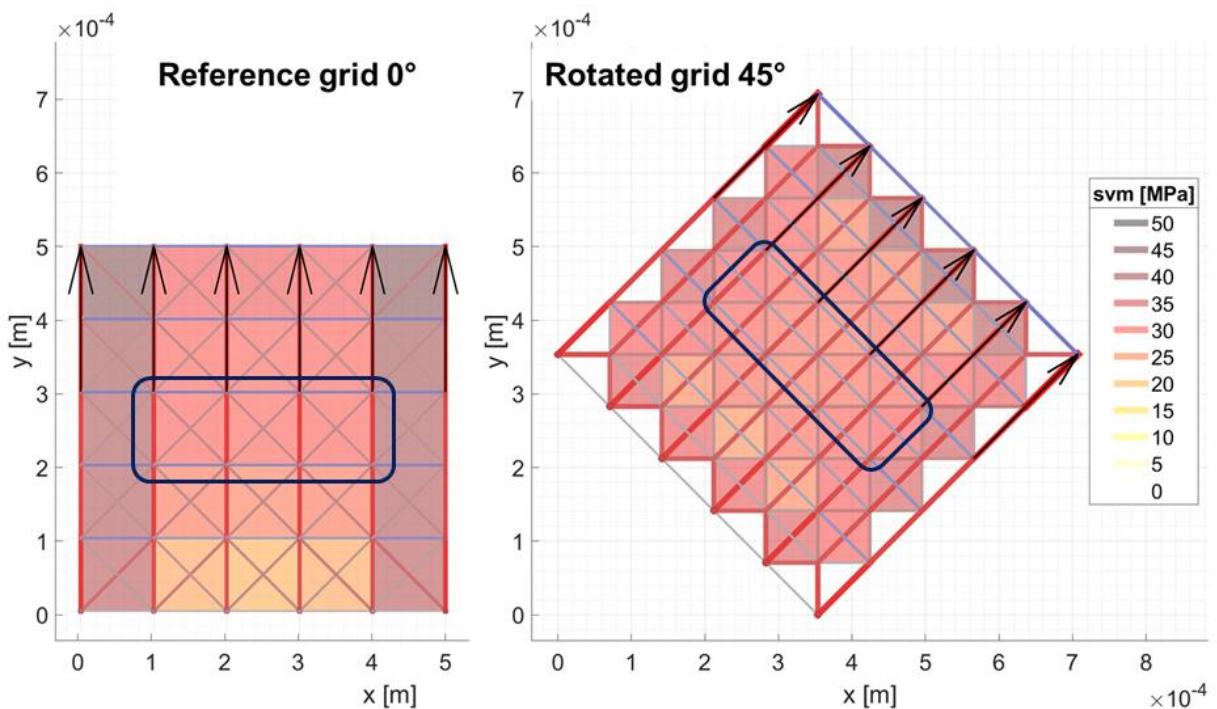


**Figure 73 - Tension test for the reference- (left) and the rotated grid (right). The focus areas for the strain analysis are marked by the blue frames. A fixed boundary condition was applied to the nodes opposite to the loaded nodes (black arrows). Elements strained in tension are marked red, those in compression blue.**

The stress visualisation of both grids indicated stress minima on the bottom of the grids and stress maxima on the edges. The former resulted from the fixed boundary conditions that limited the node displacements and strains, the latter from the higher degree of freedom of the edge nodes. Within the focus areas, however, a homogeneous stress distribution prevailed, which confirmed the definition of these areas (see Figure 73).

For the reference grid, the vertical elements bore the main strains (see thick red lines, Figure 73, left). The horizontal elements accounted for the lateral contraction, i.e. Poisson's effect. The diagonal elements acted as a support of the vertical elements and are much less strained.

For the rotated grid, this distribution shifted as the horizontal- and vertical elements had the supportive role, which the diagonals had in the reference grid (see Figure 73, right). The major tensile strains were supported by diagonal elements oriented along the direction of the applied force, which was performed by the verticals in the reference grid. The diagonals orthogonal to the direction of the applied force resisted the lateral contraction, which was performed by the horizontal elements in the reference grid.

The results suggested that the distribution of the strain field depended primarily on the orientation of the element type with respect to the direction of the applied load. The results did not reveal an element type which was strained preferably, which agreed with the finding of Figure 70 (see section 5.2.5). This promoted the working hypothesis. The grid orientations that were not covered by the study were assumed to behave accordingly.

A quantitative analysis of the strains could have answered the question of preferred element types in more detail. However, for the performed approach, this was not permitted due to different elasticities. In order to facilitate a quantitative comparison, a rotated grid of the same elasticity and the same number of elements was required. Within the frame of thesis, however, the qualitative analysis was considered to be sufficient, which suggested the assumption of the grid to be isotropic.

With respect to the modelling of anisotropy of FCG (see section 0), the finding was relevant. If the strain distribution of a grid does not prefer a specific element type, the grid's behaviour can be assumed to be isotropic. Based on this assumption, an anisotropy can be introduced to the elements of the grid, without any consideration of the element types.



In the next step, the implication of that finding for the modelling of RCF with grids of the reference type was evaluated. The impact of the tangential load, which was characterised by a coefficient of friction,  $\mu$ , was expected to determine the mostly strained element type. For a pure normal load, i.e. the case of  $\mu = 0$ , the vertical elements were expected to bear the majority of the strain load. For an increase of the tangential load, i.e.  $\mu > 0$ , the diagonals were expected to bear an increasing amount of strain.

In summary, the outcome of the grid study was that the strain field and its distribution with respect to element types developed according to the main loading direction. Based on a qualitative analysis, no element types were identified which sustained more strain than others. This suggested that the strain field and the associated FCG development depended on the applied load, not on the grid. This finding promoted the assumption of an isotropic grid, which was a precondition for a modelling of anisotropic FCG (see section 8.2).

## 6 PARAMETERISATION OF FATIGUE CRACK GROWTH

The RCF model was introduced in section 5.1. Its inherent FCG characteristic was assessed in section 5.2. In both sections, the qualitative FCG and RCF behaviour was evaluated, and the required FCG parameters  $A_2$  and  $m_2$  (see Equation 39) were assumed. In the next step, the FCG rate defined by the FCG parameters  $A_2$  and  $m_2$  was parametrised with respect to experimental data to get a quantitative fit. The applied procedure is displayed in Figure 74.

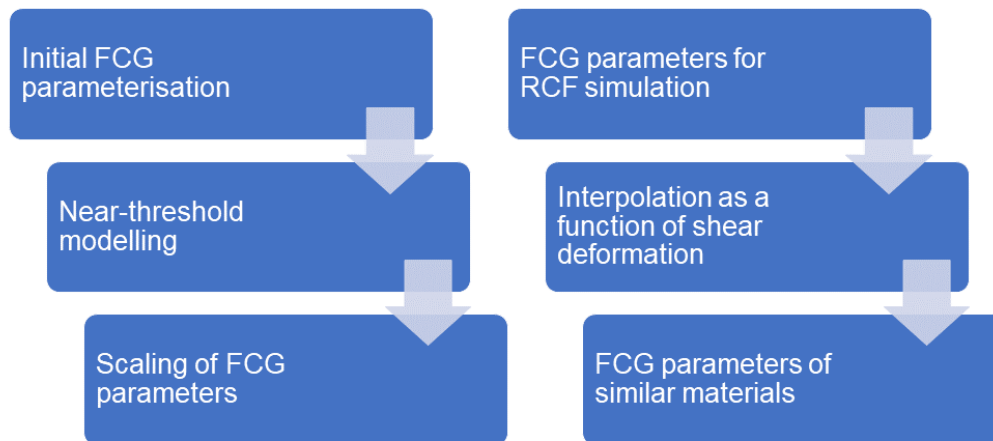


Figure 74 - Overview on the procedure to parameterise the FCG model.

Initially, this was performed for FCG Stage II (see section 6.1), i.e. the Paris stage (see Figure 8). For the RCF modelling, though, the near-threshold stage was relevant as well, which was addressed in section 6.2. The impact of different grid discretisations on the FCG parameters was addressed in section 6.3. A selection of relevant material classes for the simulation of RCF was performed in section 6.4. An interpolation function was required (see section 6.5) to assign FCG parameters to the grid as a function of shear deformation (see section 7.2). Finally, the set-up of these classes based on the R260 rail steel was transferred to the similar R350HT steel in section 6.6.

### 6.1 Initial FCG parameterisation

For the modelling of RCF, the assumption of isotropic FCG generally does not apply due to the occurrence of SPD (see section 2.1.1). This promotes an anisotropy of RCF (see section 2.1.4) resulting in different FCG orientations, which

is addressed by the work of Leitner (14). With regard to these findings, different FCG orientations must be considered for the modelling.

The aim of this section was to identify relevant material classes based on different FCG orientations to model RCF, and to perform a parameterisation to calibrate the material classes by the parameters  $A_2$  and  $m_2$ .

Leitner (14) produced severely plastically deformed samples by means of the HPT technique (see section 2.1.1). Out of these samples, FCG specimens were cut (see Figure 75, left). The specimens represent specific FCG orientations of deformed pearlitic steel, which is characterised by an alignment of ferrite-cementite lamellae (see Figure 75, right). The orientations were classified with respect to an axis system that refers to axial-, radial- and tangential directions. A classification was introduced, where the first letter describes the plane orthogonal to an axis, within which the crack proceeds. The second letter describes the FCG orientation (see Figure 75).

The DERC model represents a semi-infinite rail- or wheel section (see section 4.5). By the consideration of SPD, relevant FCG orientations were identified to be A-T and T-A (see Figure 75, right). According to Leitner's results, the former exhibits the fastest FCG rates, whereas the latter corresponds to the slowest rates. Somewhere between, the rate of the T-R orientation is positioned, which was adopted as an intermediate FCG orientation. These three orientations were selected to be parametrised.

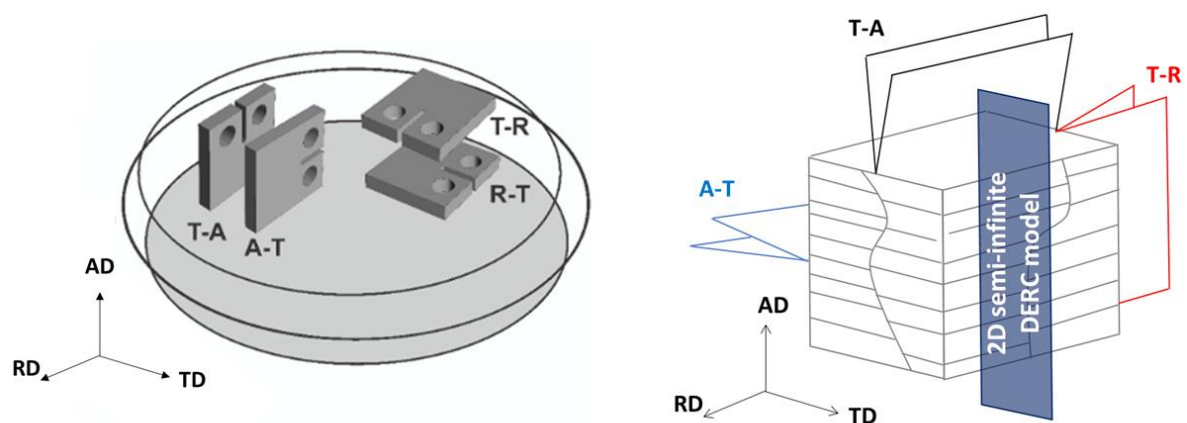


**Figure 75 - HPT sample with FCG specimen orientations (left). Illustration of FCG orientations of a deformed pearlitic material, where aligned ferrite-cementite lamellae are displayed (right). The axes refer to the axial-, radial and tangential directions. Both figures were modified from (5).**

Due to the availability of data, R260 steel was adopted for the initial parameterisation as a standard material. Regarding the applied stress ratio  $R$ , the data of  $R = 0.1$  was selected.

Another parameter varied by Leitner regards the degree of shear deformation, which can be described by the Von Mises strain,  $\varepsilon_{VM}$ , that is detailed in section 7.2 (see Equation 94). For deformations of  $\varepsilon_{VM} = 1.2$  and  $\varepsilon_{VM} = 2.3$ , only minor deviations were identified (5). Thus,  $\varepsilon_{VM} = 1.2$  was selected for the parameterisation. Higher deformations of  $\varepsilon_{VM} = 17.3$  were neglected in the initial parameterisation.

In this way, three material classes R260\_C01 to R260\_C03 were defined, which are summarised in Table 12. Further, a reference class RXXX\_CXX was added, which was required for the parameterisation of  $A_2$  (see Table 12).

Material class	RXXX_CXX	R260_C01	R260_C02	R260_C03
Material	Reference	R260	R260	R260
Deform. $\varepsilon_{VM}$	---	1.2	1.2	1.2
Stress ratio $R$	---	0.1	0.1	0.1
FCG orientation	---	T-R	A-T	T-A
FCG param $m_2$	2.5	2.5	2.5	2.5
FCG param $A_2$	1800	670	1608	241

**Table 12 - Material classes to be parametrised: The resulting FCG parameters  $A_2$  and  $m_2$  are displayed in the last rows.**

For the experimental tests, Leitner applied specimens of the C(T) type according to ASTM standard E647 (16), which were adopted for the modelling. In order to avoid edge effects (see Figure 71), the full specimen was modelled (see Figure 76). The notch and an initial crack with a total crack length of  $a_{cr} = 0.0013 \text{ m}$  were modelled. The dimensions of length,  $W_{exp} = 0.0054 \text{ m}$  and width,  $B_{exp} = 0.0013 \text{ m}$  were adopted from Leitner et al. (5). A discretisation with a unit length of  $\Delta x = 1e - 4 \text{ m}$  was adopted.

The oscillating force and the support of the specimen were applied (see Figure 77) according to the two-hole-support of the experimental case (see Figure 76).

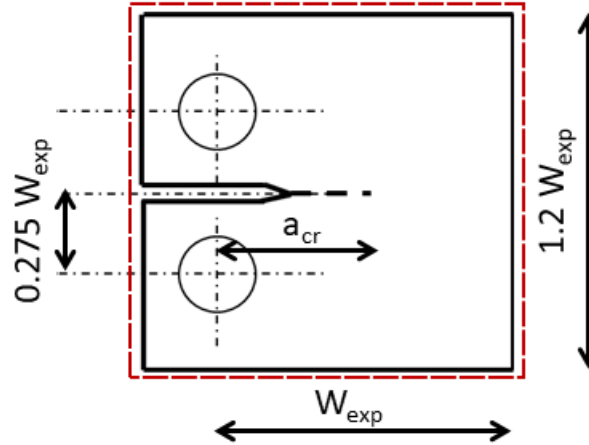


Figure 76 - C(T) type specimen with main dimensions, modified from (121). The modelled grid dimension is illustrated by the dashed red line.

The applied force was estimated from the experimental data. For each of the three data series, an initial point of Stage II was identified, i.e. a data point where the crack growth stabilises and increases in a linear way (start of FCG Stage II, see Figure 8). These points were defined by values of about  $\Delta K = 5 - 6 \text{ MPa m}^{0.5}$ . The crack length was assumed to equal that of the initial crack length,  $a_{cr} = l_{init}$ . The scope was to derive the applied force range,  $\Delta P$ , as a function of the specimen geometry and the crack length.

$$\Delta P = P_{max} - P_{min}$$

Equation 62

Thus, the equation to determine the stress intensity factor range  $\Delta K$ , given by the ASTM standard E647, was used and transformed for the derivation (16).

$$\Delta P = \frac{\Delta K B_{exp} \sqrt{W_{exp}}}{(2 + \alpha_a)} * \frac{(1 - \alpha_a)^{\frac{3}{2}}}{0.886 + 4.64 \alpha_a - 13.32 \alpha_a^2 + 14.72 \alpha_a^3 - 5.6 \alpha_a^4}$$

Equation 63

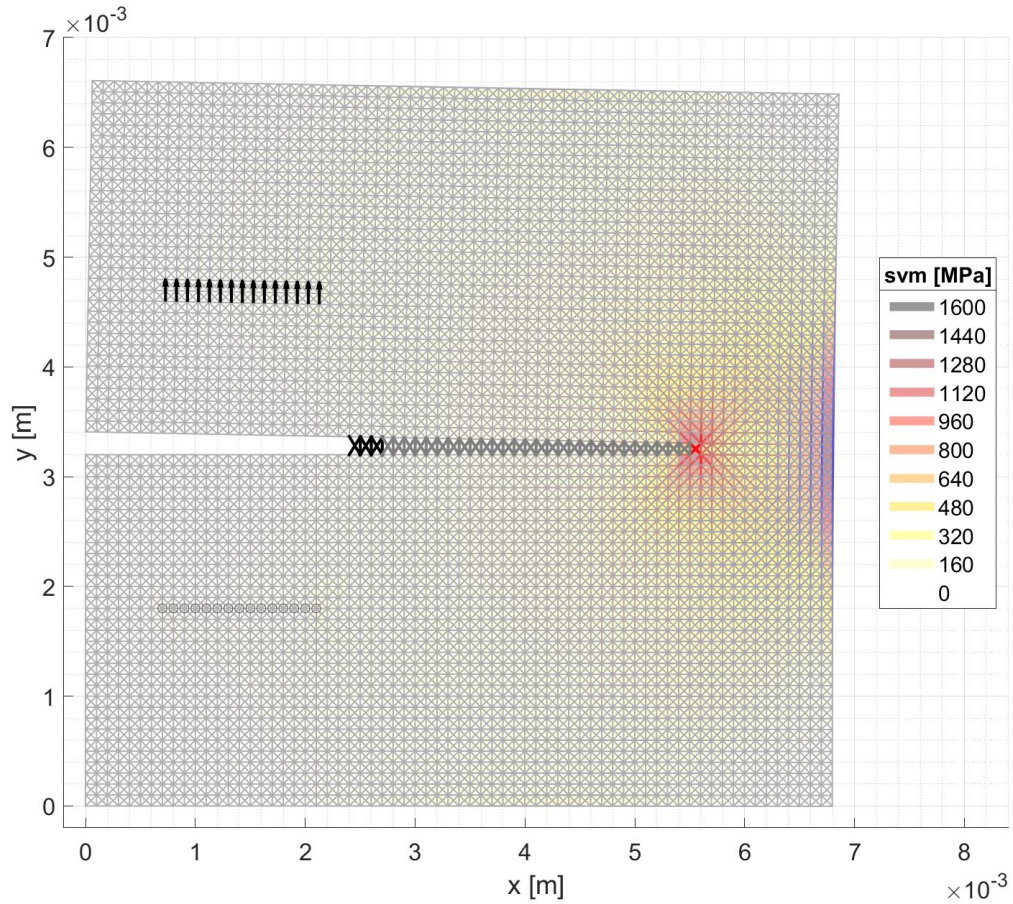


**Figure 77 - FCG parameterisation of class CG\_R260\_C01 (R260, T-R) by a 68x65 grid with an initial crack (black elements). Element strained in tension are marked red, in compression blue. The status of the crack advance (grey elements) corresponds to approximately 213.000 cycles.**

The factor  $\alpha_a$  describes the ratio between crack length,  $a_{cr}$  and specimen's main dimension,  $W_{exp}$ . According to the standard, Equation 88 is valid for  $\alpha_a > 0.2$  (16), which is given in this case.

$$\alpha_a = \frac{a_{cr}}{W_{exp}}$$

**Equation 64**

For the three cases, the force ranges were calculated to be between  $\Delta P = 99$  (N) for T-A and  $\Delta P = 119$  (N) for A-T. By combining Equation 62 with Equation 2, the maximum forces were derived to be between  $P_{max} = 111$  (N) for T-A and  $P_{max} = 133$  (N) for A-T.

$$P_{max} = \frac{\Delta P}{(1 - R)}$$

**Equation 65**

For reasons of simplicity, one force range was applied for the parameterisation of all three data series. Thus, the average of the two maximum forces,  $P_{max} = 122 (N)$ , was applied to the model (see Figure 77). This simplification is in contrast to experimental procedures (load rising- or shedding procedure), where the number of simulated cycles, i.e. the required time and costs, have to be considered. For the simulation, this issue was disregarded (see section 5.1.4), which facilitated the use of a constant load.

In the next step, the fatigue law (see Equation 39) was reviewed. According to Silling and Askari (49), the exponent  $m_2$  can be extracted directly from FCG (Paris-) diagrams, i.e. a diagram where the crack growth per cycle ( $da/dN$ ) is illustrated against the stress intensity factor range  $\Delta K$  in double logarithmic scale. This implies that the model's exponent  $m_2$  equals the exponent  $m$  of the Paris-Erdogan equation (see Equation 5).

According to Leitner, the FCG rate in a Paris diagram, which is characterised by the exponent  $m$ , can be estimated when there is information about the microscopic FCG mechanism available. If the mechanism of plastic deformation, resulting in a blunting and resharping of the crack tip, dominates the FCG process, then  $m = 2$  can be assumed. However, if the mechanism of damage accumulation dominates, then an exponent of  $m = 4$  is likely to occur. Leitner suggests the first mechanism to predominate for ductile steels like R260 (14).

Most of Leitner's experimental FCG results for deformed pearlitic steels support this assumption, but not all. Thus, Leitner summarised the exponent of HPT deformed R260 steels to be in a range of  $m = 2$  to  $m = 3$  (14). Ishida suggested the exponent of rail- and wheel steels to be in a range of  $m = 2.45$  to  $m = 2.64$ . Based on these findings,  $m$  was estimated to be constant at  $m = m_2 = 2.5$  for the parameterisation of all three material classes (see Table 12). The impact of the exponent  $m$  on the FCG curves is illustrated in Figure 78. The fitted data adopted from (14) is based on the assumption of  $m = 2.0$ , the model results on  $m = 2.5$ . The experimental data for the FCG orientations of T-A and A-T suggested to be better approximated by  $m = 2.0$ , whereas the data of T-R is better approximated by  $m = 2.5$ .

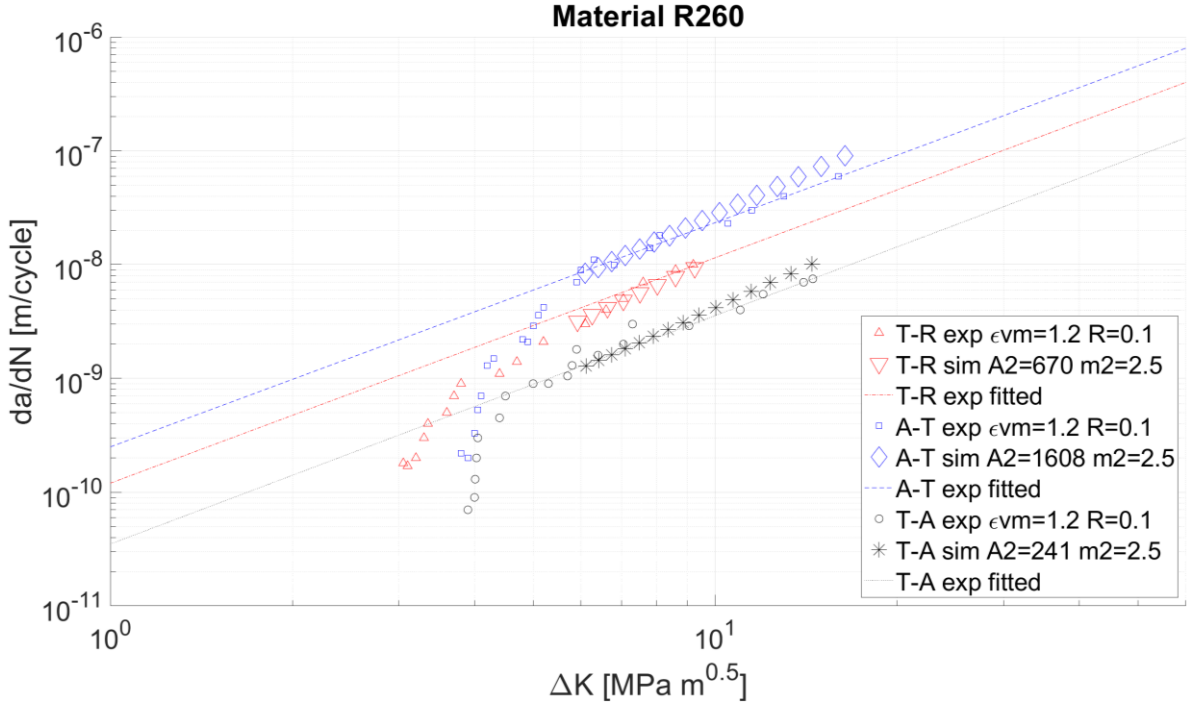


**Figure 78 - FCG diagram of three material classes (T-R, A-T, T-A): The experimental results from (14) are plotted against the simulated results (exponent  $m = 2.5$ ). Fitted lines from the experimental data (14) are added (exponent  $m = 2.0$ ).**

The second fatigue parameter,  $A_2$ , was derived with respect to the method given by Silling and Askari (49). They assumed an arbitrary parameter,  $A_2 = A'$ , which in this parameterisation was set to be  $A' = 1800$ . In this way, a reference material class was defined (see Table 12). With it, the FCG test was simulated and an initial crack growth rate of  $(da/dN)' = 1.84e-8$  (m/cycle) was calculated. Finally, the scaling formula of Silling and Askari and the initial crack growth rate from the experimental data,  $(da/dN)$ , was employed per material class to derive the second parameter,  $A_2$ . The resulting parameters for the three material classes are displayed in Table 12.

$$A_2 = A' \frac{da/dN}{(da/dN)'}$$

**Equation 66**

Another aspect of the Mode I test regarded the simulation of the maximum and the minimum increment. In order to reduce the computational effort, Silling and Askari simplified the case by processing exclusively the maximum increment, resulting in the maximum strains,  $\varepsilon^+$ . The strains of the minimum increment,  $\varepsilon^-$ , were estimated with respect to the maximum strains and the load ratio (49).



$$\varepsilon^- = R\varepsilon^+$$

Equation 67

This simplification was adopted. The resulting error was supposed to be negligible. In this way, the equation to determine the cyclic bond strain (Equation 40) was modified.

$$\Delta\varepsilon = |\varepsilon^+ - \varepsilon^-| = |(1 - R)\varepsilon^+|$$

Equation 68

With this set-up, the simulation series were run. One of the resulting stress figures of FCG orientation T-R is illustrated in Figure 77. The figures of all material classes exhibit the same layout. They only deviate in the required number of cycles to failure.

The quantitative behaviour is captured by the FCG diagram (see Figure 78), which consists of discrete data points. In order to post-process an incremental crack advance,  $da$ , from the simulation results (see Figure 77), crack advance events were defined per DEM module, i.e. the failure of two diagonal- and one vertical element represented one crack advance increment. This advance was correlated to the sum of the three required cycles,  $dN$ . In this way, three successive element failures were required to establish one data point of  $da/dN$  per  $\Delta K$  (see Figure 78).

For all three material classes, the near-threshold Stage I can be distinguished in Figure 78 as the ranges, where the experimental data series grow at a higher rate than in Stage II, where FCG proceeds in a constant way along the fitted lines. For T-R, Stage I stretches from approximately  $\Delta K = 3 - 6 (MPa m^{0.5})$ . For the orientations of A-T and T-A, it stretches approximately from  $\Delta K = 4 - 6 (MPa m^{0.5})$ . Stage I is not yet modelled, which is reflected by the simulation results.

From a stress intensity factor range of about  $\Delta K \geq 6 (MPa m^{0.5})$ , Stage II, i.e. the Paris stage, starts for all three FCG orientations. In this range, the crack growths proceed in a constant way. The simulation exhibits a good agreement with the experimental data and the fitted lines for all three orientations (see Figure 78). This indicates a successful FCG parameterisation of Stage II. For a more precise comparison of the quantitative results, a statistical analysis is required. Within the frame of the thesis, this was not performed.

For the FCG orientation A-T, the crack growth rate is about two times higher than for T-R, and about six times higher than for the slowest orientation, T-A. This reflects well the experimental findings (14), that are evidence for the anisotropy of FCG for highly shear deformed rail steels. The parameterisation of these FCG

orientations is the first step to model an anisotropic RCF behaviour (see chapter 8).

One aspect regards the accuracy of the match between the experimental- and the simulation data. For the orientations of A-T and T-A it can be seen that the simulated crack growth proceeds in a slightly faster way than the experimental data. This can be attributed to the set-up of the model exponent  $m_2$ . A moderate reduction of  $m_2$  is supposed to deliver a perfect match. Within the frame of the thesis, however, this optimisation was not performed as the accuracy was considered to be satisfactory. Another aspect regards the scatter of experimental FCG data (16), which must be regarded as well when it comes to accuracy.

After the final experimental points were reached by the simulation, which correspond to fracture of the specimens (Stage III), the simulation series were ended as the parameterisation and modelling of Stage III was not within the scope of this section. This might have been done by the introduction of an additional failure criterion, i.e. the introduction of a critical strain (stretch) where elements fail, like proposed by Oterkus et al. (52).

In this way, a method to calibrate the FCG parameters for the FCG Stage II was set up. With it, three different material classes, reflecting the anisotropic crack growth found in shear deformed rail- and wheel steels, were specified. These parameters are the pre-condition for modelling the anisotropy of RCF. An improvement of the model would be to capture the near-threshold Stage I, which is pursued in section 6.2.

## 6.2 Near-threshold modelling

In the previous section 6.1, three material classes were parameterised for the FCG Stage II (see Table 12). The parameterisation diagram (see Figure 78) highlights the limitation of the model to Stage II, as the data points of all classes run along the fitted lines.

However, for stress intensity factor ranges of  $\Delta K < 6 \text{ (MPa m}^{0.5}\text{)}$ , the experimental data series exhibit gradients that deviate from the constant crack growth lines, i.e. a non-linear FCG behaviour. This characterises the FCG Stage I (see section 2.1.3). As the crack starts to propagate for a specific threshold stress intensity factor range,  $\Delta K_{th}$  (see section 2.1.3, Figure 8), the regime is called near-threshold Stage I. The aim of the section is to approximate this behaviour, though, crack nucleation is neglected.

Zhang modified a peridynamic model to extended the FCG behaviour to Stage I (57). He adjusted the fatigue law (see Equation 39) for FCG phase  $\zeta = 2$  (crack

growth, see Figure 36) by a correlation of the PD model to the macro-mechanical property fatigue limit, i.e. the stress below which a material can be loaded infinitely without being subject to fatigue (2). In the theory of fracture mechanics, this state correlates to a threshold value,  $\Delta K_{th}$  (see Figure 8).

In fact, however, two distinct types of thresholds are defined to better resolve effects caused by crack closure- and shielding mechanisms. The effective threshold,  $\Delta K_{th\_eff}$ , which is derived by the load rising technique, and the long-crack threshold,  $\Delta K_{th}$ , which is derived by the load shedding technique (14). The former is more conservative, i.e. it represents the absolute minimum where a crack starts to propagate. Though, with respect to the available experimental FCG data of Leitner, the latter was selected as a reference for modelling as it better fitted the FCG curves. Thus, in this section, the term threshold corresponds exclusively to the long-crack threshold,  $\Delta K_{th}$ .

In order to model a loading state, below which there is no fatigue progress, Zhang defined a fatigue limit for the PD model (57), which is represented by a cyclic bond strain (see Equation 40). In this work, this property is called "numerical fatigue limit",  $\Delta\varepsilon_\infty$ . Below this limit, cyclic bond strains,  $\Delta\varepsilon$ , are neglected for the reduction of the remaining life,  $\lambda$ , which is expressed by an extended fatigue law (see also Equation 39).

$$\frac{d\lambda}{dN} = \begin{cases} -A_2 \Delta\varepsilon^{m_2} & , \text{if } \Delta\varepsilon > \Delta\varepsilon_\infty \\ 0 & , \text{else} \end{cases}$$

**Equation 69**

In order to derive the numerical fatigue limit,  $\Delta\varepsilon_\infty$ , Zhang correlated the threshold,  $\Delta K_{th}$ , to a reference state,  $\Delta K$ , for which the average cyclic bond strain field around the crack tip,  $\Delta\varepsilon_{avg}$ , is known (57). A linear relation between the states of  $\Delta K_{th}$  and  $\Delta K$  was assumed.

$$\frac{\Delta\varepsilon_\infty}{\Delta\varepsilon_{avg}} = \frac{\Delta K_{th}}{\Delta K}$$

**Equation 70**

For this model, the reference state,  $\Delta K$ , was selected to be equal for all material classes and was set to be slightly higher than the highest threshold,  $\Delta K_{th}$  (see Table 13), i.e. the threshold of the material deformed in T-A (R260\_C03). The thresholds were selected from Leitner's data. The specimen geometry and the initial crack size were adopted from section 6.1. The applied load of the reference state,  $\Delta P$ , was derived with respect to  $\Delta K$ , and with Equation 63.

For processing the average cyclic bond strain of the reference state,  $\Delta\varepsilon_{avg}$ , the full-horizon FCG activation (see Figure 71, subplot) was applied to the vertical element of the crack tip. In this way, the numerical fatigue limits per material class,  $\Delta\varepsilon_{\infty}$ , were derived (see Table 13).

	$\Delta K_{th}$ (MPa $m^{0.5}$ )	$\Delta P_{th}$ (N)	$\Delta K$ (MPa $m^{0.5}$ )	$\Delta P$ (N)	$\Delta\varepsilon_{avg}$ (-)	$\Delta\varepsilon_{\infty}$ (-)
Mat. class	Experimental: Threshold state		Model: Reference state		Model: Parameters	
R260_C01	3.0	59.7	4.2	83.6	3.57e-4	2.55e-4
R260_C02	3.8	75.6				3.23e-4
R260_C03	4.0	79.6				3.40e-4

**Table 13 - Parameterisation of the numerical fatigue limits,  $\Delta\varepsilon_{\infty}$ , for three material classes (see Table 12).**

For the simulation of all classes, the applied loads were set to be approximately 1/1000 higher than the highest threshold (see Table 13).

The results are displayed in Figure 79. For the orientation of T-R (material class R260\_C01), the model resolved a range of  $\Delta K > 3.3$  (MPa  $m^{0.5}$ ). Due to the discretisation of the grid, which determined the incremental crack advance  $da$  (see section 6.1), the model did not resolve the near-threshold range below that limit. The same applied to the orientations of A-T and T-A. A better resolution was supposed to be obtained for a reduced grid discretisation. However, due to the available resources, this was not feasible.

For the more advanced regime of  $\Delta K = 3.3 - 6$  (MPa  $m^{0.5}$ ), the model approximated the experimental results, especially for the orientation T-A. Though, for the orientations of T-R and A-T that exhibited a larger range of transition from the near-threshold Stage I to the FCG Stage II, the model overestimated the crack growth rates and did not sufficiently resolve the near-threshold behaviour. This was attributed to the fact that the model approximated an exponential curvature, which deviated from the experimental results that exhibited a more erratic behaviour. A better match was expected to be obtained by an increase of the model's gradient, which required a kind of correction of the numerical fatigue life,  $\Delta\varepsilon_{\infty}$ . Within the frame of the thesis, this was not performed.

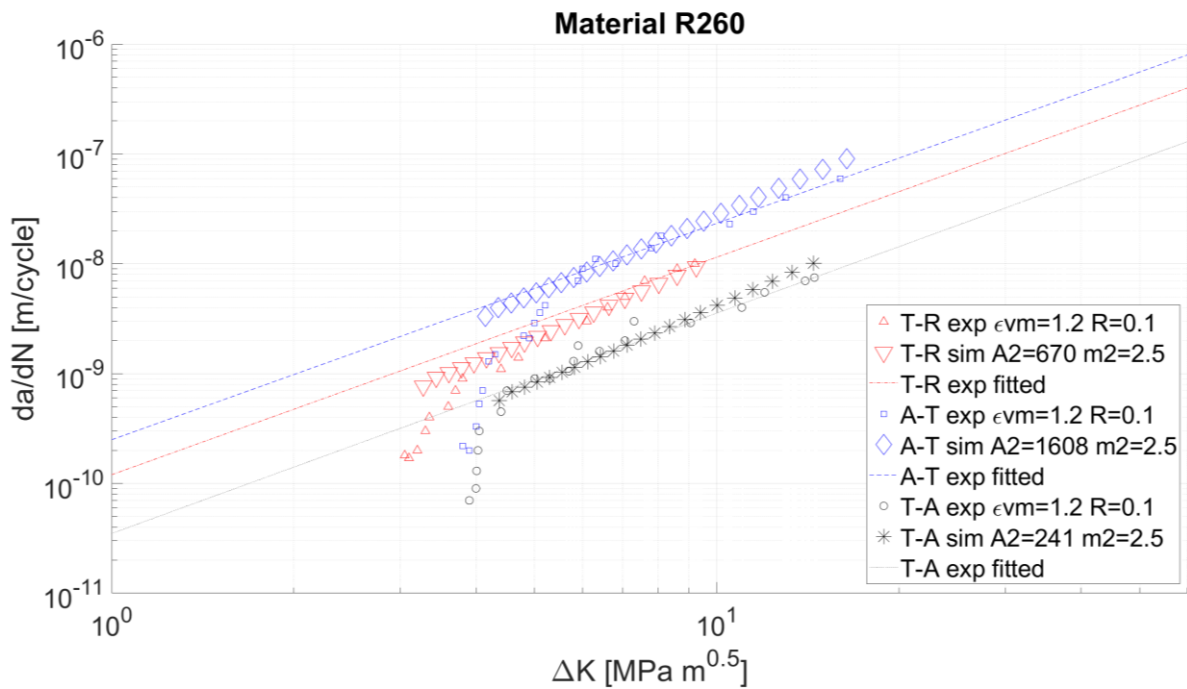


**Figure 79 - FCG diagram of three material classes (T-R, A-T, T-A): The experimental results from (30) are plotted against the simulated results. Fitted lines from the experimental data (30) are added.**

The experimental behaviour for all three orientations was supposed to be influenced by microstructural influences, which were not captured by the model. As a result, a more sophisticated approach than the one applied is required to better resolve this behaviour. Another issue regards the repeatability of the experimental data, which may be subject to a significant amount of scatter (16). This must be considered as well when it comes to an improvement of the modelling accuracy.

Regarding the transition to the FCG Stage II and above,  $\Delta K > 6$  ( $MPa m^{0.5}$ ), the model matched the experimental FCG rates (see section 6.1).

In summary, the extension of the model delivered an initial capability to model the near-threshold stage. However, the resolution close to the threshold as well as the accuracy for higher values of  $\Delta K$  still offer a margin for improvement. Within the frame of the thesis, this capability was assumed to be satisfactory.

### 6.3 Scaling of FCG parameters

In section 6.1, a method was employed to derive the FCG parameters  $A_2$  and  $m_2$  for three different material classes (see Table 12). The derivation was based on a grid with a specific discretisation,  $\Delta x = 1.0 e - 4 m$ , which is referred to as "reference discretisation " in this section. With respect to different applications, i.e. full-scale- or twin-disc simulation, and with regard to specific resolutions, however, various discretisations,  $\Delta x$ , are required.

The scope of the modelling was to render the FCG process independent of the grid discretisation. This implied that the FCG parameters could be transformed into domains other than the reference discretisation, whereas the FCG result remained the same. Thus, a method was developed in this section to adapt the FCG parameters to different discretisations,  $\Delta x$ . Finally, a test case was run for different discretisations to assess the FCG behaviour.

For the development of the method, material class "R260\_C02" (see Table 12) was selected, as it offered a broad FCG range (see Figure 78). The simulation of the Mode I test (see Figure 76) was based on the reference discretisation (see Figure 77). The employed FCG parameters  $A_2$  and  $m_2$  are summarised in Table 12.

The correction of the near-threshold modelling (see section 6.2) was adopted. Due to its limited impact on the near-threshold range, the correction based on the strain,  $\Delta \varepsilon_\infty$ , was assumed to be independent of the scaling of the discretisation.

Silling and Askari discussed the issue of scaling of the FCG parameters for a peridynamic model (49). Regarding the exponent of the fatigue law (see Equation 69),  $m_2$ , they highlighted that this parameter was derived directly from experimental data ( $m_2 = m$ , see Figure 8). This implied that the parameter was independent of the discretisation and must not be regarded for scaling.

For a scaling, they referred to the horizon  $\delta$  (see Equation 41), instead of  $\Delta x$ , as the key parameter to describe the grid discretisation. In Peridynamics, the horizon can be varied for a constant discretisation of the grid. The DERC model, though, represented a special case of Peridynamics, where the horizon,  $\delta$ , was fixed for a specific discretisation,  $\Delta x$ . This implied a direct correlation between  $\delta$  and  $\Delta x$  (see Equation 41) and facilitated the adoption of the method.

By consideration of the fatigue law (see Equation 69) and a comparison to the Paris equation (see Equation 5), Silling and Askari stated that the terms of crack growth, i.e.  $\frac{d\lambda}{dN}$  respectively  $\frac{da}{dN}$ , must remain independent of the horizon,  $\delta$ . In this

way, they derived a formulation for  $A_2(\delta)$ , which was based on a dimensionless constant  $\hat{A}_2$ , that was independent of  $\delta$  as well (49).

$$A_2(\delta) = \hat{A}_2 \delta^{(m_2-2)/2}$$

Equation 71

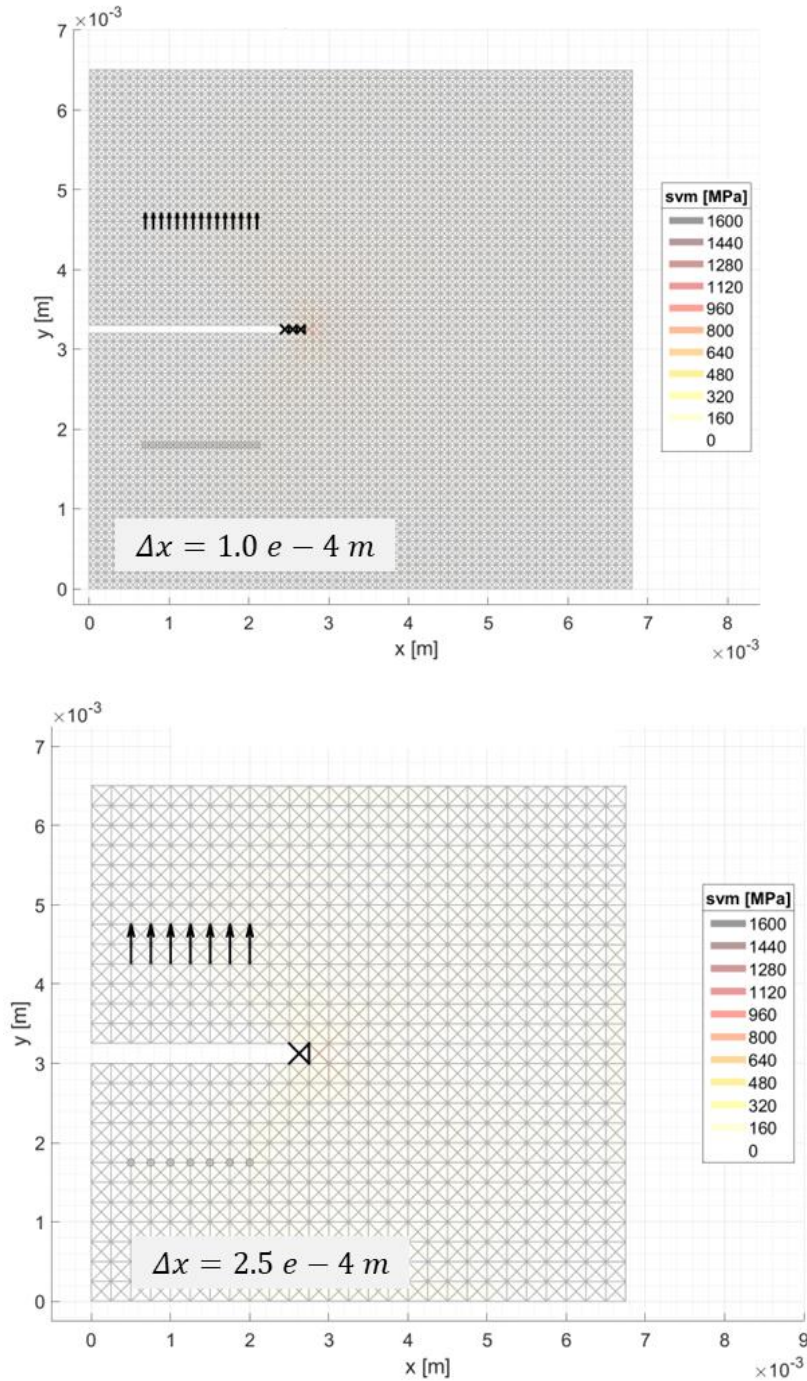


Figure 80 - Discretisation study: Mode I test modelled by a reference (top) and a coarsened (bottom) grid discretisation,  $\Delta x$ .

Thus, for a known  $A_2(\delta_{ref})$  that referred to a reference discretisation,  $\delta_{ref}$ ,  $\hat{A}_2$  was derived. By scaling of  $\delta$ , the value for  $A_2(\delta \neq \delta_{ref})$  was calculated. This method was applied to the Mode I test case of section 6.1. The reference discretisation, for which the parameterisation was performed, is displayed in Figure 80 (top). This case was remodelled by a coarsened grid of  $\Delta x = 2.5 e - 4 m$  (see Figure 80, bottom). Due to the coarsened discretisation, the modelling of the initial crack and of the load application- and bearing holes caused a minor discretisation error, which was assumed to be negligible for the study. The layout of both grids is summarised in Table 14.

	Reference grid	Coarsened grid
Discretisation, $\Delta x$ (m)	$1.0 e - 4$	$2.5 e - 4$
Horizon, $\delta$ (m)	$1.41 e - 4$	$3.54 e - 4$
FCG parameter, $A_2$ (-)	1608	2022
FCG parameter, $\hat{A}_2$ (-)	14745	
FCG parameter, $m_2$ (-)	2.5	

**Table 14 - Overview of the study for two different grid discretisations.**

The results of both simulations were post-processed and plotted in an FCG diagram against the experimental data from Leitner et al. (5) (see Figure 81). The result of the coarsened grid agreed well with the reference grid. This was emphasised by the comparable crack growth rates,  $da/dN$ .

The resolution of the FCG progress, however, was reduced due to the increased unit length,  $\Delta x$ . This fact was illustrated by the smaller number of data points of the coarsened model. Another consequence of the degraded resolution regarded the potential modelling of fracture, i.e. the condition of the last experimental data point. An accurate modelling of fracture was already compromised by the discretisation of the reference grid (see Figure 81). This issue was worsened by the coarsened discretisation. This reflects a common aspect of numerical modelling.

A potential refinement of the reference grid would have been desirable in order to perform a convergence study. However, due to the available processing capacity, this was not feasible.

The method regarding the scaling of FCG parameters as a function of the horizon,  $\delta$ , proved to be reasonable and was implemented. In this way, the



parameterisation of  $A_2$  was performed by means of the reference discretisation, and then scaled with respect to the horizon.

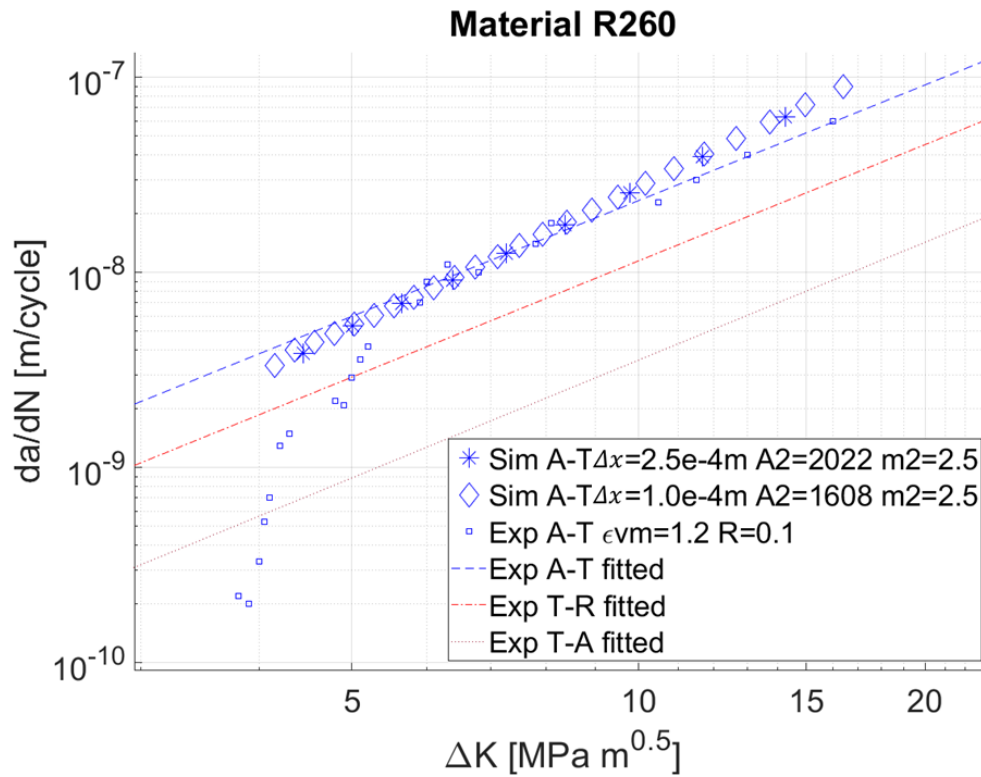


Figure 81 - FCG diagram of the discretisation study: The simulation results for two discretisations,  $\Delta x$ , are plotted against experimental results (37).

In summary, the issue of scaling of the FCG parameters  $A_2$  and  $m_2$  as a function of the grid discretisation was discussed in this section. A method was adopted from the literature, and a test case was run for two differently discretised grids. The results demonstrated the FCG behaviour to be independent of the grid, which confirmed the method.

## 6.4 FCG parameters for RCF simulation

In section 6.1, three distinctive material classes were modelled for an intermediate degree of shear deformation,  $\varepsilon_{VM} = 1.2$  (see Table 12). As the scope of the model development was to model RCF as a function of SPD (see chapter 0), a set of specific material classes had to be identified to capture the conditions of rail steels subject to SPD. The aim of this section is to estimate the required material classes, and to parametrise them in accordance with the procedures described in the sections 6.1 and 6.2.

As a source for the experimental FCG data of highly deformed rail steels, the work of Leitner et al. (5) was adopted in section 6.1. The data deals primarily with different FCG orientations of R260. For R350HT, only one degree of deformation ( $\varepsilon_{VM} = 1.2$ ) was captured. A paramount aspect of material subject to SPD is the gradient of deformation with the depth (see Figure 5, section 7.2), which rules the development of RCF. Leitner et al. highlighted that the FCG orientation along the main shear layers (see Figure 75, "A-T") represented the one with the highest FCG rates. In order to model the impact of these layers as a function of depth, at least two FCG data sets of orientation A-T were required for modelling. This led to the conclusion that sufficient data was only available for R260. Thus, this section emphasised the parameterisation of R260.

Leitner performed FCG tests for R260 and the orientation A-T for different degrees of deformation:  $\varepsilon_{VM} = 1.2$ ,  $\varepsilon_{VM} = 2.3$  and  $\varepsilon_{VM} = 17.3$  (5). The results for the first two degrees of deformation, however, demonstrated a similar behaviour. For this reason, only the deformations of  $\varepsilon_{VM} = 1.2$  and  $\varepsilon_{VM} = 17.3$  were considered. The former was already parameterised in sections 6.1. This identified the first additional material class to be modelled. Furthermore, undeformed R260 was selected as a reference class (see Table 15). Experimental data for that class was found in (85).

Material class	R260_C00	R260_C22
Material	R260	R260
Deform. $\varepsilon_{VM}$	0	17.3
Stress ratio $R$	0.1	0.1
FCG orientation	AR	A-T
FCG param $m_2$	3	6.5
FCG param $A_2$	7500	1.27e16

**Table 15 - Material classes to be parametrised: The resulting FCG parameters  $A_2$  and  $m_2$  are displayed in the last rows.**

In this way, two additional material classes were identified to be modelled (see Table 15). In accordance with the previous parameterisation, data sets for a stress ratio of  $R = 0.1$  were selected. The undeformed class "R260\_C00" was abbreviated by "AR" for "as-received". The highly deformed class of orientation A-T was called "R260\_C22" with respect to the low deformed class, R260\_C02 (see Table 12). For both parameterisations, the same specimen dimensions and grids were used like in section 6.1 (see Figure 76).

In the first step, the class of as-received material was modelled. In deviation to the low deformed materials of section 6.1, which were modelled with an exponent of  $m_2 = 2.5$ , Leitner stated the gradient of the as-received material to be  $m = 3$  (85), which was adopted for modelling by  $m_2 = 3$  (see Table 15).

The near-threshold stage was modelled in accordance with the procedure given in section 6.2. In this way, the numerical fatigue limit,  $\Delta\varepsilon_\infty$ , was derived (see Table 16). Based on the threshold state,  $\Delta K_{th}$ , the corresponding force,  $\Delta P_{th}$ , was used to calculate the maximum force,  $P_{max} = 122\text{ N}$ , by means of Equation 65. This corresponded to a stress of  $\sigma_{max} = 69.3\text{ MPa}$ . In order to be slightly above the threshold, the applied stress was rounded to  $\sigma_{max} = 69.5\text{ MPa}$ , which equalled a force of  $P_{max} = 126\text{ N}$

	$\Delta K_{th}$ (MPa $m^{0.5}$ )	$\Delta P_{th}$ (N)	$\Delta K$ (MPa $m^{0.5}$ )	$\Delta P$ (N)	$\Delta\varepsilon_{avg}$ (-)	$\Delta\varepsilon_\infty$ (-)
Mat. class	Experimental: Threshold state		Model: Reference state		Model: Parameters	
R260_C00	5.5	109.4	4.2	83.6	3.57e-4	4.67e-4
R260_C22	2.25	44.8				1.91e-4

**Table 16 - Parameterisation of the numerical fatigue limits,  $\Delta\varepsilon_\infty$ , for the specified material classes (see Table 15).**

The parameter  $A_2$  (see Table 15) was derived by the method specified in section 6.1. With this set of parameters, the FCG simulation was run. The result is displayed in Figure 82.

The near-threshold range of  $\Delta K = 5.5 - 7\text{ (MPa } m^{0.5})$  was not resolved appropriately due to the reasons discussed in section 6.2. In the first part of the FCG Stage II at  $\Delta K = 7 - 9\text{ (MPa } m^{0.5})$ , the simulation matched the experimental behaviour. For the range of  $\Delta K = 9 - 18\text{ (MPa } m^{0.5})$ , no experimental data was

available. In the final part of Stage II at  $\Delta K = 18 - 25$  ( $MPa m^{0.5}$ ), the model slightly underestimated the crack growth rate.

The reason for the underestimation was caused by the model's assumption of a fixed gradient,  $m_2$ . The experimental data suggested that the crack growth in the range of  $\Delta K = 9 - 18$  ( $MPa m^{0.5}$ ) proceeds with an exponent of  $m > 3$ , whereas for  $\Delta K = 18 - 25$  ( $MPa m^{0.5}$ ), a gradient of  $m = 3$  was exhibited. In order to improve the modelling, a more sophisticated fatigue law would have been required. However, the model result provided an acceptable solution for the broad FCG range of the material class.

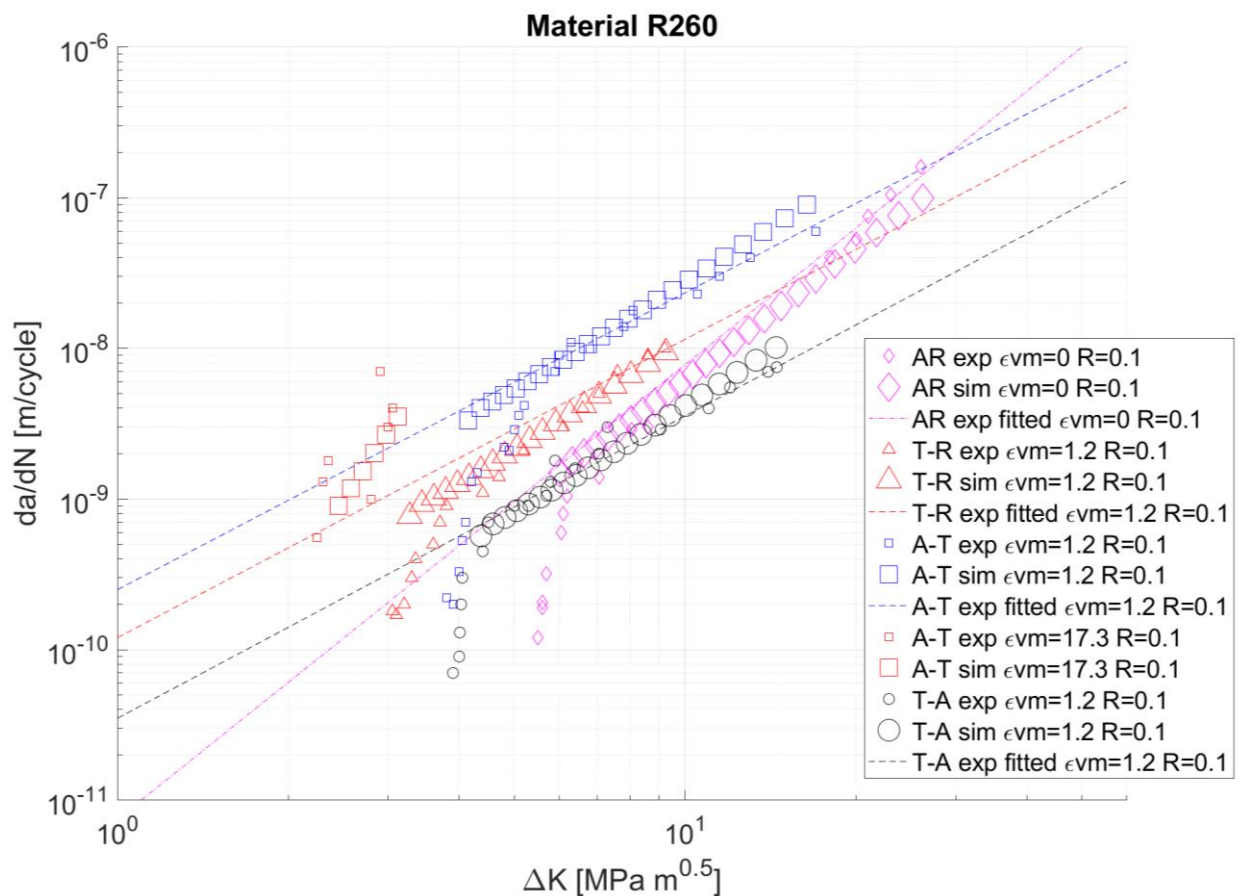


**Figure 82 - FCG diagram of parameterised material classes against the experimental data of Leitner et al. (5,85). The added class for the undeformed material is marked by the **diamonds in magenta**, the highly deformed material in A-T by the **red squares**.**

In the next step, the highly deformed material in orientation A-T was parameterised (class R260\_C22, see Table 15). The experimental result for this class (see Figure 82) suggested the modelling would be more challenging. The

gradient  $m$  was higher than for the other classes, the range of  $\Delta K = 2 - 3$  ( $MPa m^{0.5}$ ) was narrow, and the data was significantly scattered.

As the experimental gradient  $m$  was not explicitly specified in (5), it was derived manually from the available data. The Paris equation (see Equation 5) was set up for the first- and the last data point of the experimental series (see Figure 82, small red squares). The associated stress intensity factor ranges and crack growth rates are summaries in Table 17.

	$\Delta K$ ( $MPa m^{0.5}$ )	$\frac{da}{dN}$ ( $m/cycle$ )
Initial (threshold)	2.25	5.5e-10
Final (fracture)	3.05	4.0e-9

**Table 17 - Initial- and final data points of experimental FCG data for class R260\_C22.**

This resulted in two equations with two unknowns, the Paris coefficient,  $C$ , and the desired exponent,  $m$ .

$$\left(\frac{da}{dN}\right)_{init} = C \Delta K_{init}^{m_2}$$

**Equation 72**

$$\left(\frac{da}{dN}\right)_{final} = C \Delta K_{final}^{m_2}$$

**Equation 73**

The two equations were transformed to resolve the constant,  $C$ , and were merged.

$$\frac{\left(\frac{da}{dN}\right)_{init}}{\Delta K_{init}^{m_2}} = \frac{\left(\frac{da}{dN}\right)_{final}}{\Delta K_{final}^{m_2}}$$

**Equation 74**

This equation was transformed to bring both expressions of the exponent on one side.

$$\frac{\Delta K_{final}^{m_2}}{\Delta K_{init}^{m_2}} = \left(\frac{\Delta K_{final}}{\Delta K_{init}}\right)^{m_2} = \frac{\left(\frac{da}{dN}\right)_{final}}{\left(\frac{da}{dN}\right)_{init}}$$

**Equation 75**

Resolving the equation by the application of the logarithm, the exponent,  $m_2$ , was derived. In this way,  $m_2 = 6.5$  was calculated for the highly deformed material class (see Table 15).

$$m_2 = \log\left(\frac{\Delta K_{final}}{\Delta K_{init}}\right) \left(\frac{da}{dN}\right)_{final} - \log\left(\frac{\Delta K_{final}}{\Delta K_{init}}\right) \left(\frac{da}{dN}\right)_{init}$$

**Equation 76**

The exponent was derived with respect to the first and the last experimental data point. The method represented an initial approach, as the scatter of the data was not considered. An approach to capture the complete data set would be a linear regression. Within the frame of the thesis, however, this method was not applied.

For ductile materials like pearlitic rail steels, Suresh describes the exponent  $m$  to be in a range of  $m = 2 - 4$  (86). A comparison of the derived exponent for the highly deformed material,  $m_2$ , to that range suggested that the former does not refer to the behaviour of FCG Stage II, but rather represented the near-threshold Stage I. This aspect was further evaluated in section 6.5.

The parameter,  $A_2$ , was derived in accordance with the procedure in section 6.1. A challenge was to identify the crack growth rate  $\frac{da}{dN}$  properly, as the experimental data was subject to scatter, which delivered FCG rates between  $\frac{da}{dN} = 5.5e^{-10} - 1.3e^{-9}$  for comparable stress intensity factor ranges. Thus, the initial rate was estimated to be  $\frac{da}{dN} = 9e^{-10}$ , for which the parameter  $A_2$  was derived (see Table 15).

The simulation was set up with the derived FCG parameters. The load was modelled close to the threshold (see Table 16) by an applied force of  $P_{max} = 52 N$ , which corresponded to a stress of  $\sigma_{max} = 28.35 MPa$ . The simulated result is displayed in Figure 82.

Compared to the experimental threshold at  $\Delta K = 2.25 (MPa m^{0.5})$ , the simulation exhibited a minor offset, starting at  $\Delta K = 2.35 (MPa m^{0.5})$ . This fact was attributed to the grid discretisation and the resulting size of the crack increment,  $da$ . The state of fracture was captured by the simulation, which agrees with the experiments. The gradient of the experimental results was, with regard to the scattered data, approximated in the best way possible. In this way, the highly deformed R260 material of orientation A-T was modelled.

For a more precise comparison of the quantitative results, a statistical analysis was required. Within the frame of the thesis, this was not performed.

This section made an estimation for the material classes required to model RCF as a function of SPD. In addition to the previous results for R260, two material classes for undeformed- and highly deformed state were parameterised. The simulation results were compared against experiments, which demonstrated an acceptable agreement. This data was used as an input for the anisotropic RCF modelling (see chapter 0).

## 6.5 Interpolation as a function of shear deformation

In the previous sections, FCG material classes for different degrees of deformation of R260 material were derived (see Figure 82). For the key orientation "A-T", classes for  $\varepsilon_{VM} = 1.2$  and  $\varepsilon_{VM} = 17.3$  were defined. However, the process of SPD generates a material with continuous degrees of deformation, ranging from  $\varepsilon_{VM} = 0$  to  $\varepsilon_{VM} = 17.3$  (5).

The aim of this section was to develop a method to mediate the FCG parameters ( $A_2$ ,  $m_2$ ,  $\Delta\varepsilon_\infty$ ,  $\Delta K_{th}$ ) between the degrees of deformation, for which data is available ( $\varepsilon_{VM} = [1.2, 2.3, 17.3]$  (5)). The method was assessed for specific material classes with interpolated degrees of deformation.

In the first step, the minimum- and maximum classes were defined as limits of the interpolation. With respect to the defined material classes, the classes "R260\_C02" and "R260\_C22" were selected. The data of the classes was adopted from Table 12 and Table 15 and is summarised in Table 18. The threshold data was adopted from Table 13 and Table 16.

Class	Note	Deform $\varepsilon_{VM} (-)$	Factor $f_{\varepsilon_{VM}} (-)$	FCG $A_2(-)$	FCG $m_2(-)$	FCG $\Delta\varepsilon_\infty (-)$	$\Delta K_{th}$ (MPa $m^{0.5}$ )
R260_C02	Min	1.2	0.00	1608	2.50	3.23e-4	3.80
R260_X13	Inter	7.3	0.38	4.84e15	4.02	2.73e-4	3.21
R260_X14	Inter	12.3	0.69	8.81e15	5.26	2.32e-4	2.73
R260_C22	Max	17.3	1.00	1.28e16	6.50	1.91e-4	2.25

**Table 18 - FCG parameters of the minimum-, maximum and interpolated classes (FCG regimes I and II).**

Further, two "experimental" series (R260\_X13, R260\_X14) with linearly spaced degrees of deformation,  $\varepsilon_{VM} = 7.3$  and  $\varepsilon_{VM} = 12.3$ , were defined between the limits. For the interpolation, a Von Mises strain factor,  $f_{\varepsilon_{VM}} = [0, 1]$ , was introduced (see Table 18).

$$f_{\varepsilon_{VM}} = \frac{(\varepsilon_{VM} - \varepsilon_{VM \min})}{(\varepsilon_{VM \max} - \varepsilon_{VM \min})}$$

**Equation 77**

With it, the FCG parameters  $A_2$  and  $m_2$  as well as the threshold parameters  $\Delta\varepsilon_{\infty}$  and  $\Delta K_{th}$  were derived.

$$A_2(\varepsilon_{VM}) = A_{2 \min} + (A_{2 \max} - A_{2 \min}) * f_{\varepsilon_{VM}}$$

**Equation 78**

$$m_2(\varepsilon_{VM}) = m_{2 \min} + (m_{2 \max} - m_{2 \min}) * f_{\varepsilon_{VM}}$$

**Equation 79**

$$\Delta\varepsilon_{\infty}(\varepsilon_{VM}) = \Delta\varepsilon_{\infty \min} + (\Delta\varepsilon_{\infty \max} - \Delta\varepsilon_{\infty \min}) * f_{\varepsilon_{VM}}$$

**Equation 80**

$$\Delta K_{th}(\varepsilon_{VM}) = \Delta K_{th \min} + (\Delta K_{th \max} - \Delta K_{th \min}) * f_{\varepsilon_{VM}}$$

**Equation 81**

In this way, the parameters were interpolated (see Table 18) and applied for a Mode I simulation (see sections 6.1 and 6.2) to process the FCG diagram. For the minimum- and maximum classes, Figure 82 indicated the FCG rates ( $da/dN$ ) to be in a range of  $1e^{-10} - 1e^{-8}$ . All results for the interpolated series, however, delivered values in a range of  $1e^{-4}$ , which was not reasonable.

The reason was assumed to be the high difference between the exponents,  $m_2$ , and the parameters,  $A_2$ . An analysis indicated the exponents of ductile materials like rail steels to be in a range of  $m = [2 - 4]$  (86), which applied to the lowly deformed material (R260\_C02,  $\varepsilon_{VM} = 1.2$ ), but not to the highly deformed one (R260\_C22,  $\varepsilon_{VM} = 17.3$ ). The exponent of the latter,  $m_2 = 6.5$ , rather suggested the material to fatigue exclusively in the FCG Stage I, before failure occurs (see Figure 82). This was not considered yet.

As a result, the interpolation method was based on the wrong assumption that both classes of the minimum and maximum referred to the same physical domain, i.e. Stage II, where the same mechanisms of fatigue apply. This, however, was not



valid. This fact was interpreted to be the reason for the misleading results of the interpolation.

In the next step, the minimum class was redefined to be "closer" to the maximum class. The experimental data for  $\epsilon_{VM} = 2.3$  (5) was parameterised to derive class "R260\_C12" for this reason (see Table 19). However, deviating from the procedure in section 6.1, not Stage II, but Stage I was parameterised (see Figure 83, right). The exponent was derived like explained in section 6.4. For reasons of uniformity, also the near-threshold method from section 6.2 was adopted.

Class	Note	Deform $\epsilon_{VM} (-)$	Factor $f_{\epsilon_{VM}} (-)$	FCG $A_2 (-)$	FCG $m_2 (-)$	FCG $\Delta\epsilon_{\infty} (-)$	$\Delta K_{th}$ (MPa $m^{0.5}$ )	$\epsilon_{trans}$ (-)
R260_C12	Min	2.3	0.00	5.92e15	7.00	3.23e-4	4.00	1.9e-3
R260_X13	Inter	7.3	0.38	8.20e15	6.83	2.79e-4	3.42	1.5e-3
R260_X14	Inter	12.3	0.69	1.05e16	6.67	2.35e-4	2.83	1.2e-3
R260_C22	Max	17.3	1.00	1.28e16	6.50	1.91e-4	2.25	8.3e-4

Table 19 - FCG parameters of the minimum-, maximum and interpolated classes (FCG Stage I only).

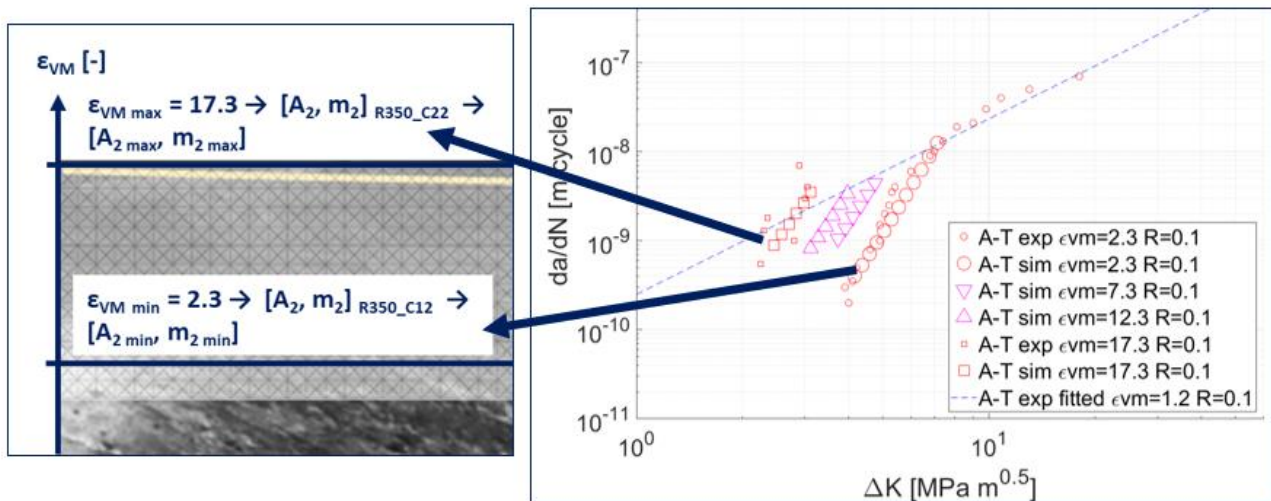


Figure 83 - Principle of the interpolation, displayed for the parameters  $A_2$  and  $m_2$  (left). FCG diagram of material classes in FCG orientation A-T (right). The simulation series for the deformations of  $\epsilon_{VM} = 7.3$  and  $\epsilon_{VM} = 12.3$  were derived by the interpolation.

The interpolation procedure was repeated by the application of the new minimum class (see Table 17). The principle of the interpolation is visualised in Figure 83. A summary of the minimum- and maximum classes is given in the next section (see Table 20). The Mode I test was run for the series of class R260\_C12 and the two interpolated series (see Figure 83, right).

The results are compared against the material class of the highly deformed material, which was derived in section 6.4. The interpolation of the thresholds,  $\Delta K_{th}$ , and the associated modelling of a minimum applied stress, had the effect that both interpolated series started at stress intensity factor ranges,  $\Delta K$ , which are located between the minimum- and maximum classes. This behaviour was as desired. The gradients,  $m$ , of the interpolated classes can hardly be differentiated from the limit classes. The parameter had no major effect in this case.

The crack growth rates,  $(da/dN)$ , were compared with regard to a fixed value of  $\Delta K$ , i.e.  $\Delta K = 4 \text{ MPa m}^{0.5}$ . For the medium deformed class at  $\varepsilon_{VM} = 2.3$ , the rate equals  $(da/dN) = 2e - 10 \text{ m/cycle}$ . For the interpolated class of  $\varepsilon_{VM} = 7.3$ , the rate yielded  $(da/dN) = 2e - 9 \text{ m/cycle}$ . For the class of  $\varepsilon_{VM} = 12.3$ , the rate was not simulated for  $\Delta K = 4 \text{ MPa m}^{0.5}$ , but an extrapolation of the series indicates the rate to be about 3 times higher. The same trend was valid for the highest deformed material class. These results confirmed the intention of the interpolation. The method was applied for the interval of  $\varepsilon_{VM} = [2.3, 17.3]$ , but it can be extended to the lower data series of  $\varepsilon_{VM} = 1.2$  as well.

The major limitation of the method regarded the restriction to FCG Stage I. The question was how to check this restriction. With respect to a common method to model fracture (FCG Stage III) in Peridynamics, where the strain state of the last data point was defined to be a critical strain (49,52),  $\varepsilon_{crit}$ , a transition strain,  $\varepsilon_{trans}$ , was derived for the class R260\_C12 (see Table 19) at  $\Delta K = 7 \text{ MPa m}^{0.5}$  (see Figure 83, right). This strain defined the end of the valid range of the FCG parameters for FCG Stage I. For class R260\_C22, this strain was assumed to represent the fracture strain,  $\varepsilon_{trans} = \varepsilon_{crit}$ . This restriction was checked for the modelling (see section 8.2.1). Due to the elastic character of the grid, the transition strains were assumed to be independent of the discretisation.

A potential improvement to remove the restriction would be to implement a bilinear fatigue law, which shifts the FCG parameters after passing a transition state. Another alternative would be the formulation of an FCG law based on an e-function. Within the frame of the thesis, however, this was not implemented.

In brief, the problem, that FCG data was only available for three specific degrees of deformation,  $\varepsilon_{VM}$ , was solved by the introduction of an interpolation method. The method derived the required parameters between two limits as a function of the deformation,  $\varepsilon_{VM}$ . In this way, material series of deformations located between the limits were parameterised, which was demonstrated and plotted in an FCG diagram. The interpolation was defined for limits of the FCG Stage I, which must be checked for the application by means of a transition strain,  $\varepsilon_{trans}$ . The method was adopted in section 8.2.

## 6.6 FCG parameters of similar materials

A method to parameterise the FCG parameters with respect to experimental data was performed in section 6.1. In section 6.2, an initial method to model the near-threshold stage was implemented. In order to adapt the FCG parameters to different grid discretisations, a scaling method was adopted in section 6.3. In this way, a material library of different material classes required for RCF modelling was issued in section 6.4.

The library, however, was based only on materials of R260 origin. In this section, a method was adopted to perform an extension of the library to the material R350HT. The method represented a benefit, as only limited FCG data of deformed rail steels was available.

The derivation of FCG parameters was performed with regard to the experimental data of Leitner et al. (5,14,85), which dealt with the FCG behaviour of deformed rail steels. For materials of similar strength, Leitner suggested the FCG rates  $\frac{da}{dN}$  to be inversely proportional to the strength,  $\sigma_y$ , respectively hardness,  $H$ , of materials (5).

$$\left(\frac{da}{dN}\right)_{R350HT} \cong \frac{\sigma_y^{R260}}{\sigma_y^{R350HT}} * \left(\frac{da}{dN}\right)_{R260}$$

Equation 82

$$\left(\frac{da}{dN}\right)_{R350HT} \cong \frac{H^{R260}}{H^{R350HT}} * \left(\frac{da}{dN}\right)_{R260}$$

Equation 83

$$\left(\frac{da}{dN}\right)_{R350HT} \cong 0.87 * \left(\frac{da}{dN}\right)_{R260}$$

Equation 84

In this way, Leitner derived a correlation between the FCG rates of the materials R260 and R350HT. This correlation was exploited for modelling in this section. A comparison of Equation 84 to the Paris equation (see Equation 5) revealed that the gradient  $m$  stays constant. With regard to the fatigue law used for modelling (see Equation 39), this implied for the modelling parameter to be independent of the specific material,  $m_2 = m = const.$

As Silling and Askari highlighted (49) in the derivation for the adopted fatigue law (see Equation 39), the model equation corresponds to the Paris equation (see Equation 5) in a linear way.

$$\frac{d\lambda}{dN} \cong \frac{da}{dN}$$

**Equation 85**

Based on this consideration, the correlation of Leitner et al. (see Equation 84) was adopted to derive the FCG parameter  $A_2$  for R350HT from R260 by a modification of the fatigue law. In brief, the parameter  $A_2$  of R260 was multiplied by a factor of 0.87.

$$\left(\frac{d\lambda}{dN}\right)_{R350HT} = 0.87 * (-A_2 * \Delta\varepsilon^{m_2})_{R260}$$

**Equation 86**

This relation assumed materials that have similar strengths, whereas Leitner et al. did not specify a range. In this work, the derived correlation was adopted exclusively to R350HT. In this way, the classes of R260 (see Table 20) were duplicated to derive the classes of R350HT (see Table 21).

Material class	R260_C00	R260_C01	R260_C02	R260_C03	R260_C12	R260_C22
Material	R260	R260	R260	R260	R260	R260
Deform. $\varepsilon_{VM}$	0	1.2	1.2	1.2	2.3	17.3
Stress ratio $R$	0.1	0.1	0.1	0.1	0.1	0.1
FCG orientation	AR	T-R	A-T	T-A	A-T	A-T
FCG param $m_2$	3	2.5	2.5	2.5	7	6.5
FCG param $A_2$	7500	670	1608	241	5.92e15	1.27e16
Fatigue limit $\Delta\varepsilon_\infty$	4.67e-4	2.55e-4	3.23e-4	3.40e-4	3.22e-4	1.91e-4

**Table 20 - Summary of FCG parameters  $A_2$ ,  $m_2$  and  $\Delta\varepsilon_\infty$  for the classes of R260.**

Material class	R350_C00	R350_C01	R350_C02	R350_C03	R350_C12	R350_C22
Material	R350	R350	R350	R350	R350	R350
Deform. $\varepsilon_{VM}$	0	1.2	1.2	1.2	2.3	17.3
Stress ratio $R$	0.1	0.1	0.1	0.1	0.1	0.1
FCG orientation	AR	T-R	A-T	T-A	A-T	A-T
FCG param $m_2$	3	2.5	2.5	2.5	7	6.5
FCG param $A_2$	6525	583	1399	210	5.15e15	1.11e16
Fatigue limit $\Delta\varepsilon_\infty$	4.67e-4	3.57e-4	3.57e-4	3.40e-4	3.57e-4	1.91e-4

**Table 21 - Summary of FCG parameters  $A_2$ ,  $m_2$  and  $\Delta\varepsilon_\infty$  for the classes of R350.**

Regarding the near-threshold modelling, the procedure detailed in section 6.2 was applied. However, due to the limited availability of FCG data for R350HT, some assumptions were made. For the R350HT FCG orientations of T-R and A-T at  $R = 0.1$  and  $\varepsilon_{VM} = 1.2$  (classes R350\_C01, R350\_C02), the thresholds were stated to be  $\Delta K_{th} = 4.2 \text{ (MPa m}^{0.5}\text{)}$  (14). With it, the numerical fatigue limit,  $\varepsilon_\infty$ , was derived (see Table 21). For the remaining classes of R350HT, no data was available. As for the R260 orientation of A-T at  $\varepsilon_{VM} = 1.2$  and  $\varepsilon_{VM} = 2.3$ , the thresholds were similar, the threshold of R350HT A-T at  $\varepsilon_{VM} = 2.3$  was adopted from the data of  $\varepsilon_{VM} = 1.2$ . For the remaining R350HT classes, the values of R260 were adopted as an initial value.

In the next step, a Mode I test was set up for the R350HT class of orientation A-T at  $\varepsilon_{VM} = 1.2$  (material class R350\_C02). The result was compared against the twin-class of R260 (R260\_C02), which is displayed in Figure 84.

It can be seen that the simulated FCG rates of R350HT are slightly below that of R260, which was expected. However, the difference is quite small. For Stage II, both simulation series covered the experimental results. Like mentioned in section 6.2, the modelling of the near-threshold stage cannot be modelled sufficiently. Regarding the fracture behaviour, R350HT exhibited less endurance than R260. For this reason, the simulation was stopped prematurely.

An important aspect regards the repeatability of experimental FCG results. In reality, it is often challenging to resolve the differences in FCG rates of similar materials like R260 and R350HT. Thus, the method delivered a satisfying result, which, though, must not be overestimated.

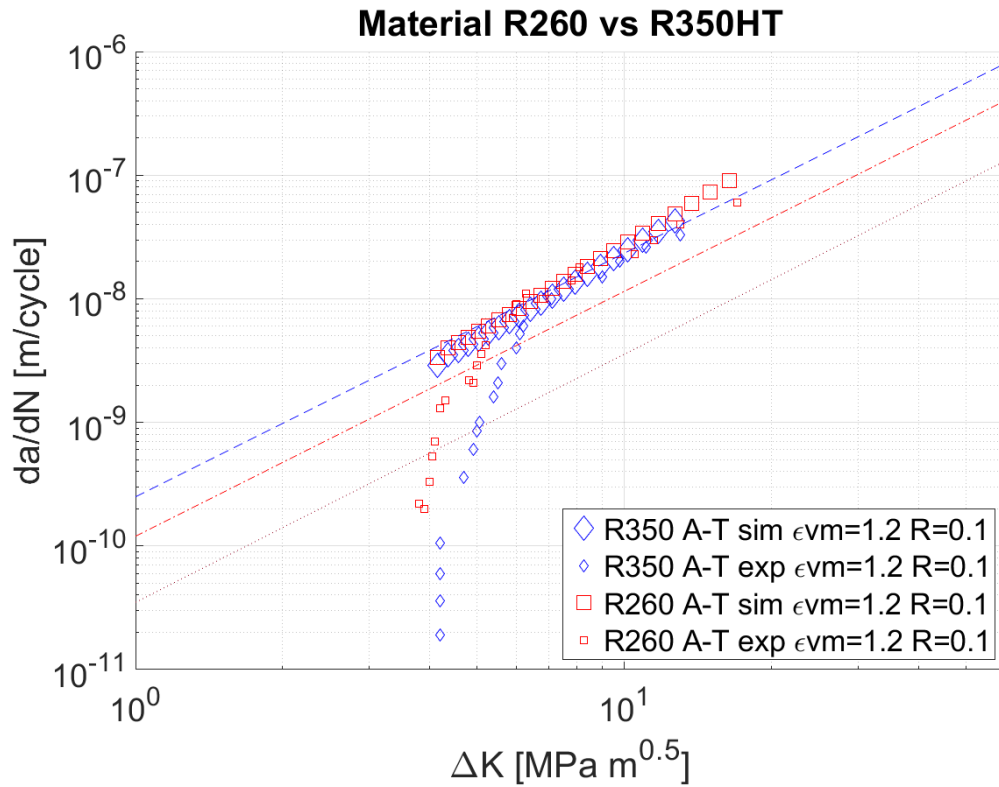


**Figure 84 - FCG diagram with simulation- and experimental data for deformed rail steels of type R260 and R350HT.**

In summary, a correlation of FCG data for materials of similar strengths was adopted from the literature. With it, the material library was extended in an easy way to cover R350HT by scaling the parameter,  $A_2$ , and by a modification of the threshold set-up. The developed method can be applied to materials of similar strengths.

## 7 MODELLING OF SEVERE PLASTIC DEFORMATION

Multiple rolling contacts lead to SPD (see chapter 2), which is a precondition for further forms of damage, i.e. RCF and wear. The objective of this section was to model SPD (see section 2.1.1) by the DERC model.

Initially, the modelling of the shear deformation was attempted in an explicit way (see Figure 85 left), which finally proved to be not feasible (see section 7.1). In the next step, SPD was modelled in an implicit way (see section 7.2).

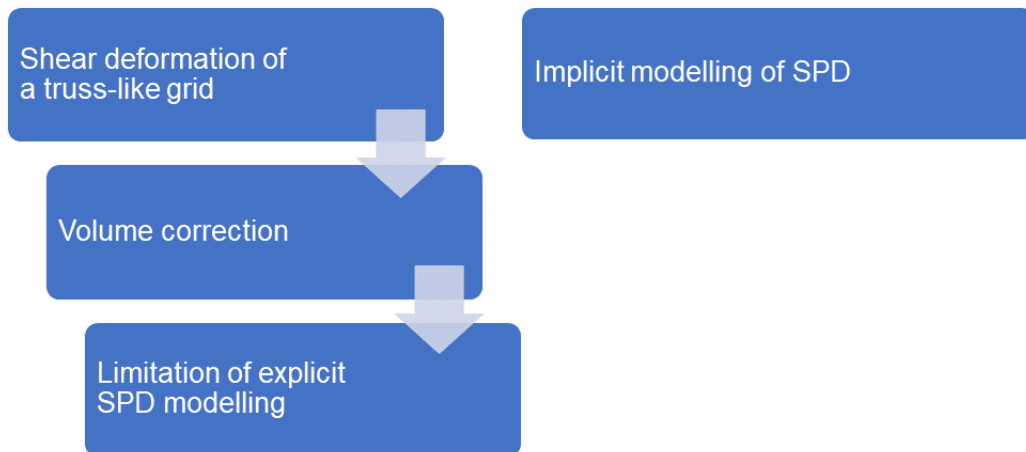


Figure 85 - Overview on the procedure applied in chapter 7 to model SPD explicitly (left) and implicitly (right).

### 7.1 Explicit modelling of SPD

In this section, the attempt to explicitly model high shear deformation by the truss-like DEM model is described. By "explicit" it is meant that the grid actually represents the shear deformation it is subject to (see Figure 20), i.e. the grid deformation is visible. In contradiction, by "implicit" it is meant that the grid does not display the degree of deformation, which, however, is described in a more abstract way (see section 7.2). This means that the deformation is not illustrated in the figures of the grid.

In order to explicitly model shear deformation, the mechanical behaviour under a compressive shear load was analysed (see section 7.1.1). As consequence of the grid's inherent characteristic, a volume correction was developed (see section 7.1.2). This ultimately revealed the limitations of the explicit approach (see section

7.1.3). Based on that finding, the conclusion was made to proceed with an implicit modelling approach (see section 7.2).

### 7.1.1 Shear deformation of a truss-like grid

The mechanical behaviour of a truss-like DEM grid under compressive shear load was assessed in this section. Basically, shear deformation can be described by the engineering shear strain  $\gamma_{xy}$  (see Equation 36). With respect to the literature, the goal was to simulate shear deformations of up to 1000 % (1), which corresponds to a shear strain of  $\gamma_{xy} = 10$ .

For the assessment, the response of single DEM modules under compressive shear load ( $p_0=1500$  MPa,  $\mu=0.5$ ) was evaluated for incremental degrees of deformation  $\gamma_{xy}$ . A periodic boundary condition was applied. The modules were initially deformed (pre-processing), i.e. the square modules were transformed into parallelograms. Then, the load was applied (processing). The results for the first ( $\gamma_{xy} = 0$ ) and the last increment ( $\gamma_{xy} = 3.8$ ) are visualised in Figure 86.

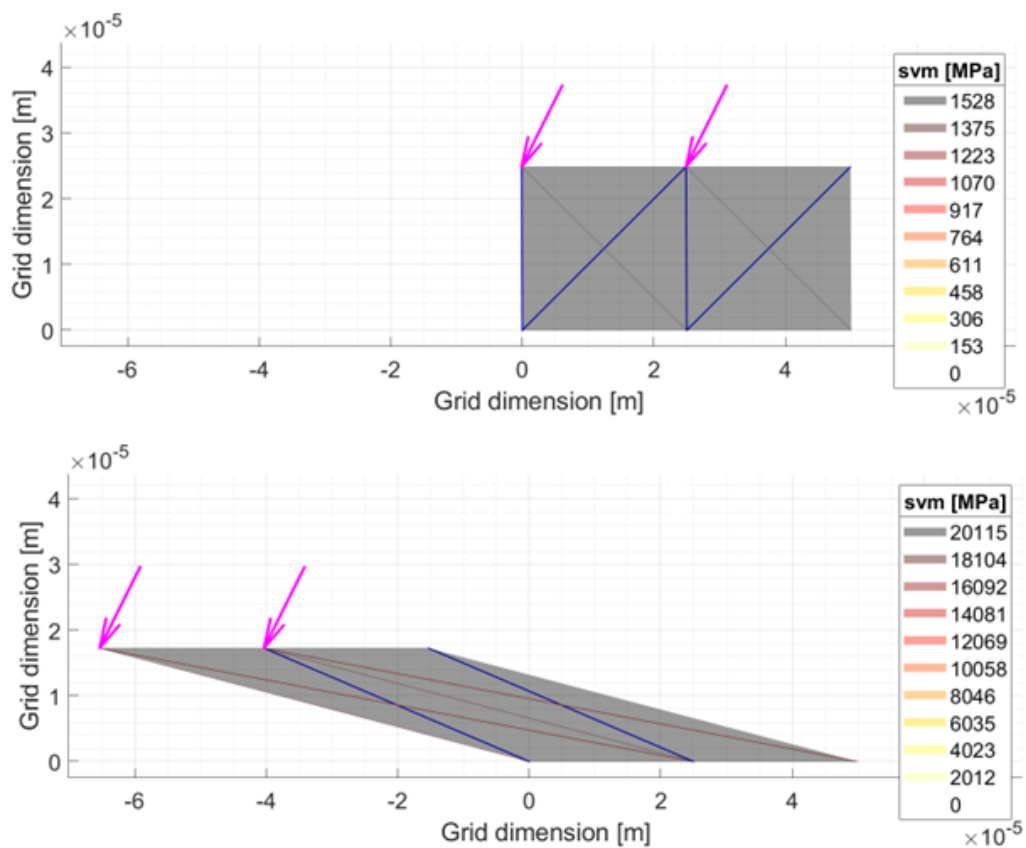
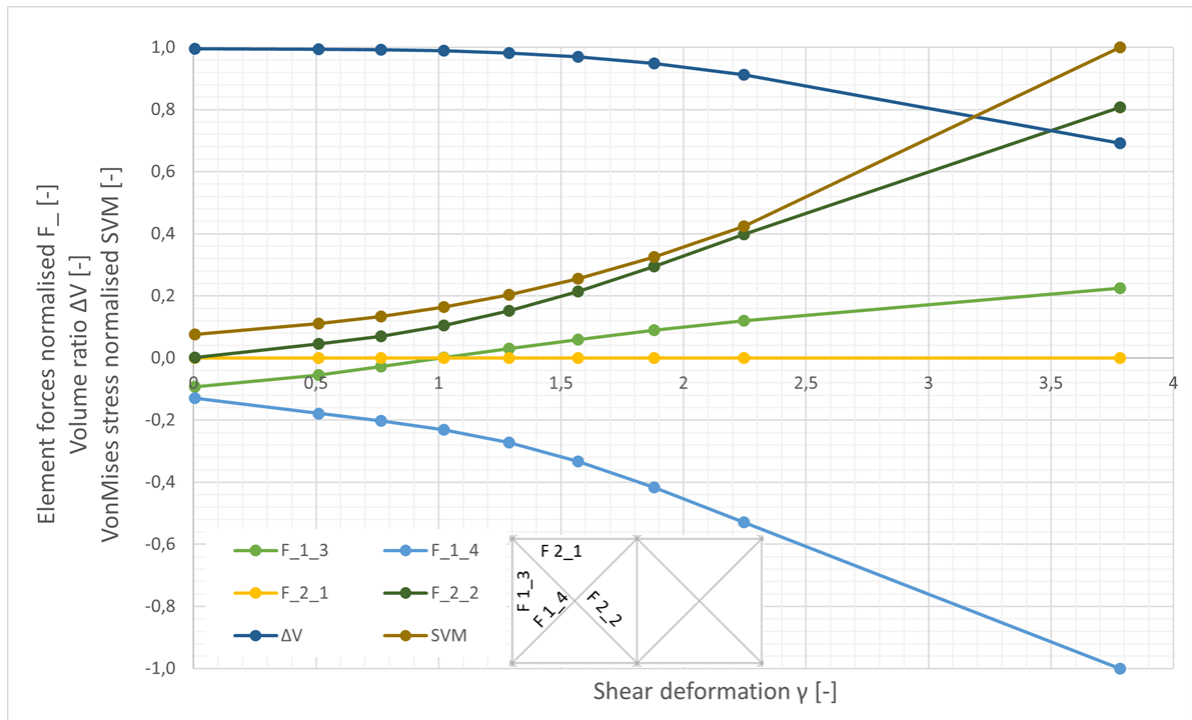


Figure 86 - Mechanical response of initially deformed DEM modules under compressive shear load. The undeformed state ( $\gamma_{xy} = 0$ ) is displayed above, the



deformed state ( $\gamma_{xy} = 3.8$ ) below. A periodic boundary condition (see section 4.11) was applied to the lateral edges of the DEM modules.

Further, a detailed analysis of the element's normalised forces  $F_-$ , the volume ratio  $\Delta V$  and the normalised Von Mises stress  $SVM$  was performed in Figure 87.



**Figure 87 - Analysis of incrementally shear deformed modules: Normalised element forces  $F_-$  (see subfigure), volume ratio  $\Delta V$  and normalised Von Mises stress  $SVM$ .**

The normalised forces were derived by the element forces  $F_{el,k,1}$  (see Equation 13), divided by the absolute maximum of the selected element forces  $F_{el,max,1}$  at the maximum deformed state ( $\gamma_{xy} = 3.8$ ). The nomenclature in Figure 87 refers to the included subfigure.

$$F_- = \frac{F_{el,k,1}}{|F_{el,max}|}$$

**Equation 87**

The ratio  $\Delta V$  refers to the ratio between the module surfaces  $V_0$  and  $V_1$  at the states "0" and "1". As plane strain was assumed, the surfaces correlate to volumes, whereas  $\Delta V$  was called volume ratio.

$$\Delta V = \frac{V_1}{V_0}$$

**Equation 88**

The Von Mises stress  $\sigma_{VM_i}$  for increment "i" was normalised in the same way as the element forces in order to process the normalised Von Mises stress  $SVM$ .

$$SVM = \frac{\sigma_{VM_i}}{\sigma_{VM_{max}}}$$

**Equation 89**

The first finding of Figure 86 was that the equivalent stresses diverged largely, despite the same load being applied. Further, for the deformed state there was a significant lowering of the surface. These aspects were investigated in Figure 87.

There, the development for initially shear deformed modules as a function of  $\gamma_{xy}$  is displayed. The element forces increased steadily. However, as a result of the rising element forces, the post-processed stresses increased. That correlated with a decrease in volume, which was highlighted by the surface lowering in Figure 86.

As the applied load was constant, the increase of the forces as a function of  $\gamma_{xy}$  was attributed to a higher degree of deformation. In other words, the higher the degree of initial shear deformation, the higher the module deformation was, and respectively the lower the overall elasticity of the modules was. This was related to the kinematics of the deformed truss.

The conclusion was that the truss-like structure in this form is not suited for application to high shear deformations. This is due to the kinematics, as the stiffness of the module decreases as function of  $\gamma_{xy}$ . Less stiffness implies more deformation and higher stresses. This is not acceptable. Therefore, a modification of the mechanical behaviour or a complete shift of method is required.

### **7.1.2 Volume correction**

In order to overcome the limitation imposed by a reduction of module stiffness as a function of the shear deformation  $\gamma_{xy}$  (see section 7.1.1), a new concept was considered. The primary goal was to stiffen each module as function of the volume ratio  $\Delta V$  (volume correction). The second goal was to conserve the stresses, i.e. to make the equivalent stress  $\sigma_{VM}$  as well as the stress tensor  $\tau_\sigma$  (see Equation 28) independent of the volume correction.

In order to conserve  $\sigma_{VM}$ , the definition was analysed (see Equation 33). Generally, an application of correction forces in x and y direction has an impact on the associated stresses  $\sigma_{xx}$  and  $\sigma_{yy}$ , which was neglected initially. The only way to conserve  $\sigma_{VM}$ , regardless of the variation of  $\sigma_{xx}$  and  $\sigma_{yy}$ , was to apply the corrective forces in a hydrostatic way, i.e. the stresses resulting from the correction forces must agree with a hydrostatic stress state. This was a first design criterion.

It was assumed that the correction forces  $F_{corr}$  were applied to each of a module's nodes. Each correction force was assumed to be independent of the element vectors, and to have equal magnitudes. Regarding the "control parameter",  $\Delta V$  was assumed to be equivalent to the shear strain,  $\gamma_{xy}$ , but easier to manage. With it, the equation for the magnitude of  $F_{corr}$  was established, whereas the variable  $c_{corr}$  was a correction constant to be defined.

$$F_{corr} = c_{corr} \Delta V$$

**Equation 90**

Then, an angle  $\rho$  was defined. For simplicity, it was assumed that there is one angle to be applied to all correction forces  $F_{corr\_1}$  to  $F_{corr\_2}$ . As square modules were used, and the condition of Equation 91 had to be satisfied for a hydrostatic state, an angle of  $\rho = 45^\circ$  was adopted.

$$\sigma_{xx} = \sigma_{yy} = \sigma_{zz}$$

**Equation 91**

With it, the equations for the 2D correction forces in vector form were derived, which is displayed for one force in Equation 92. The concept of the volume correction, to which that equation refers to, was illustrated in Figure 88.

$$\vec{F}_{corr\_1} = F_{corr} \begin{pmatrix} -\cos \rho \\ -\sin \rho \end{pmatrix}$$

**Equation 92**

In the processing phase, the correction forces were added to the element forces (net forces), resulting in the total forces. Then, the post-processing was performed separately for the net-, correction and total forces. Further, the stress component  $\sigma_{zz}$  of the correction forces had to be adapted by the substitution of Equation 29 with Equation 45 in order to agree with the hydrostatic state.

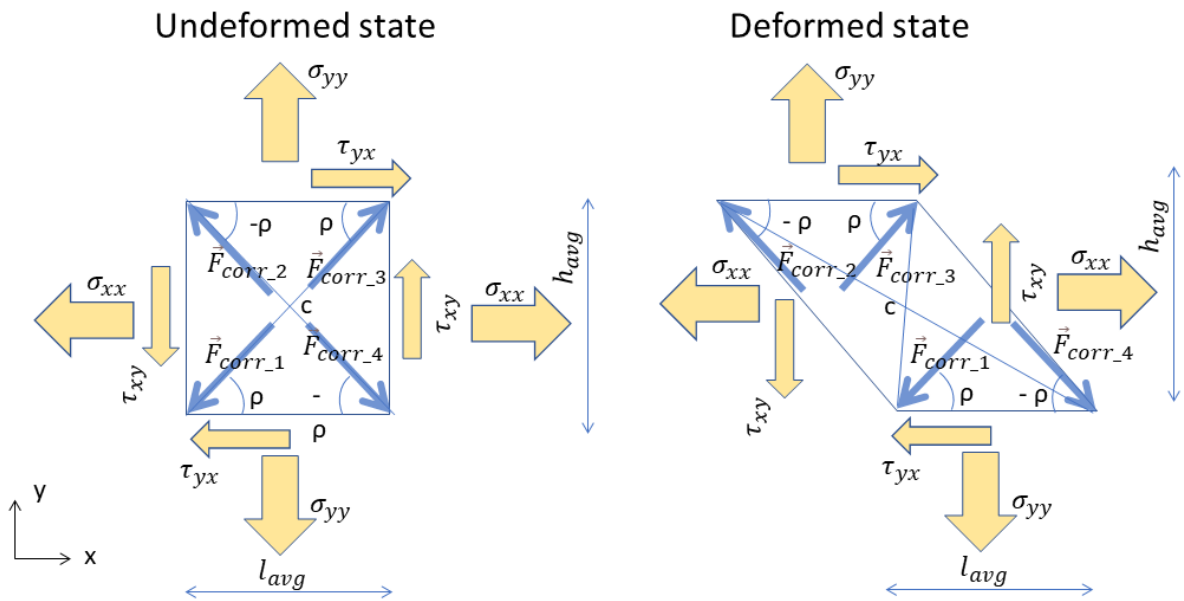


Figure 88 - Concept of a hydrostatic volume correction, which was applied to an undeformed (left) and a shear deformed module (right).

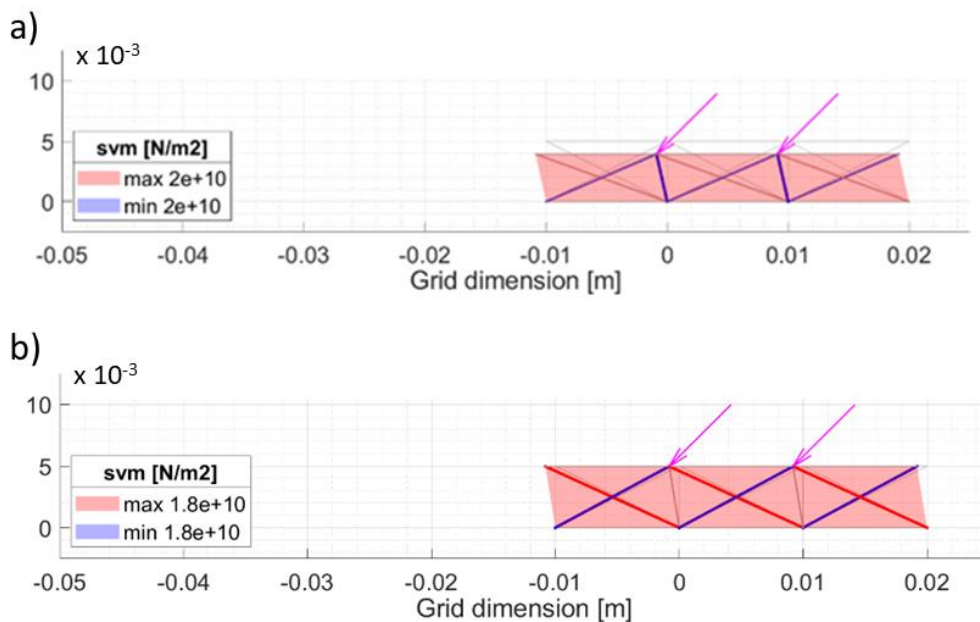


Figure 89 - Test of the volume correction. a) illustrates the case without the correction; b) represents the case with correction.

In the next step, a test was performed for a simple grid. A compressive shear load was applied to charge the modules. A periodic boundary condition was applied.

The first test was performed without volume correction, the second with correction. The result is displayed in Figure 89. The equivalent stresses for the net and the total case were analysed, each for the uncorrected and the corrected case (see Table 22).

The results (see Figure 89, see Table 22) indicated a satisfactory correction of the volume, which was the primary goal. The results were only processed for a modestly deformed grid, but this was considered to be sufficient for the analysis.

Results WITHOUT VolCorr							Results WITH VolCorr				
Volume	-21,3%						-0,6%				
Stress	sxx	syy	szz	tau	svm true	svm eng	sxx	syy	szz	tau	svm true
net	-1,5E+10	-1,0E+10	-7,5E+09	-1,1E+10	2,04E+10	1,76E+10	1,5E+08	-8,0E+07	2,0E+07	-1,0E+10	1,73E+10
total	-1,5E+10	-1,0E+10	-7,5E+09	-1,1E+10	2,04E+10	1,76E+10	-9,8E+09	-1,0E+10	-5,9E+09	-1,0E+10	1,78E+10

**Table 22 - Volume and stress results (net and total) for the cases without- (left) and with volume correction (right).**

The stresses revealed that the equivalent stresses for the uncorrected and corrected cases diverged. As true stresses were processed (see section 4.9), this was attributed to the different edge lengths that resulted from the surface lowering of the uncorrected case. Therefore, the result was referenced to the original length (engineering stress), which revealed a good agreement with the results of the corrected case. For the corrected case, there is a minor deviation between the net and the total result, which, however, was negligible. This proved that the correction fulfilled at least part of its goal, to conserve the equivalent stress.

Besides the equivalent stress, the stress tensors were compared. Unsurprisingly, the introduction of artificial correction forces had a mutual effect on the element forces. As a result, the stress tensor  $\tau_\sigma$  was not applicable for the corrected case.

Besides the test result, another shortcoming of the correction was identified by a look at the deformed case of Figure 88. Due to the shear deformation, a torque was introduced by the correction forces around the centre of gravity marked by "c". By consideration of Equation 90, the torque was dependent of the volume of each module. Thus, the application of the correction would lead to the introduction of artificial torques of different quantity, which would significantly compromise the grid's mechanical response. This was deemed to be unacceptable.

Maybe a differentiation of the correction force quantity  $F_{corr}$  regarding the forces "1" to "4" and of the correction angle  $\rho$  would provide a solution. Another possibility

could have been to substitute the control parameter of  $\Delta V$  by  $\gamma_{xy}$ . Nevertheless, due to complexity, both considerations were not attempted.

Finally, it was not possible to develop a concept that corrects the decrease of module stiffness as function of  $\Delta V$  without compromising the stress processing. The latter, however, was considered to be essential for a proper modelling of crack growth (see chapter 5). Thus, the concept was dropped.

### **7.1.3 Limitation of explicit SPD modelling**

The goal of section 7.1 was to model high shear deformation in a direct, explicit way. This means that the grid basically deforms like a real material (i.e. see Figure 5).

Therefore, tests were simulated for undeformed and deformed grids (see section 7.1.1). The development of the equivalent stress and the volume were analysed. The finding was that, for the same applied load, the shear deformed grid responded in a significantly "softer" way than the undeformed grid did. This was attributed to the truss kinematics and led to a higher degree of deformation and stress as a function of the shear strain.

Thus, a modification of the grid's mechanical behaviour was attempted by means of a volume correction (see section 7.1.2). The goal was to selectively stiffen the grid as a function of the volume loss, which occurred for highly deformed grids. To achieve this, a hydrostatic correction was applied per DEM module, which was designed to conserve the equivalent von Mises stress.

The tests revealed the shortcomings of the concept as artificial torques were introduced by the correction for higher deformations. Further, the stress tensor was compromised. Both implications were deemed to be unacceptable with respect to the modelling scope (see chapter 3).

As a result, the explicit modelling attempt was put to one side. In the end, the degree of shear deformation was modelled in an implicit way (see chapter 7.2).

## 7.2 Implicit modelling of SPD

In this section, SPD (see section 2.1.1) is modelled in an implicit way, i.e. the process of plastic deformation is not modelled, only its result. The goal is to describe the shear deformation as a function of depth in order to correlate the deformation to experimental FCG data (see chapter 6).

The material was assumed to be in a run-in state, i.e. no further plastification takes place, and a linear-elastic behaviour was supposed. Further, the deformation was assumed to be dependent in depth,  $y'$ , only (1D). This implied that a lateral variation of SPD in x-direction was neglected.

The major outcome of SPD is that the pearlite colonies are deformed with respect to the main strain direction. This results in a lamellar structure of fragmented pearlite (see Figure 5). Under these assumptions, the deformation was described by the engineering shear strain,  $\gamma_{xy}$ , as a function of depth,  $y'$  (see Figure 90).

$$\gamma_{xy} = \frac{u_p}{y'} = \tan(\alpha)$$

Equation 93

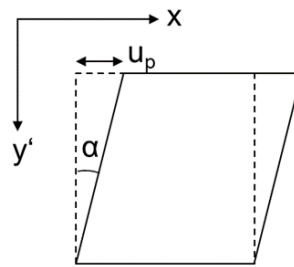


Figure 90 - Shear deformation of a square, modified from (8).

The angle  $\alpha$  represented the plastic angular shear strain (8). A more general description of the shear deformation was applied by Leitner (14), who described the degree of deformation by the von Mises strain,  $\varepsilon_{VM}$ .

$$\varepsilon_{VM} = \frac{\gamma_{xy}}{\sqrt{3}}$$

Equation 94

A relation between the properties  $\alpha$ ,  $\gamma_{xy}$  and  $\varepsilon_{VM}$  is illustrated in Table 23. The degrees of deformation, for which Leitner published FCG data (14), are marked.

Plastic angular shear strain		Shear strain	Von Mises strain	Comment
$\alpha$ (deg)	$\alpha$ (rad)	$\gamma_{xy}$ (-)	$\varepsilon_{VM}$ (-)	
0,0	0	0,00	0,0	-
15,0	0,26	0,27	0,2	-
30,0	0,52	0,58	0,3	-
45,0	0,79	1,00	0,6	-
60,0	1,05	1,73	1,0	-
64,5	1,13	2,10	1,2	FCG Leitner
75,0	1,31	3,73	2,2	-
76,0	1,33	4,01	2,3	FCG Leitner
80,0	1,40	5,67	3,3	-
85,0	1,48	11,43	6,6	-
88,1	1,54	29,99	17,3	FCG Leitner
89,0	1,55	57,29	33,1	-

**Table 23 - Relation between the plastic angular shear strain,  $\alpha$ , the engineering shear strain,  $\gamma_{xy}$  and the Von Mises strain,  $\varepsilon_{VM}$ . The degrees of shear deformation, for which Leitner published FCG data (14), are marked explicitly.**

In order to examine SPD, twin-disc (TD) experiments are performed. With respect to in-service tests, they offer the advantages that the loading condition can be set precisely, the deformation history is known exactly and that the tests are more economical. For this examination, a TD test case from The University of Sheffield (SUROS test rig) of an R350 rail disc was selected. The scope was to use the test case for the SPD modelling and the validation (see section 0).

The rail disc was driven by a wheel disc of the same material. A normal pressure of  $p_0 = 1500$  (MPa) and an axial creep of  $c_x = 5$  (%) were applied under dry conditions. The rotating speed was set to  $N_{rot} = 400$  (rpm). A modified micrograph of the rail disc and its microstructure is displayed in Figure 91. It can be seen that the shear deformation takes place up to a depth of about  $y' = 500 \mu m$ .

The goal of the examination was to approximate the SPD profile, i.e. the plastic angular shear strain,  $\alpha$ , as a function of depth,  $y'$ . A representative displacement trajectory was identified and superposed to the micrograph (see Figure 91). A coordinate system  $(x', y')$  and a sampling grid were introduced. The angles,  $\alpha$ , were measured for the sampled depths,  $y'$ . In this way, the SPD profile  $\alpha = f(y')$  was approximated.



This "manual method" was applied in a straightforward way. However, the selection of a representative displacement trajectory as well as the manual measurement of the angles  $\alpha$  were an approximation and led to a certain error. Actually, both issues decreased the accuracy of the measured SPD profile. A more accurate and reliable method to measure the SPD profile was developed by Trummer et al. (87).

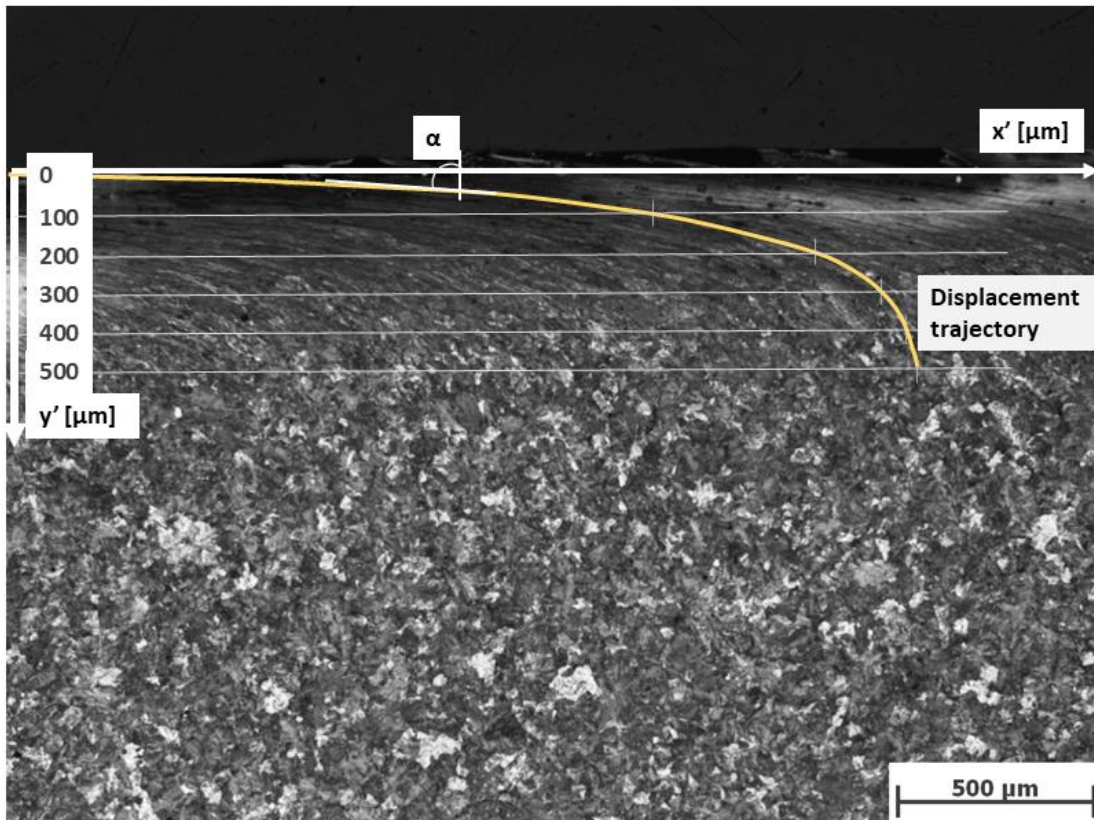


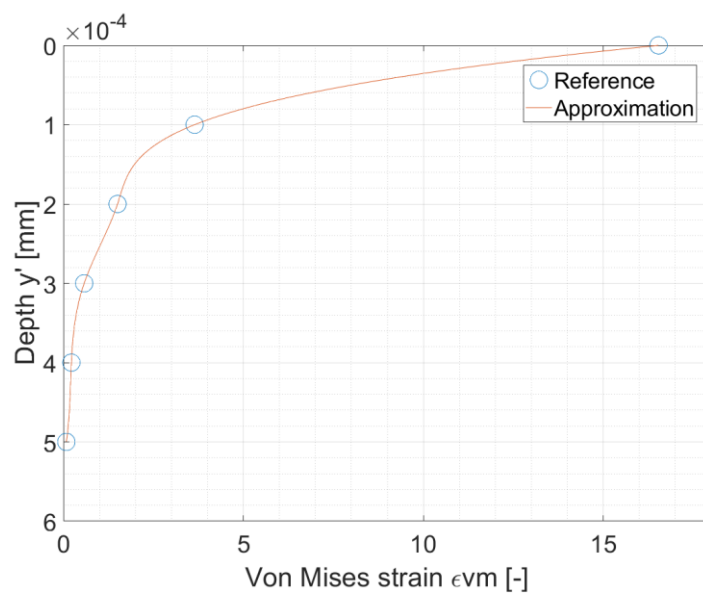
**Figure 91 - Micrograph of an R350 rail disc after twin-disc testing [courtesy of The University of Sheffield]. The SPD profile was approximated by a representative displacement trajectory (yellow) to estimate the SPD profile,  $\alpha = f(y')$ .**

In the next step, the SPD profile  $\alpha = f(y')$  was transformed into a profile of Von Mises strains,  $\varepsilon_{VM} = f(y')$ , by the adoption of Equation 93 and Equation 94. This profile (see Figure 92) provided a correlation to the available FCG data of deformed rail steels (see section 6.1).

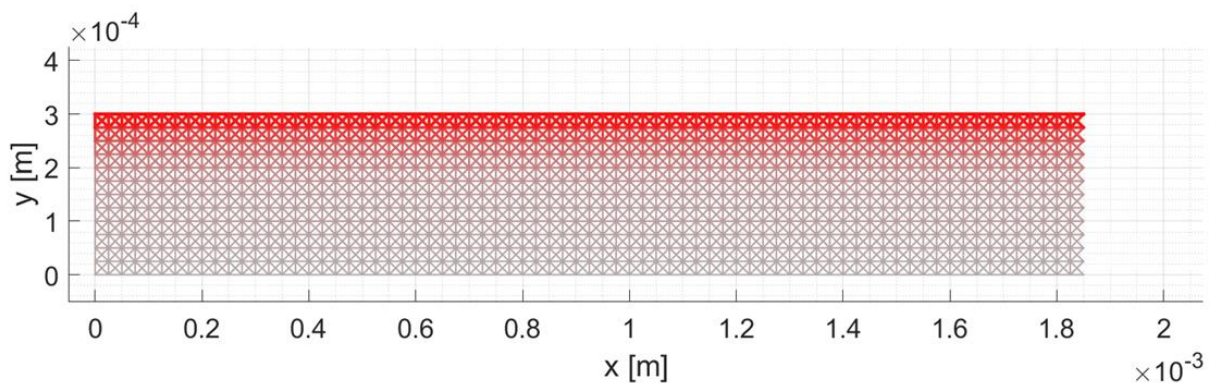
The profile was introduced to the model. As the model consisted of elements, the SPD profile had to be assigned elementwise to the grid. Therefore, a medium-sized RCF grid of 74 x 12 and a unit length of  $l_0 = 2.5e - 5 (m)$  were adopted (see

Figure 93). The grid was aligned to the surface of the TD micrograph (see Figure 91) in order to capture a depth of  $y' = 0 - 300 \text{ } (\mu\text{m})$ .

The sampled data of the SPD profile,  $\varepsilon_{VM} = f(y')$ , was approximated by a cubic spline interpolation to refine the data set (see Figure 92). For each element of the grid, the depth,  $y'$ , was determined. With it, a Von Mises strain,  $\varepsilon_{VM}$ , per element was derived by correlation to the expanded data and interpolation. In this way, each element was assigned a degree of deformation,  $\varepsilon_{VM}$ , as a function of the depth,  $y'$  (see Figure 93). However, the assignment of the deformation represents only an implicit property per element. The grid assembly is not affected by that (see Figure 93).



**Figure 92 - SPD profile of the Von Mises strain as a function of depth,  $\varepsilon_{VM} = f(y')$ : The sampled reference (see Figure 91) and an approximated spline are displayed.**



**Figure 93 - Grid with an illustration of the assigned Von Mises strain,  $\varepsilon_{VM}$ , per element. The line width is referenced to the maximum strain,  $\varepsilon_{VM} = 16.53$  (see Figure above).**

In summary, the SPD profile of a TD test sample was analysed. The measured profile,  $\alpha = f(y')$ , was transformed into a Von Mises strain profile,  $\varepsilon_{VM} = f(y')$ , which was approximated by a spline curve. The curve was used to assign a Von Mises strain to each element of the RCF model. This discretisation of the shear deformation (SPD) provided the precondition to assign deformation dependent FCG parameters to each element of the grid (see chapter 8).

## 8 MODELLING RCF AS A FUNCTION OF SPD

Based on the rolling contact simulation (see chapter 4), a fatigue model was implemented (see chapter 5) and parameterised (see chapter 6). In chapter 7, SPD was modelled. The procedure to integrate SPD to the RCF model and an approach towards validation is displayed in Figure 94.

In the first step, a validation case was defined in order to model anisotropic RCF (see section 8.1). In section 8.2, a test concept was introduced to check the applicability of the FCG parameters to the RCF model. The check was performed for material classes of highly and lowly deformed materials (see sections 8.2.1 and 8.2.2). In this way, a shortcoming of the applied fatigue law was highlighted, which has a fundamental implication for the validation of this and similar RCF models (see section 8.2.3). A parameter study was performed to back this finding (see section 8.2.4). Finally, an overall assessment of the DERC model was performed in which the achievements and open issues with regard to the RCF validation are discussed (see section 8.3).

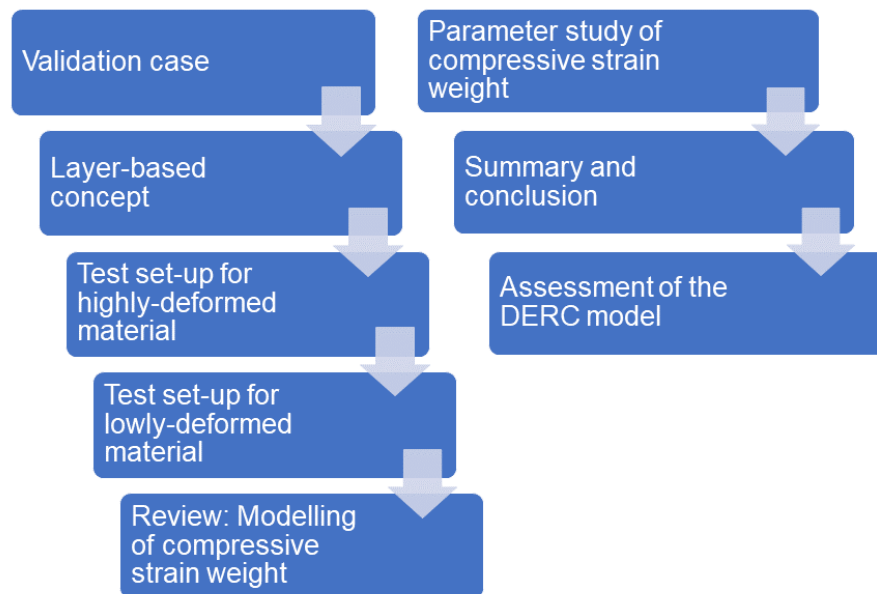


Figure 94 - Overview on the procedure to model RCF as a function of SPD.

### 8.1 Validation case

The aim of this section was to identify an experimental test case as a reference for the model validation. The test case was expected to demonstrate a microstructure of SPD and to be subject to RCF after a specific number of cycles. Furthermore, a

grid was dimensioned and discretised, and the processing time was estimated as a check.

The selection of the validation case was performed according to the basic procedure illustrated in Figure 95. Though, a few iterations were required. First, experimental methods to provide potential references cases were evaluated and a methodology was selected. Based on the selection, an estimation of the applied normal load was performed to approximate the size of the contact patch. With it, a grid was dimensioned and discretised. This provided a reference to conduct a study of the processing time. With respect to the available material data (see Table 20 and Table 21), the available test cases were assessed. A focus was laid on the micrographs in order to study the SPD microstructure and RCF cracks. Finally, a test case was selected.

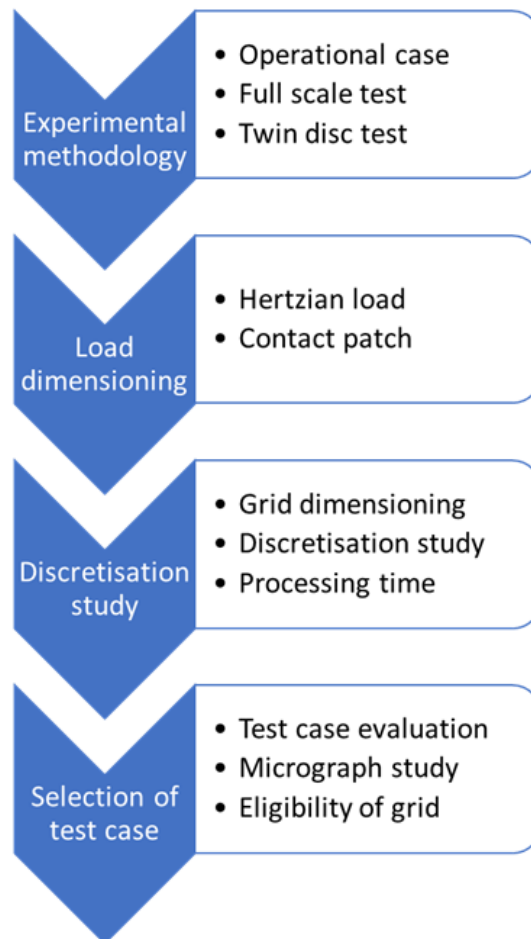


**Figure 95 - Procedure for the identification of a validation test case.**

The first question regarded the experimental methodology (see Figure 95, top chevron). Test cases from railway operations were not considered, as the load- and ambient history are generally not known. The possibility of a full-scale rig was considered initially (8). However, an estimation of the contact patch size revealed the semi-contact length,  $a \approx 8 \text{ mm}$ , to be much longer than the observed crack,  $a_{cr} \approx 1 \text{ mm} \ll a$ . In order to resolve such a crack, a large and fine grid was required, which is a challenge for modelling.

An easier approach offered TD tests, like tests performed at the SUROS test rig of The University of Sheffield. For a typical normal stress of  $p_0 = 1500 \text{ MPa}$  and an assumed Hertzian contact, the semi-contact length was estimated to be  $a \approx 0.3 \text{ mm}$  (a description is given below). Available test data suggested crack lengths to be of a similar order like that of the full-scale rig,  $a_{cr} \approx 1 \text{ mm}$ . This eased modelling as it offered the possibility to reduce the lateral grid size, and to resolve the crack in a satisfying way. For this reason, test results of the TD methodology were selected.

Tests on the SUROS rig were performed with discs of radii of  $R_1 = R_2 = 23.5 \text{ mm}$  and a width of  $w = 10 \text{ mm}$ . For a detailed explanation of the tests and an analysis of the RCF behaviour, the reader is referred to (70). For an applied normal stress of  $p_0 = 1500 \text{ MPa}$ , the Hertzian contact was calculated for a line-line contact. The Young's modulus  $E$  and the Poisson's ratio  $\nu$  were adopted from section 5.1.6. With it, the semi-contact length was calculated to be  $a = 0.31 \text{ mm}$ , which provided the basic parameter for the grid dimensioning.

A finding from the study of the lateral boundary condition (see section 5.2.1) was the identification of a minimum lateral grid width,  $5a$ , to avoid edge effects. This criterion was applied for the derived semi-contact patch width,  $a$ , and resulted in a minimum required grid width of  $5a = 1.55 \text{ mm}$ .

In the next step, the coefficient of friction was estimated to estimate the required grid depth. For the TD tests described in (70), Trummer described the coefficient of traction for axial creepages between  $c_x = 1 - 5\%$  to be in a range of  $\mu = 0.34 - 0.45$ . This condition was assumed. For such a range of  $\mu$ , the maximum of the stress field was expected to be at the surface of the rolling contact (see Figure 31) (77). Thus, a minimum grid depth of  $1a \approx 0.3 \text{ mm}$  was estimated to be sufficient to capture the RCF condition. In this way, a minimum grid dimension of  $1.55 \times 0.3 \text{ mm}$  was identified.

In the next step, the discretisation was assessed. The major criterion for the set-up of the discretisation was the potential to resolve surface cracks. A review of the available TD data indicated a dependence of the depth of surface cracks on the material. Due to the available material library (see Table 20 and Table 21), only tests for R260 and R350HT were considered. The micrographs for the weaker

R260 exhibited a higher degree of SPD, which suggested the maximum crack depth to be  $d_{cr} < 50 \mu m$ . The stronger R350HT was subject to less SPD, resulting in cracks that grew with a higher inclination into the material. The data suggested the maximum crack depths to be higher than  $d_{cr} > 100 \mu m$ . Due to the better eligibility to resolve surface cracks with a grid, test data of R350HT was preferred to R260. Based on an estimated crack depth of  $d_{cr} > 100 \mu m$ , a minimum discretisation of  $\Delta x = 25 \mu m = 2.5 e - 5 m$  was defined.

For the stated grid dimension and the defined discretisation, this resulted in a  $62 \times 12$  grid. The grid was set up, the elasticity parameter was derived (see section 5.1.6) and a normal pressure of  $p_0 = 1500 MPa$  was applied. One increment was run, and the required processing time was measured to be approximately  $t_{proc} = 45 s$ . For a grid with 62 increments per rolling contact cycle, this resulted in a total processing time of  $t_{proc} = 45 min$  per cycle. This effort was considered to be an acceptable maximum processing time. As a result, no further grid refinement was considered. Moreover, the result confirmed the capability of the model to simulate a TD validation case in a realistic time.

In the next step, TD test series of R350HT were evaluated. Only series of a dry contact condition were assessed, as the influence of lubrication was not captured by the model. The material pairing was selected to be R350HT for both, the rail- and the wheel disc. The idea was to eventually model the wheel condition at a later stage, which was not performed in this work. Further, a test with a high loading of  $p_0 = 1500 MPa$  and an axial creep of  $c_x = 5\%$  was selected. Regarding the coefficient of traction, a value of  $\mu = 0.45$  was measured. The test set-up is summarised in Table 24.

Test ID	Rail/Wheel discs	Pressure $p_0$ (MPa)	Ax. creep $c_x$ (%)	Rot $N_{rot}$ (rpm)	Contact (-)	Cycles $N$ (-)
Dyn9/B09	R350HT/ R350HT	1500	5	400	dry	25.000

**Table 24 - Test condition of the selected TD validation case, performed at the SUROS test rig of The University of Sheffield.**

An analysis of the available micrographs of the rail disc was performed. The SPD microstructure is displayed in the etched micrograph of Figure 91. It illustrates the alignment of the deformed microstructure, which was highlighted by the marked displacement trajectory. In Figure 96, the surface section after 25.000 cycles is

displayed. Several cracks of comparable size and depth are illustrated. The crack length was estimated to be  $a_{cr} = 1000 \mu m$ , the crack depth to be  $d_{cr} = 100 \mu m$ .

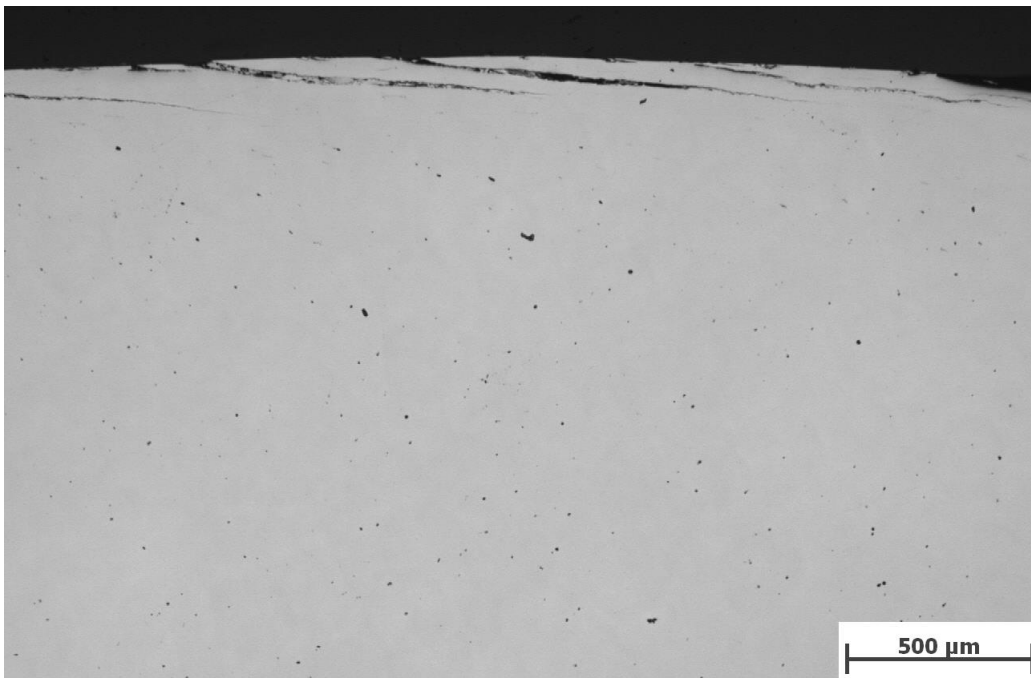


**Figure 96 - Micrograph of a R350HT rail disc section [courtesy of The University of Sheffield]. In the central part of the figure, below the surface, two cracks of an approximate length of 1 mm are illustrated.**

In the final step, the eligibility of the grid to resolve the test case was assessed. A minimum grid discretisation of  $\Delta x = 25 \mu m$  was proposed. With it, the crack path of a highly shear deformed surface layer can be approximated. The discretisation provides for an acceptable processing time. From a modelling point of view, a grid refinement would be desirable to improve the resolution. This measure, however, would lead to a considerable penalty of the numerical efficiency.

Regarding a crack depth,  $d_{cr} = 130 \mu m$ , the proposed grid depth of  $300 \mu m$  is appropriate to avoid edge effects. Concerning the expected crack length of up to  $1800 \mu m$ , the proposed grid width of  $1.55 mm$  is hardly sufficient, although the periodic boundary condition (see section 4.11) eases this matter. Thus, the grid width was extended to  $1850 \mu m$ , which represents  $5.8a$  with respect to the contact patch (see Figure 93). Further, a periodic boundary condition was applied, which facilitated the crack exiting on one lateral edge of the grid and entering on the opposite side.



Regarding the modelling of the SPD profile, which exhibited a depth of approximately  $500 \mu\text{m}$  (see Figure 91), the proposed grid depth captured most but not all of the shear deformed layers. However, a complete coverage of the SPD profile was not required, as the focus was laid on the crack modelling.

In summary, the TD methodology was selected to provide a validation test case that encompasses the phenomena of SPD and RCF. The applied load and the resulting contact patch were estimated. A grid with a specific discretisation were drafted, and the resulting processing time was estimated. An analysis of the available TD test series was performed, and a validation case for a rail disc of R350HT material was selected. The test case was discussed with regard to the final SPD microstructure and the RCF state. In this way, a reference case for the validation of the DERC model was established. In the next section, a concept to model the FCG anisotropy is introduced to the grid (see section 8.2).

## 8.2 Layer-based concept

In order to model the validation case (see section 8.1), the material library for R350HT (see Table 21) was adopted, including the developed interpolation method (see section 6.5). The latter provided a way to parameterise the highly deformed material of FCG orientation "A-T" as a function of shear deformation,  $\varepsilon_{VM}$ .

The material library was derived by a standard method for a Mode I set-up (49). In the next step, the parameters of the library were transferred to the RCF model, which represented a major shift. Thus, the first step for the introduction of the anisotropy was to introduce a simple test concept to check the applicability of the FCG parameters of the material library with regard to the RCF model (see section 8.2.1). For that purpose, a simplified test set-up was introduced, which modelled exclusively one layer of SPD (see section 7.2) and the associated FCG orientation (see section 6). In this way, a preferred FCG path was introduced deliberately to check the validity of the FCG parameters (see section 6.4) and the SPD interpolation method (see section 6.5) for an RCF condition.

As the check revealed a restriction of the FCG parameters of the highly deformed material, the introduction was re-performed with a less deformed material class (see section 8.2.2). The results were analysed and revealed that a review of the fatigue law (see Figure 36) with respect to the weighting of the compressive strains was required (see section 8.2.3). In section 8.2.4, a parameter study of the weighting was performed. A summary of this attempt is given in section 8.2.5.

### 8.2.1 Test set-up for highly-deformed material

The FCG parameters of the material library were derived by Mode I tests (see chapter 6). In the next step, the parameters were integrated to the RCF model, which represented a major shift. The aim of this section was to introduce a simplified test set-up to check the applicability of these parameters for the simulation of the validation case.

The focus was laid on the FCG orientation "A-T" (see Figure 75), which represented the orientation with the fastest rate (5). Analysis of rail materials subject to SPD suggested that RCF cracks preferably proceed along specific paths or layers (3) (see Figure 5). These layers can be associated to the SPD structure of a material, i.e. to a displacement trajectory (see Figure 91). This shape of layer was adopted and modelled as a single entity to validate the applicability of the interpolated FCG parameters (see section 6.5) for the validation case (see section 8.1). The layer represents a preferred, but not exclusive FCG path, as basically all elements are subject to FCG processing (see section 5.1). The set-up served exclusively to assess the validity of the FCG parameters, not to model the TD validation case (see section 8.1).

The grid dimension, discretisation and applied stress were set up in agreement with the validation case (see section 8.1). The grid was superposed to the micrograph, which was used to model SPD (see Figure 91). The illustration is displayed below (see Figure 97). The figure highlights the importance to balance the grid dimension and discretisation with the modelling scope. The influence of the radial geometry of the disc on the grid was neglected.

The superposed displacement trajectory was used as a reference to define the layer of the FCG orientation "A-T". All elements that were crossed by the trajectory were marked and defined to be part of an element class A-T, which is displayed in Figure 98. For each module (see Figure 19) that was crossed by the trajectory, elements of all relative orientations (horizontal, vertical, diagonal) were selected for class A-T to reduce the effect of the element orientation (see section 5.2.6). In order to avoid surface effects (see section 5.1.7), the surface line of elements was excluded from the assignment.

All other elements not marked to be class A-T were defined to be of a residual class, which was defined to be of FCG orientation "T-A" (see Figure 75).

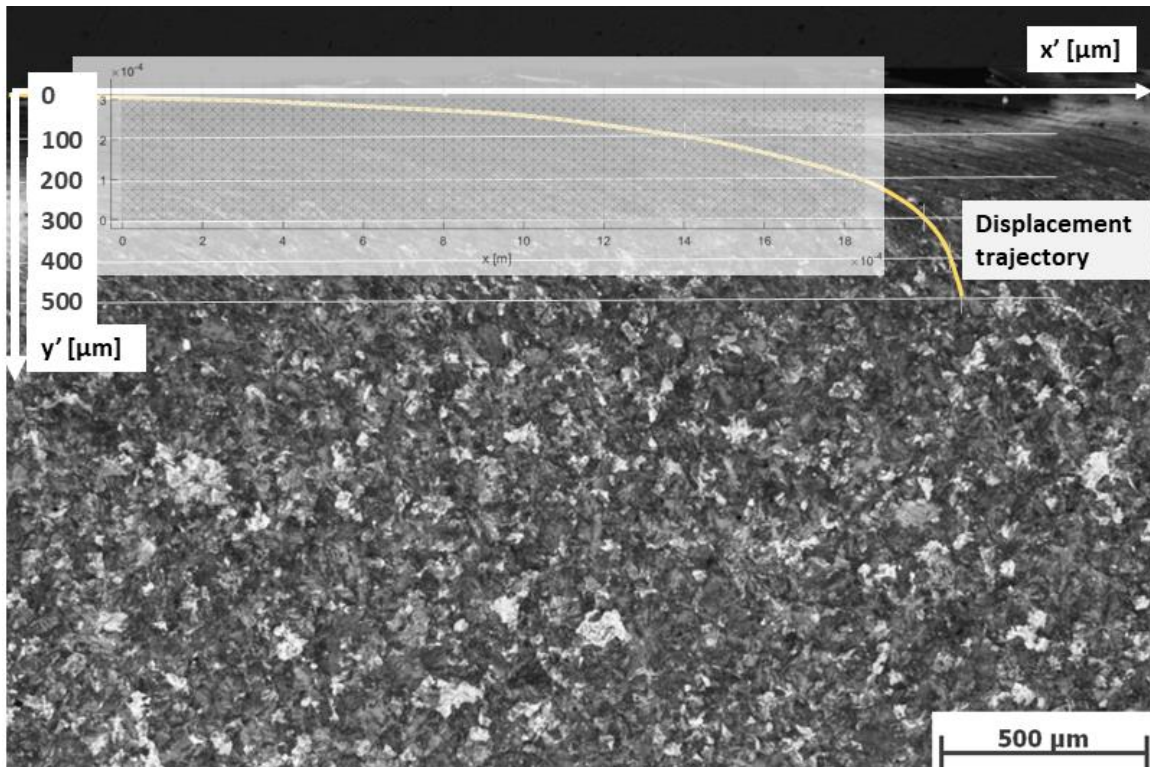


Figure 97 - Micrograph of an R350 rail disc after twin-disc testing [courtesy of The University of Sheffield]. The SPD profile was approximated by a representative displacement trajectory (yellow). The validation grid was superposed (window).

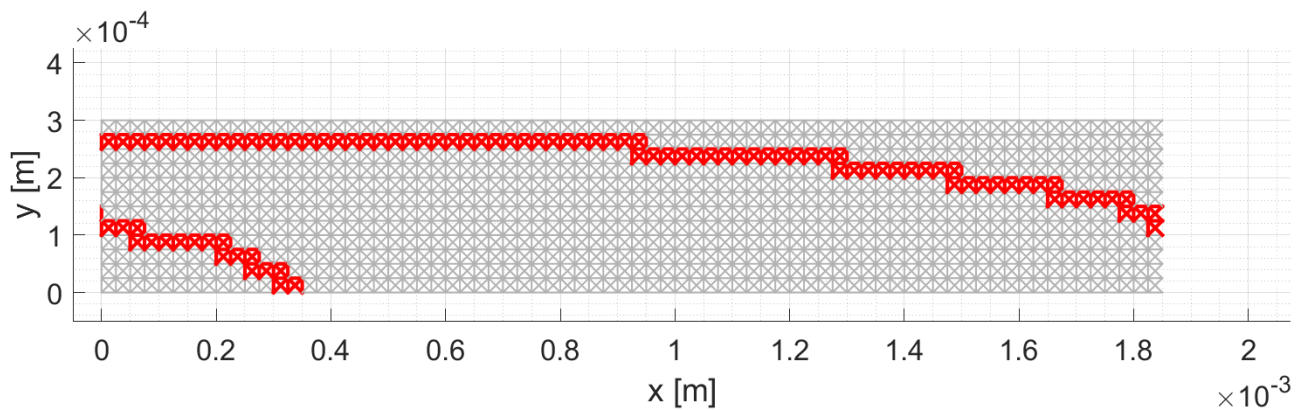
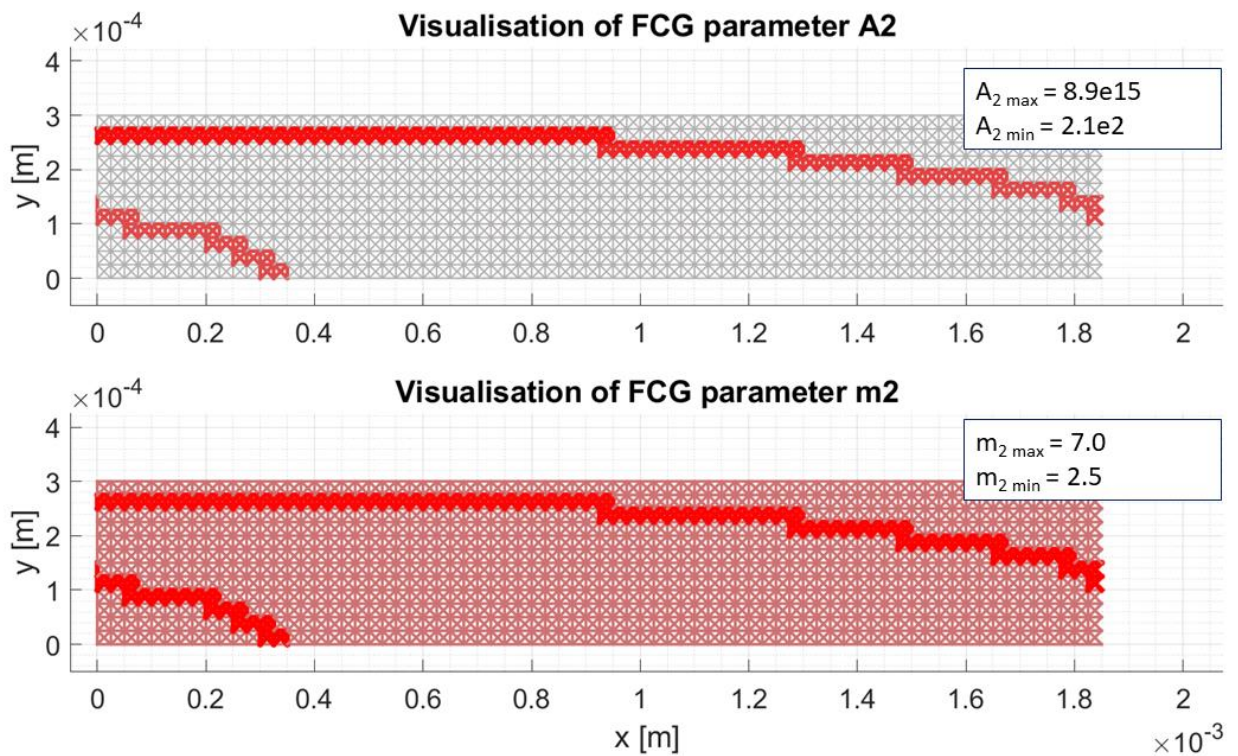


Figure 98 - Validation grid with elements of class A-T marked in red. For the class of A-T, the interpolation of FCG parameters (see section 6.5) was performed within the specified depth interval (see Figure 83).

A limitation of the model regards the modest grid discretisation, which is manifest in the coarse modelling of the displacement trajectory (see Figure 98). The figure highlights the requirement for an optimisation to improve the performance, which

would facilitate a grid refinement and boost the resolution of crack patterns. Further, materials with a higher degree of SPD could be modelled (see section 8.1).

For the FCG parameterisation of the residual class, material class "R350\_C03" was adopted. For the definition of the minimum- and maximum classes of the A-T class, the material classes of "R350\_C12" and "R350\_C22" were employed (see Table 22). The maximum- and minimum classes corresponded to deformations of  $\varepsilon_{VM} = 16.5$  and  $\varepsilon_{VM} = 2.3$ , which corresponded to depths of  $y' = 0 \mu m$  and  $y' = 130 \mu m$  (see Figure 92). The scaling of the parameters,  $A_2$ , to account for the reduced grid discretisation, was performed according to the described procedure (see section 6.3), which reduced the values. In this way, the FCG parameters  $A_2$  and  $m_2$  (see Figure 99) as well as the threshold parameter  $\Delta\varepsilon_\infty$  were assigned.



**Figure 99 - Assignment of FCG parameters to the anisotropic grid: Elements of the class AT display the maxima for both parameters (see bright red lines).**

An initial crack was set on the left edge of the grid's surface. The specified stress was applied (see section 8.1). The surface row of elements was excluded from FCG processing to avoid edge effects. The goal of the test was to check the applicability of the FCG parameters of class A-T, which required a strain analysis.

The objective was to compare the strains of class A-T to the transition strains,  $\epsilon_{trans}$  (see Table 19), defined in section 6.5. Therefore, only three cycles were run (see Figure 100).

The result displayed the failure of four failed elements, all of class A-T. This fact suggested the strains around the initial crack to be high, or the FCG parameters to be sensitive. The maximum strains,  $\epsilon_{max}$ , of the A-T elements were analysed (see Table 25). Before their failure, the three elements exceeded their specified transition strain. This meant that the FCG data, which was applied to process the fatigue state, was out of specification.

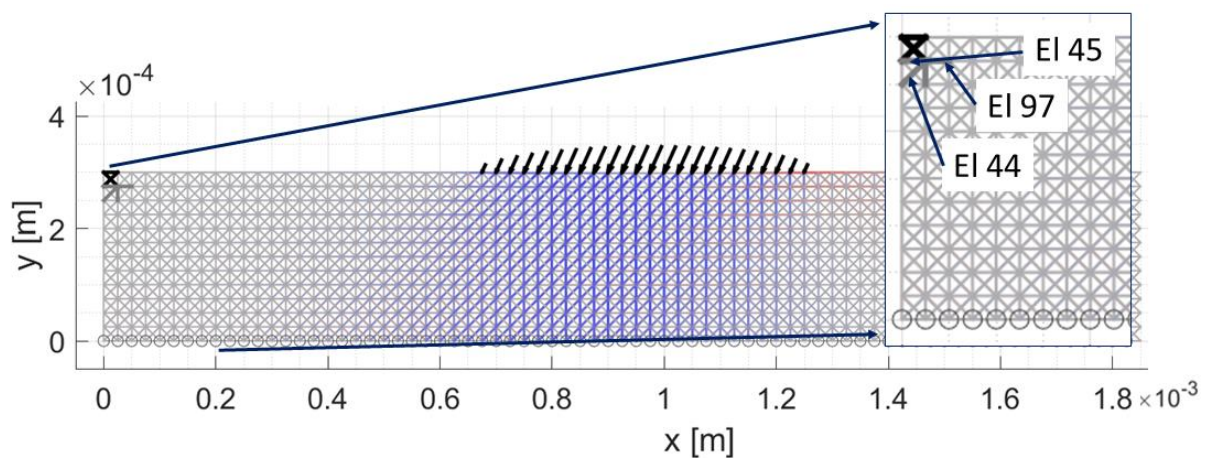


**Figure 100 - Anisotropic RCF grid: The elements of the initial crack are marked black, elements of the proceeding crack grey, elements strained in compression blue, tensile strained elements red. In the magnification, elements are marked that exceeded  $\epsilon_{trans}$ .**

Element	$\epsilon_{trans}$ (-)	$\epsilon_{max}$ (-)
44	1.4e-3	7.6e-3
45	1.2e-3	1.8e-2
97	1.2e-3	2.0e-3

**Table 25 - Strain analysis of the elements of class AT before failure.**

With regard to the specification given in Figure 83, this fact indicated that either the transition to FCG Stage II occurred for the elements, or fracture. Due to the lack of experimental data between the two limiting material classes, the question was not answered. However, it was clear that the specification for the application



of the FCG parameters was exceeded, and that the parameters were not specified to be used for the set-up of the simulation. On a physical level that implied that the load was sufficiently high to position the crack tip in FCG Stage II, not Stage I.

Thus, material data for FCG Stage II was required that describes the FCG rate in the A-T direction. A view on the material data (see Figure 82) revealed that besides the highly deformed class of  $\varepsilon_{VM} = 17.3$ , only the A-T material class for  $\varepsilon_{VM} = 1.2$  was parameterised. A comparison with the series for  $\varepsilon_{VM} = 2.3$  in (5) suggested the FCG rates of both series in FCG Stage II to be similar. With regard to the expected scatter of experimental FCG data, there was no significant difference.

In this section, a simplified set-up was introduced to assess the applicability of the FCG parameters respect to the RCF application. The anisotropy was modelled by a layer, which was defined by the SPD displacement trajectory. This layer was modelled by a class of elements, to which the FCG parameters of the highly deformed FCG orientation A-T were assigned. A gradient of deformation in depth was modelled with respect to the developed interpolation. The strain analysis after a few cycles indicated that the strains were higher than specified, which suggested the elements to fatigue in FCG Stage II, or to suffer fracture (Stage III). This denied the employment of the FCG data and required valid parameters for FCG Stage II.

Thus, class "R350\_C02" of the lowly deformed material,  $\varepsilon_{VM} = 1.2$ , was selected to model the FCG orientation of A-T. A modelling of a depth gradient was neglected. The suitability of this parameter set was checked in section 8.2.2.

### **8.2.2 Test set-up for lowly-deformed material**

In the previous section, a simplified anisotropy concept (test set-up) was introduced to check the application of the FCG parameters of deformed rail steel for a rolling contact set-up (see section 8.2.1). The test demonstrated that the high applied stress of the contact caused strains in the surface area that exceeded the specification of the employed material classes. The conclusion was that parameters were required that capture the FCG Stage II.

An analysis of the available data led to the conclusion to adopt the lowly deformed class "R350\_C02", that represented a deformation of  $\varepsilon_{VM} = 1.2$ . The aim of this section was to run the model for the same set-up, but with a modification of the introduced anisotropic layer A-T, and to check the FCG rate with respect to the experimental validation case (see section 8.1).

The grid set-up, the applied stress, the initial crack, and the deactivation of the FCG processing on the surface were adopted (see section 8.2.1). The elements of class A-T (see Figure 98) were assigned with the parameters from class "R350\_C02" (see Table 21). Deviating from the first trial, no gradient in depth was implemented to the parameters of A-T. The residual class was modelled by the assignment of FCG orientation T-A.

The experimental reference case exhibited a crack length of about  $a_{cr} = 1 \text{ mm}$  after 25.000 cycles (see Figure 96). That crack grew in a near-surface layer of highly deformed material, where the degree of deformation was estimated to be  $\varepsilon_{VM} > 16$  (see Figure 91 and Figure 92). The simulation set-up of the "highly deformed layer", however, was based on FCG data of a modest deformation of only  $\varepsilon_{VM} = 1.2$ . Thus, a cycle rate of at least 50% higher than the experimental reference was expected for the model.

The result of the simulation after 800 cycles is illustrated in Figure 101, which displays a crack with a length of  $a_{cr} = 0.35 \text{ mm}$ , propagating along the elements of class A-T. This represented a major overestimation of the FCG rate, as 35% of the expected final crack length were obtained after just 3% of the cycles of the reference.

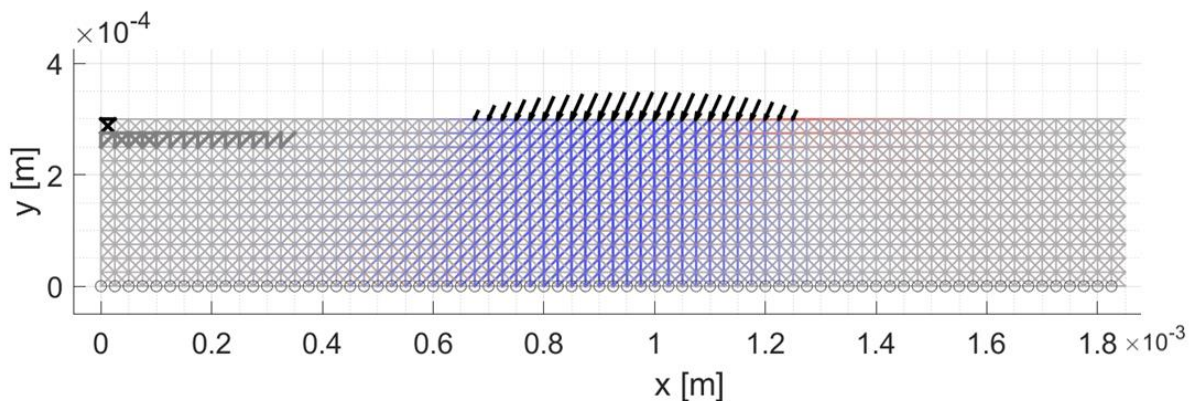


**Figure 101 - Anisotropic RCF grid after 800 cycles: Elements of the initial crack are marked black, the proceeding crack in grey, elements strained in compression blue, and the ones strained in tension red.**

The further progress was estimated to proceed in a rather linear way. Based on this consideration, only 2000 - 3000 cycles were expected to reach the crack length of the experimental reference. This highlighted that the model of the lowly deformed material still overestimated the FCG rate to a major degree.

Thus, the modelling approach was reviewed. The parameters  $A_2$  and  $m_2$  that determine the FCG rate for Stage II were derived with respect to a procedure adopted from the literature for a Mode I test. The result was compared against an experimental reference, which demonstrated a satisfying agreement for Stage II (see Figure 82). The scaling of the parameter  $A_2$  with respect to the discretisation was performed according to a procedure and was proven by a discretisation study (see Figure 81).

This identified the transfer from Mode I to the RCF ambient as an issue of interest. For Mode I and stress ratios of  $R > 0$ , the strain field around the crack tip revealed exclusively tensile strains (see Figure 77), i.e. bold elements coloured in red. The strain field of the RCF model (see Figure 100), though being remote from the crack tip, exhibited predominantly compressive strains, i.e. bold blue elements.

The difference of the two strain fields obviously had a significant contribution on the fatigue law (see Equation 39), which was due to the definition of the cyclic bond strain,  $\Delta\varepsilon$ , (see Equation 40). This definition was identified to be a key aspect, which was scrutinised in section 8.2.3.

In brief, the simplified anisotropic RCF set-up was run for a material class of low deformed material. Instead of an expected underestimation, the model significantly overestimated the FCG rate. The modelling approach was reviewed, and a key issue was identified, i.e. the contribution of tensile- and compressive strains to the FCG development. Thus, a literature review (see section 8.2.3) and a parameter study were performed (see section 8.2.4).

### **8.2.3 Review: Modelling of compressive strain weight**

In section 8.2.2, the layer-based test concept was applied. The subsurface layer was parameterised with a class of lowly deformed material. For this set-up, the model overestimated the crack growth rate by a factor of 10.

A review of the model approach identified the definition of the cyclic bond strain,  $\Delta\varepsilon$ , to be the key factor, which is the difference between the maximum- (tensile) and minimum (compressive) strain. This parameter is the driving factor for crack growth in the model. The result of the previous section (see Figure 101) strongly suggested the influence of the compressive strains to be overrated. The aim of this section was to review and discuss the state of the art with respect to the adopted fatigue law and the cyclic bond strain definition.

The focus of the review was laid on peridynamic models, where the fatigue law of Silling and Askari (49) was adopted. Papers with a focus on rolling contact



modelling were analysed. All papers were published in the recent years, which highlighted the novelty of the modelling approach.

Regarding the derivation of the FCG parameters, the procedure based on the Mode I case (see chapter 6) is state of the art. The reviewed models with a focus on rolling contact were parameterised with positive load ratios,  $R > 0$ , (54,65,88). This suggested an agreement about neglecting negative load ratios,  $R < 0$ , for the FCG parameterisation.

The cyclic bond strain definition of  $\Delta\varepsilon$  (see Equation 40) represented the standard approach (53,54,65), which implied an equal influence of tensile- and compressive strains. For the estimation of a Mode I case, Silling and Askari (49) estimated the strain minimum,  $\varepsilon^-$ , with respect to the strain maximum,  $\varepsilon^+$ , by a correlation to the stress ratio,  $R$ , to improve the simulation efficiency (see Equation 67).

This simplification was adopted in some cases (53,55,57), which, however, is a valid approximation for Mode I only. For an RCF case, where elements are strained in tension and compression, the assumption would effectively eliminate the influence of compressive strains. In order to model plasticity effects, Liu et al. (89) performed a modification of the definition of  $\Delta\varepsilon$ , which, though, was not considered in this work.

Finally, the aspect of validation of rolling contact models was reviewed. Freimanis et al. highlighted the issue of the bond law in case of failure (see 2.2.4) to be critical for the validation of the squat model (53). Wang et al. compared the results of the proposed RCF model to similar numerical solutions (65), whereas Ma et al. (63) emphasised the importance of experimental test methods like TD rigs for validation.

In brief, fatigue modelling by means of discrete and peridynamic models is a recent development. The initially introduced definition of the cyclic bond strain,  $\Delta\varepsilon$ , was not challenged yet by the modelling community. With respect to the modelling of RCF, however, the result of section 8.2.2 suggested a modification. Moreover, the review highlighted the challenge to validate discrete rolling contact models, which agreed with the findings of this work. In the next step, a parameter study was performed to estimate the influence of the compressive strains on FCG (see section 8.2.4).

#### **8.2.4 Parameter study of compressive strain weight**

Based on the previous findings (see sections 8.2.2 and 8.2.3), the influence of the compressive strains on the FCG development was investigated in this section.

The model set-up was adopted from section 8.2.2. In order to assess the influence of compressive strains on the cyclic bond strain,  $\Delta\varepsilon$  (see Equation 40), a weighting factor,  $f_w$ , was introduced.

$$\Delta\varepsilon = |\varepsilon^+ - f_w * \varepsilon^-|, \quad \text{for } \varepsilon^- < 0$$

Equation 95

This modification was performed only for compressive minimum strains, i.e.  $\varepsilon^- < 0$ . For minimum strains of a tensile character, i.e.  $\varepsilon^- \geq 0$ , the original equation (see Equation 40) was applied.

For the model reference, the weighting factor was set  $f_w = 1$ . Additionally, the model was run for a weighting of 50%, i.e.  $f_w = 0.5$ , and 0%, i.e.  $f_w = 0$ . Due to the quasi-linear progress of the FCG simulation, the model was stopped prematurely, before reaching the reference crack length of  $a_{cr} = 1 \text{ mm}$ . The result for the three series with respect to the experimental reference is illustrated in Figure 102.

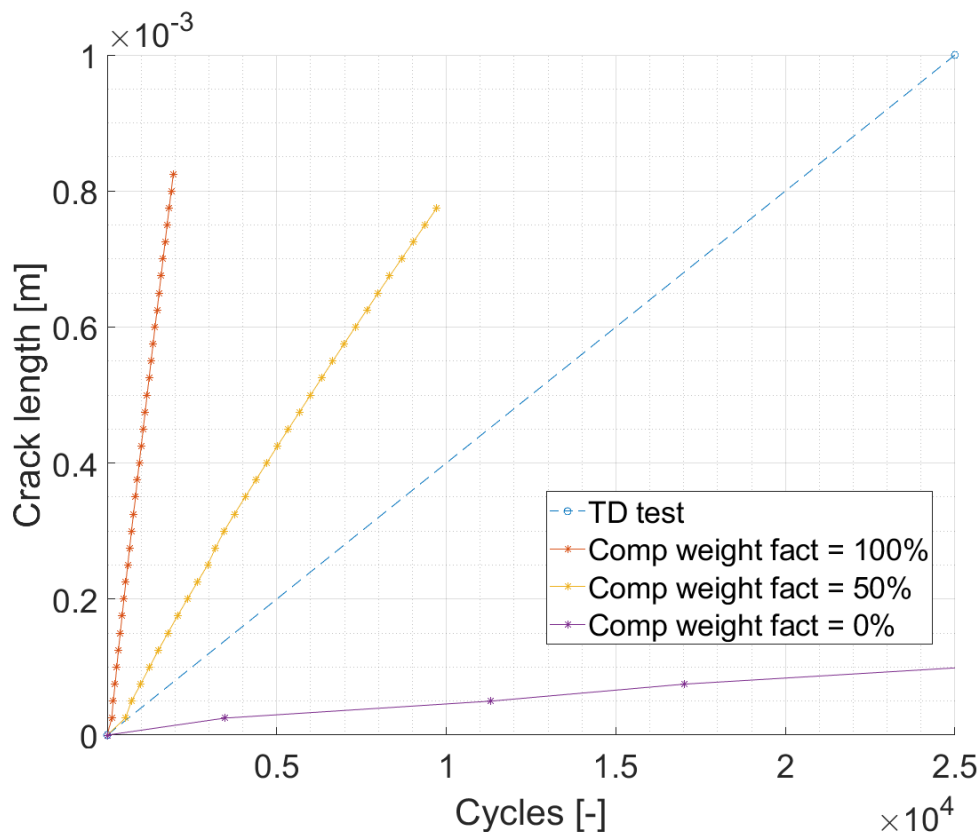


Figure 102 - Parameter study for different compressive weight factors,  $f_w$ . The progress of the experimental TD test was assumed to be linear.

For the experimental TD reference (see section 8.1), only the final crack length was known (see Figure 96). Regarding the initial state, it was assumed that the crack initiated. For the behaviour in between, a linear progress was assumed.

The model result for  $f_w = 1$  demonstrated the highly overestimated rate discussed in section 8.2.2. The FCG rate is about 10 times higher than for the reference. A reduction of the compressive strain weighting by 50% resulted in a significantly reduced FCG rate, which overestimated the reference by a factor of 2. However, a removal of the compressive strains caused an FCG rate, which was significantly below that of the reference.

The results suggested that there existed a sweet spot in a range of  $f_w = 0 - 50\%$ , where the model could capture the experimental crack length. However, it had to be considered that the FCG parameter for the lowly deformed material was applied, which was expected to underestimate the experimental FCG rate.

The aim of this section was to investigate the influence of the compressive strains on the FCG behaviour. Therefore, a weighting factor,  $f_w$ , was introduced. The study revealed this factor to have a major influence. Its outcome strongly suggested that such a weighting factor was required to accurately predict the FCG progress of an RCF simulation. The correct set-up of the factor was interpreted to be as important as the set-up of the derived FCG parameters (see chapter 6). This implied the question, "how can such a factor can be derived?", which is discussed in the next section.

### **8.2.5 Summary and conclusion**

A layer-based test concept was introduced to evaluate the applicability of FCG parameters of the material library to an RCF regime (see section 8.2.1). A preferred layer of crack growth was modelled with respect to the displacement trajectory of the pre-defined validation case (see section 8.1). Elements assigned to this layer were set to be a specific material class, which represented the FCG orientation in A-T direction (see section 6.1).

This test concept was introduced to the validation grid (see section 8.2.1). The element class A-T was FCG parameterised with the data derived from highly deformed R350HT material. A gradient of deformation in depth was modelled. However, due to the characteristics of the experimental data, the parameters were specified exclusively for FCG Stage I. The remaining elements were set to be a residual class, to which the FCG parameters of class of T-A were assigned.

The model was run for this test set-up for a few cycles. The strain field was analysed in order to check the specification of the highly deformed material class (see section 8.2.1). The outcome was that the strains of the highly deformed material class A-T exceeded the specification. On a physical level, this implied that the material either fatigued in FCG Stage II or was subject to fracture. For a better understanding, an extension of the experimental FCG data for R260 and R350HT was required. This regarded especially the FCG orientation A-T in a deformation range between  $\varepsilon_{VM} = 2.3 - 17.3$  to better resolve the transitions from Stage I to II and III.

In order to run the model, the element class A-T was re-parameterised and assigned with FCG parameters of lowly deformed material (see section 8.2.2). As a result, an underestimation of the FCG rate compared to the TD reference case was expected. The modelled FCG rate, however, was far higher than that of the TD reference. As potential cause, the definition of the cyclic bond strain of the fatigue law was identified.

A review of the literature (see section 8.2.3) revealed the assumption, on which the cyclic bond strain was defined, to be state of the art for rolling contact models. The aspect, that compressive loads are supposed to have a different impact on fatigue than tensile ones, was not addressed yet. Furthermore, the review emphasised the difficulties to validate this kind of model.

For a better understanding of the result of section 8.2.2, a parameter study was performed, where the impact of compressive strains on the cyclic bond strains was weighted (see section 8.2.4). The study confirmed the definition of the cyclic bond strain to have a major effect on the FCG rates. With respect to the experimental TD data, the result suggested the influence of compressive element strains to be significantly overrated. Furthermore, it suggested the requirement to implement and parameterise a weighting factor to the model.

The implication of that finding was that an accurate RCF prediction did not work exclusively by the derived FCG parameters. These parameters were required, but additionally, a set-up of the weighting factor to balance the compressive- and tensile strains of the cyclic bond strain was required. This requirement was identified to be a key issue for the validation. Without a proper setting of the weighting factor, the validation cannot be performed. A validation procedure is proposed in section 8.3

The layer-based concept introduced in section 8.2 represents a test set-up. The goal was exclusively to check the applicability of the FCG parameters which were derived in chapter 6, not to model the TD validation case (see section 8.1). Within

the frame of this work, the latter was not performed. An overall assessment of the model is performed in the next section (see section 8.3).

### 8.3 Assessment of the DERC model

The intention of the model development was to overcome the limitations of FEM-based models with regard to fatigue- and fracture simulation (see chapter 3). For this scope, the DERC model was developed as a hybrid approach between DEM and PD modelling. In this section, the development of the anisotropic RCF model is reviewed. The applied assumptions, achieved capabilities, existing limitations and open issues are discussed. An outlook for the future model development is given in chapter 9.

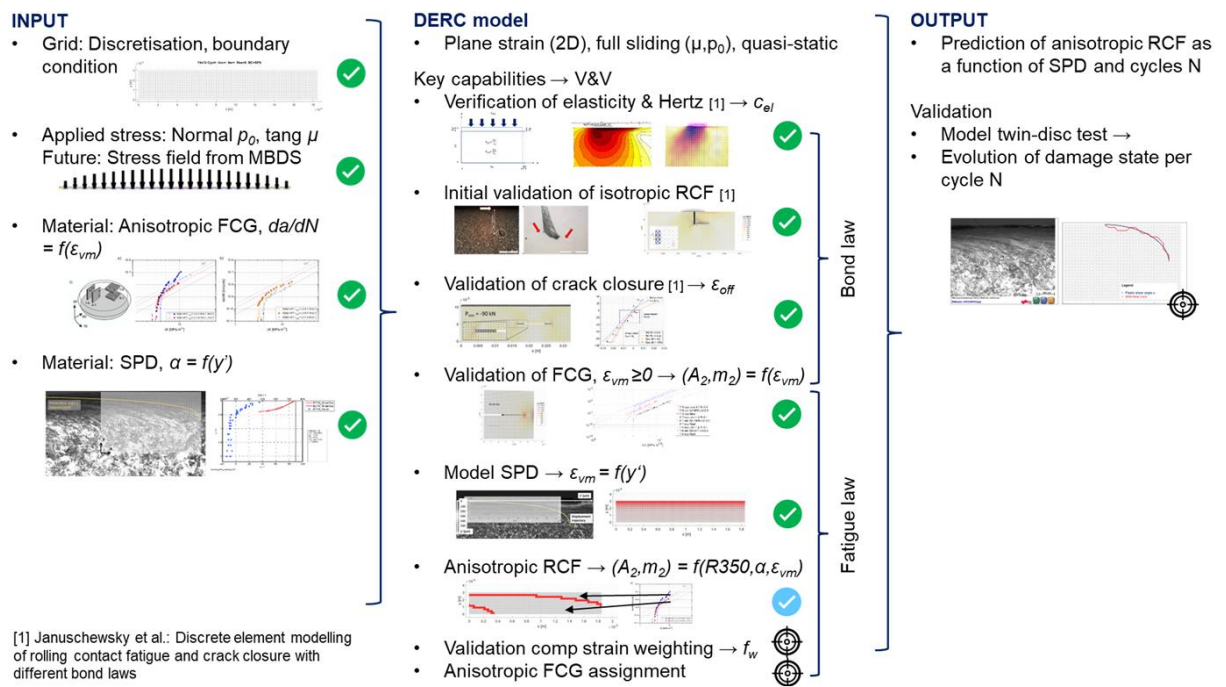


**Figure 103 - Overview of the DERC model: The input is defined in the left column, main assumptions and key capabilities are stated in the centre column, the output is displayed in the right column. Verified and validated capabilities are marked with a green check, initial capabilities by a blue check, open issues by a target symbol.**

The model development is summarised in Figure 103. The grid is dimensioned and discretised in a pre-processing phase (see Figure 103, left). Linear-elastic elements are defined, and modules are introduced to post-process the stress field. Boundary conditions are set up.

As an input, the applied stress distributions in normal- and tangential direction are required (see Figure 103, left). Regarding the stress, a Hertzian contact and full sliding are assumed. The stress field is modelled by discrete forces that attach to

surface nodes of the grid (see section 4.8). The applied stress field can be adopted from an operational environment, i.e. from MBD simulations.

For the modelling, different sets of experimental data are required (see Figure 103, left). First, data that describes the FCG behaviour of rail- and wheel materials for different FCG orientations and degrees of deformation is required (see chapter 6). Second, crack tip opening data is required to parameterise the bond law with respect to crack closure (see section 5.1.8). Finally, experimental micrographs are required to model the SPD structure of the material (see section 7.2).

Key assumptions of the DERC model are that a state of plane-strain and a quasi-static behaviour are assumed. In this way, material sections in the core of a rail- or wheel can be modelled. The application of the model to edge areas has to be considered carefully. Dynamic effects cannot be captured.

The build-up of an SPD state is assumed as an input for the model (see Figure 103, centre). No form of plastification is modelled. For this state, a linear-elastic behaviour is assumed. The elastic characteristic of the model is set by an elasticity parameter, which is derived by procedures that capture the basic elastic deformation behaviour (see section 5.1.6), i.e. Young's modulus and Poisson's ratio. Furthermore, an optimisation is implemented that optimises the Von Mises strain field below a Hertzian contact (see sections 4.13). A model inherent limitation is its restriction to a Poisson's ratio of  $\nu = 0.25$ , which, however, is an acceptable approximation for steel. As a result, the accuracy of the stress field representation is reduced.

Based on the elastic set-up, the RCF model is implemented (see Figure 103, centre; see section 5.1). A single elasticity parameter, and a strain based, linear-elastic bond law are applied. The bond law to model the failed state of elements can be specified. In order to overcome a limitation of the original failure assumption, an improved bond law for failure is introduced, which captures the effect of crack closure (see section 5.1.8). The method represents an initial stage, which offers potential for improvement as crack closure is a complex phenomenon. This set-up offers a relevant improvement for similar bond-based RCF models.

The formation of long cracks is neglected. One- or multiple initial cracks must be introduced to the model (see section 5.2.2). Regarding the modelling of FCG Stage I (near-threshold), an initial capability is implemented (see section 6.2). However, the results of this work (see section 8.2.1) emphasise to improve the modelling of FCG Stage I.

The modelling of FCG Stage II was validated not only for one material, but for multiple material classes (see Figure 103, centre). The introduced procedure

facilitates the derivation of FCG parameters from experimental FCG diagrams (see chapter 6). In this way, a library for specific FCG orientations and degrees of deformation is derived for two rail materials (see section 6.4). Further, a method to scale the FCG parameters as a function of the model horizon is implemented (see section 6.3).

For the FCG parameterisation of highly deformed materials, the exponent that describes FCG Stage II was approximated by means of an initial- and a final data point (see section 6.4). This method, however, neglected the remaining data points. For a more reliable and accurate derivation, a linear regression approach is recommended.

In order to model materials with unspecified degrees of deformation, an interpolation method for materials of similar exponential gradients is defined (see section 6.5). A limitation the method highlighted is the lack of sufficient experimental FCG data, which is required to facilitate the modelling, especially in a range of  $\varepsilon_{VM} > 2.3$  (see section 8.2.1). With that data, the RCF anisotropy can be modelled more accurately. Besides that, a method is defined to expand the derived FCG material library to materials of similar strengths, which helps to ease the lack of experimental data (see section 6.6).

The failure of elements (FCG Stage III) is not yet modelled but can be modelled in a straightforward way by the introduction of a critical strain criterion.

One aspect regards the surface effect introduced by the grid (see section 5.1.7). This effect is caused by the fact that surface elements have a reduced number of adjacent elements, and thus, are subject to more strain. This effect is acknowledged in the literature. The implementation of appropriate measures can facilitate to simulate the FCG behaviour of surface elements in a more reliable way.

The model possesses a processing function that calculates only load cycles, where failure occurs for at least one element (see section 5.1.4). This function enables the simulation to work more efficiently. However, in order to facilitate grids with a higher resolution, an additional optimisation of the solver or the algorithm is required.

A major aspect for the introduction of an RCF anisotropy (see Figure 103, centre) is the grid's inherent FCG characteristic, which was assessed by a study (see section 5.2) with respect to factors like lateral boundary condition, initial crack definition, grid discretisation and FCG activation. The latter aspect (see section 5.2.5) was modified and adopted for the last part of the study, i.e. the analysis of the effect of the grid orientation (see section 5.2.6), and for the subsequent model development.



The SPD microstructure was modelled based on a micrograph derived from a TD test (see Figure 103, centre). A representative displacement trajectory was identified to measure the profile of the plastic angular shear strain as a function of depth (see section 7.2). With it, the Von Mises strain was derived to specify the degree of deformation. Both, the manual identification and the measurement, represent a source of inaccuracy. In order to optimise the approach, it is an option to improve the procedure by an automated processing routine.

A test set-up to check the applicability of FCG parameters to RCF was proposed (see Figure 103, centre). The applied FCG parameters were selected to represent the anisotropy introduced by SPD. The set-up models a single layer (see section 8.2), in which the FCG orientation of A-T was integrated. By adopting the SPD model, a deformation gradient as a function of depth was implemented. For this set-up, the integration of FCG parameters was assessed (see sections 8.2.1 - 8.2.2). The major finding was that the FCG parameters of the material library are required for a validation of the RCF development but are not sufficient (see section 8.2.2). The results of a parameter study (see section 8.2.4) suggested the introduction of a weighting factor to the fatigue law to calibrate the influence of tensile- and compressive strains.

For the validation of the model, a TD validation case was identified (see section 8.1). An open issue, however, is how the FCG anisotropy due to SPD is introduced to the model, i.e. an anisotropic FCG assignment (see Figure 103, centre). The objective is to associate different FCG material classes (see section 6) and the SPD structure of the material (see section 7.2) to the elements of the grid. This modelling aspect is a precondition for the validation.

The open steps to achieve a validation of the DERC model with respect to the specified validation case are:

- a. The identification of correct FCG parameters in FCG orientation A-T. Therefore, an expansion of the experimental data is required. Alternatively, a modelling method can be adopted to derive the parameters from available data in a reliable way.
- b. The derivation of a weighting factor for compressive strains with respect to experimental data. Therefore, the methodology of the performed parameter study can be adopted.
- c. A concept and implementation regarding the assignment of FCG material parameters to the elements of the grid to model the anisotropy imposed by SPD.

- d. For the parameters delivered by steps a. and b. and the set-up defined in step c., the validation case can be performed.

With regard to the validation of discrete RCF models that consider the impact of SPD, the proposed procedure is seen to be of critical importance.

## 9 OUTLOOK

In the previous section (see section 8.3), the status quo of the DERC model was summarised (see Figure 103). In this section, an outlook is given on how the model can be developed in the future.

The next development step regards the RCF validation of the model. This includes the expansion of the material library of FCG parameters. The most desirable option is to have a broad set of experimental FCG data, i.e. for different rail materials and degrees of deformation. However, as the experimental derivation of FCG data for deformed rail steel is challenging and expensive, an alternative is to define a reliable method by which the missing data can be modelled on the basis of existing data sets.

The second step on the way to validation is to adopt the simplified model set-up defined in section 8.2, implement the FCG parameters for the corresponding degree of deformation and derive a weighting factor by means of a parameter study. In this way, the FCG rate of the model can be calibrated to the experimental result of the TD test.

Additionally, a concept is required how to assign FCG parameters of different FCG orientations to the grid. In this way, the material library can be exploited, and the anisotropy implied by SPD can be modelled. Finally, the RCF validation can be performed.

A paramount aspect of numerical simulation regards the efficiency of the algorithm, as it limits the model's performance and accuracy (see section 5.2.3). The latter is required for a better resolution of the crack development. Thus, an optimisation of the algorithm and the solver function to improve the efficiency is desired. With it, a better resolution around initial cracks and crack tips will be achievable.

The DERC model represents a special case of the peridynamic model family, where the grid's horizon is fixed. This effectively limits the grid layout and its accuracy. The introduction of a variable set-up of the horizon will contribute to a better resolution of FCG effects. However, this set-up will multiply the number of elements to be processed for a given grid dimension. Thus, the aspect of numerical efficiency must be considered carefully. Another benefit will be that the results of the model can be compared more easily to that of peridynamic models.

The DERC model represents a versatile platform to model discontinuities. One potential application is the modelling of damage due to phase transformation, i.e. white-etching-layers (WEL). This concept was already implemented by the application of pre-strains to elements, which were classified to be of WEL phase.

In this way, the residual stresses state after a martensite formation was modelled (90).

## 10 CONCLUSION

This work promotes the application of a hybrid Discrete Element Method- and Peridynamic modelling approach to model the anisotropy of rolling contact fatigue. The proposed DERC model is designed to simulate multiple rolling contact cycles, whereas a linear-elastic behaviour was assumed. A fatigue capability, based on a standard approach from the literature, was introduced.

The contribution of this work, especially for similar discrete model approaches, is that it evaluates common assumptions and inherent shortcomings, which regard the bond law in case of failure, the fatigue law, and its definition of the cyclic bond strain.

The common assumption of failure implies a complete removal of the element's load carrying capability. For the rolling contact case, this assumption was interpreted to be insufficient. Thus, a novel solution was developed, which assigns each failed bond a specific stiffness in the compressive regime. This model set-up was validated with respect to experimental crack closure experiments.

An important aspect of rolling contact fatigue regards severe plastic deformation, which is considered to have a dominant effect on the fatigue development. In order to address this anisotropy, the fatigue properties of relevant classes of undeformed- and deformed materials were parameterised. In this way, a material library, an interpolation to capture different degrees of deformations and a method to transfer these fatigue parameters to materials of similar strength were introduced.

A simplified set-up to validate the anisotropy of rolling contact fatigue was proposed. The result of the initial validation suggested a modification of the fatigue law, which emerged to be a standard application for Peridynamic models in the recent years. The modification regards a review of the cyclic bond strain definition and proposes a weighting of compressive strains. Based on that, a potential validation procedure was proposed.

Discrete models are considered to be of major importance to model the anisotropy of rolling contact fatigue. This work delivers a contribution to address key aspects of this emerging family of models.

## REFERENCES

1. Lewis R, Olofsson U. Wheel–rail interface handbook. 1st ed. Cambridge, UK: Woodhead publishing limited; 2009.
2. Callister W, Rethwisch D. Materials Science and Engineering. 9th ed. Hoboken, NJ, USA: John Wiley & Sons; 2014.
3. Franklin FJ, Garnham JE, Fletcher DI, Kapoor A. The evolution and failure of pearlitic microstructure in rail steel – observations and modelling. In: Wheel–rail interface handbook. 1st ed. Cambridge, UK: Woodhead publishing limited; 2009. p. 311–48.
4. Dylewski B, Risbet M, Bouvier S. The tridimensional gradient of microstructure in worn rails – Experimental characterization of plastic deformation accumulated by RCF. *Wear*. 2017;392–393:50–9.
5. Leitner T, Hohenwarter A, Pippan R. Anisotropy in fracture and fatigue resistance of pearlitic steels and its effect on the crack path. *Int J Fatigue*. 2019;124:528–36.
6. Garnham JE, Davis CL. Rail materials. In: Wheel–Rail Interface Handbook. 1st ed. Cambridge, UK: Woodhead publishing limited; 2009. p. 125–71.
7. Fletcher D., Franklin F., Kapoor A. Rail surface fatigue and wear. In: Wheel–Rail Interface Handbook. 1st ed. Cambridge, UK: Woodhead publishing limited; 2009. p. 280–310.
8. Trummer G, Marte C, Dietmaier P, Sommitsch C, Six K. Modeling surface rolling contact fatigue crack initiation taking severe plastic shear deformation into account. *Wear*. 2016;352–353:136–45.
9. Sadeghi F, Jalalahmadi B, Slack TS, Raje N, Arakere NK. A review of rolling contact fatigue. *J Tribol*. 2009;131:1–15.
10. Franklin FJ, Chung T, Kapoor A. Ratcheting and fatigue-led wear in rail-wheel contact. *Fatigue Fract Eng Mater Struct*. 2003;26(10):949–55.
11. Garnham JE, Davis CL. The role of deformed rail microstructure on rolling contact fatigue initiation. *Wear*. 2008;265(9–10):1363–72.

12. Franklin FJ, Garnham JE, Fletcher DI, Davis CL, Kapoor A. Modelling rail steel microstructure and its effect on crack initiation. *Wear*. 2008;265(9–10):1332–41.
13. Chowdhury P, Sehitoglu H. Mechanisms of fatigue crack growth - A critical digest of theoretical developments. *Fatigue Fract Eng Mater Struct*. 2016;39(6):652–74.
14. Leitner T. Fatigue crack growth of nanocrystalline and ultrafine grained metals processed by severe plastic deformation. Montanuniversität Leoben; 2017.
15. Anderson TL. *Fracture Mechanics - Fundamentals and Applications*. 3rd ed. Boca Raton, FL, USA: Taylor & Francis Group; 2005.
16. ASTM International. *Standard Test Method for Measurement of Fatigue Crack Growth Rates - E647*. West Conshohocken, PA, USA; 2019.
17. Zerbst U, Mädler K, Hintze H. Fracture mechanics in railway applications - An overview. *Eng Fract Mech*. 2005;72(2):163–94.
18. Toribio J, Matos JC, González B. A macro- and micro-approach to the anisotropic fatigue behaviour of hot-rolled and cold-drawn pearlitic steel. *Eng Fract Mech*. 2014;123:70–6.
19. Suresh S, Ritchie R. A geometric model for fatigue crack closure induced by fracture surface roughness under mode I displacements. Berkeley, CA, USA; 1982.
20. Fleck NA, Shin CS, Smith RA. Fatigue Crack Growth Under Compressive Loading. *Eng Fract Mech*. 1985;21(1):173–85.
21. Hermann R. Fatigue Crack Growth in Ductile Materials Under Cyclic Compressive Loading. *Fatigue Fract Eng Mater Struct*. 1994;17(1):93–103.
22. Kasaba K, Sano T, Kudo S, Shoji T, Katagiri K, Sato T. Fatigue crack growth under compressive loading. *J Nucl Mater*. 1998;258–263:2059–63.
23. Silva FS. The importance of compressive stresses on fatigue crack propagation rate. *Int J Fatigue*. 2005;27(10–12):1441–52.
24. Stoychev S, Kujawski D. Methods for crack opening load and crack tip

- shielding determination: A review. *Fatigue Fract Eng Mater Struct.* 2003;26(11):1053–67.
25. Romeiro FFJ, Domingos CA, De Freitas MJM. Measurement of fatigue crack closure for negative stress ratio. *ASTM Spec Tech Publ.* 1999;(1343):321–36.
  26. Januschewsky M, Trummer G, Six K, Lewis R. Discrete element modelling of rolling contact fatigue and crack closure with different bond laws. *Wear.* 2024;
  27. Franklin FJ, Kapoor A. Modelling wear and crack initiation in rails. *Proc Inst Mech Eng Part F J Rail Rapid Transit.* 2007;221(1):23–33.
  28. Vinogradov A, Estrin Y. Analytical and numerical approaches to modelling severe plastic deformation. *Prog Mater Sci.* 2018;95:172–242.
  29. Rege K, Lemu HG. A review of fatigue crack propagation modelling techniques using FEM and XFEM. *IOP Conf Ser Mater Sci Eng.* 2017;276(1).
  30. Larijani N, Kammerhofer C, Ekh M. Simulation of high pressure torsion tests of pearlitic steel. *J Mater Process Technol.* 2015;223:337–43.
  31. Larijani N, Brouzoulis J, Schilke M, Ekh M. The effect of anisotropy on crack propagation in pearlitic rail steel. *Wear.* 2014;314:57–68.
  32. Ghodrati M, Ahmadian M, Mirzaeifar R. Modeling of rolling contact fatigue in rails at the microstructural level. *Wear.* 2018;406–407:205–17.
  33. Park K, Paulino GH. Cohesive zone models: A critical review of traction-separation relationships across fracture surfaces. *Appl Mech Rev.* 2011;64(6).
  34. Kosteski L, Iturrioz I, Batista RG, Cisilino AP. The truss-like discrete element method in fracture and damage mechanics. *Eng Comput.* 2011;28(6):765–87.
  35. Hahn M, Bouriga M, Kröplin BH, Wallmersperger T. Life time prediction of metallic materials with the Discrete-Element-Method. *Comput Mater Sci.* 2013;71:146–56.



36. Cheng M, Liu W, Liu K. New discrete element models for elastoplastic problems. *Acta Mech Sin.* 2009;25(5):629–37.
37. Liu K, Liu W. Application of discrete element method for continuum dynamic problems. *Arch Appl Mech.* 2006;76(3–4):229–43.
38. Kosteski L, Barrios D'Ambra R, Iturrioz I. Crack propagation in elastic solids using the truss-like discrete element method. *Int J Fract.* 2012;174(2):139–61.
39. Zhu B, Feng R. Discrete solid element model applied to plasticity and dynamic crack propagation in continuous medium. *Comput Part Mech.* 2019;6(4):611–27.
40. Zhu B, Feng R. Investigation of a boundary simulation of continuity using the discrete solid element method. *Adv Mech Eng.* 2019;11(1):1–18.
41. Iturrioz I, Riera JD, Miguel LFF. Introduction of imperfections in the cubic mesh of the truss-like discrete element method. *Fatigue Fract Eng Mater Struct.* 2014;37(5):539–52.
42. Nguyen NHT, Bui HH, Nguyen GD, Kodikara J, Arooran S, Jitsangiam P. A thermodynamics-based cohesive model for discrete element modelling of fracture in cemented materials. *Int J Solids Struct.* 2017;117:159–76.
43. Raje N, Slack T, Sadeghi F. A discrete damage mechanics model for high cycle fatigue in polycrystalline materials subject to rolling contact. *Int J Fatigue.* 2009;31(2):346–60.
44. André D, Iordanoff I, Charles JL, Néauport J. Discrete element method to simulate continuous material by using the cohesive beam model. *Comput Methods Appl Mech Eng.* 2012;213–216:113–25.
45. Zhang G, Le Q, Loghin A, Subramaniyan A, Bobaru F. Validation of a peridynamic model for fatigue cracking. *Eng Fract Mech.* 2016;162:76–94.
46. Maheo L, Dau F, André D, Charles JL, Iordanoff I. A promising way to model cracks in composite using Discrete Element Method. *Compos Part B.* 2015;71:193–202.
47. Leonard BD, Sadeghi F, Shinde S, Mittelbach M. Rough surface and

- damage mechanics wear modeling using the combined finite-discrete element method. *Wear*. 2013;305(1–2):312–21.
48. Kostas LE, Riera JD, Iturrioz I, Singh RK, Kant T. Analysis of reinforced concrete plates subjected to impact employing the truss-like discrete element method. *Fatigue Fract Eng Mater Struct*. 2015;38(3):276–89.
  49. Silling S, Askari A. Peridynamic model for fatigue cracks. SANDIA Rep SAND2014-18590. 2014;1–40.
  50. Silling SA, Askari E. A meshfree method based on the peridynamic model of solid mechanics. *Comput Struct*. 2005;83(17–18):1526–35.
  51. Silling SA, Epton M, Weckner O, Xu J, Askari E. Peridynamic states and constitutive modeling. *J Elast*. 2007;88(2):151–84.
  52. Oterkus E, Guven I, Madenci E. Fatigue failure model with peridynamic theory. In: 2010 12th IEEE Intersociety Conference on Thermal and Thermomechanical Phenomena in Electronic Systems. IEEE; 2010.
  53. Freimanis A, Kaewunruen S. Peridynamic analysis of rail squats. *Appl Sci*. 2018;8(2299).
  54. Ma X, Wang L, Xu J, Feng Q, Liu L, Chen H. A two-dimensional ordinary state-based peridynamic model for surface fatigue crack propagation in railheads. *Eng Fract Mech*. 2022;265(November 2021).
  55. Karpenko O, Oterkus S, Oterkus E. Peridynamic analysis to investigate the influence of microstructure and porosity on fatigue crack propagation in Additively Manufactured Ti6Al4V. *Eng Fract Mech*. 2022;261(January):108212.
  56. Silling SA, Lehoucq RB. Peridynamic Theory of Solid Mechanics. *Adv Appl Mech*. 2010;44:73–168.
  57. Zhang G. Peridynamic models for fatigue and fracture in isotropic and in polycrystalline materials. PhD thesis. University of Nebraska; 2017.
  58. Ahadi A, Krochmal J. Anisotropic peridynamic model-formulation and implementation. *AIMS Mater Sci*. 2018;5(4):742–55.
  59. Ghajari M, Iannucci L, Curtis P. A peridynamic material model for the

- analysis of dynamic crack propagation in orthotropic media. *Comput Methods Appl Mech Eng.* 2014;276:431–52.
60. Hu YL, Madenci E. Bond-based peridynamic modeling of composite laminates with arbitrary fiber orientation and stacking sequence. *Compos Struct.* 2016;153:139–75.
  61. Diehl P, Prudhomme S, Lévesque M. A Review of Benchmark Experiments for the Validation of Peridynamics Models. *J Peridynamics Nonlocal Model.* 2019;1:14–35.
  62. Ghaffari MA. Multiscale modeling and simulation of rolling contact fatigue. The University of Iowa; 2016.
  63. Ma X, Xu J, Liu L, Wang P, Feng Q, Xu J. A 2D peridynamic model for fatigue crack initiation of railheads. *Int J Fatigue.* 2020;135(January):105536.
  64. Wang L, Sheng X, Luo J. A peridynamic frictional contact model for contact fatigue crack initiation and propagation. *Eng Fract Mech.* 2022;264:108338.
  65. Wang L, Sheng X, Luo J. A peridynamic damage-cumulative model for rolling contact fatigue. *Theor Appl Fract Mech.* 2022;121(June):103489.
  66. Littlewood DJ. Roadmap for Peridynamic Software Implementation. SANDIA Rep SAND2015-9013. 2015;
  67. Ghaffari MA, Xiao S. Peridynamic Modeling and Simulation of Rolling Contact Fatigue. *J Appl Mech Eng.* 2017;06(03).
  68. Gok E, Yolum U, Güler MA. Mode II and mixed mode delamination growth in composite materials using peridynamic theory. *Procedia Struct Integr.* 2020;28:2043–54.
  69. Franklin FJ, Widiyarta I, Kapoor A. Computer simulation of wear and rolling contact fatigue. *Wear.* 2001;250(251):949–55.
  70. Trummer G. Simulation und Prognose von Rollkontaktermüdung im Rad-Schiene-Kontakt. Technische Universität Graz; 2016.
  71. Ma X, Wang Y, Wang X, Yin W, Liu L, Xu J. Investigation on fatigue crack propagation behaviour of U71Mn and U75V rails using peridynamics. *Eng*

- Fract Mech. 2023;281:109097.
72. Madenci E, Oterkus S. Ordinary state-based peridynamics for plastic deformation according to von Mises yield criteria with isotropic hardening. *J Mech Phys Solids*. 2016;86:192–219.
  73. Pashazad H, Kharazi M. A peridynamic plastic model based on von Mises criteria with isotropic, kinematic and mixed hardenings under cyclic loading. *Int J Mech Sci*. 2019;156(March):182–204.
  74. Warren TL, Silling SA, Askari A, Weckner O, Epton MA, Xu J. A non-ordinary state-based peridynamic method to model solid material deformation and fracture. *Int J Solids Struct*. 2009;46(5):1186–95.
  75. Bazazzadeh S, Zaccariotto M, Galvanetto U. Fatigue degradation strategies to simulate crack propagation using peridynamic based computational methods. *Lat Am J Solids Struct*. 2019;16(2):1–31.
  76. Larijani N, Johansson G, Ekh M. Hybrid microemacromechanical modeling of anisotropy evolution in pearlitic steel. *Eur J Mech A/Solids*. 2013;38:38–47.
  77. Johnson KL. *Contact Mechanics*. 1st ed. Cambridge, UK: Cambridge University Press; 1987.
  78. Ulbrich H. *Technische Mechanik I - Stereostatik*. Fachschaft Maschinenbau - Technische Universität München, editor. München, Deutschland; 2003.
  79. MathWorks. Solve system of nonlinear equations - MATLAB fsolve [Internet]. [cited 2021 Aug 27]. Available from: <https://www.mathworks.com/help/optim/ug/fsolve.html#butbmfz-5>
  80. Kelly PA. *Solid Mechanics Part I: An Introduction to Solid Mechanics*. Solid Mech part 1 [Internet]. 2015;342. Available from: [http://homepages.engineering.auckland.ac.nz/~pkel015/SolidMechanicsBooks/Part\\_I/BookSM\\_Part\\_I/10\\_Viscoelasticity/10\\_Viscoelasticity\\_Complete.pdf](http://homepages.engineering.auckland.ac.nz/~pkel015/SolidMechanicsBooks/Part_I/BookSM_Part_I/10_Viscoelasticity/10_Viscoelasticity_Complete.pdf)
  81. Januschewsky M., Trummer G, Six K., Lewis R. CM 2022 : Modelling rolling contact fatigue cracking with a 2D truss-like discrete element method. In:

- 12th International Conference on Contact Mechanics and Wear of Rail/Wheel Systems: CM 2022. Melbourne, Australia; 2022.
82. Le Q V., Bobaru F. Surface corrections for peridynamic models in elasticity and fracture. *Comput Mech.* 2018;61(4):499–518.
  83. James MN, Sharpe WN. Closure Development and Crack Opening Displacement in the Short Crack Regime for Fine and Coarse Grained A533B Steel. *Fatigue Fract Eng Mater Struct.* 1989;12(4):347–61.
  84. Romeiro FF., Domingos CA, Freitas MJ. Measurement for fatigue crack closure for negative stress ratio. *ASTM Spec Tech Publ - Adv Fatigue Crack Clos Meas Anal (Second Vol.* 1999;1343:321–36.
  85. Leitner T, Trummer G, Pippan R, Hohenwarter A. Influence of severe plastic deformation and specimen orientation on the fatigue crack propagation behavior of a pearlitic steel. *Mater Sci Eng A.* 2018;710(July 2017):260–70.
  86. Suresh S. *Fatigue of Materials.* 2nd ed. Cambridge, UK: Cambridge University Press; 1998.
  87. Trummer G, Six K, Marte C, Meierhofer A, Sommitsch C. Automated measurement of near-surface plastic shear strain. In: *Second International Conference on Railway Technology.* 2014. p. 1–16.
  88. Freimanis A, Kaewunruen S, Ishida M. Peridynamics Modelling of Rail Surface Defects in Urban Railway and Metro Systems. In *Brno, Czech Republik: Symposium on Rail Infrastructure Systems Engineering;* 2018.
  89. Liu B, Wang K, Bao R, Sui F. The effects of  $\alpha/\beta$  phase interfaces on fatigue crack deflections in additively manufactured titanium alloy: A peridynamic study. Vol. 137, *International Journal of Fatigue.* 2020.
  90. Januschewsky M. Discrete element modelling of fatigue cracks at white etching layers. In *Gothenburg, Sweden: Charmec Conference 2022;* 2022.